



Mechanical Failure Risk Management for In-Service CSP Nitrate Hot Tanks

Timothy Pickle,¹ Chad Augustine,² and Zhenzhen Yu¹

1 Colorado School of Mines

2 National Renewable Energy Laboratory

**NREL is a national laboratory of the U.S. Department of Energy
Office of Energy Efficiency & Renewable Energy
Operated by the Alliance for Sustainable Energy, LLC**

This report is available at no cost from the National Renewable Energy Laboratory (NREL) at www.nrel.gov/publications.

Contract No. DE-AC36-08GO28308

**Technical Report
NREL/TP-5700-87615
February 2024**



Mechanical Failure Risk Management for In-Service CSP Nitrate Hot Tanks

Timothy Pickle,¹ Chad Augustine,² and Zhenzhen Yu¹

1 Colorado School of Mines

2 National Renewable Energy Laboratory

Suggested Citation

Pickle, Timothy, Chad Augustine, Zhenzhen Yu. 2024. *Mechanical Failure Risk Management for In-Service CSP Nitrate Hot Tanks*. Golden, CO: National Renewable Energy Laboratory. NREL/TP-5700-87615. <https://www.nrel.gov/docs/fy24osti/87615.pdf>.

**NREL is a national laboratory of the U.S. Department of Energy
Office of Energy Efficiency & Renewable Energy
Operated by the Alliance for Sustainable Energy, LLC**

This report is available at no cost from the National Renewable Energy Laboratory (NREL) at www.nrel.gov/publications.

Contract No. DE-AC36-08GO28308

Technical Report
NREL/TP-5700-87615
February 2024

National Renewable Energy Laboratory
15013 Denver West Parkway
Golden, CO 80401
303-275-3000 • www.nrel.gov

NOTICE

This work was authored in part by the National Renewable Energy Laboratory, operated by Alliance for Sustainable Energy, LLC, for the U.S. Department of Energy (DOE) under Contract No. DE-AC36-08GO28308. Funding provided by the U.S. Department of Energy Office of Energy Efficiency and Renewable Energy Solar Energy Technologies Office under grant # DE-EE00037373. The views expressed herein do not necessarily represent the views of the DOE or the U.S. Government.


This report is available at no cost from the National Renewable Energy Laboratory (NREL) at www.nrel.gov/publications.

U.S. Department of Energy (DOE) reports produced after 1991 and a growing number of pre-1991 documents are available free via www.OSTI.gov.

Cover Photos by Dennis Schroeder: (clockwise, left to right) NREL 51934, NREL 45897, NREL 42160, NREL 45891, NREL 48097, NREL 46526.

NREL prints on paper that contains recycled content.

Preface

Agency/Office/Program	DOE/EERE/Solar Energy Technology Office	
Award Number	DE-EE00037373	
Project Title	Mechanical Failure Risk Management for In-Service CSP Nitrate Hot Tanks	
Principal Investigator	Dr. Chad Augustine Senior Analyst chad.augustine@nrel.gov +1(303)384-7382	
Business Contact	Dr. Craig Turchi Thermal Energy Systems Group Manager Craig.Turchi@nrel.gov	
Submission Date	10/25/2023	
DUNS Number	8059480510000	
Recipient Organization	National Renewable Energy Laboratory	
Project Period	Start: 10/1/2020	End: 6/30/2023
Project Budget	Total \$\$ (DOE: \$525,000; C/S: \$0)	
Submitting Official Signature		

Acknowledgment

This work was authored by the National Renewable Energy Laboratory (NREL), operated by Alliance for Sustainable Energy, LLC, for the U.S. Department of Energy (DOE) under Contract No. DE-AC36-08GO28308. Funding provided by the U.S. DOE of Energy Efficiency and Renewable Energy's Office of Solar Energy Technologies Office.

This research used resources (HB-2B) at the High Flux Isotope Reactor, a DOE Office of Science User Facility operated by the Oak Ridge National Laboratory. Additional thanks to Dr. Jeffrey R Bunn, Dr. E. Andrew Payzant, Paris Cornwell, and Dr. Benjamin Schneiderman for beamline assistance at ORNL.

This research used microscopy resources funded through National Science Foundation grant #DMR-1828454.

Additional thanks to Sarah Harling and Karsten Anderson for performing manual welding experiments and Cameron Morey for metallurgical sample preparation.

Disclaimer

This report was prepared as an account of work sponsored by an agency of the United States Government. Neither the United States Government nor any agency thereof, nor any of their employees, makes any warranty, express or implied, or assumes any legal liability or responsibility for the accuracy, completeness, or usefulness of any information, apparatus, product, or process disclosed, or represents that its use would not infringe privately owned rights. Reference herein to any specific commercial product, process, or service by trade name, trademark, manufacturer, or otherwise does not necessarily constitute or imply its endorsement, recommendation, or favoring by the United States Government or any agency thereof. The views and opinions of authors expressed herein do not necessarily state or reflect those of the United States Government or any agency thereof.

Acronyms

AACEI	Association for the Advancement of Cost Engineering International
API	American Petroleum Institute
ASME	American Society of Mechanical Engineers
AWS	American Welding Society
BCC	body-centered cubic
CSM	Colorado School of Mines
CSP	concentrating solar power
DOE	U.S. Department of Energy
EBSD	electron backscatter diffraction
EDS	electron dispersive spectroscopy
FCAW	flux core arc welding
FEA	finite element analysis
FEM	finite element model
FZ	fusion zone
GB	grain boundary
GCB	gradient control band
GMAW	gas metal arc welding
HAZ	heat affected zone
HB	heat band
HIDRA	High Intensity Diffractometer for Residual Stress Analysis
hr	hour
IPF	Inverse pole figure
in	inch
LD	longitudinal direction
LMP	Larson Miller Parameter
LOM	light optical microscope
max	maximum
min	minute
ND	normal direction
NDE	non-destructive evaluation
NREL	National Renewable Energy Laboratory
OG	original

ORNL	Oak Ridge National Energy Laboratory
PA-UT	phased array-ultrasonic testing
PMZ	partially melted zone
PWHT	post weld heat treatment
RCF	refractory ceramic fiber
RT	room temperature
SB	soak band
SEI	secondary electron image
SEM	scanning electron microscope
SMAW	shielded metal arc welding (stick welding)
SRC	stress relaxation cracking
SS	stainless steel
TD	transverse direction
TES	thermal energy storage
UT	ultrasonic testing
UTS	ultimate tensile strength
YS	yield strength
WM	weld metal

Executive Summary

Stress relaxation cracking (SRC), or simply reheat cracking, can occur in structural alloy 347H stainless steel (SS) at temperatures above 540°C. SRC in structural welds of Generation 2 concentrating solar power (CSP) hot thermal energy storage (TES) tanks is a concern since 347H SS welds are susceptible at a service temperature of 565°C in a pressurized or high residual stress state. Post weld heat treatment (PWHT) conditions and alternative alloys are investigated as potential mitigation solutions to SRC. Optimized commercial PWHT configuration and parameters at a laboratory and field scale have been studied to minimize temperature variation within thick welded sections, demonstrate target stress reduction, and provide microstructure control to mitigate mechanical failure and SRC of hot tank walls. A cost-benefit analysis of PWHT for newly constructed hot tanks has been demonstrated in addition to a cost analysis of a Grade 92/347H SS clad system as another possibility for future Gen2 TES. Protocols for updating sections in American Society of Mechanical Engineering (ASME) code for PWHT in 347H SS welds have been provided and recommended. The key takeaways corresponding to welding fabrication, PWHT, and use of alternative fillers for existing and future generation TES tanks experiencing a service temperature of 565°C are:

For Existing Tanks of 347H SS:

1. PWHT may be feasible using 950°C as a peak temperature and 222°C/h based on finite element model simulations and susceptibility maps generated from SRC test using Gleeble.
 - a. Gleeble SRC test results indicate improvement to crack resistance after PWHT of lab and original weld (after three years of service for hot tank).
 - b. PWHT on repaired welds may be challenging due to even higher residual stresses.
 - c. Both-sided insulation, if access allows, should be used to reduce temperature gradients. Maintaining minimum PWHT temperature gradient recommendations based on the American Welding Society's (AWS) Standard D10.10 are critical to reduce crack susceptibility at temperature and during PWHT. Excessive gradients may facilitate cracking during PWHT, and insulation should not be removed until surrounding temperatures are ambient.
2. Weld inspection non-destructive evaluation (NDE) using phased array ultrasonic testing should be performed after welding, PWHT, and repair. If feasible, a periodic examination (e.g., annually) is recommended.
3. E16.8.2 filler could introduce lower peak residual stress in repairs than E347 filler and has demonstrated to have higher resistance to SRC.

For Future Tanks Being Manufactured With 347H SS

4. Weld design should be optimized, including floor plate layout, weld procedure, and joint geometry, to minimize residual stress.
5. Alternative E16.8.2 filler improves resistance to SRC in 347H SS fusion zones (FZ). However, further analysis on phase stability at 565°C would still be needed. BCC phases were observed after 24hr SRC test that are either diffusional α ferrite or displacive martensite upon cooling due to aging effects on austenite stability.

6. PWHT during manufacturing and prior to service may still be needed, since the 347H SS heat affected zone (HAZ) may still be susceptible to SRC even with E16.8.2 as a filler.

General Recommendations for Welding Procedures

7. Based on analysis of defects that are most concerning, reduce use of flux-based welding processes (i.e., shielded metal arc welding) to reduce slag inclusions. Instead, utilize gas tungsten arc welding for all root pass welds and a low heat input arc pulsation/oscillation gas metal arc welding method for filler passes.
8. Overall, arc current should be kept below 150 Amps to reduce weld heat input, especially during repair welding, and to control heat affected zone width and grain coarsening (coarser grains facilitate SRC in the heat affected zone).

Table of Contents

1	Introduction	1
2	Project Objectives	3
3	Background	4
3.1	347H Stainless Steel	4
3.2	347H SS Weldability and SRC	6
3.3	SRC Mitigation Solutions in 347H SS Welds	7
3.4	Summary of 33458 Results	10
3.5	Post Weld Heat Treatment Parameters and Code Limitations	25
3.6	Repair Welding	30
4	Project Results and Discussion	31
4.1	Milestone 1.1.1 Heat Transfer Limitations in PWHT with Ceramic Heating	32
4.2	Milestone 1.1.2 Heat Transfer Limitations in PWHT with Induction Heating	56
4.3	Milestone 1.2.1 PWHT Effects on Cracking Susceptibility	64
4.4	Milestone 1.3.1 Detection Capability of Phased Array UT Technique for Industrial-Scale Applications	73
4.5	Milestone 1.4.1 Cost-Benefit Analysis of PWHT for Existing and/or Newly Fabricated Hot-Salt Tanks	77
4.6	Milestone 1.5.1 Protocols for Updating ASME Code on PWHT of 347 SS Welds	78
4.7	Milestone 1.6.1 Cost Estimate and Technical Feasibility of a Grade 92/347H Clad Gen2 Hot Tank	80
4.8	Milestone 2.2.1 Metallurgical Characterization of Hot Storage Tank Field Samples	81
4.9	Milestone 2.2.2 Thermomechanical Testing of Field Sample Tanks Weldments	98
5	Significant Accomplishments and Conclusions	127
5.1	Conclusions	127
5.2	Key Takeaways	129
6	Budget and Schedule	131
7	Path Forward	133
8	Inventions, Patents, Publications, and Other Results	134
	Appendix: PWHT Memorandum to Crescent Dunes	137
	References	143

1 Introduction

The energy industry has adopted a thermal energy storage (TES) system as a functioning form of renewable and clean energy in concentrating solar plants (CSP). Specifically, the National Renewable Energy Laboratory (NREL) has developed a system of solar salt hot-and-cold tanks as seen in Figure 1 [1]. These molten nitrate salt TES tanks are of considerable interest because they allow for electricity generation when the sun is not shining, increasing the plant capacity factor, utilization of capital equipment, and total annual generation and reducing energy costs [1]. Due to the nature of the molten salt, the current temperatures experienced in the hot tanks during service are approximately 565°C. 347H stainless steel (SS) has been the prescribed alloy for this application due to best corrosion resistance, maximum allowable stress and sensitization resistance (intergranular corrosion) compared to other 3XX alloys (e.g., 304H SS).

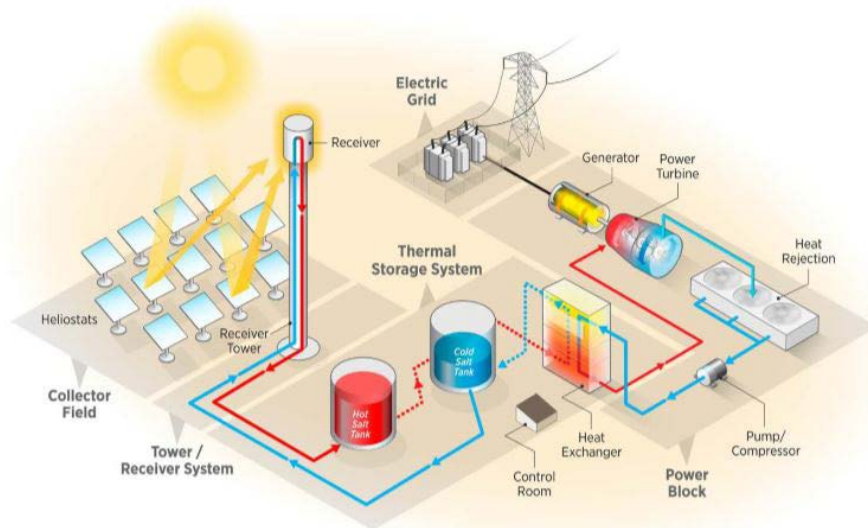


Figure 1. NREL Gen3 Roadmap TES Schematic [1]

The problem in welding of 347H SS occurs from stress relaxation cracking (SRC) or reheat cracking during service without prior stress relief [2-5] or during post weld heat treatment (PWHT) [6, 7] in trying to reduce residual stress. Elevated temperatures, where creep strain may develop, and a susceptible microstructure (both the heat affected zone (HAZ) and E347 fusion zone (FZ)) combined with sufficient stress leads to SRC. There are multiple root causes that can accelerate reheat cracking and SRC mechanisms, namely stress, whether it be internal (residual stress), external applied pressure (e.g., thermal stresses) or a combination of both. The time to failure depends on the specific component (accounting for temperature, stress, and location), which can take a few months to a few years for this catastrophic failure to unfold [5], where repair welding accelerates time to failure compared to an original weld. PWHT and alternative fillers (i.e., E16.8.2) provide some possible solutions to prevent SRC during elevated temperature service as investigated in previous project #33458. However, PWHT is typically not performed due to lack of requirements in ASME Boiler Pressure & Vessel codes, i.e., ASME Section II and VIII. However, nonmandatory Appendix A, ¶A-206 of Section II addresses SRC, draws attention to 347H as being susceptible, and notes Section I, PG-19 and Section VIII, Div. 1 UHA-44 were developed in part to minimize risk of relaxation cracking. The appendix UHA-A-4 in ASME Section VIII provides a recommendation for PWHT for thicknesses greater than ½", if deemed necessary, following Table

UHA-44 post forming solution anneal heat treatment temperature between 1,095°C –1,235°C. However, the PWHT temperatures regimes and thickness requirement in the ASME Section VIII UHA-A-4 may need adjustments based on cracking concerns for plates less than ½” thickness and low Larson Miller Parameter (LMP) with a 1,050°C temperature based on this study.

This project was funded under the DOE EERE FY21 Lab Call and seeks to address the pragmaticism of using localized PWHT on 347H SS weld components and non-destructive evaluation (NDE) techniques (specifically, phased array ultrasonic testing (PA-UT)) for regular field inspection. The project was a collaboration between NREL, the Colorado School of Mines (CSM), and Advisian, part of the Worley Group. This work may be used as a reference to update ASME Sections II and VIII codes on reheat cracking and PWHT of 347H SS welds. Additionally, field samples attained from service and the repair welding procedures are studied to understand the effect of repair welding, using matching E347 and alternative E16.8.2 filler, on SRC susceptibility. Using 347H as a thin cladder to a thick Gr91/Gr92 backer may be another possible solution instead of a 347H SS shell. A cost analysis is provided for both PWHT of 347H SS and a 347H SS/Gr92 cladded tank.

2 Project Objectives

The overarching goal of this project is to optimize cost-effective, thickness-dependent, localized PWHT procedures and to investigate feasible NDE methods at commercial scale for hot tanks in Gen2 CSP using 347H SS or clad systems with thin 347H plates as the cladder with thick Grade 92 as the backer.

The approach is to investigate lab-scale ceramic heat pads and induction heating methods for PWHT using finite element modeling (FEM) and experimental heat treatments on 2” thick plates/welds, phased array ultrasonic testing (UT) for NDE of reheat cracks after PWHT, and thermomechanical testing for demonstrating improved ductility after PWHT.

The detailed table for the period 1 six milestones and period 2 two milestones of the project are outlined in Table 1. The updated planned end dates reflect a no-cost time extension (NCTE) to the TWP that was requested by NREL and accepted by the U.S. Department of Energy’s Solar Energy Technology Office.

Table 1. Milestone table with start date, planned end dates and completion status

Milestone	Planned Start Date	Planned End Date (updated)	% Completion
Milestone 1.1.1 Identification of heating/cooling rates and temperature gradient limitations with ceramic pads and induction heating for industrial scale application	04/01/2021	12/31/2021	100%
Milestone 1.2.1 Demonstration of PWHT effects on cracking susceptibility control	07/01/2021	9/30/2022	100%
Milestone 1.3.1 Detection capability of phased array UT technique for industrial scale applications	07/01/2021	9/30/2022	100%
Milestone 1.4.1 Cost-benefit analysis of PWHT for existing and/or newly fabricated hot-salt tanks	07/01/2021	12/31/2022	100%
Milestone 1.5.1 Protocols for updating ASME code on PWHT of 347H SS welds	07/01/2021	12/31/2022	100%
Milestone 1.6.1 Cost estimate and technical feasibility of a Grade 92/347H clad Gen2 hot tank	10/01/2021	12/31/2022	100%
Milestone 2.2.1 Metallurgical characterization of hot storage tank field samples	06/01/2022	12/31/2022	100%
Milestone 2.2.2 Complete thermomechanical testing of field sample tank weldments at operational and elevated temperatures to determine threshold for SRC	07/01/2022	06/30/2023	100%

3 Background

This background section consists of a literature review of SRC in 347H SS, effects of PWHT, repair welding, and summary of previous SRC project results. The mitigation solutions of PWHT and alternative fillers are addressed and included in this project.

3.1 347H Stainless Steel

Austenitic stainless steels (SS) with good corrosion and creep resistance constitute many elevated temperature components in energy-related industries such as concentrating solar power (CSP) plants, where they are used in the construction of thermal energy hot storage tanks that contain molten nitrate salts at 565°C [1]. In the case of a corrosive environment, 347H SS is often selected over other 3XX grades for its resistance to stress corrosion cracking, due to the alloying addition of Nb that lowers sensitization tendency [8]. The chemical composition of chemical range allowed for 347H SS and the experimental substrate and filler metal compositions used for the project are tabulated in Table 2. The as-received condition for the substrate must follow the chemical composition guidelines from ASTM A240 [9]. The plates are conventionally casted and hot rolled to final thickness followed by solution anneal at 1,050–1,100°C (minimum) and water quenching. The typical microstructure consists of fine intragranular and coarse intergranular Nb carbonitrides (Nb (C,N)) and preferentially form over Cr carbides ($M_{23}C_6$) [2, 10]. 347H SS is essentially 304H SS with added Nb content to facilitate fine Nb (C,N) precipitates for precipitation strengthening at moderately elevated temperature and is typically chosen based on higher maximum allowable stresses in AME Section II-D [11].

The weld filler chemical compositions must follow AWS A5.9/5.9M specifications [12]. Both E347-16 and E16.8.2-15 filler compositions are reported in Table 2. Overall, E16.8.2 (16Cr-8Ni-2Mo) contains less Cr and Ni, more Mo, and lacks Nb. E16.8.2 has been shown to reduce solidification cracking reheat crack susceptibility with improved weldability for elevated temperature applications using 3XX austenitic stainless steel [13]. A study on E16.8.2 fillers showed that reducing Mo content from 2 to 1-1.2 wt% reduced potential for embrittling Chi phase to develop after extended aging times in 649–732°C aging temperature regime, and a reduction of Cr to ~16 wt% reduces the amount of δ -ferrite to facilitate sigma phase during aging [14]. With respect to E347-16, E16.8.2-15 would be less susceptible to elevated temperature embrittlement, which would theoretically improve weldability and crack resistance in the FZ.

Table 2. Chemical composition of hot-rolled plate substrates 347/347H SS and weld fillers (E347-16 and E16.8.2-15)

	Alloy	C	N	Ni	Cr	Mo	Mn	Nb + Ta	Ti	Co	Si	Cu	P	S
Code-allowable ranges (wt%)	347/347H ASTM A240 [9]	0.04-0.1	-	9-13	17-19	-	<2	8 x (C+N)	-	-	<0.75	-	<0.045	<0.03
	E347-16 AWS 5.9 [12]	0.08 max	-	9-11	19-21.5	<0.75	1-2.5	(10 x C) min-1.0 max	-	-	<0.65	<0.75	<0.03	<0.03
	E16.8.2-15 AWS A5.9 [12]	<0.1	-	7.5-9.5	14.5-16.5	1-2	1-2	-	-	-	0.3-0.65	<0.75	<0.03	<0.03
Experimental compositions (wt%)	347/347H 5/8" plate	0.05	0.031	9.11	17.29	0.3	1	0.58	-	-	0.51	0.21	0.029	0.002
	347/347H 2" plate	0.049	0.025	9.19	17.29	0.11	1.06	0.59	0.049	0.22	0.5	0.22	0.026	0.001
	E347-16 Excalibur	0.03	0.03	10.1	19.5	0.19	1.5	0.36	-	-	0.54	0.16	0.02	0.01
	E16.8.2-15	0.041	0.03	8.5	16	1.17	1.78	-	-	-	0.22	0.08	0.022	0.008

3.2 347H SS Weldability and SRC

The weldability challenges of 347H SS welds are summarized in Table 3. The weld location (FZ, HAZ, or partially melted zone (PMZ)), type of cracking, when cracking occurs, and some mitigation solutions are included. Sigma embrittlement and reheat cracking or SRC are the most concerning weldability challenges associated with the elevated temperature conditions of CSP technology. Overall, reduction of δ -ferrite to prevent development of embrittling phases in FZ (composition and phase control) and reduction in residual stress are two key mitigation solutions for improving elevated temperature weldability.

Table 3. Weldability summary of 347H SS welds

Weldability Issue	Locations	Type of Cracking	When?	Some Mitigation Techniques
Liquation Cracking [15-17]	PMZ/FZ	Hot	Welding	Lower C&F parameter (1/2Nb/(30C+50N)) (composition/phase control)
Ductility Dip Cracking [18, 19]	FZ (possibly HAZ)	Warm	Multi-pass welding and/or elevated T service	1. Tortuous grain boundaries (process control-low G/v ratio) 2. Promote new grain nucleation during solidification
Sigma Embrittlement [2, 3, 7, 20]	FZ	Warm	Service or PWHT	Reduction of δ -ferrite (composition/phase control)
Reheat Cracking/ SRC [2-7, 21]	FZ, PMZ/HAZ	Warm	Service or PWHT	1. Residual stress/restraint management (process control-welding and PWHT) 2. Alternative weld fillers (composition/phase control)

The cracking mechanism known as SRC may occur in 347H SS welds during service without prior stress relieving or during PWHT [3-8, 22-26]. SRC, often referred to as reheat cracking, consists of three main contributing factors: stress, temperature, and susceptible microstructure. More than 50 service failures were reported around the world concerning austenitic SSs (including 347H) and Ni-base alloy welds [4], and SRC was identified as the most likely failure mechanism for these alloys at elevated temperature (500°–750°C) and high-pressure service conditions [3-5, 8, 27].

Both the HAZ and FZ contain SRC susceptible microstructural features in 347H welds [3, 5, 8]. Microstructural evidence points to a mostly brittle, intergranular fracture surface likely stemming from creep cavities developing under stress over time. Precipitate free zones between the grain boundary precipitates and grain interior strengthened by fine intragranular precipitates [6,7] in the HAZ facilitate creep cavity development [4, 5, 22]. The primary precipitates in 347H SS are Nb (C,

N) in MX form that nucleate and grow mostly within the 700°–1,000°C temperature range, while secondary precipitates of M_6C and $M_{23}C_6$ may develop as well with slow cooling rates or extended elevated temperature service if the microstructure is not completely stabilized by Nb (C, N). δ -ferrite stringers in the as-received hot rolled and solutionized wrought plate have been reported to promote formation of Nb-rich and austenite eutectic phases in the HAZ of 347H [15]. Additionally, there have been reports of transformation-induced plasticity mechanisms allowing for α' martensite to be present in the HAZ of a two-pass weld pipe, where cracks developed during 595°C service temperature [26]. The FZ microstructure using matching E347 filler contains approximately 5–10 vol.% δ -ferrite in a ferritic-austenitic solidification mode with mostly skeletal ferrite morphology [8, 28]. δ -ferrite, sigma (σ) phase and the precipitates present could influence the SRC behavior in the FZ, including the reversion of solidified δ -ferrite [29], nucleation and growth of sigma after aging service conditions [20, 28, 30], and the precipitate interaction with grain boundaries. The morphological conditions of the weld FZ (e.g., grain boundary tortuosity) could impact the susceptibility to cracking as well.

The determination of threshold stress to crack as a function of temperature conditions and susceptible microstructural features would assist in potentially predicting time to failure in service and enable design of a PWHT procedure to mitigate SRC. At least three types of accelerated Gleeble stress relaxation tests with various materials have been developed and used by researchers to study the time to failure, usually within an 8-hour period [6, 24, 28, 31–33]. The temperature and stress/strain conditions needed for SRC to occur in 347H SS have been reported in a few studies with various test conditions [6, 7, 28]. Results indicate that SRC occurs over a temperature range of 700°–1,000°C at 10% plastic strain in the HAZ [6] or 70%–100% of the yield strength in as-welded 347 FZ [7]. It was also reported that higher stress generally led to more rapid failures in HAZ and FZ. The most recent study on SRC in 347 cross-welded samples did not show cracking using the 90%–95% yield strength values of the 347H substrate within an 8-hour period [28].

3.3 SRC Mitigation Solutions in 347H SS Welds

Post Weld Heat Treatment

PWHT has a dual purpose and benefits for components prior to elevated temperature service: 1) reduce residual stress, and 2) stabilization of microstructure [3, 8]. Two potential PWHT treatments from literature are 1) one-step isothermal 875°C for three hours, and 2) multi-step procedure with a stress relief, solutionize, and stabilization (optional) heat treatment. A multi-step process PWHT could be the best option for preventing SRC for thick 347/347H weldments, but the procedure must be carefully engineered to prevent relaxation cracking during PWHT. Parameters such as the heating rates, holding times, temperatures, and quenching rates are all important parameters that influence the final stress state and microstructure. A multi-step PWHT thermal cycle, using a three-step procedure, consists of 1) initial stress relief, 2) solutionizing microstructure and stress relief, and 3) stabilization of precipitates [8, 25, 34]. Figure 2 shows the overlay of PWHT temperatures and time relative to critical C-curve formation [3, 34]. The three-step PWHT method has been successful in industry for decades, with an example of a furnace PWHT schedule shown in Figure 3 [34].

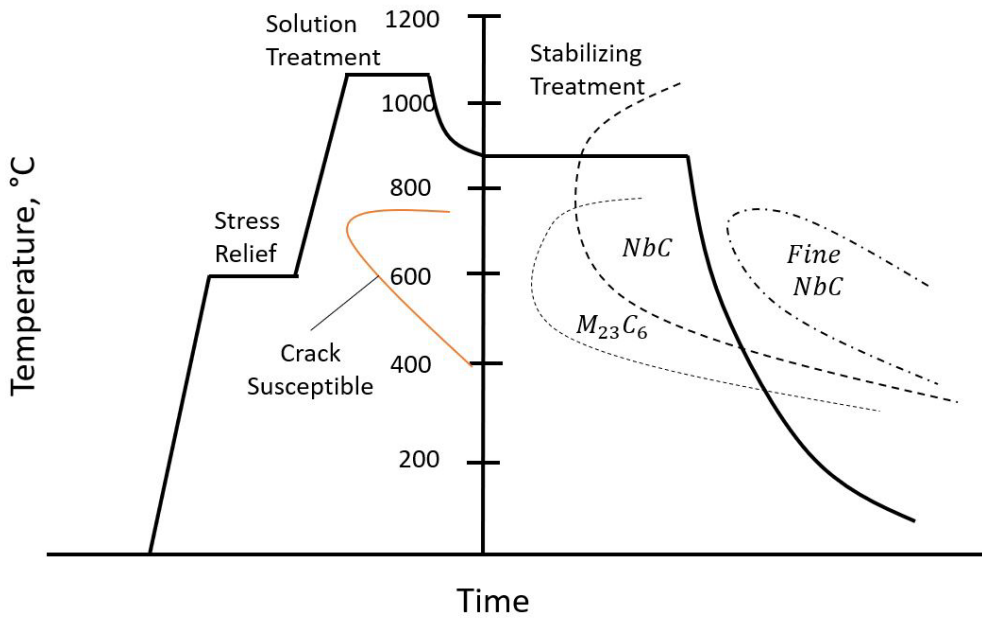


Figure 2. Multi-step PWHT overlaid on cracking and precipitation c-curves (adapted from [8])

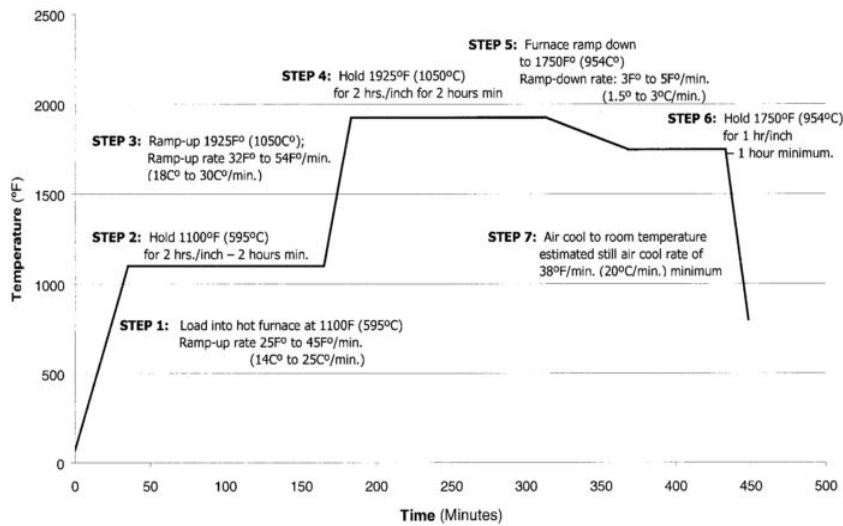


Figure 3. Example of 3-step PWHT treatment used for 347H SS welds [34]

Residual stresses and strains have been quantified in 12” long 347H SS welds in literature [25] as seen in Figure 4. The as-welded residual stresses were measured to be approximately 350 MPa. A tempering parameter (i.e., LMP) is used to incorporate both temperature and time effects on peak stress reduction. For example, 10,000 hours at 570°C reduced the stress from ~350 MPa to ~210 MPa, and a PWHT of 2 hours at 900°C resulted in a stress reduction to ~75 MPa (78% stress reduction). A higher temperature (e.g., 1,050°C) would theoretically reduce the residual stresses to near zero, but pragmatically a PWHT at too high of a temperature may be a challenge and could result in other issues. Therefore, this project’s work was to determine and identify a safe temperature window for PWHT of 347H SS welds.

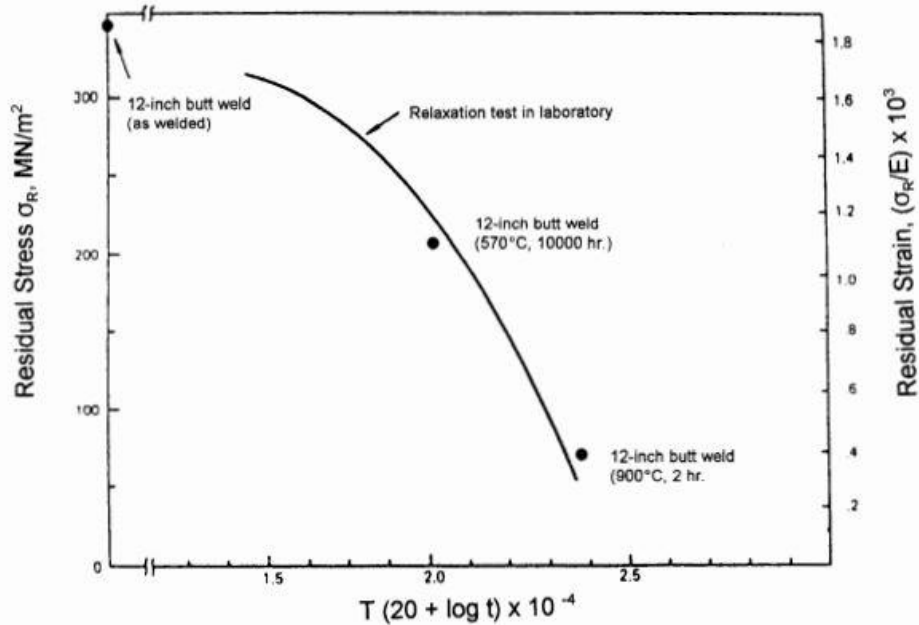


Figure 4. Residual stress reduction after 570°C at 10,000 hr and after PWHT at 900°C for 2 hr (taken from [2] which comes from [25])

Alternative E16.8.2 Filler

E16.8.2 has been prescribed as a filler that provides better resistance to elevated temperature embrittlement than the matching E347 filler. A recent study on weldability of E16.8.2 with respect to matching filler for 347H (E347) and 304H (E308H) SS alloys confirmed improvement in weld room temperature Charpy impact toughness values (absorbed energy needed to fracture samples), as seen in Figure 5 [28]. Specifically, the 347H/16-8-2 SS cross-weld toughness exceeded the 347H/347H (matching) cross-weld for both the as-welded condition and heat-treated conditions at 1,650°F (899°C) for 4 hours and 168 hours at temperature. The mechanisms that contributed to toughness reduction after heat treatment was attributed to sigma embrittlement. It should be noted that the adverse sigma embrittlement impact on toughness was observed more severely in the 304H/308H cross-weld samples with a heat treatment at 1,300°F (704°C) for 168 hr [28].

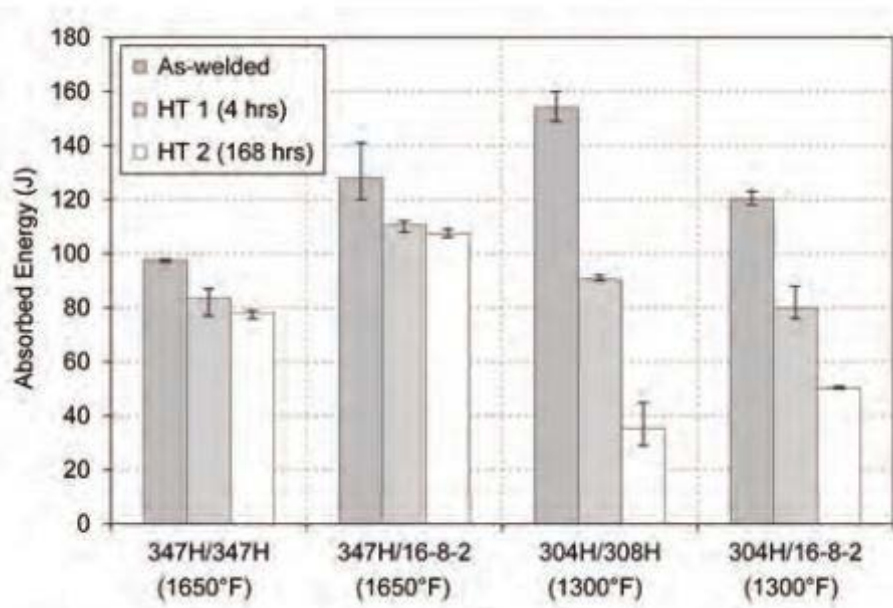


Figure 5. Demonstration of improvement in Charpy v notch toughness (absorbed energy) when using 16-8-2 as a weld filler for both 347H and 304H SS welds.

3.4 Summary of 33458 Results

The goal of work completed during the 33458 project was to determine the SRC or reheat cracking susceptibility using a Gleeble 3500 by discovering the critical stress/strain and time to failure as a function of elevated temperatures in both the physically simulated 347H HAZ and FZ, as demonstrated by the flow chart in Figure 6. First, weld procedures were procured and experimental welds were completed to provide weld geometry and weld parameter information for FEM simulation using Goldak double ellipsoid moving heat source [35]. The FEM provides the stress and strain values that can be then used as inputs for Gleeble 3500 SRC testing. Ultimately, by coupling the predicted residual stresses from a validated FEM [36] with the critical stress values, failure locations can be predicted. Determining stress-strain-temperature-time failure relationships was the ultimate objective.

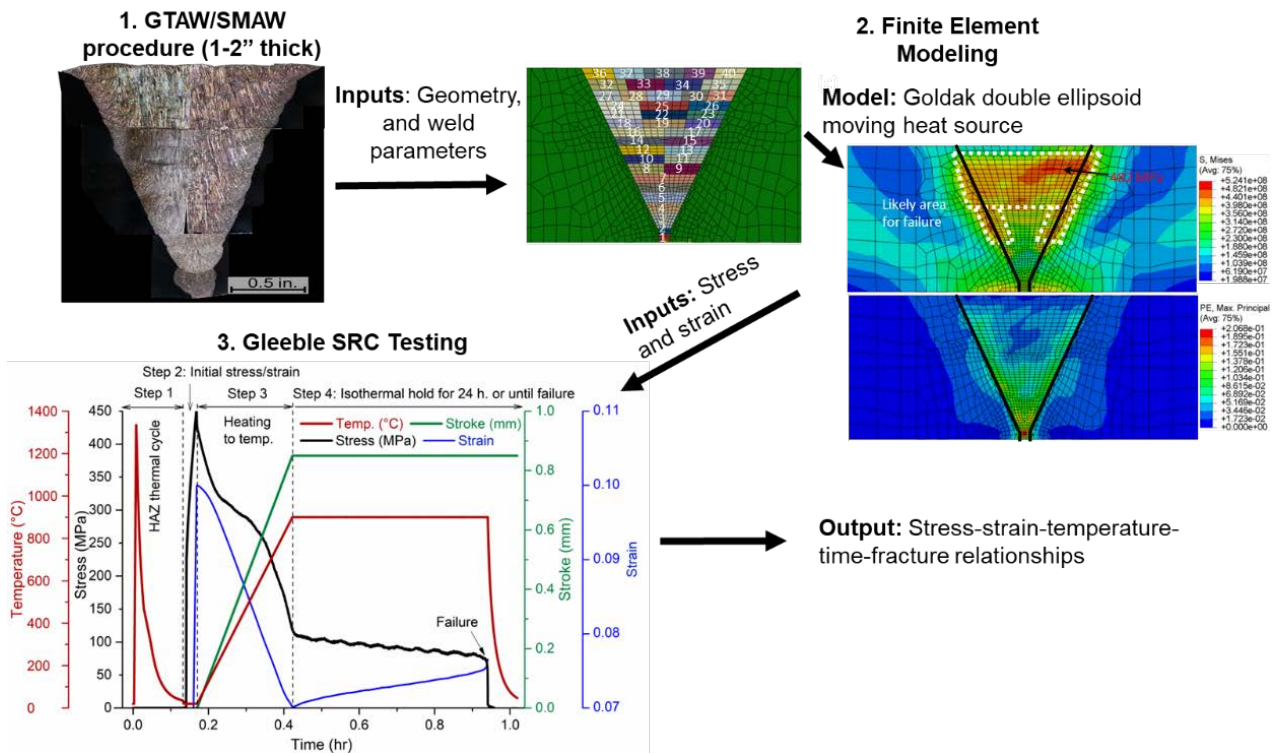


Figure 6. Flow chart of work completed in project 33458, including welding experiments, FEM, and Gleeble SRC testing

Microstructure of Weld and Physically Simulated HAZ and Weld E347 FZ

The physically simulated 1,335°C HAZ and weld microstructures (including HAZ and FZ) can be compared in light optical microscopy (LOM) images in Figure 7. A weld microstructure in a E347-347H SS weld, including FZ and HAZ, can be seen in Figure 7 (a). Liquefaction is observed between the HAZ and FZ that stems from δ -ferrite stringers, indicating presence of the PMZ. The physically simulated HAZ with a 1,335°C peak temperature is shown in Figure 7 (b), which seems to have similar liquation features and equiaxed grain morphology as seen in the weld HAZ in Figure 7 (a). The FZ microstructure region of interest is shown in Figure 7 (c), representing a part of FZ in extracted gauge section. The E347-16 microstructure shows evidence of a ferritic-austenitic solidification mode, meaning ferrite forms first in the melt followed by austenite solidification. The weld morphology consists of a mix of lathy and skeletal δ -ferrite, which is represented by the black etched features. The measured ferrite in the E347-16 FZ using a Feritescope was 10.8 ± 1.5 vol%. The grain morphology, secondary phases, and tortuosity may influence the susceptibility to reheat cracking in HAZ and E347 FZ.

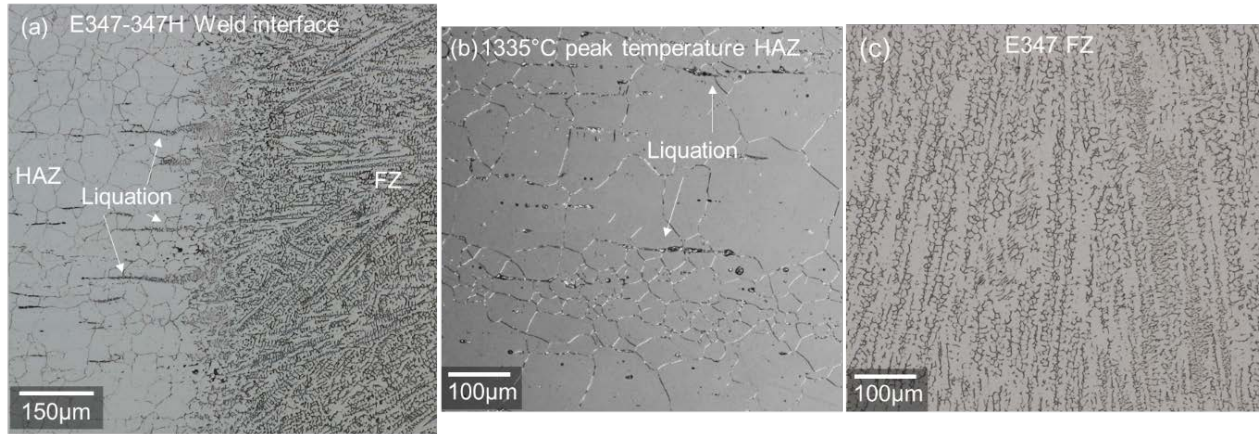


Figure 7. Light optical microscopy of weld microstructures of (a) weld FZ boundary region showing HAZ and FZ, (b) Gleeble 3500 physically simulated HAZ microstructure with 1,335°C peak temperature and (c) E347 FZ microstructure

FEM Results

The results in this section can be found in further detail in reference [36] and are briefly included here to summarize highlights of FEM stress models. Prior to extensive modeling simulation, model validation was first developed by comparing experimental strain measurements to FEM strain measurements as seen in Figure 8. Neutron diffraction strain measurements were conducted on 2” thick 347H stainless steel welds at Oak Ridge National Laboratory (ORNL) using the High Flux Isotope Reactor. The transverse direction (TD) and longitudinal direction (LD) setup orientations are shown in Figure 8 (a). For example, the TD strain FEM map is observed in Figure 8 (b), and the experimental TD strain values (normalized by compositional strain) are compared to the FEM in Figure 8 (c). Overall, there is good agreement between FEM and experimental strain values. Line 3 shows the least agreement, which can be affected by a large diffraction volume that averages residual stresses within the region as marked out by the yellow dotted box in Figure 8 (b).

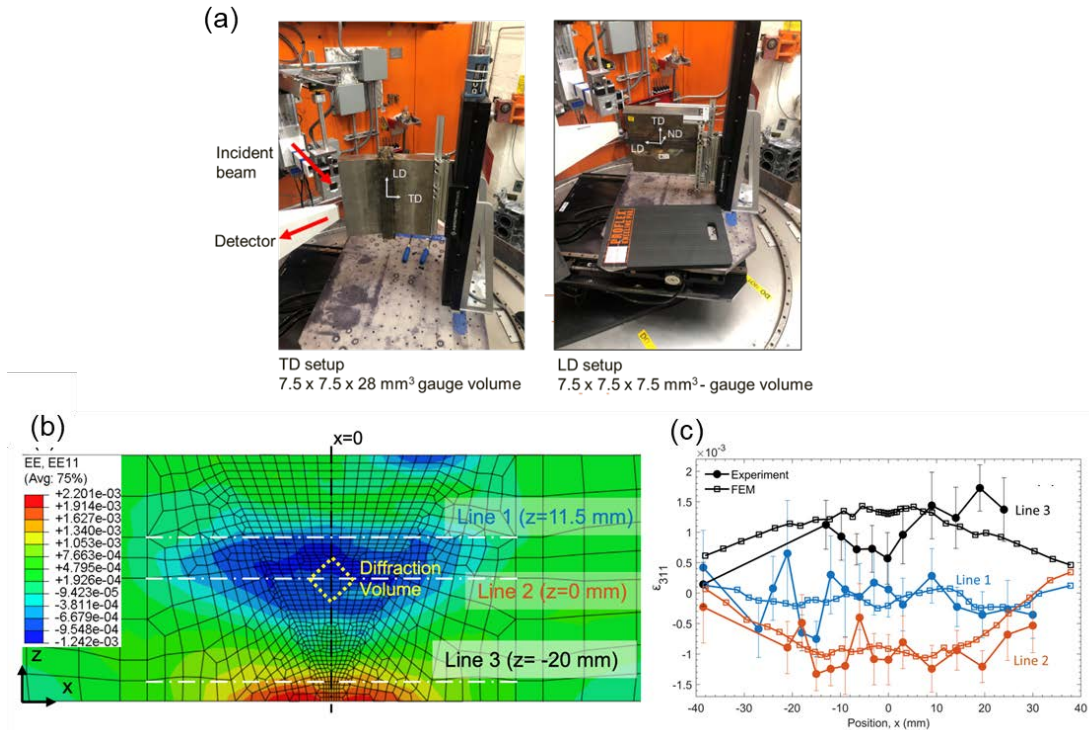


Figure 8. FEM model validation using (a) neutron diffraction HIDRA beamline at ORNL’s High Flux Isotope Reactor, (b) FEM transverse elastic strain (EE11), and (c) experimental transverse elastic strain compared to FEM elastic transverse strain (EE11). (b-c figures come from [36])

The von Mises stress of single V welds with 2”, 1”, and 0.5” thick welds are shown in Figure 9 (a-c). The highest stress distribution with highest peak stress values like sub-surface and with thinner welds are mostly concentrated in mid-thickness location. The ½” thick weld (seen in Figure 9 (c)) shows overall lower peak stresses and a lower stress concentration compared to 1 and 2” thick single V welds. It should be noted that the peak residual stress is highly dependent on the pass numbers and heat inputs used in welding procedures. Within the same thickness plate, fewer welding passes were observed to introduce higher residual stresses in the welds.

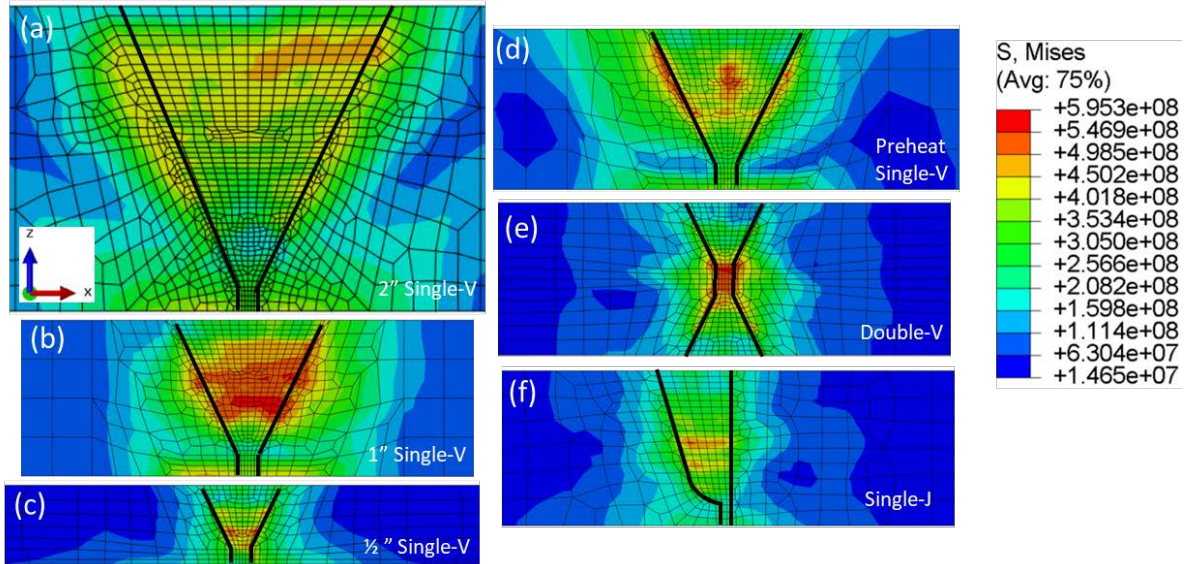


Figure 9. Effect of weld joint geometry, thickness, and preheat on von Mises residual stress. (a) 2" thick plate single V, (b) 1" thick plate single V, (c) ½" thick plate single V, (d) 1" thick single V w/ 232°C preheat and interpass temperature, (e) 1" thick plate double-V, and (f) 1" thick plate single J groove weld. (adapted from [36])

Alternative solutions to reduce residual stresses, such as preheating and using double-V and single-J grooves, are shown in Figure 9 (d-f). Preheating seems to reduce the extent of high stress in FZ, but HAZ stresses are still present. A double-V joint seems to reduce the area of highest stresses in comparison to single-V joint of similar thickness, but stresses are still high enough to possibly allow for cracking to develop in weld root. The single-J groove provides the best option in reducing overall residual stress, likely because of a significant reduction in weld passes and weld volume. Residual stress exceeding 400 MPa is still likely in all weld conditions, including ½" thick single-V and 1 thick single-J welds. Overall, single-J grooves are recommended in contrast to single-V and double-V grooves.

SRC Results of Lab-Generated 347H SS HAZ

This section summarizes the work completed on SRC in 347H SS HAZ, including new analysis since the 33458 project report. These updated figures and analysis are included in experimental publication submissions for 33458 papers.

SRC testing was completed on 1,150°C, 1,275°C, and 1,335°C peak temperature HAZ microstructure using Gleeble 3500. The procedure used can be seen in Figure 6, where the main variables are initial stress/strain (0.01-0.174) and temperature (750-1,050°C). An example of SRC test results in stress vs. time is shown in Figure 10 (a) for 1,335°C HAZ with 950°C test condition and varying initial plastic strains (0.05, 0.08, and 0.1). The HAZ SRC test results are summarized in a temperature and time-to-failure plot in Figure 10 (b). Increasing pre-strain generally results in faster times to failure for all temperatures as represented by the blue arrow in Figure 10 (b), which can be explained with a higher dislocation density and thus fast recrystallization and fine precipitate distributions resisting deformation. However, exceptions exist, primarily with 0.06 pre-strain at 900 and 950°C test temperature for 1,335°C HAZ, where 0.06 pre-strain failed at faster times than the 0.08 pre-strain. Further analysis of these tests

showed inconsistencies in extent of stress relief during reheating to temperature, where the 0.06 pre-strain sample had a higher stress upon reaching the SRC test temperature.

With respect to the various physically simulated HAZ peak temperatures using the 0.1 initial pre-strain condition, the 1,275°C tests failed slightly sooner than the 1,335°C samples using the same stress conditions at 900 and 850°C, while 1,150°C samples failed at slightly later times. This indicates there should be a potential minor difference in critical stress or pre-strain thresholds to cracking among the three HAZ subzone microstructures. The physically simulated coarse-grain HAZ (1,275°C) may be slightly more susceptible than the PMZ (1,335°C) and fine-grain HAZ (1,150°C) in terms of faster time to failure. Subtle variations in microstructure (e.g., grain size or liquation) may explain time to failure differences in SRC susceptibility, but most significantly, the pre-strain/stress, the development of susceptible microstructure during stress relief, and starting stress at reheat temperature strongly affect SRC susceptibility. Since weld-induced residual stress/strain could be comparable to the testing conditions [36], careful PWHT parameter design is needed, e.g., a slow heating rate or potentially the use of a multi-step PWHT process [25], to prevent SRC during PWHT in the 347H SS HAZ.

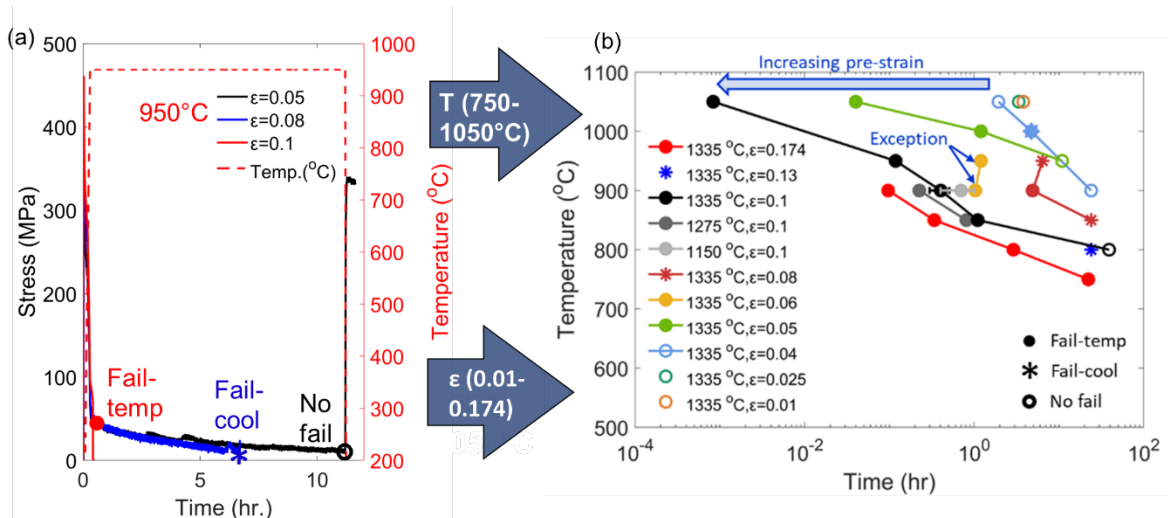


Figure 10. SRC curves for 950°C temperature condition as example and temperature-time plot grouped as a function of plastic strain for all 1,335°C HAZ tests

Figure 11 (a) illustrates the SRC failure conditions (i.e., susceptibility map) as a function of plastic strain and temperature. Linear fits were applied to outline and separate regions of samples that failed at temperature and the samples that did not fail, designated as high susceptibility and low susceptibility regions, respectively. The fitting indicates the critical pre-applied plastic strain to failure decreases from 0.15 at 800°C to 0.06 at 900°C, and temperatures between 900°C-1,050°C maintained a consistent value of 0.06. Overall, the biggest decrease in critical plastic strain occurs from 800°C to 900°C test temperature, and beyond 900°C the critical plastic strain to fracture remains relatively unchanged. To note, the critical plastic strain as a function of temperature accounts for both pre-strain at room temperature (RT) and plastic strain accumulation during heating and prior to reaching test temperature, which was determined from additional FEM modeling of the Gleeble experiment.

Figure 11 (b) shows the SRC map of plastic strain as a function of LMP. The LMP is a time-temperature formula that accounts for stress and temperature to creep rupture [37]. The LMP can be written as Eq. 1:

$$LMP = \frac{(T(K) * (C + \log(t(hr))))}{1,000} \quad (1)$$

where T is temperature in Kelvin, C is LMP constant (assuming C=20 [38]), and t is time in hours (h). Overall, the plastic strain to failure decreases with an increasing LMP, where samples with plastic strains below 0.06 did not fracture.

Figure 11 (c) shows the SRC map of prestress and starting stress upon reaching test temperature in step 4 as a function of test temperature. The critical prestress and starting stress at temperature can be represented as non-linear fits of the samples that did not fail at temperature, which outlines the lower susceptibility regions. The critical stress for starting stress at temperature ranges from ~180 MPa at 800°C to ~75 MPa at 950°C and ~50 MPa at 1,050°C. With increasing temperature, there is a lower tolerance for threshold stress to failure. Figure 11 (a) and (c) together serve as the SRC susceptibility map that determines the plastic strain and stress thresholds as a function of temperature below which low to no susceptibility to SRC is expected. Additionally, the prestress and starting stress at T as a function of LMP is plotted in Figure 11 (d), where the fitted lines represent the trends of time-temperature and stress relationship. The LMP fits show a general increase in LMP with decreasing stress, except samples tested at 1,050°C. The 1,050°C tests exhibit very short time (t) to failure with low critical stresses and the 1,050°C tests lie outside the general trend of decreasing stress with increasing LMP. It suggests the 347H SS HAZ should not experience long exposure at 1,050°C (e.g., during PWHT) due to the extreme short time to failure at a low stress.

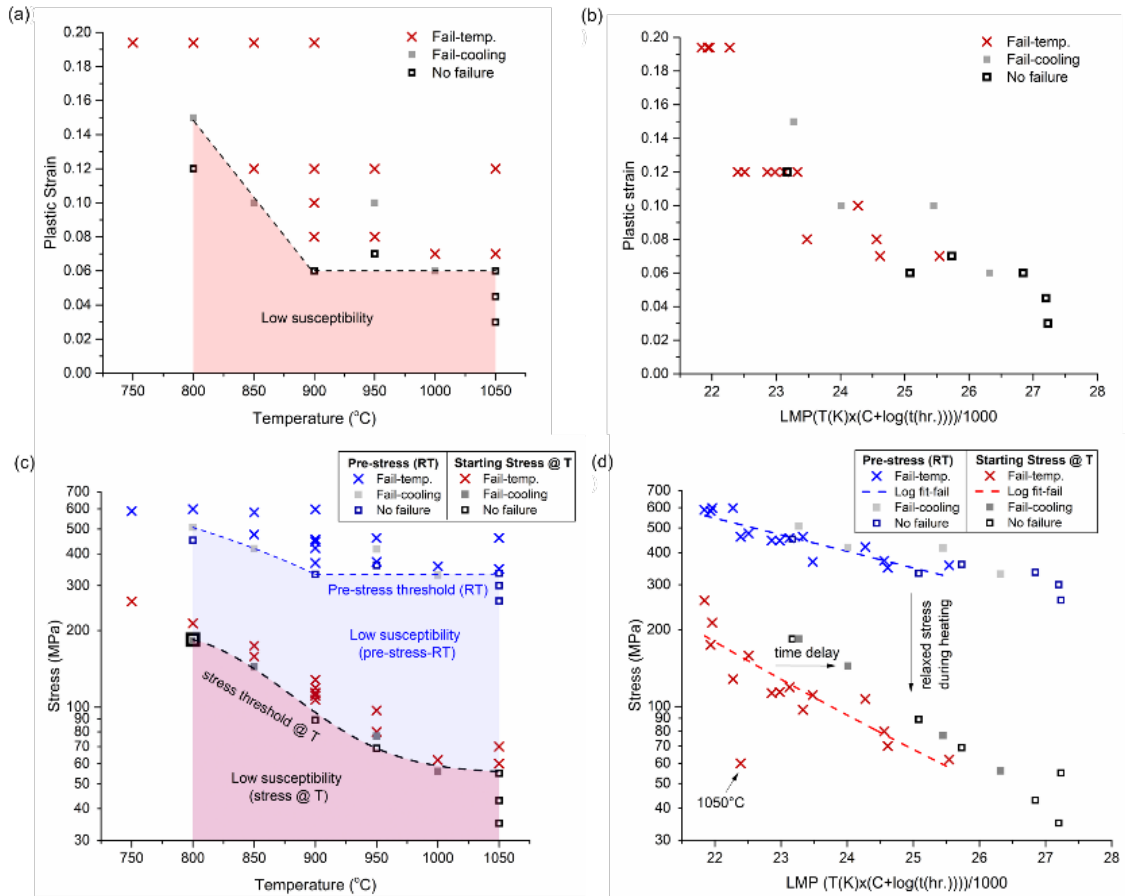


Figure 11. Stress-strain and temperature susceptibility maps (a) corrected plastic strain, as a function of temperature, (b) starting stress upon reaching test temperature (step 4) as a function of temperature, (c) plastic strain as a function of LMP and (d) starting stress upon reaching test temperature (step 4) as a function of LMP (C=20).

Figure 12 (a) illustrates the sensitivity of creep strain to fracture as a function of the plastic pre-strain normalized to the FEM corrected values. A Boltzmann power law fit was applied to the fractured samples, which reveals a sharp decrease and flatline in creep strain to fracture as plastic strain increases above 0.1. It indicates a low creep strain tolerance to cracking exists at plastic strains above 0.1. It should be noted that the pre-strain correlates to microhardness. An estimated pre-strain of 0.1 would yield an estimated minimum 200 HV microhardness based on interpolation of microhardness experimental values and from literature [6], where higher microhardness was reported to correlate with lower elevated temperature ductility.

Figure 12 (b) shows the relationship between average bulk creep strain rates (%/h.) and test temperature. The average creep strain rate monotonically increases with increasing test temperature and with increasing starting stresses at temperature. The first no failure/fail on cooling data points for each temperature were fit to show the threshold for where creep strain rates lead to fracture. The behavior of increasing creep rates as a function of temperature are inversely correlative with stress and plastic strain thresholds, as seen in Figure 11 (a & c).

A variety of creep mechanisms could explain the results from Figure 12. Strain recovery (improvement in ductility) is delayed due to competing mechanisms of dislocation recovery and

precipitation kinetics while at prime Nb (C, N) aging temperatures, such as the lower creep rates at 800-900°C conditions. Re-precipitation upon heating to temperature limits dislocation creep, allowing for Coble creep and grain boundary sliding. The 1,050°C samples with no failure and higher creep strain rates likely consist of Nabarro-Herring (diffusion based) with a homologous temperature of ~ 0.8 (T/T_m -melting temperature) and a creep parameter, n , approaching 1 (experimental $n=1.46$ @ 1,050°C), based on 316 SS [5, 39]. Improvement in creep ductility above 900°C may be due to thermal activation of dislocation or Nabarro-Herring creep, while grain boundary, Coble, creep is predicted to occur mostly during lower temperature tests (750-900°C) [39].

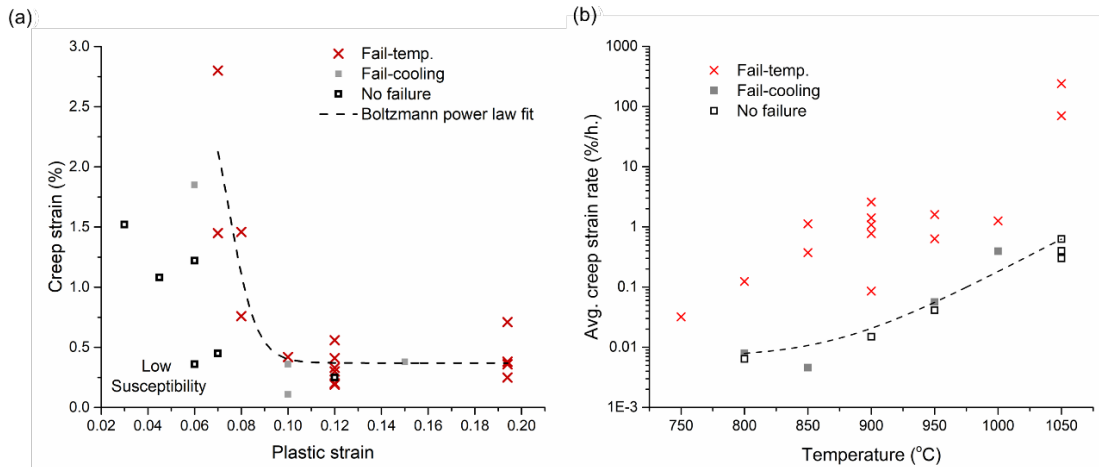


Figure 12. Creep strain as a function of plastic strain (a) and LMP (b) with respect to fail and no failure samples

The fracture surfaces of failed SRC specimens examined on the macro level exhibit many similarities as shown in Figure 13 (b-c), such as brittle intergranular fracture with micro voids on the grain boundaries. A cross sectional view along the tensile axis of the sample shows secondary cracks preceding the primary fracture surface in Figure 13 (e-h). Figure 13 (f, g) reveals wedge or w-type cracks in the 0.194 pre-strain specimen. Wedge cracks are indicative of grain boundary sliding, which is a common creep mechanism that can lead to intergranular failure at elevated temperatures with an applied stress [40]. The cracks initiate primarily transverse to the maximum applied stress direction, while there will be a combination of local shear and normal stresses, depending on the grain boundary orientation with respect to the tensile axis.

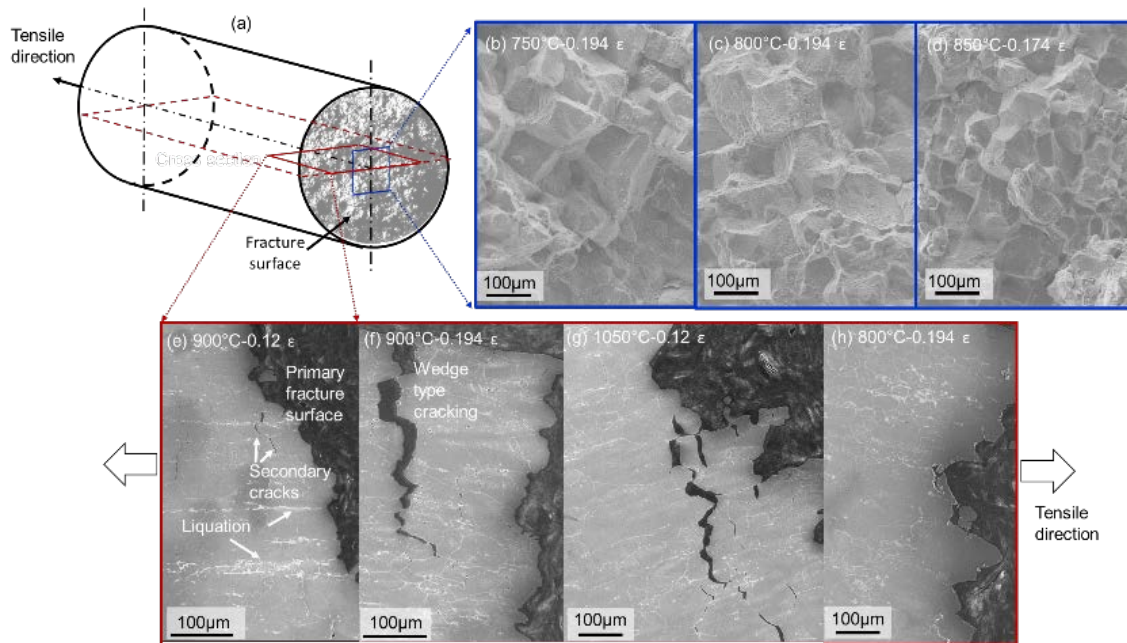


Figure 13. Microstructural features of fractured samples: (a) schematic of gauge section of tensile sample, (b-d) fracture surfaces in center of specimens tested at 750, 800, and 850°C with 0.194 plastic strain, and (e-h) secondary electron images (SEI) (etched) of cross section parallel to the tensile axis showing a mix of secondary cracks, liquation, and wedge type cracking along grain boundaries ahead of primary fracture surfaces

The microstructure after testing, particularly behind the primary fracture surfaces, shows the presence of grain boundary precipitates and secondary phases, as demonstrated in 800°C specimen with the highest strain conditions in Figure 14. The electron dispersive spectroscopy (EDS) line in Figure 14 shows an increase in Nb and Mo and depression in Fe, Cr, and Ni within the grain boundary precipitates that are likely Nb and Mo carbonitrides. Grain boundaries with coarse, incoherent Nb, Mo (C,N) precipitates may have high interfacial surface energy. The presence of microcracks seen on high magnification fracture surfaces and cross sections likely develop from dis-bonding between incoherent grain boundary Nb, Mo (C, N) and γ -austenite grains when under stress.

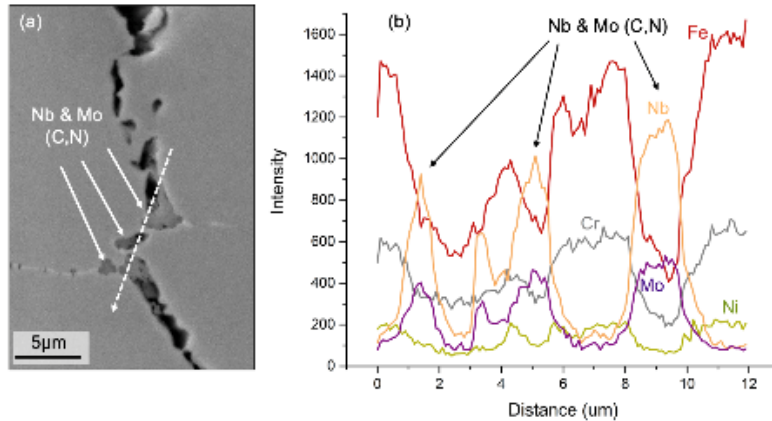


Figure 14. EDS line scan showing Nb and Mo rich carbonitrides along the microcracks of specimen tested at 800°C and 0.194 plastic strain (a) SEM-SEI micrograph (unetched), and (b) line scan of Fe, Nb, Cr, Mo, and Ni

SRC Susceptibility of 347H SS HAZ and E347 FZ

Similar initial stresses and test temperatures were applied for cross-welded E347-347H SS welds. The stress susceptibility map is illustrated in Figure 15(a), where the designated initial stress at room temperature is plotted as a function of test temperature for both the HAZ and cross-welded FZ, or weld metal (WM), microstructures. Samples that failed isothermally at temperature (solid dark symbols), failed on cooling (lighter solid symbols), and no failure (open symbols) are all summarized in Figure 15 (a). It was found that the E347 FZ in the transverse direction is susceptible to cracking at lower initial stresses compared to the HAZ at all testing temperatures. The susceptibility map suggests that the WM should have a lower tolerance for failure than the HAZ under the same testing conditions. For the E347 FZ, 950°C exhibits a slightly better resistance to cracking with a threshold stress of 279 MPa than 800°–900°C and 1,000°C with a threshold stress below 200 MPa (44% of the yield strength of FZ). The HAZ would require about 100 MPa more of initial stress for the same testing temperature of 950°C for cracking to occur. The physically simulated 1,335°C HAZ may have a steady decrease in critical stress (also proportional to cold work) as a function of temperature until 900°C when the critical stress/strain flatlines at higher temperatures. A postmortem characterization of one of the no-failure tests at 800°C in the HAZ indicated a progression of grain boundary voids (such as creep voids) that lead to the eventual microcracks while at the isothermal step (step 4), as seen in the optical micrograph in Figure 15 (a).

Coupling the critical stress values for cracking in 347H SS welds with FEM can assist with prediction of failure location, depending on the welding parameters. The von Mises stress profile of the 2” thick FEM, as seen in Figure 15 (b), shows the presence of overall highest stress regions of about ~480 MPa in the FZ and regions in the HAZ of the FEM with stress values exceeding 400 MPa. Details about the modeling procedure can be found in [36]. Stress contours from another FEM study [41] verify similar values of longitudinal stress (parallel to weld direction in the WM). Primarily, the top subsurface region highlighted by the white box in Figure 15 (b) and root area seem to be the most susceptible regions for SRC. Depending on the stress relaxation and redistribution behavior during reheating, the stress could evolve to possibly cause microscale localized stress rise, e.g., within precipitate free zones. It should be noted that the yield strength of the FZ is 450 MPa as tested along the transverse direction, which is just below

the predicted localized peak stress of 482 MPa (as marked by the blue dotted line in Figure 15 (a)). On the other hand, the physically simulated HAZ yield strength is about half of the FZ (225 MPa), and depending on the weld conditions and not assuming recovery and recrystallization during multi-pass welding, some HAZ strains and stresses can exceed 8% plastic strain and 400 MPa, as predicted in the FEM. In other words, studying the HAZ microstructure with 8% initial strain (400 MPa) would be representative of predicted HAZs in the field. Overall, initial stresses above 200 MPa in the FZ and above 300 MPa in the HAZ are concerning for SRC for the temperatures and tensile orientations studied. In literature, most failures were reported in the HAZ [3, 5, 8], likely because of a large fraction of the CGHAZ region experiencing residual stresses exceeding 400 MPa as illustrated in Figure 15 (b).

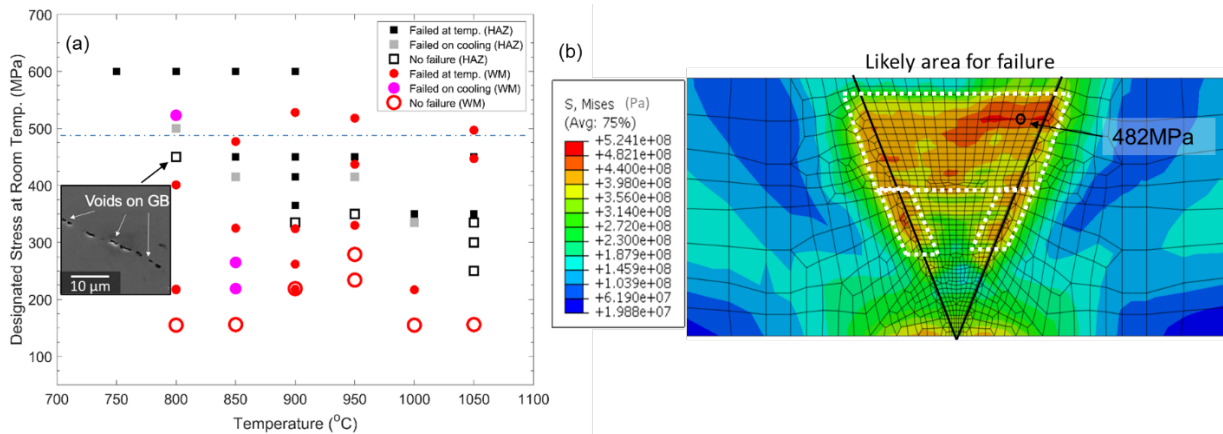


Figure 15. (a) Crack susceptibility map of initial applied stress as a function of test temperatures for 347H 1,335°C HAZ and E347-347H SS cross-welded samples with failure in the weld metal (WM) and (b) FE von Mises map of 2" thick single-V weld

Further analysis of the starting stress at temperature vs. test temperature SRC susceptibility map for both HAZ and E347 can be observed in Figure 16 (a). The main finding from this work was that critical stresses in the E347 FZ cross-welded orientation are lower than the HAZ for test temperatures between 800°–1,050°C. Figure 16 (b) illustrates the comparison between E347 FZ (or WM) and HAZ using both temperature and time using LMP. Based on starting stress values, the time to failure and LMP is less in E347 FZ than 347H HAZ. Similarly observed in Figure 11 (d), some E347-347H SS samples tested at 1,050°C showed rapid time to failure with low starting stresses at temperature (~40 MPa).

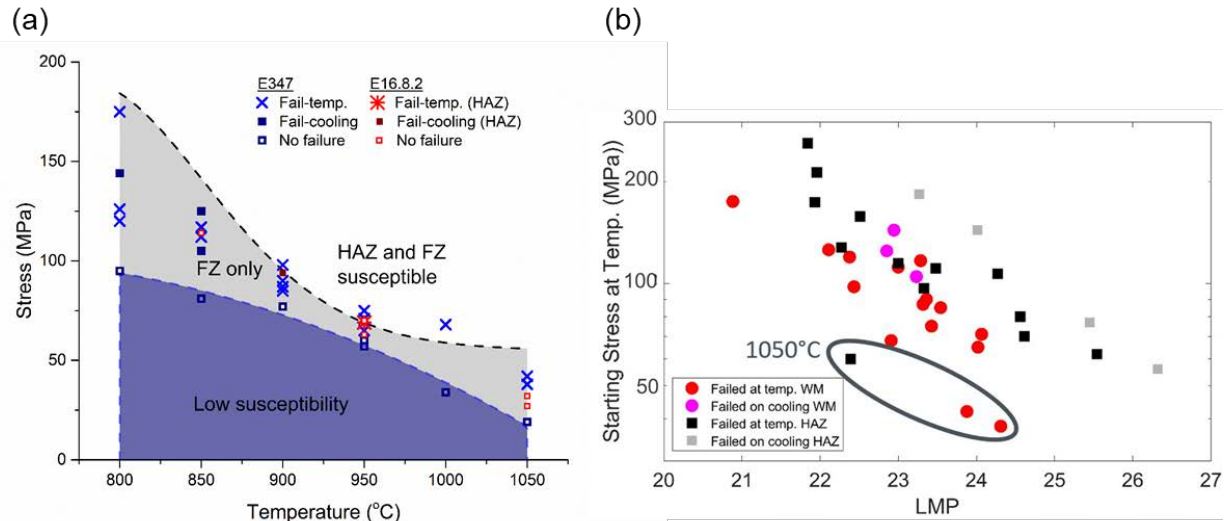


Figure 16. As-welded critical stress vs temperature for lab samples of 347H 1335°C HAZ, transverse E347 weld samples, and E16.8.2 weld samples; (b) Same stress values vs LMP of 347H HAZ and E347 weld metal

The secondary cracks of some test conditions were examined, and the presence of intergranular and interdendritic fracture was observed in the HAZ and FZ, respectively. Figure 17 shows the relationship of the tensile stress direction with respect to the microcracks, such that the microcracks primarily propagate perpendicular to the maximum stress direction. Some of the samples that did not fail during the test showed a progression of microcracks that is expected to develop into a primary fracture surface, as shown in Figure 17 (a). A significant amount of grain boundary voids (as small as $\sim 1\mu\text{m}$) was present at the center of the gauge length of the same sample. The subsurface secondary cracks for another HAZ sample tested at 800°C with a higher strain indicate coarse grain boundary Nb (C, N) precipitates as seen in Figure 17 (b) and based on electron dispersive spectroscopy (EDS) analysis. A precipitate free zone may be present in Figure 17 (b) between the grains and intergranular precipitates, but transmission electron microscopy imaging would be needed to confirm at higher resolutions. The coherency of the Nb (C, N) and austenite matrix exists at very small Nb (C, N) sizes ($<10\text{ nm}$ in diameter). Such coherency is lost when the Nb (C,N) precipitates coarsen above 10 nm because there is approximately an Nb (C,N)/ γ interface mismatch of 20% [8]. Thus, incoherent precipitates at grain boundaries may lead to creep voids when under sufficient stress during the isothermal period of the SRC test.

The cracks seem to mostly occur along interdendritic boundaries of the original solidification grain boundary in the FZ (Figure 17 (c–d)). While it seems that the solidification grain boundary is the most susceptible to cracking, migrated grain boundaries, if present, may be crack sensitive because they form more low tortuous grain boundaries during cooling from welding or during reheating in the Gleeble test. In the E347-16 FZ, the microstructure seems to have mostly a ferritic-austenitic solidification mode, where the first letter signifies what phase first develops a solid in the melt. The solidification rates and local composition (Cr/Ni equivalent ratio) determine which solidification mode and amount of ferrite ($\sim 10\%$ volume ferrite) develops in certain regions. For the 950°C sample that failed at 8.5 minutes in Figure 17 (d), there seems to be very little change in the microstructure from the as-welded ferritic-austenitic solidification

microstructure due to very limited diffusion of interdendritic elements. However, the 800°C that failed upon cooling after 24 hours at temperature showed possible evidence of sigma (σ) phase in the etched condition, which is typically seen as a darker etch (due to richer Cr content) than δ -ferrite, as seen in other similar microstructures confirmed in literature [28]. The ferrite-to-sigma transformation has been reported to take place most rapidly between 750° and 875°C with a minimum aging time of 2 hours [8]. However, electron backscatter diffraction (EBSD) is needed to confirm whether sigma (σ) phase develops during SRC testing at 800°C. The presence of sigma phase can greatly reduce the WM ductility for service temperatures. Re-resolutionizing δ -ferrite during PWHT may be desired to prevent service embrittlement, but this would require a temperature above 1,050°C. Based on SRC testing and results from Figure 15 and Figure 16, a temperature above 950°C may not be desirable.

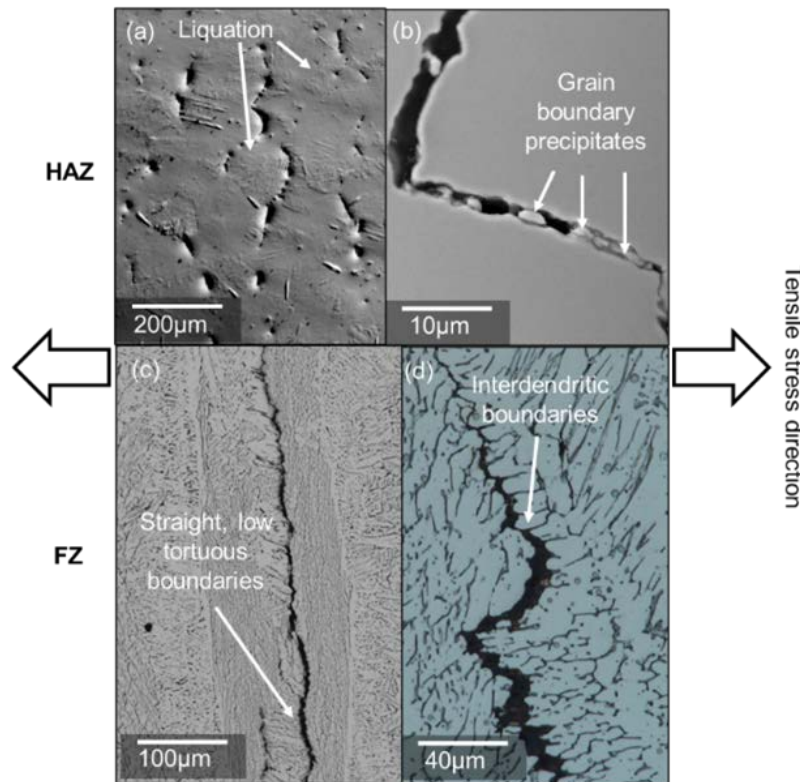


Figure 17. Secondary intergranular cracks in (a) HAZ with 800°C and 0.1 strain with polarized light in LOM, (b) SEI-SEM image of HAZ with 800°C and 0.174 strain, (c) LOM E347 FZ with 523°C and 800°C test temperature, and (d) LOM E347 FZ with 437 MPa initial stress and 950°C test temperature.

SRC Resistance of E16.8.2 FZ

Cross-welded E16.8.2-347H SS welds were completed using the same welding procedure for cross-welded E347-347H SS welds. An example of comparison between E347 and E16.8.2 FZ with an initial strain of 1% for 850 and 950°C can be seen in stress vs. time in Figure 18 (a and b), respectively. For the time duration of the test allowed, E16.8.2 did not fail. E347 FZ, on the other hand, failed within 4 hours using similar stress conditions. Additionally, the E16.8.2 starting stress at temperature can be seen in Figure 16 (a), where it appears that for similar stresses, cracking does not occur in the E16.8.2 FZ within a 24-hour period. All the E16.8.2-

347H SS samples with a failure icon cracked in the 347H HAZ instead of the E16.8.2 FZ, and those stress values are comparable to the HAZ critical stress threshold line for the physically simulated 1,335°C HAZ. The E16.8.2-347H SS cross weld samples preferentially failed in the 347H HAZ over E16.8.2 with extreme strain conditions (6% strain), as observed in Figure 18 (c). E16.8.2 has been demonstrated to resist cracking compared to E347 for elevated temperatures of 850°–1,050°C.

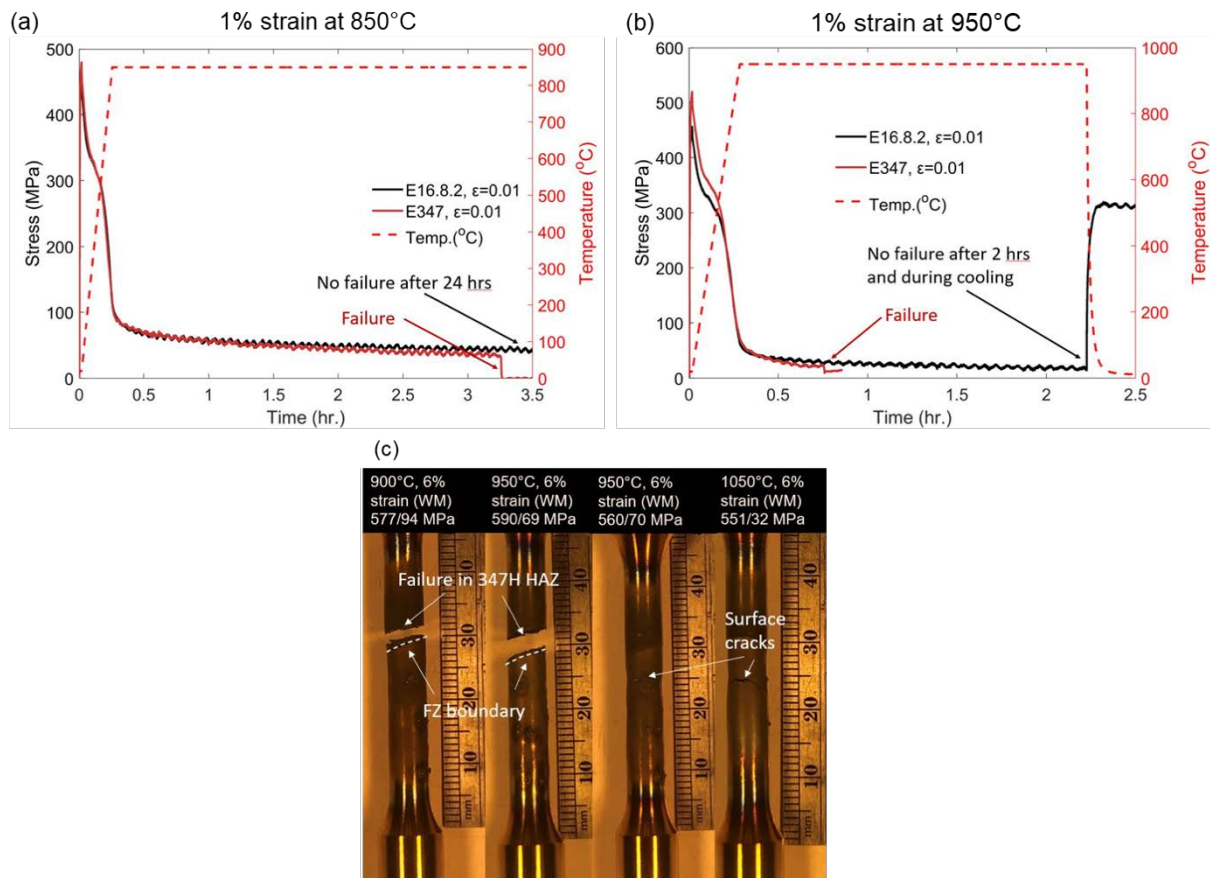


Figure 18. Comparison of SRC susceptibility between E347 and E16.8.2 FZ for (a) 1% strain at 850°C test condition (b) 1% strain at 950°C. (c) Demonstration of preferential cracking in 347H HAZ over E16.8.2 FZ for E16.8.2-347H SS cross weld samples.

Summary of Results for Project 33458

A few high-level conclusions were made based on work completed under project #33458, with a focus on identifying SRC susceptibility in general:

1. Residual stress prediction in FEM in combination of Gleeble SRC tests can predict failure susceptibility locations in the weld of E347-347H SS welds
2. J-groove reduces overall residual stress compared to single-V and double-V weld geometries with similar weld procedures.

3. E347 cross weld samples fail at lower critical stresses compared to HAZ, and E16.8.2 is more resistant than E347 to SRC. The 347H HAZ may still be susceptible to SRC with alternative fillers.

Work Planned for Project 37373

The work proposed for project 37373 was a continuation of 33458 with a focus on PWHT effectiveness and practical limitations and additional understanding of field based samples, including effects of repair welding:

1. PWHT simulation considering field application limitation in combination with SRC susceptibility maps to evaluate SRC susceptibility and provide recommended PWHT procedures.
2. Thermomechanical testing of PWHT lab and TES field samples, including repair welds, to verify similar SRC susceptibility in field samples, determine SRC resistance after PWHT, and determine repair welding effects on SRC susceptibility and residual stress.

3.5 Post Weld Heat Treatment Parameters and Code Limitations

The most common techniques for PWHT of pressure vessels are outlined in ASME Section VIII Division 1 and 2, with section UW-40a outlining eight possible PWHT methods, with furnace and localized heating being the most common methods [42]. The implementation of PWHT for large structural tanks is a challenge when intending to use furnaces. The main shell components of the thermal energy storage tanks are typically welded in the field. The tanks shell may be as large as 10 meters high by 40 meters in diameter with multiple seam and circumferential butt welds, as well as double sided fillet annular joints on the base of the tanks. From a practical point of view, complete immersion of the tank in a furnace (most recommended PWHT procedure [42]) is very unlikely due to the large size of the tank. However, localized methods of heating may be used via 1) ceramic heating pads, and 2) induction heating methods. The two methods and important parameters are introduced in this section as well as a brief review of PWHT used for 347H SS.

Review of PWHT of 347H SS Welds

Table 4 below details four slightly different schedules. Method 1 only includes the first two steps, while Method 3 includes only the first two steps with slightly slower rates. Method 4 uses higher heating rates than the first two steps [34]; however, heating rates are limited to a maximum of 444°C/hr divided by thickness in inches according to AWS D10.10: “Recommended Practices for Localized Heating of Welds in Piping and Tubing” [43]. Slower heating rates give time for grain boundary creep to occur along precipitate free zones, which may make it susceptible to brittle failure during stress relief at PWHT temperatures. Faster heating rates are argued to reduce cracking susceptibility because higher heating rates allow for the temperature-time slope to miss susceptible C-curve regions for failure [3, 44], but control of temperature gradients are important to reduce undesired thermal stresses redistribution. A range of heating rates will be investigated with FEM and combined with Gleeble crack susceptibility stress values to determine what heating rate is optimal to reduce crack susceptibility. Cooling rates are typically representative of air-cooling conditions and are more acceptable for PWHT having a third stabilization step, but there are minimum cooling rates needed to prevent any formation of $M_{23}C_6$ with maximum rates for preventing excessive thermal gradients. The

maximum cooling rate is 278°C/hr divided by thickness in inches, for localized PWHT under AWS D10.10 [43]. ASME B31.1 and Section III list similar requirements on heating and cooling rates, but the maximum allowed is highest for ASME B31.1 at 333°C/hr divided by half the thickness. The most important factor when selecting heating and cooling rates is to maintain stable temperature gradients, which will be discussed in the next section.

Table 4. Summary of a variety of PWHT schedules using multiple steps from literature

PWHT Steps	Purpose	Method 1 [8]	Method 2 [25]	Method 3 [8]	Method 4 [34]
Step 1a	Stress Relief	Ramp up to 593°C at 167°C/hr (2.8 °C/min)	Ramp up to 593°C at 167°C/hr (2.8°C/min)	Ramp up to 600°C at 150°C/hr (2.5°C/min)	Ramp up to 595°C at a rate of 840-1,500°C/hr (14-25°C/min)
Step 1b	Stress Relief	Hold at 593°C for 2 hr	Hold at 593°C for 2 hr	Hold at 600°C for 2 hr	Hold at 595°C for 2 hr/in (4 hr for 2 in thick)
Step 2a	Solutionize	Ramp up to 1,052°C at 333°C/hr (5.55°C/min)	Ramp up to 1,052°C at 333°C/hr (5.55°C/min)	Ramp up to 1,050°C at 315°C/hr (5.25°C/min)	Ramp up to 1,050°C at 18-30°C/min
Step 2b	Solutionize	Hold at 1052°C for 2 hr	Hold at 1052°C for 2 hr	Hold at 1052°C for 2 hr	Hold at 1050°C for 2 hr/in
Step 3a	Stabilize	None	Air cool to 900°C	none	Ramp down to 954°C at 1.5-3°C/min
Step 3b	Stabilize	None	Hold at 900°C (no time specified)	none	Hold at 954°C for 1 hr/in
Step 3c	Finish PWHT	Air cool to room temperature	Air cool to room temperature	Air cool to room temperature	Air cool to room temperature at a minimum rate of 20°C/min

Based on the 33458 SRC project, the soak temperatures for PWHT, including the first and second step PWHT, was driven by the susceptibility map obtained from the Gleeble thermomechanical tests, particularly Figure 15 (a) where the initial stress required for cracking in both HAZ and FZ was best at 950°C compared to 900 and 1,000°C. The recommended first step soak temperature is 600°C, and the second step soak temperature is 950°C. The heating rates are driven by two requirements: 1) maintaining a stable minimum temperature gradient based on codes for mechanical stability, and 2) reduction of stress to below the critical stress at temperature prior to reaching temperature. Keeping those two requirements in mind, a proper heating and cooling rate is desired to avoid SRC occurring during PWHT and maintain the same temperature gradient upon cooling, particularly at temperatures above 427°C [43].

Recommended maximum heating and cooling rates are summarized according to separate codes in Table 5. AWS D10.10 provides an intermediate ranking of allowed heating and cooling rates for localized PWHT. For example, PWHT of a 2" thick weld would restrict the heating rate to 222°C/hr and cooling rate to 139°C/hr. Some codes allow for more leniency at temperatures

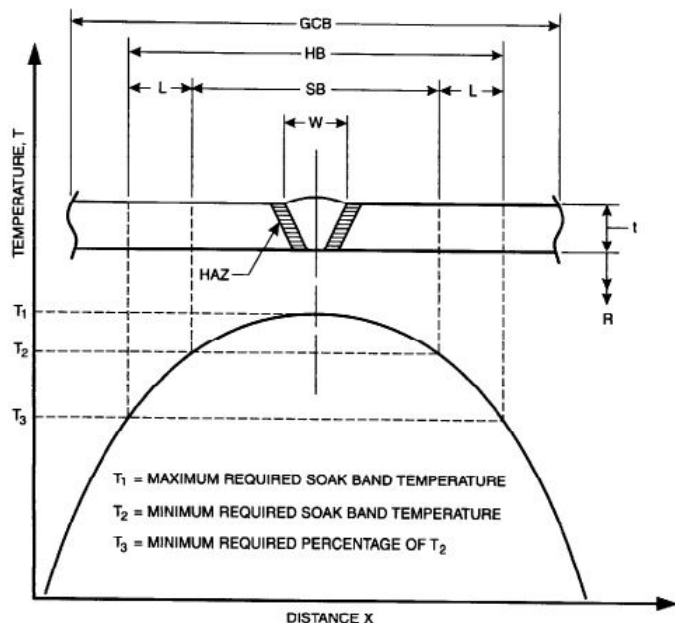
below 427°C where the heating and cooling rates are not restricted. However, there should be some caution with not controlling heating and cooling rates even below 427°C because of sufficient thermal stresses that can rise with fast abrupt cooling conditions.

Table 5. Summary of recommended maximum heating and cooling rates as a function of thickness associated with ASME and AWS codes

Fabrication Code	Maximum Heating Rates	Maximum Cooling Rates	Ranking of Rates
B31.1	333°C/hr/0.5t (inches) above 316°C (333°C/hr/ max)	333°C/hr/0.5t (inches): e.g., 2 in thickness above 316°C would be 333°C/hr	Maximum
ASME Section III Subsection NB	222°C/hr/t (in) above 427°C (222°C/hr/max)	222°C/hr/t (in) above 427°C (222°C/hr/ max); 55°C/hr minimum	Lowest
AWS D10.10	444°C/hr/t (in) using heat band width recommendations	278°C/hr/t (in) using heat band width recommendations	Intermediate

Localized Ceramic Heating

Localized heating using ceramic pads involves three main regions: 1) soak band (SB), 2) heated band (HB), and 3) gradient control band (GCB), as seen in Figure 19. The SB contains a peak temperature T_1 in the center of the weld and a minimum temperature T_2 on the SB boundary, which is desired to be no more than 55°C lower than the peak temperature T_1 . The heated band width is typically the width of the ceramic heat source and can be defined by the width where its temperature, T_3 , is a minimum of one-half the value of T_2 . As an example, for a T_2 temperature of 895°C, the minimum temperature drop allowed at T_3 is 448°C. The length of the HB is usually $SB + 4 \times \sqrt{Rt}$ where t is the thickness and R is the inside radius of the piping or vessel, or can be $SB + 2$ in, whichever is larger. However, there are variations of recommendations on how wide the HB (or heat source) could be, which would depend on the geometries of the weld and type of weld, such as flanges, annular welds, overlapping welds, spacing between welds, etc. The GCB width includes the full insulation surface and is typically the HB width plus $4 \times \sqrt{Rt}$. With very large R and t , the GCB could be relatively large. The intention of the GCB length is to ensure the temperature difference between the edge of SB and HB is kept below half of T_2 , meaning $T_3 > \frac{1}{2} T_2$. For double sided insulation, the HB and GCB may be smaller in width since the temperature gradient within the thickness direction would be better controlled. Table 6 summarizes the minimum SB, HB, and GCB width calculations for a pressure vessel (in this case pipe relevant dimensions).



Nomenclature:
W = Widest width of butt or attachment weld.
HAZ = Heat-affected zone.
SB = Soak band (width of the volume of the material where the holding temperature equals or exceeds the minimum and equals or is below the maximum required. The minimum width is typically specified as W plus a multiple of t on each side of the weld).
L = Minimum distance over which the temperature may drop to a percentage of that at the edge of the soak band.
HB = Heated band (width of heat source).
GCB = Gradient control band (minimum width of insulation and/or gradient heat source).
t = Nominal thickness of piping, branch connection, nozzle neck, or attachment.
R = Inside radius of piping, branch connection, or nozzle neck.

Figure 19. Schematic diagram for description of ceramic localized heating with a parabolic temperature distribution of a single-V groove shell weld or pipe [43]

Table 6. Description and definitions of soak band (SB), heated band (BD), and gradient control band (GCB)

Region	Minimum Width
Soak Band (SB) [42]	$4t+w$ (~9-10inches)
Heated Band (HB) [43, 45]	Larger of 1. $SB+2$ inch 2. $\frac{Ht \left[\frac{OD^2-ID^2}{2} + (ID)(SB) \right]}{OD}$ 3. $SB+4\sqrt{Rt}$ inch
Gradient Control Band (GCB) [43, 45]	$HB+4\sqrt{Rt}$ inch

Localized Induction Heating

The main benefit of using induction heating methods is the fast heating rates through the thickness of the weld without needing conduction to heat up. Some parameters are discussed here for relevance of experimental design. The induction heating coils, generally consisting of

copper hollow tubes that are water cooled, have a high alternating current passing through them that generates a magnetic field that penetrates the weld. The magnetic field induces currents in the material that leads to increased resistance and heating in the sub-surface location of the material. An example of an induction heating of a pipe is shown in Figure 20, where a layer of insulation lies between the weld surface and induction coils.

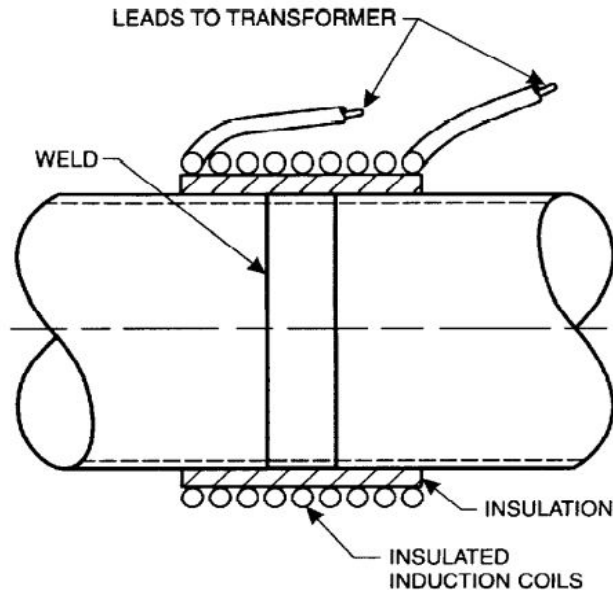


Figure 20. Schematic depiction of induction coil setup on a pipe weld [43]

For thick materials, the frequency of the alternating current affects the depth at which the magnetic field penetrates the surface of the plates [43]. Lower frequencies increase the penetration of the currents that help generate the resistive heating subs-surface. Higher frequencies reduce the penetration of the currents, and the surface is heated faster than the mid-thickness. Increasing the current and the number of coil turns increase the energy input and are needed to increase the temperature in the mid-thickness, which may be a challenge for non-ferromagnetic austenitic stainless steel [43]. Also, the width of the coil relative to the weld width is dependent on the radius and thickness of the plate, which is $3 \times \text{sqrt}(Rt)$ [43]. An optimization of the induction heating unit, including frequency, current, coil turns, and coil width are needed to meet AWS D10.10 and ASME code localized PWHT guidelines, including temperature gradients.

The main limitation of induction heating in thick welds is the skin effect, which can be described with the following relationship in Eq. 2:

$$\delta = \sqrt{\frac{\rho}{\pi \mu_0 \mu_r f}} \quad (2)$$

where δ is current penetration depth, ρ is material resistivity (material property), μ_0 is magnetic permeability (material property), and f is alternating current (AC) frequency of coil (process parameter). The main controllable parameter that affects eddy current density is frequency,

where smaller AC frequencies result in a larger skin effect, which would be proportional to a reduced temperature gradient.

3.6 Repair Welding

The objective of this new subtask was to ultimately perform more SRC tests on field samples and compare results to lab-produced samples, including the 1) original condition samples, 2) PWHT samples and 3) repair welded samples. Prior to machining the field samples, repair welds with E16.8.2 were planned for providing the third set of SRC samples for Gleeble testing. Repair procedures depend on the location of the crack and length of crack. For instance, if the crack is identified to be present in the HAZ in a single-V girth weld, a repair weld will be offset from the original girth weld and would be centered on the HAZ as observed in Figure 21 [46]. The same authors who performed the repair weld experiment performed neutron diffraction measurements of strain and stress [46]. Two main conclusions resulted from the study: 1) shorter repair welds in length have higher axial tensile stresses than repair welds with longer repair weld lengths (i.e., providing an optimal start and stop length to provide reduced residual stresses) and 2) repair welding increased residual stresses in the ID of the pipe in the HAZ, which is the opposite trend seen in original girth weld HAZ as the OD surface contains the highest residual stress. Repair welding has been claimed to increase SRC susceptibility if using the same matching E347 filler, with even more rapid failure than the first original crack [5].

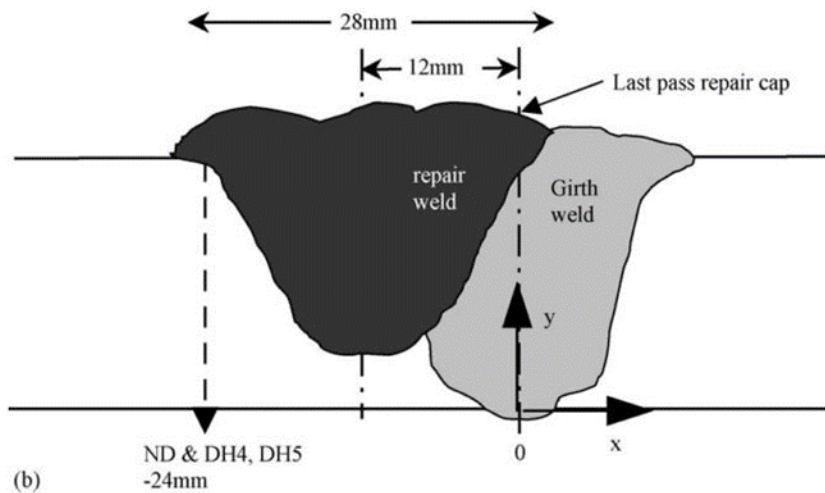


Figure 21. Repair weld schematic of 316H SS pipe girth welds [46]

4 Project Results and Discussion

The background, results, and discussion are separated by milestones and subtasks in this section. Table 7 summarizes updated sample conditions for all experimental subtasks. Of note, one 2” thick single-V weld was PWHT during milestone 1.1.1, followed by NDE using phased array UT during milestone 1.3.1. The same weld was machined to include tensile test samples for Gleeble SRC testing during milestone 1.2.1.

Table 7. Updated sample plan for first three milestones

Subtask	Samples	Purpose	Repetition
1.1.1 (ceramic heating pad)	1) Unwelded substrate of 12” x 12” x 2” plate (x1)	1) Demonstration of temperature gradient	1) 4 tests on the same plate with same thermocouple locations
	2) 40-pass lab weld	2) Demonstrate comparable results to item #1	2) 1 weld in as-welded condition sent to vendor for PWHT
1.1.2 (induction heating)	1) Unwelded substrate of 12” x 12” x 2” plate (x1)	1) Demonstration of temperature gradient	1) 5 tests on the same plate with measurements using pyrometers and sub surface thermocouples
1.2.1(TM/SRC testing-lab samples)	1) 2” thick lab welded plate in PWHT (950°C/2hr) condition 2) 1” thick lab welded plate in as-welded condition	Comparison of properties before and after PWHT and crack susceptibility	Thermomechanical samples extracted from lab samples. 2” thick lab weld was analyzed using phased array UT.
1.3.1 (NDE)	1) Welded plate in 40 pass-PWHT condition 2) In-service hot tank thick (1.5” thick) wall and floor welds	Determine if PWHT is acceptable by NDE verification; Determine the presence of critical and sub-critical flaws in serviced 347H SS plates.	Transverse phased array UT scans for the whole length (12”) of the lab weld, and in-service hot tank welds.
2.2.1 (Met. characterization of CD samples)	1) Cracked “boat” sample from Crescent Dunes wall weld. 2) Old wall girth weld before and after repair 3) 347H superheater tubes with crack problems	1) Failure analysis on primary and secondary microcracks, including phase analysis using SEM/EDS 2-4) Macro and micro characterization of received old welds prior to repair welding experiments	1) Includes two sides of gouged fracture surfaces from current crack and smaller cross section samples 2-4) Macro and micro analysis, using a few samples from each type of sample before and after PWHT.
2.2.2 (TM/SRC testing-field and lab repair weld)	1) In-service E347 hot tank wall welds before and after PWHT 2) Repaired wall welds using E16.8.2 and E347	SRC testing and elevated temperature tensile tests for as-received 347H SS-E347 weld, PWHT of 347H-E347 welds, and repair welds using E16.8.2 to determine crack susceptibility and mechanical property results from each condition.	Thermomechanical samples extracted from wall field samples and repair weld of field wall weld sample in lab. Samples will be offset to include both weld metal and HAZ behavior. Room temperature and elevated temperature tensile tests at 565°C, 800°C, and 950°C. SRC tests at same temperatures.

4.1 Milestone 1.1.1 Heat Transfer Limitations in PWHT with Ceramic Heating

The objective of task 1.1 was to determine the PWHT limitations on 347H SS welds using ceramic heating technology (milestone 1.1.1) and induction heating technology (milestone 1.1.2). The milestone’s details are laid out in Table 8. The main components to identify 1) thickness limitations on PWHT parameters (e.g., heating and cooling rate), 2) temperature gradient requirements, and 3) insulation requirements.

Table 8. Milestone 1.1.1-2 Details

Milestone	Description	Metric	Success Value
1.1.1 & 1.1.2: Identification of heating/cooling rates and temperature gradient limitations with ceramic pads and induction heating for industrial scale application	<ul style="list-style-type: none"> • Advisian will support via providing commercial tank joint/thicknesses, best current practices for PWHT in field for application (TYP 1.1.1, 1.1.2) • Identify the heat transfer limitations of each PWHT method in plate thicker than 1/2" [1,2] based on both thermocouple/laser pyrometer measurements and FEM simulations • Report the pros and cons of each method based on current standards and technological feasibility • Recommend the most feasible and economic heating method for commercial applications with acceptable temperature gradient within thick welded curvilinear plates. <p>[1] R.D. Thomas et al., WRC Bulletin 421, Welding Type 347 Stainless Steel - An Interpretive Report, 1997 [2] ASME Section VIII, Div 1-2019</p>	<p>1. Temperature gradient across the thickness of the 2" thick welds determined from FEM simulation and top/bottom surface temperature measurement from induction heating and conduction heating using ceramic heating pads, respectively</p> <p>2. Heating rate measured using thermocouple or laser pyrometer measurement of thermal history during heating</p>	<p>1. < the allowable PWHT temperature window determined from Gleeble reheat cracking test (the PWHT temperature window is now developed as a part of project #33458; and will be ready in time for welding)</p> <p>2. > the allowable rate determined from the reheat cracking susceptibility database (the reheat cracking susceptibility</p>

Preliminary FEM Studies on 2" Thick Substrates

Preliminary finite element analysis (FEA) using ABAQUS software was performed to provide the temperature field and stress relief with different heating rates, to determine the appropriate heating rate range that avoids cracking during heating based on the SRC susceptibility map generated from Gleeble testing in the previous project, while maintaining an allowable temperature gradient across the thickness direction for stress relief.

The PWHT process with a focus on heating process was simulated using the as-welded thermomechanical model as an input established from the previous SRC project. During heating, a constant temperature boundary condition was applied on the top surface of the plate model with a linear heating rate of 333, 222 and 111°C/hour, respectively, to simulate the ceramic pad heating. The bottom and side boundaries were set to experience convective heat loss, as seen Figure 22. To simulate the actual experimental procedure boundary conditions in the unclamped condition during PWHT, motion along three directions (x, y, z) on one of the bottom corners were fixed. On the opposing side (i.e., the other side of the weld), motion of two (y, z) directions on one bottom corner and one direction (z) on the other bottom corner were also fixed. Note that x, y, z are parallel to the transverse direction, welding direction, and normal direction, respectively. These boundary conditions were applied similarly to the PWHT simulations of the unclamped condition in the SRC project modeling results.

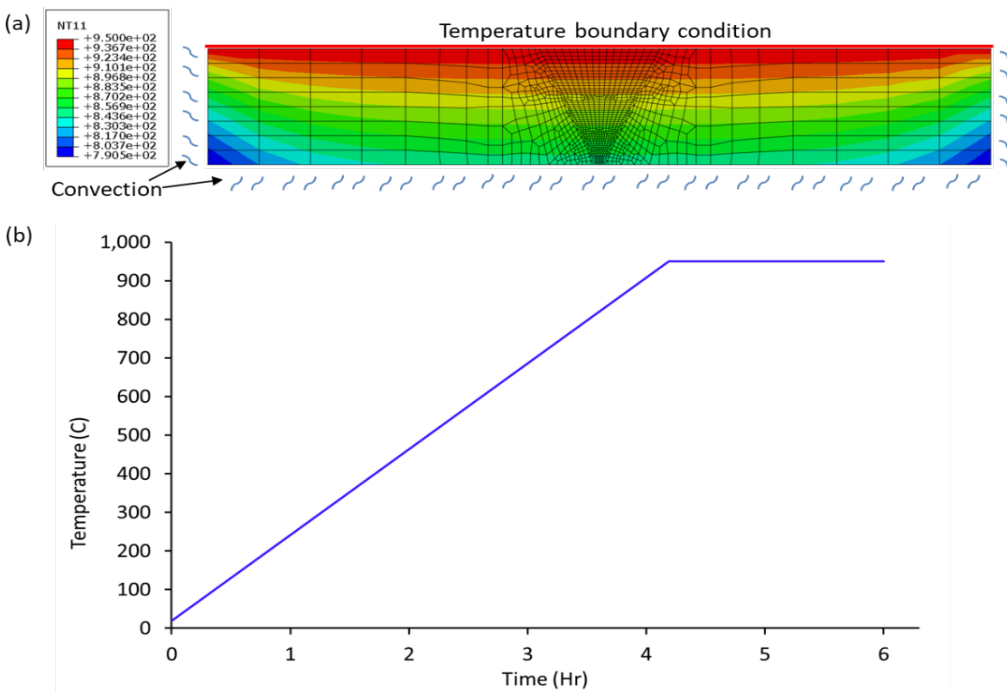


Figure 22. (a) PWHT heating boundary conditions and temperature field; (b) Top surface heating temperature boundary condition (222 C°/h)

The temperature and stress profiles at a node within the region with the highest stress, the most susceptible region to SRC, are shown in Figure 23 (black circle). Heat treatment reduces the stress significantly in the 2” thick weld in comparison to the as-welded condition. For example, the highest stress regions experience a reduction from 481 to 53 MPa during the heating stage. The temperature-stress failure criteria obtained from experiments in the previous SRC project are used to identify the appropriate heating rate range. For instance, in Figure 23 (c), the open triangle, square and diamond sign show no failure at their plotted stress and temperature after 24 hours (95 MPa at 800°C, 81 MPa at 850°C and 77 MPa at 900°C), while the solid symbols (120 MPa at 800°C after 7.1 hr, 105 MPa at 850°C after 4.8 hr, and 85 MPa at 900°C after 70 min) show failure in experiment. During PWHT, the stress as a function of temperature and time should be at least located underneath the solid symbols, or more conservatively, close to or below the open symbols, to avoid formation of cracks or micro-voids. As mentioned earlier,

faster heating rates (within the maximum allowable heating rate due to temperature gradient concerns) have been recommended to avoid meeting the crack c-susceptible curves. However, too fast of a heating rate (e.g., 333°C/h.) may lead to fast cracking or formation of micro-voids based on Gleeble SRC susceptibility tests since the stress did not relax sufficiently in time to fall below the critical stress values up to 900°C. It is obvious that 111°C/h is a safer condition to use than 333°C/h case based on a stress relaxation that falls below the critical stress values for 850°C and above. Since time to failure at 120 MPa and 800°C (solid symbol) condition was 7.1 hr, there would be little to no concern for cracking to occur since the stress drops below the critical stresses for temperatures above 800°C during heating, and there is not that much time spent near 800°C during heating up. While slow heating rates are recommended to allow for sufficient stress relaxation to occur during heating before reaching susceptible temperatures (>800°C), too slow of a heating rate will allow for extended times at temperature during heating that may lead to undesired microstructural changes and low efficiency for PWHT. Thus, an appropriate heating rate range needs to be established, which is likely between 222 and 111°C/h.

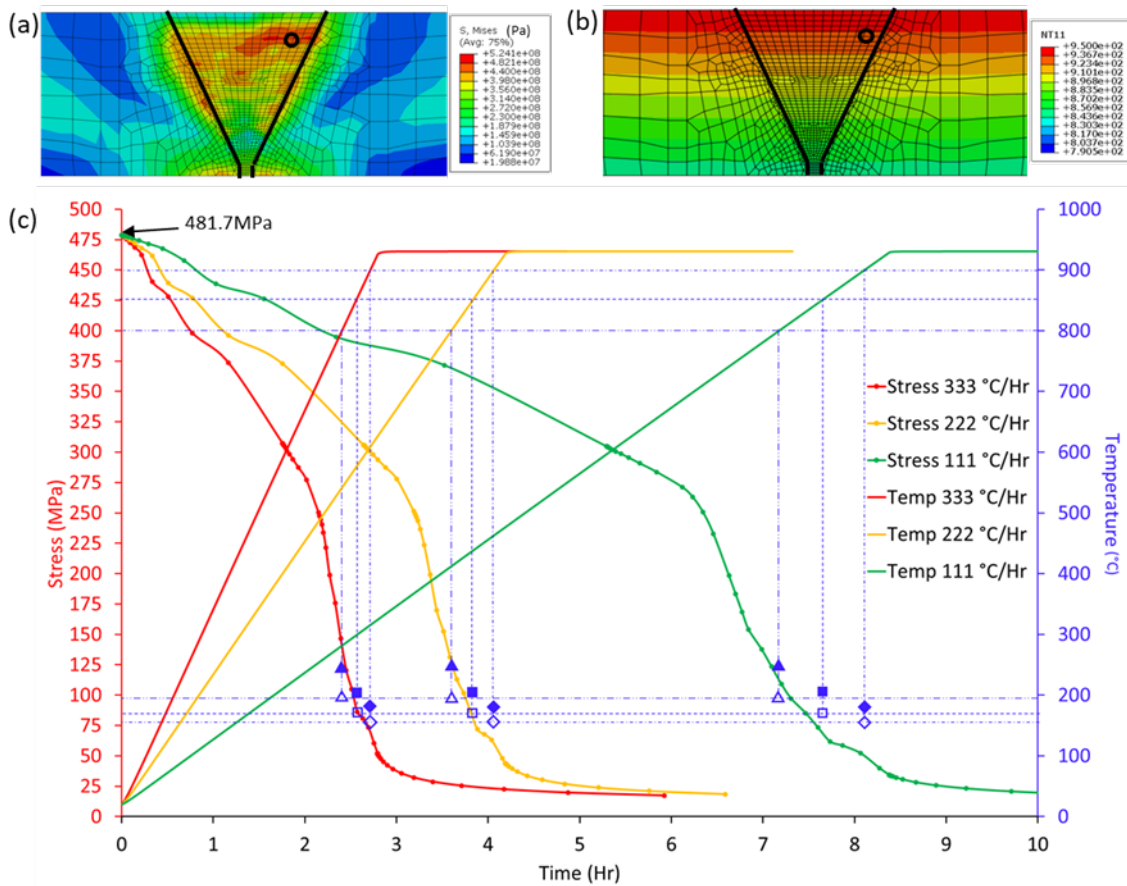


Figure 23. (a) Von Mises stress contour under as-welded condition after unclamping; (b) Temperature field after 4-hour holding at 950°C, (c) Stress relief along the heating with different heating rate. Solid and open symbols show failure and no failure at certain temperatures and stresses in experiment, respectively.

Determining the necessity of surrounding insulation was important for temperature gradient requirements. FEA has confirmed the benefit of backside insulation using the model in Figure 24. Green parts are the weld plates (24" x 24"), pink ones are the ceramic heating pads (12"x24")

and gray parts are refractory ceramic fiber (RCF) insulators. The heating pad is set with a temperature boundary condition of heating from 20°C to 950°C and held for 4 hours. With RCF insulation on top of the plate only (Figure 24(b)), the temperature field reached a steady state after heating at 950°C for 4 hours with a temperature difference through thickness of around 100°C. However, after 4 hours at peak temperatures of 950°C with insulation on both sides (Figure 24(a)), the temperature difference is less than 55°C. Both-sided RCF insulation would be preferred to maintain minimum temperature gradients during PWHT, if feasible and especially in thick plates.

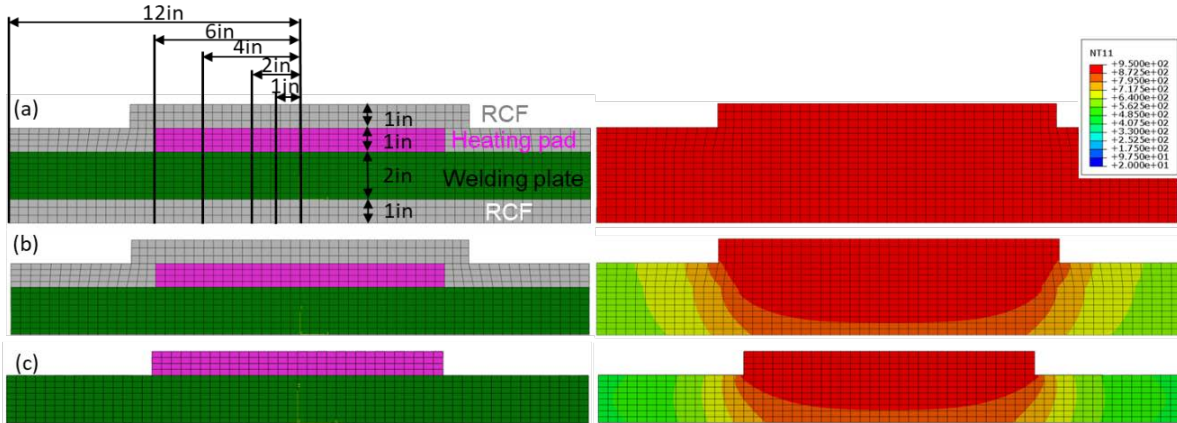


Figure 24. (a) Ceramic pad heating model and temperature field after 4 hours with insulation RCF on both top and bottom surface; (b) Ceramic pad heating model and temperature field after 4 hours with insulation RCF on top only; (c) Ceramic pad heating model and temperature field after 4 hours without insulation RCF

PWHT Experiments on 2" Thick Substrates Using Varying Heating Rates and Insulation Conditions

Ceramic heating experiments on a 12" x 12" x 2" thick 347H plate were completed to measure temperature gradients and temperature as a function of time during PWHT. The overall objectives of these experiments are to determine the corresponding temperature gradients to: 1) two different heating rates, 2) with or without backing RCF insulation, and 3) two step PWHT with a vertical orientation. After determination of meeting standard temperature gradient requirements, qualified PWHT thermal profile will be duplicated in a thermal model and applied to the previous 2" thick 40-pass 347H weld model to calculate the stress relaxation behavior, in order to confirm reheat cracking can be completely avoided during PWHT using the stress threshold map developed from Gleeble experiment. Note that previous modeling efforts suggested that a heating rate of 222°C/hr should be safe for reheat cracking. The main purpose of this new simulation is to evaluate the impact of temperature gradient across plate thickness associated with practical PWHT procedure on reheat cracking.

Ceramic Heating Experiment Setup

Based on preliminary modeling results (discussed in detail in previous reports) and AWS D10.10 code recommendations with different heating rates, four experiments were carried out using localized ceramic heating methods, as summarized in Table 9. There are two heating rates of 111°C/hr and 222°C/hr considered for PWHT. There are three tests with a one-step PWHT and one test with a two-step PWHT. The first test examines the temperature gradient without

insulation on the root side (back side) of the single-V groove. The soak band width, 10 inches for two-inch thick plate, represents the region in which there needs to be a very small temperature differential (maximum of 55°C temperature difference through thickness and transverse to the weld region as seen in Figure 25). The temperature difference through thickness should similarly not exceed 55°C. Three heating pads were stacked along the whole surface of the 12” x 12” inch plate. The RCF insulation was wrapped around the ceramic heating pad and sides of the plate for all four experiments and with backside insulation for experiments two through four.

Table 9. Ceramic heating pad experimental parameters

Experiment #	Soak Band Width	Backside RCF Insulation	Step 1 Heating Rate	Step 1 Temp.	Step 1 Hold time	Step 2 Heating Rate	Step 2 Temp.	Step 2 Hold time	Cooling Rate	Max ΔT for SB
1	10 inches	No	111°C/hr	950°C	Temp. Stabilization	-	-	-	Controlled cool with 139°C/hr as max; air cool below 400°	55°C
2		Yes	111°C/hr	950°C		-	-	-		
3		Yes	222°C/hr	950°C		-	-	-		
4		Yes	222°C/hr	600°C		222°C/hr	950°C	Temp Stabilization		

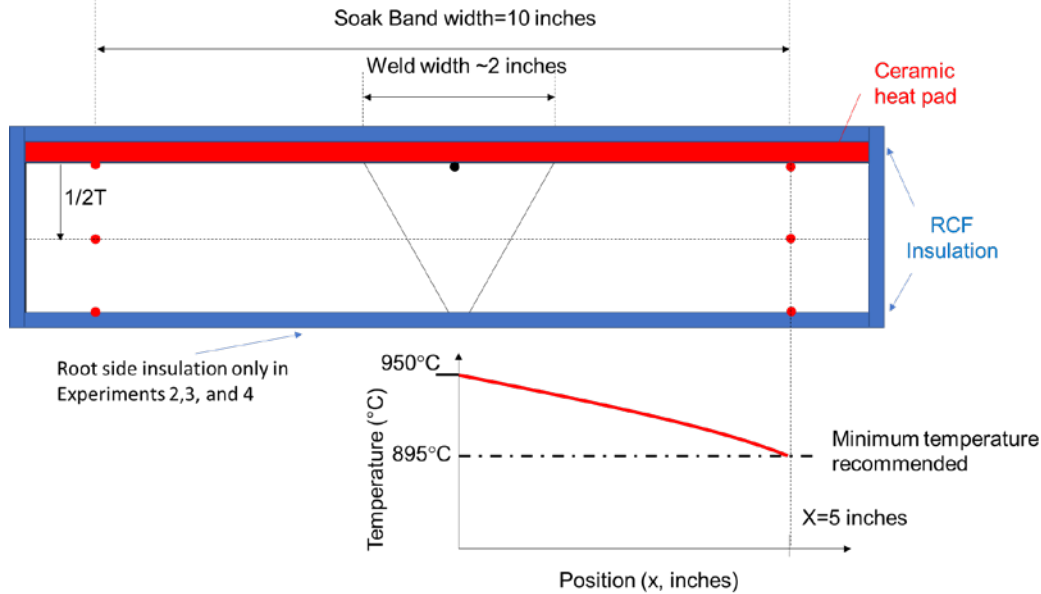


Figure 25. Schematic of thermocouple locations on a plate cross section with ceramic heating pad on top and RCF insulation layers surrounding the plates, except for Experiment 1 listed in Table 9, which has no backside insulation. The temperature difference over soak band width and thickness is not recommended to be below 55°C of the peak temperature (~895°C)

Thermocouple locations for the top surface, mid-thickness, and bottom surface are schematically illustrated in Figure 29. The heaters are stacked on the top surface, with the main control thermocouple in the center of the plate (black TC), while there are multiple output thermocouples that read the temperature gradients in the plate (red TCs). The bottom surface has thermocouples near the edges, like the top surface, to measure the same location through

thickness to measure temperature gradients through thickness and along the soak band width. Each thermocouple location is given a designated peak temperature based on temperature gradient limitations transverse on the top surface and through thickness. Based on a peak temperature of 950°C, the desired maximum temperature drop is 55°C five inches away on the SB edge from the center control thermocouple and through thickness. Table 10 tabulates the thermocouples with acceptable peak temperatures based on relative location within the plate, including top surface center (950°C), top surface SB edge (895°C), bottom surface center (895°C), bottom surface SB edge (840°C), mid-thickness center (922°C), and mid thickness SB edge (867°C). Maximum peak temperatures are collected to determine the net temperature difference between the actual temperature and desired temperature. Tabulating the net temperature differences are compared with FEM temperature values for temperature model validation.

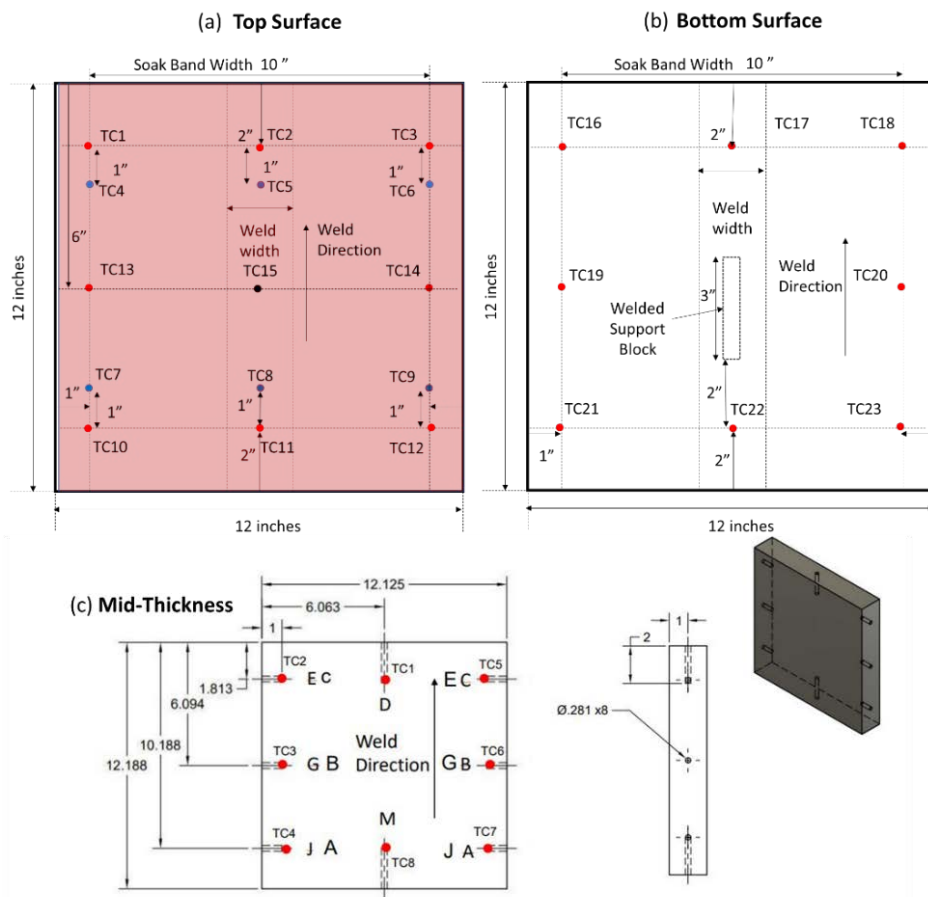


Figure 26. Surface thermocouple locations on (a) top (front) and (b) bottom (back) surface of 12'' x 12'' x 2'' thick substrate plates, and (c) mid-thickness thermocouple locations. Red dots indicate output thermocouples, black dot represents the control thermocouple, and blue thermocouples represent redundant thermocouples. The heating pads (triple stacked) lie on the top (front) surface.

Table 10. Peak soak temperature expected in surface and mid-thickness thermocouples measurements, including step 1 designated temperature

Surface Thermocouples	Location	Peak Soak Temp. (°C)	Step 1 Peak Temp. (only for Exp. 4) (°C)
2,5,8,11,15	Top surface center	950	600
1,3,4,6,13,14,7,9,10,12	Top surface SB edge	895	545
17,22	Bottom surface center	895	545
16,18,19,20,21,23	Bottom surface SB edge	840	490
Mid-thickness thermocouples	Location	Peak Soak Temp. (°C)	Step 1 Peak Temp. (only for Exp. 4) (°C)
1,8	Center mid-thickness	~922	572
2-7	SB edge	~867	517

Ceramic Heating Experiment Results

The final three experiments did not have heater burnout like Experiment 1. An ambient temperature boundary condition on the root side of the plate leads to significant heat convection during heating experiments. It suggests mandatory double-sided insulation to meet the maximum temperature gradient restrictions during PWHT. The final three experiments showed success in providing stable temperature gradients at a soak temperature of 950°C, whether a first step is used or using a heating rate of 111 or 222°C/hour.

Table 11 tabulates peak temperatures recorded in Experiment 2 (111°C/hour) compared to the designated temperatures, while Table 12 collects peak temperature values for Experiment 3 (222°C/hour) and Table 13 for Experiment 4. The detailed heating conditions for these Experiments 2-4 can be found in Table 9. The ΔT readings for Experiments 2-4 have a couple outlier thermocouple results, surface TC # 4,14, and 22 and mid-thickness are TC # 3, 4, and 5. A 3” long x 1/2” thick block was welded on the back side to help support a vertical experimental setup, but it was determined on further FEA that the welded block should not cause a significant heat loss upon reaching temperature as the heating rates are relatively slow to allow for thermal stabilization. It is assumed that these thermocouples had bad connections. Overall, most of the thermocouple readings are within 50°C of their desired temperatures. Also, temperatures trends seen in Experiment 2 with a 111°C/hour are similar to Experiment 3 with a faster heating rate of 222°C/hour. While the 222°C/hour has slightly lower temperatures ($\sim\Delta 5-10^\circ\text{C}$) in the lowest thermocouples temperature reading locations than with a 111°C/hour heating rate, a faster heating rate will have a reduced heating time. Thus, a 222°C/hour was implemented for the final stress model. Temperature results from Experiment 4 in Table 13 indicate a slightly improved temperature gradient upon reaching the peak soak temperature compared to the other three single step PWHT experiments.

Table 11. Experiment 2 (111°C/hour) peak temperature measurements according to thermocouple location and number as well as difference Δ of designated temperature and measured temperature in °C. Color code corresponds to a color designation of the specific thermocouple time-temperature plot on the thermal plots.

Thermocouples		Designated Temp. (°C)	Actual Peak Temp. (°F)	Peak Temp. in °C	ΔT (°C)
Top Surface Center	15	950	1750	954	4
	2		1665	907	-43
	5		1705	929	-21
	8		1720	938	-12
	11		1745	952	2
Top surface SB edge	1	895	1650	899	4
	3		1685	918	23
	4		1495	813	-82
	6		1690	921	26
	13		1715	935	40
	14		1538	837	-58
	7		1715	935	40
	9		1650	899	4
	10		1702	928	33
	12		1672	911	16
Bottom Surface Center	17	895	1668	909	14
	22		1430	777	-118
Bottom Surface SB edge	16	840	1586	863	23
	18		1637	892	52
	19		1532	833	-7
	20		1510	821	-19
	21		1590	866	26
	23		1605	874	34
Mid-thickness center	1	922	1643	895	-27
	8		1682	917	-5
Mid-thickness SB edge	2	867	1650	899	32
	3		1462	794	-73
	4		1513	823	-44
	5		1450	788	-79
	6		1633	889	22
	7		1632	889	22

Table 12. Experiment 3 (222°C/hour) peak temperature measurements according to thermocouple location and number as well as difference Δ of designated temperature and measured temperature in °C. Color code corresponds to a color designation of the specific thermocouple time-temperature plot on the thermal plots.

Thermocouples		Designated Temp. (°C)	Actual Peak Temp. (°F)	Peak Temp. in °C	ΔT (°C)
Top Surface Center	15	950	1750	954	4
	2		1665	907	-43
	5		1705	929	-21
	8		1725	941	-9
	11		1750	954	4
Top surface SB edge	1	895	1720	938	43
	3		1685	918	23
	4		1488	809	-86
	6		1690	921	26
	13		1647	897	2
	14		1505	818	-77
	7		1720	938	43
	9		1647	897	2
	10		1700	927	32
	12		1673	912	17
Bottom Surface	17	895	1663	906	11
	22		1422	772	-123
Bottom Surface SB edge	16	840	1583	862	22
	18		1635	891	51
	19		1532	833	-7
	20		1532	833	-7
	21		1585	863	23
	23		1605	874	34
Mid-thickness	1	922	1640	893	-29
	8		1680	916	-6
Mid-thickness SB edge	2	867	1650	899	32
	3		1457	792	-75
	4		1503	817	-50
	5		1445	785	-82
	6		1630	888	21
	7		1623	884	17

Table 13. Experiment 4 (Two-step-222°C/hour) peak temperature measurements according to thermocouple location and number as well as difference Δ of designated temperature and measured temperature in °C. Color code corresponds to a color designation of the specific thermocouple time-temperature plot on the thermal plots.

Thermocouples		Designated Temp. (°C)	Actual Peak Temp. (°F)	Peak Temp. in °C	ΔT (°C)
Top Surface Center	15	950	1760	960	10
	2		1695	924	-26
	5		1710	932	-18
	8		1737	947	-3
	11		1730	943	-7
Top surface SB edge	1	895	1685	918	23
	3		1650	899	4
	4		1530	832	-63
	6		1685	918	23
	13		1670	910	15
	14		1525	829	-66
	7		1695	924	29
	9		1655	902	7
	10		1685	918	23
Bottom Surface Center	17	895	1640	893	-2
	22		1430	777	-118
Bottom Surface SB edge	16	840	1595	868	28
	18		1615	879	39
	19		1570	854	14
	20		1545	841	1
	21		1610	877	37
	23		1640	893	53
Mid-thickness	1	922	1615	879	-43
	8		1660	904	-18
Mid-thickness SB edge	2	867	1665	907	40
	3		1505	818	-49
	4		1530	832	-35
	5		1455	791	-76
	6		1630	888	21
	7		1605	874	7

Finite Element Modeling of PWHT Using Ceramic Pads Heating Conditions

The PWHT model consists of two steps: 1) build a thermal model that simulates the experimental thermal profile during PWHT and validate the model using ceramic heating experiment results; and 2) apply the calculated thermal profile to the 40-pass weld model to calculate the stress relaxation.

Thermal Model and Validation

The first step is to build a model for the experimental heat treatment. Four heat treatment regimens were conducted during the ceramic heating pad experiments. Table 9 outlines the parameters of each heat treatment. Heat treatment Experiment #2 was selected as the basis of the temperature modeling validation. The selected heat treatment consists of a heating phase from 20°C to 950°C at a heating rate of 222°C/hour, a short temperature stabilization soak time of 600s (10 minutes) followed by an air-cooling period back to ambient temperature (20°C).

Geometry and Materials

The geometry of the welded plate, the ceramic heating pad and the surrounding RCF insulation was replicated in ABAQUS and is shown in Figure 27. The welding plate was represented by a 12"x12"x2" block with temperature dependent material properties of SS347H. A 1"x3"x3" backing bar was added to simulate the heat transfer conditions imposed by the supporting bar that was welded to the bottom of the 347H plate during heat treatment experiment. The bar was assigned the same material properties as the plate and its geometry was built as a simple extension of the plate (no contact resistance and no weld material added). A 12"x12"x1" geometry was placed on the top surface of the simulated plate which represents the ceramic heating pad. The heating pad will be discussed in detail in later sections. The RCF blanket material used in the experimental setup is the biggest modeling uncertainty due to the variation in thickness in real applications. A 1" thick plate of insulation was added to all sides of the conjoined ceramic heating pad and plate geometries. A hole in the bottom RCF was added to allow the backing plate to protrude through.

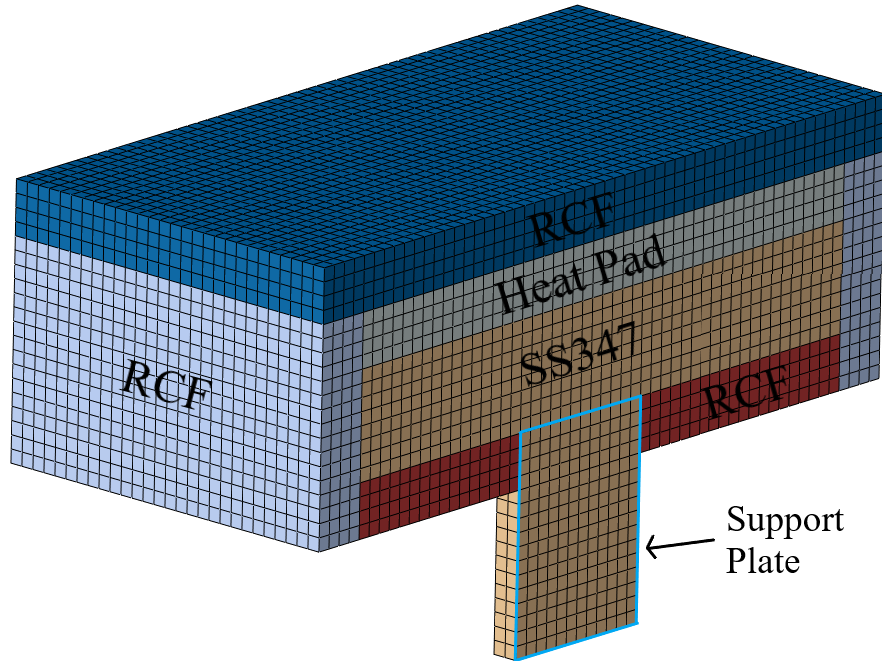


Figure 27. Model geometry color coded by element set: heat pad in blue, 347h plate in grey, and RCF in brown/white/red.

Boundary Conditions

Simulating the temperature distribution generated by the ceramic heating experiment consisted of two tasks. Accurately simulating the heat generation ceramic heating element and tuning the material properties of the simulated RCF insulation was the first step. The three-region parabolic temperature control scheme used to control the ceramic heating pad was rebuilt in the model as an expression field that modifies the volumetric temperature boundary condition applied to the ceramic heating elements at any given time step using Eq. 3 below. For example, as the temperature is ramping up at 222°C/hour the simulation applies a volumetrically homogenous boundary condition to the entire heat pad node set. The expression field then modifies each nodal temperature value depending on its distance from the center of the plate in the x direction and in accordance with the given equation.

$$T(x) = 1 - 3.81600359 * X^2 \quad (3)$$

With the heat generation mechanism accurately represented, the insulation thermodynamics was then built to finish the model. Surface film (conduction) and radiation conditions were applied to the exposed plate geometries and all exterior RCF surfaces to simulate ambient heat loss. The heat treatment was run iteratively, and the thermodynamic values of the insulation were modified until the thermal history generated by the model was in good agreement with the experimental history. The raw temperature-dependent material properties for the RCF were already defined so the primary tool for tuning the insulation performance was modifying the interactions between the insulation and the large environment.

Thermal Model Validation

Figure 28 shows a transverse temperature contour plot halfway through the plate during the beginning of the soak phase.

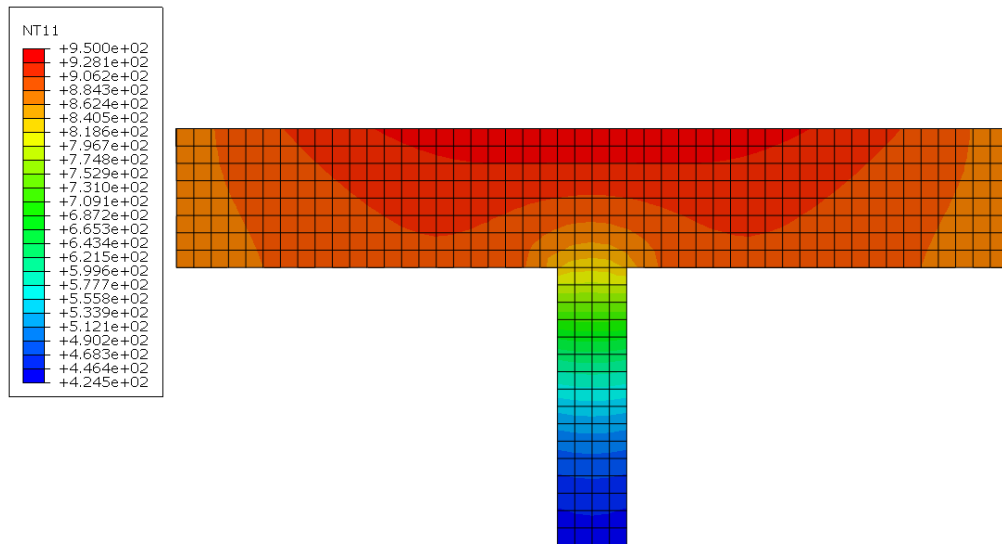


Figure 28. Temperature (°C) contour plot at the beginning of soak

Temperature values at the beginning of the soak step were compared between the experimental and model values and thus were used as the method of validation. Table 14 outlines the agreement between the two models. The model values are in good agreement with both the desired values as well as the experimental values. When averaged over every datapoint, the model was 1.53% higher than the desired values and 2.36% higher than the experimental values, indicating a good agreement.

Table 14. Comparison of model values with experimental values

Thermocouples		Designated Temp. (°C)	Actual Peak Temp. (°F)	Peak Temp. in °C	ΔT (°C)	Model Temp. (°C)	Percentage of Designated	Percentage of Experimental
Top Surface Center	15	950	1750	954	4	950	100.00%	99.58%
	2		1665	907	-43	950	100.00%	104.74%
	5		1705	929	-21	950	100.00%	102.26%
	8		1720	938	-12	950	100.00%	101.28%
	11		1745	952	2	950	100.00%	99.79%
Top surface SB edge	1	895	1650	899	4	894.9	99.99%	99.54%
	3		1685	918	23	894.9	99.99%	97.48%
	4		1495	813	-82	894.9	99.99%	110.07%
	6		1690	921	26	894.9	99.99%	97.17%
	13		1715	935	40	894.9	99.99%	95.71%
	14		1538	837	-58	894.9	99.99%	106.92%
	7		1715	935	40	894.9	99.99%	95.71%
	9		1650	899	4	894.9	99.99%	99.54%
	10		1702	928	33	894.9	99.99%	96.43%
	12		1672	911	16	894.9	99.99%	98.23%
Bottom Surface Center	17	895	1668	909	14	918.809	102.66%	101.08%
	22		1430	777	-118	915.993	102.35%	117.89%
Bottom Surface SB edge	16	840	1586	863	23	880.846	104.86%	102.07%
	18		1637	892	52	880.846	104.86%	98.75%
	19		1532	833	-7	881.802	104.98%	105.86%
	20		1510	821	-19	881.802	104.98%	107.41%
	21		1590	866	26	880.668	104.84%	101.69%
	23		1605	874	34	880.668	104.84%	100.76%
Mid-thickness center	1	922	1643	895	-27	928.405	100.69%	103.73%
	8		1682	917	-5	926.473	100.49%	101.03%
Mid-thickness SB edge	2	867	1650	899	32	884.332	102.00%	98.37%
	3		1462	794	-73	885.124	102.09%	111.48%
	4		1513	823	-44	884.184	101.98%	107.43%
	5		1450	788	-79	884.332	102.00%	112.22%
	6		1633	889	22	885.124	102.09%	99.56%
	7		1632	889	22	884.184	101.98%	99.46%

Thermal History Development

After being validated from the experiment conditions, the calculated PWHT thermal profile needs to be applied to the sequential thermal stress calculation to devise a suitable heat treatment regime. Differences in the above-mentioned thermal model and the multi-pass stress model made it extremely difficult to transfer the thermal history directly from the former to the latter. This was primarily due to a difference in geometry, the existence of exogenous node sets, and discrepancies in the coordinate systems. Therefore, a second approach was taken, where a geometrically identical model of the welded plate was created, and the insulation and heat pad were simulated by surface boundary conditions instead of physical elements. The heat pad has the same parabolic temperature distribution as the validated model, but in this case, it is applied to the surface nodes on the top of the welded plate geometry. Table 15 compares the two models' agreement with the experimental thermal history. The values in grey at the bottom of Table 15 show the deviation of the accuracy for each column. The two models are in good agreement

proving the PWHT heat generation model to be a sufficient method of thermal history reproduction.

Table 15. Comparison of validation and PWHT generation model

Model Temp. (°C)	Percentage of Designated Temp	Percentage of Experimental Temp	Thermal Field Generation Temp	Percentage of Designated Temp	Percentage of Experimental Temp
950	100.00%	99.58%	950	100.00%	100%
950	100.00%	104.74%	950	100.00%	105%
950	100.00%	102.26%	950	100.00%	102%
950	100.00%	101.28%	950	100.00%	101%
950	100.00%	99.79%	950	100.00%	100%
894.9	99.99%	99.54%	875.815	97.86%	97%
894.9	99.99%	97.48%	875.815	97.86%	95%
894.9	99.99%	110.07%	876.547	97.94%	108%
894.9	99.99%	97.17%	876.547	97.94%	95%
894.9	99.99%	95.71%	877.051	97.99%	94%
894.9	99.99%	106.92%	877.051	97.99%	105%
894.9	99.99%	95.71%	876.547	97.94%	94%
894.9	99.99%	99.54%	876.547	97.94%	98%
894.9	99.99%	96.43%	875.15	97.78%	94%
894.9	99.99%	98.23%	875.15	97.78%	96%
918.809	102.66%	101.08%	918.432	102.62%	101%
915.993	102.35%	117.89%	918.432	102.62%	118%
880.846	104.86%	102.07%	875.815	104.26%	101%
880.846	104.86%	98.75%	875.815	104.26%	98%
881.802	104.98%	105.86%	877.051	104.41%	105%
881.802	104.98%	107.41%	877.051	104.41%	107%
880.668	104.84%	101.69%	875.815	104.26%	101%
880.668	104.84%	100.76%	875.815	104.26%	100%
928.405	100.69%	103.73%	928.4	100.69%	104%
926.473	100.49%	101.03%	928.4	100.69%	101%
884.332	102.00%	98.37%	881.228	101.64%	98%
885.124	102.09%	111.48%	882.11	101.74%	111%
884.184	101.98%	107.43%	881.228	101.64%	107%
884.332	102.00%	112.22%	881.228	101.64%	112%
885.124	102.09%	99.56%	882.11	101.74%	99%
884.184	101.98%	99.46%	881.228	101.64%	99%
Accuracy	101.53%	102.36%		100.70%	101.53%

PWHT Experiment on 2” Thick Single-V Lab Weld: Using 950°C Soak Temperature and 222°C/hr Heating Rate

Ceramic heating experiments on a 40-pass 2” thick single-V groove 12” x 12” 347H-E347 weld plate were completed using Experiment #3 PWHT parameters (950°C/2-hr soak with 222°C/hr heating rate) with surrounding insulation on all sides. The soak band width, 10 inches for two-inch thick plate, represents the region in which there needs to be a very small temperature differential (maximum of 55°C temperature difference through thickness and transverse to the weld region). Three heating pads were stacked along the whole surface of the 12” x 12” inch

plate with the main control thermocouple in the top center of the plate and multiple output thermocouples that read the temperature gradients in the plate, as seen in Figure 29(a). The RCF insulation was wrapped around the ceramic heating pad, sides, and back of the welded plate and placed on a clamped rig as seen in Figure 29(b). The bottom surface has thermocouples near the edges, like the top surface, to measure the same location through thickness to measure temperature gradients through thickness and along the soak band width. The same number of surface thermocouples used for the preliminary experiments were used, but the mid-thickness thermocouple probes were not used.

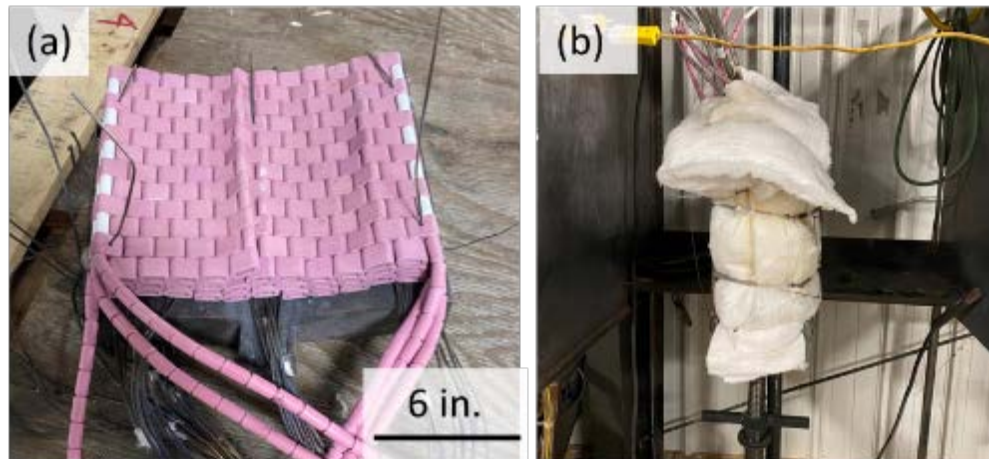


Figure 29. (a) Top view of 12" x 12" x 2" thick 347H-E347 SS weld with three heaters stacked on the top face of weld, (b) vertical setup for PWHT with surrounding insulation and clamped on the bottom side of plate

The temperature versus time plots for the top side and back side surface thermocouples are shown in Figure 30 and Figure 31, respectively. Many thermocouples seem to show and meet the thermal gradient requirement. However, there are a certain number of thermocouples that seem to have bad calibration or connecting issues with the plate, such as T10 and T14 as seen in Figure 30 on the top surface and all of the green colored thermocouples (likely clamping edge). Most of the thermocouples with lower temperatures close to 800°C are close to the thermocouple locations reading 950°C as seen in Figure 30(b). Figure 31(b) shows that five of the eight thermocouples on the back side surface were 700°C and below but one thermocouple at difference locations (each color) along the length of the plate read a temperature of 900°C or greater, which is the necessary requirement for thermal gradients. After PWHT, the sample was shipped to Crescent Dunes for NDE using phased array UT.

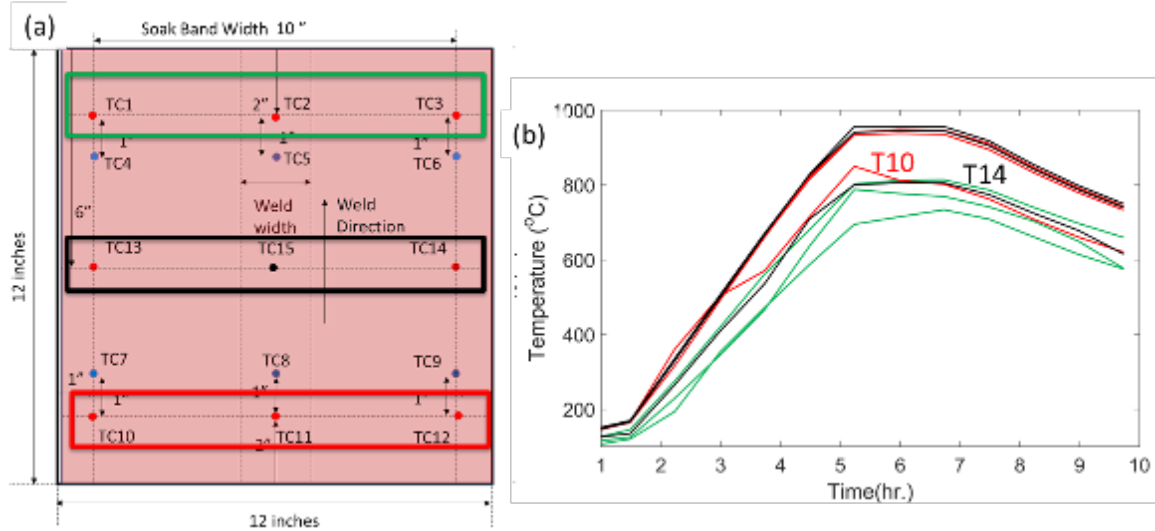


Figure 30. (a) Thermocouple placement on top surfaces (where heaters are placed) with different box color outlines associated with those group of thermocouples as seen in the (b) temperature vs. time plot

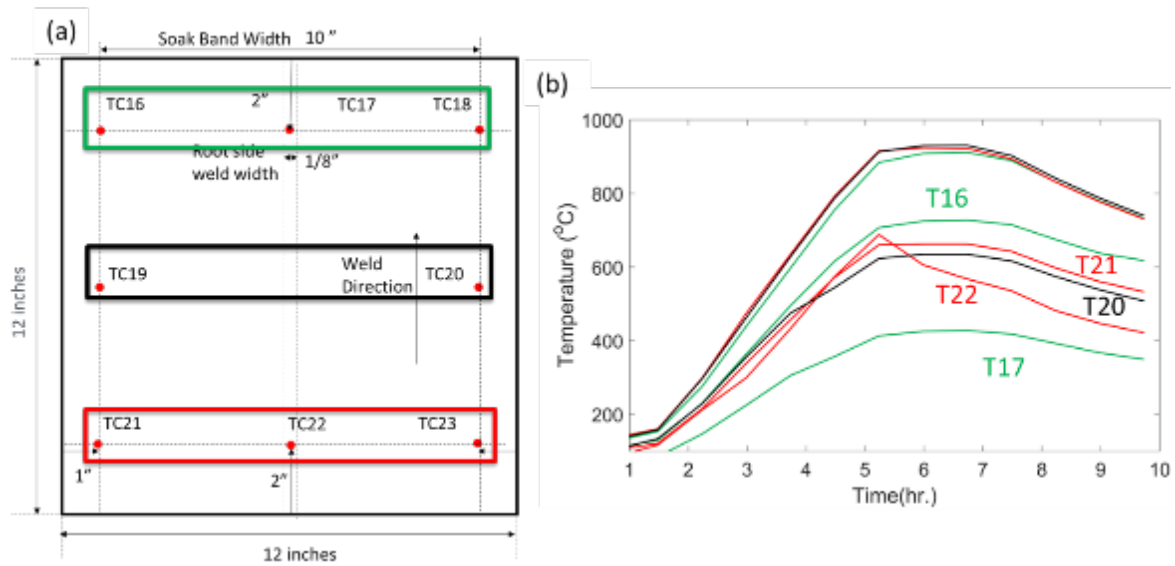


Figure 31. (a) Thermocouple placement on back surfaces with different box color outlines associated with those group of thermocouples as seen in the (b) temperature vs. time plot

PWHT Model: Stress Relaxation Using 950°C Temperature and 222°C/hr

The 2” thick 40 pass as welded model was given a PWHT simulation to determine stress reduction below critical stress to fracture using Experiment #3 PWHT parameters. Using a thermally validated model from Experiment #3 parameters and temperature measurements, the same temperature profile was applied to the 2” thick 40 pass weld for stress relaxation analysis. Comparisons of an older PWHT weld model without insulation was compared to the updated new PWHT weld model using surrounding insulation.

Heating Model

The geometry of the welded plate, the ceramic heating pad, and the surrounding RCF insulation was replicated in ABAQUS and is shown in Figure 27 (a). The welding plate was represented by a 12"x12"x2" block with temperature-dependent material properties of SS347H. A 12"x12"x1" geometry was placed on the top surface of the simulated plate, which represents the ceramic heating pad. The RCF blanket material used in the experimental setup is the biggest modeling uncertainty due to the variation in thickness in real applications. A 1" thick plate of insulation was added to all sides of the conjoined ceramic heating pad and plate geometries. The heating model result for a heating rate of 222°C/s to a holding temperature of 950°C is demonstrated in Figure 27 (b), which demonstrates a temperature gradient less than 10°C along the plate thickness direction with the aid of double side RCF insulation. The modeling results reached 95.71% ~117.89% percentage of experimental values recorded by thermal couples during the ceramic pad heating experiment. Hence, the model was validated to generate reasonable thermal input profiles for the following stress calculations during PWHT.

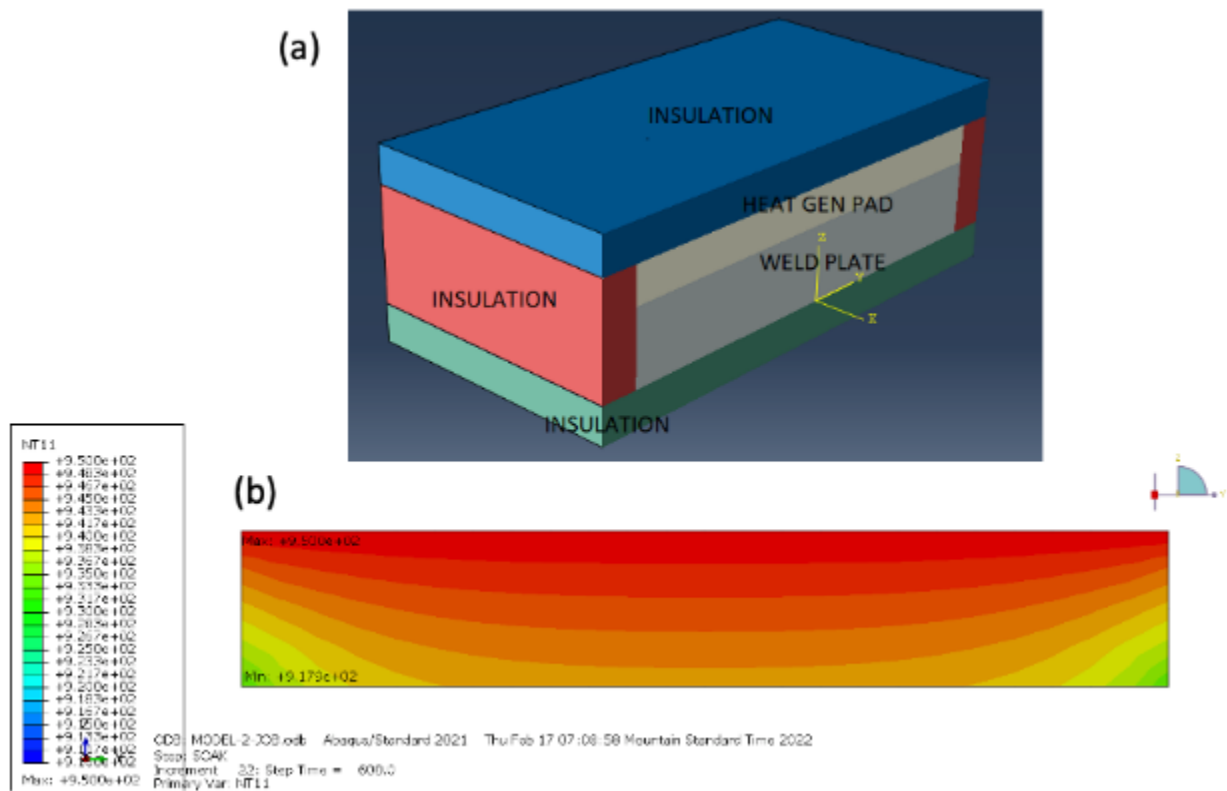


Figure 32. (a) Heating model geometry color coded by element set, and (b) temperature contour for 222°C/s heating rate to a holding temperature of 950°C

Stress Relaxation Results in 40-Pass Welded Model Using Experiment 3 parameters

The validated thermal history was imposed on the 40-pass weld stress model for a sequential thermal stress analysis. Figure 33 to Figure 39 demonstrate temperature gradients, principal stresses along transverse (S11) and longitudinal (S22) directions, as well as the von Mises effective stress at various steps during heating, at temperature, and cooling. Note that temperature and stress values are depicted using contour limits that are calculated for each frame.

The temperatures given is the peak temperature of the ceramic heating pad at that given time and the surface being viewed is a transverse cross section six inches longitudinally into the weld. Figure 33 shows stress profiles in the as-welded condition before heating. Figure 34 shows the stress profiles during heating to a peak temperature of 600°C. By comparing Figure 34 to Figure 33, it can be seen marginal stress relief was achieved up to 600°C. As the heating temperature further increased to 950°C, as shown in Figure 35, the residual stresses were significantly reduced to lower than 55 MPa in general. During the soaking stage at 950°C up to 2 hours, there is very slight further decrease in residual stresses in Figure 36 and Figure 37. Figure 38 and Figure 39 show slight stress increase associated with cooling down from 950°C after one and three hours, respectively.

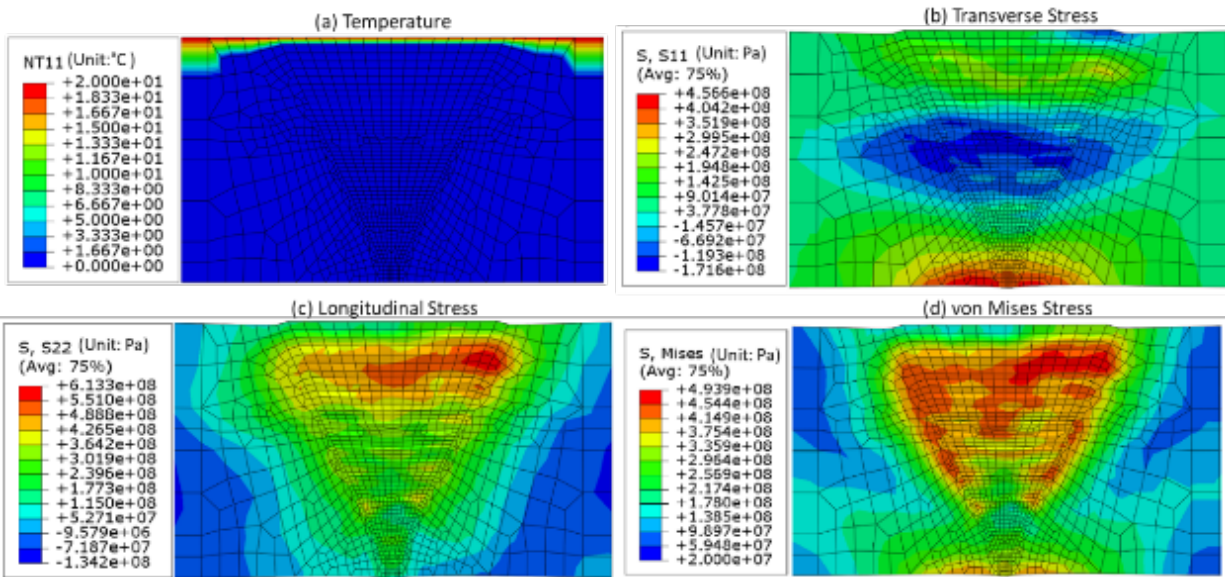


Figure 33. (a) Nodal temperature, and (b) transverse, (c) longitudinal and (d) von Mises stresses in the as-welded condition before PWHT

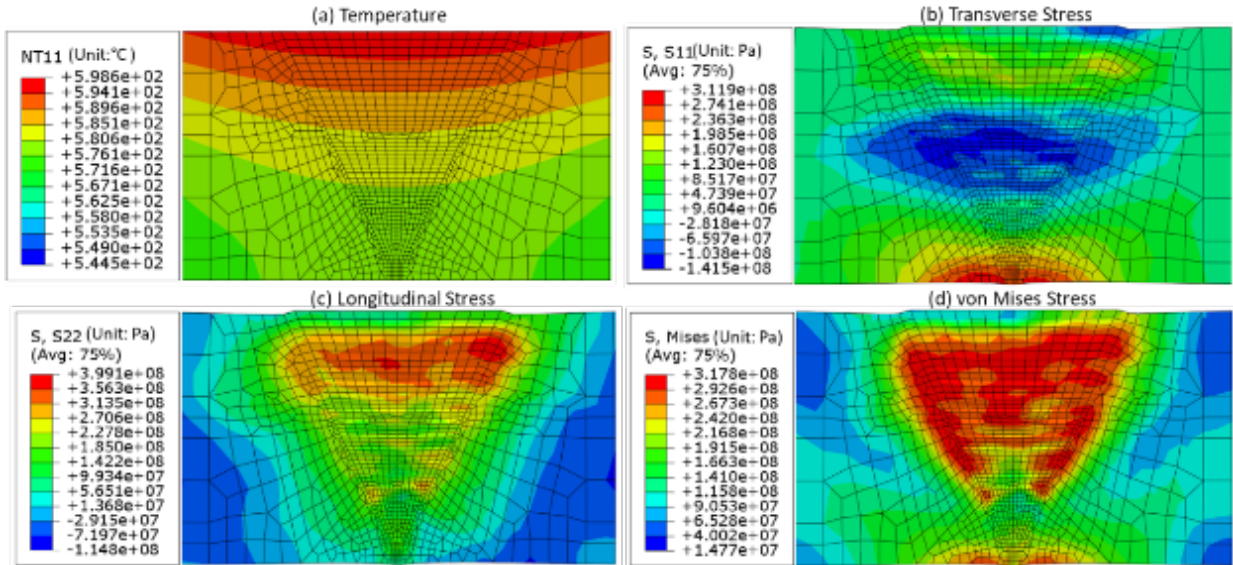


Figure 34. (From top left to lower right) (a) Nodal temperature, and (b) transverse, (c) longitudinal and (d) von Mises stresses during heating to ~600°C

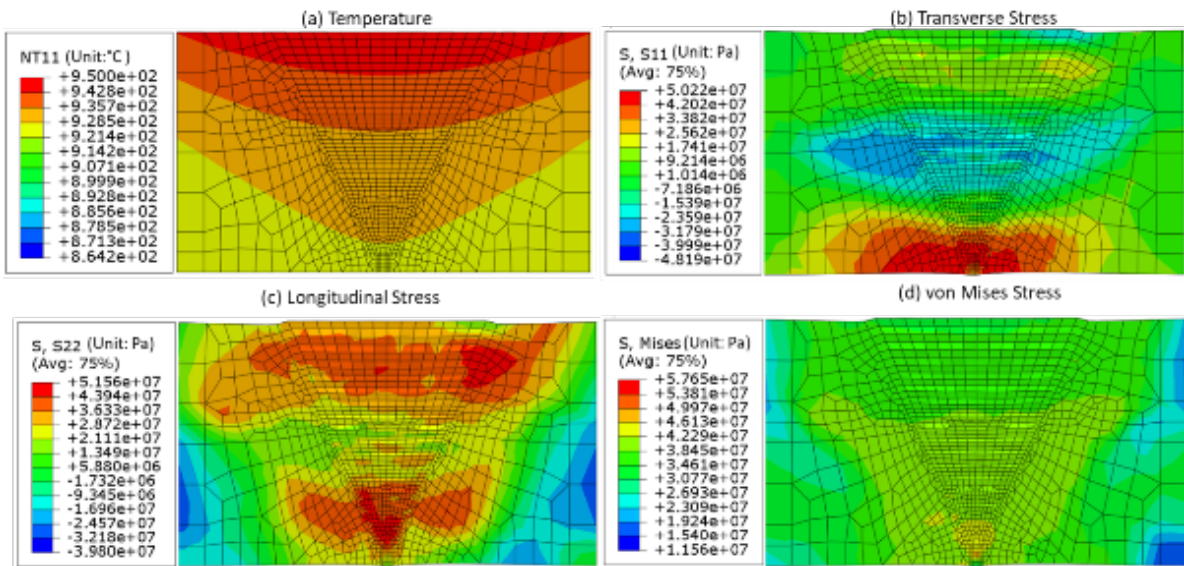


Figure 35. (From top left to lower right) (a) Nodal temperature, and (b) transverse, (c) longitudinal and (d) von Mises stresses during heating to ~950°C

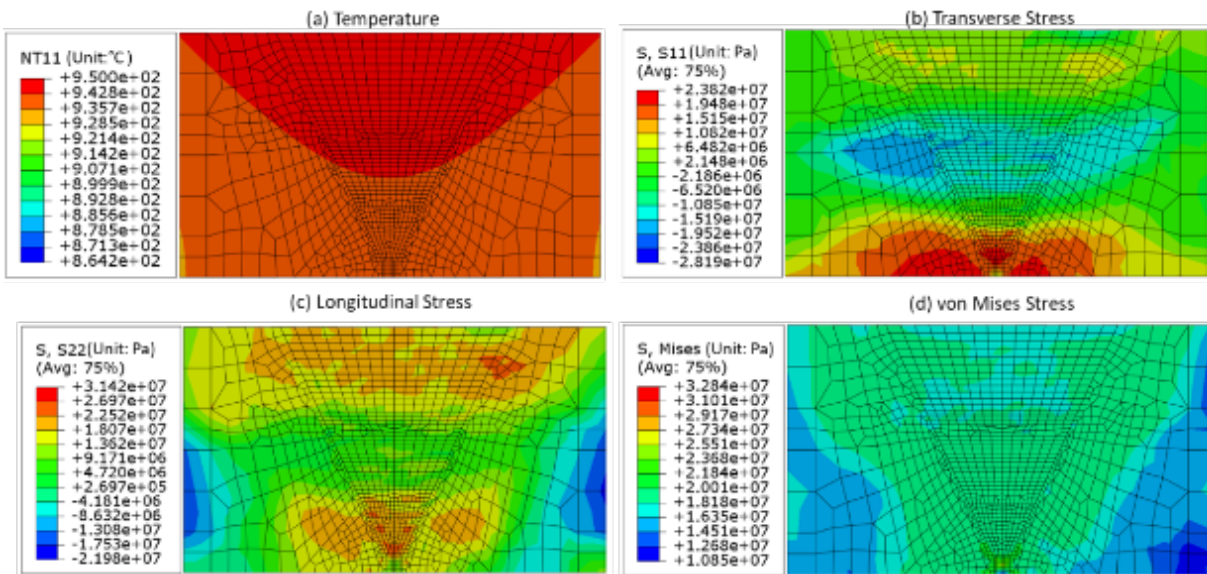


Figure 36. (From top left to lower right) (a) Nodal temperature, and (b) transverse, (c) longitudinal and (d) von Mises stresses after one hour holding at $\sim 950^{\circ}\text{C}$

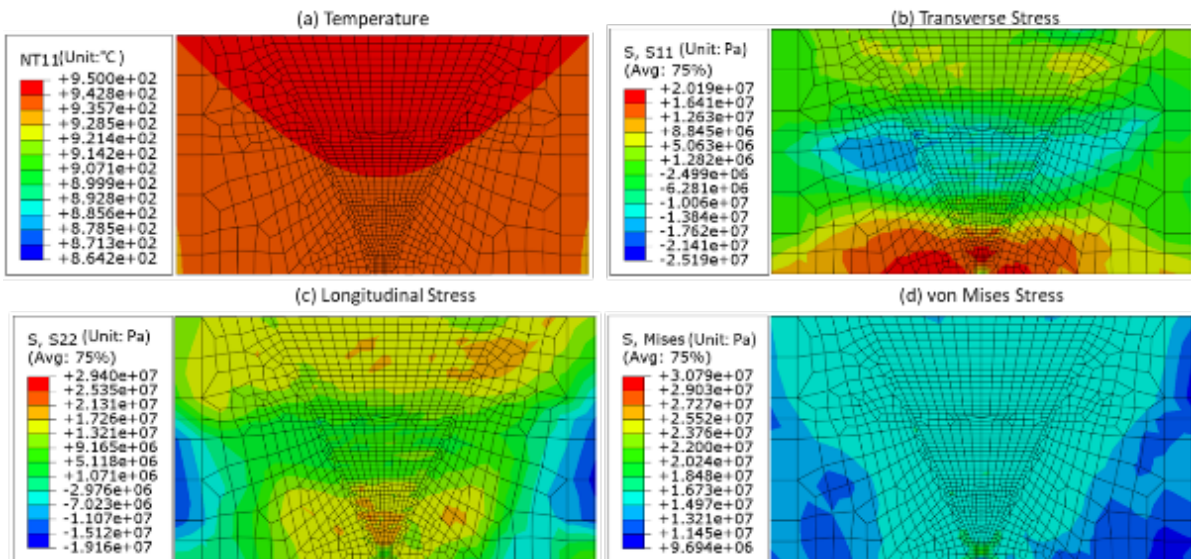


Figure 37. (From top left to lower right) (a) Nodal temperature, and (b) transverse, (c) longitudinal and (d) von Mises stresses after two hours holding at 950°C

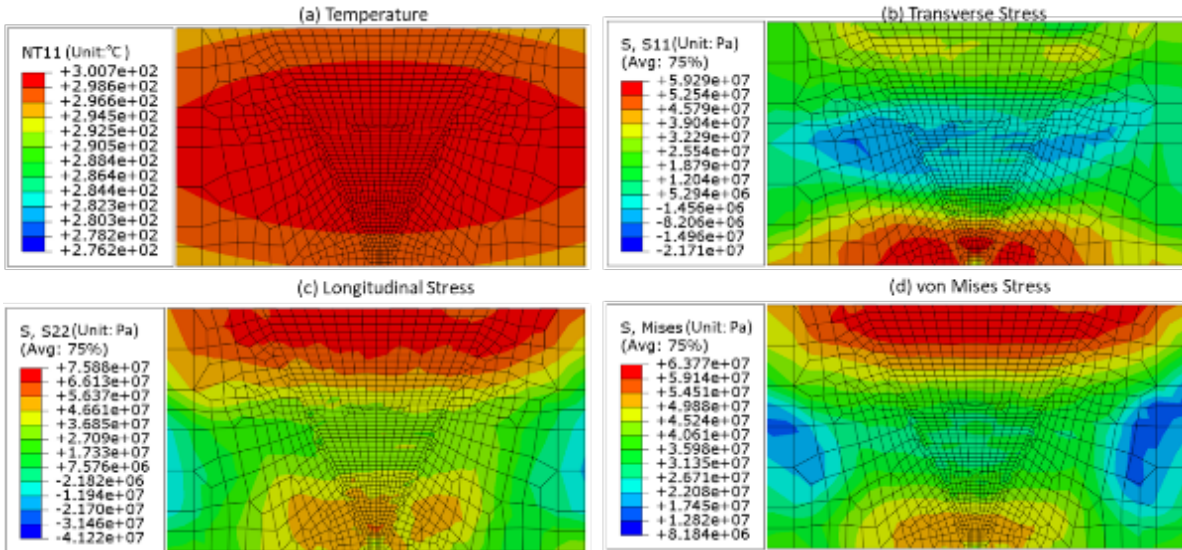


Figure 38. (From top left to lower right) (a) Nodal temperature, and (b) transverse, (c) longitudinal and (d) von Mises stresses after one hour into cooling from 950°C

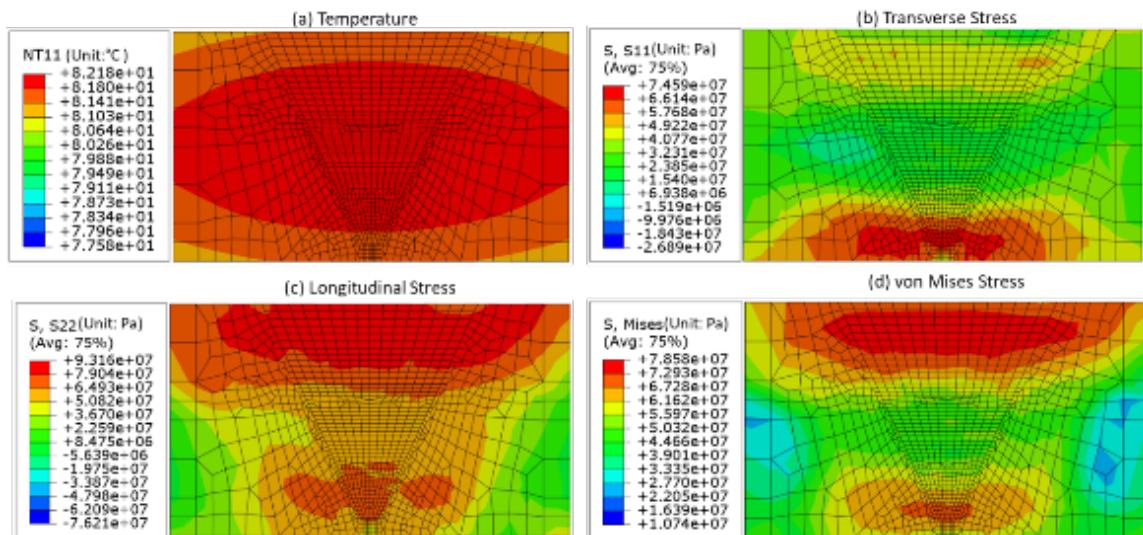


Figure 39. (From top left to lower right) (a) Nodal temperature, and (b) transverse, (c) longitudinal and (d) von Mises stresses after three hours into cooling from 950°C

The modeling results indicate that most stress relaxation occurs during heating, particularly above 600°C. The heating rate will likely influence stress relaxation percentage as a function of temperature, as seen in previous FE analysis. Stress relaxation results from the validated thermal profile, the peak stress values lie below the critical stress to failure as a function of temperature based on Gleeble reheat crack tests as seen in Figure 40. The only point of concern is around 800°C; however, those samples failed after heating to 800°C and a holding time of 4 hr Upon heating to 850°C within a time of 15 minutes, the stress has relaxed below the no failure sample at 850°C and above. Because of fast heating, there is no concern for cracking near 800°C.

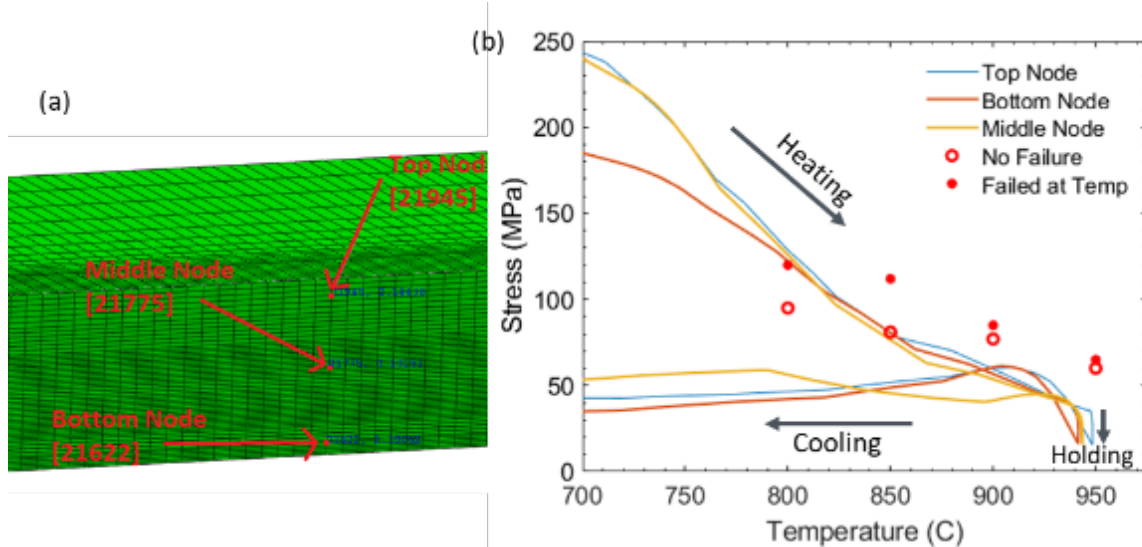


Figure 40. (a) Top, middle, and bottom node (b) stress versus temperature plot during heating, holding, and cooling along with E347 weld metal crack susceptibility critical stress values generated from Gleeble SRC experiments.

Stress Relaxation Results in 40-Pass Welded in Old (No Insulation) vs New (With Insulation) Model

After analysis of the steady state region, analysis of the highest stress regions on the edges of the model (see Figure 41(a)) were analyzed in both the old PWHT model with no insulation (Figure 41(b)) and the new PWHT model with insulation (Figure 41(c)). The biggest improvement in the new insulated model is a lower temperature gradient through thickness. At the maximum von Mises stress location near the bottom of the plate, the peak temperature of old model reached was 812°–820°C during soaking, while the new model shows a peak temperature of 928°–942°C within the short time of reaching soak temperature. In the old model, Figure 41(b) suggests that the maximum von Mises stress location may experience potential failure since the stress curves doesn't relax below the no failure stress value for a relatively long time and the temperature saturates at 820°C. The new model shows stress relaxation below the threshold upon heating to 850°C and above as seen in Figure 41(c). The insulation applied provides the necessary stress relaxation through thickness upon heating to 950°C as shown in Figure 42.

Figure 42

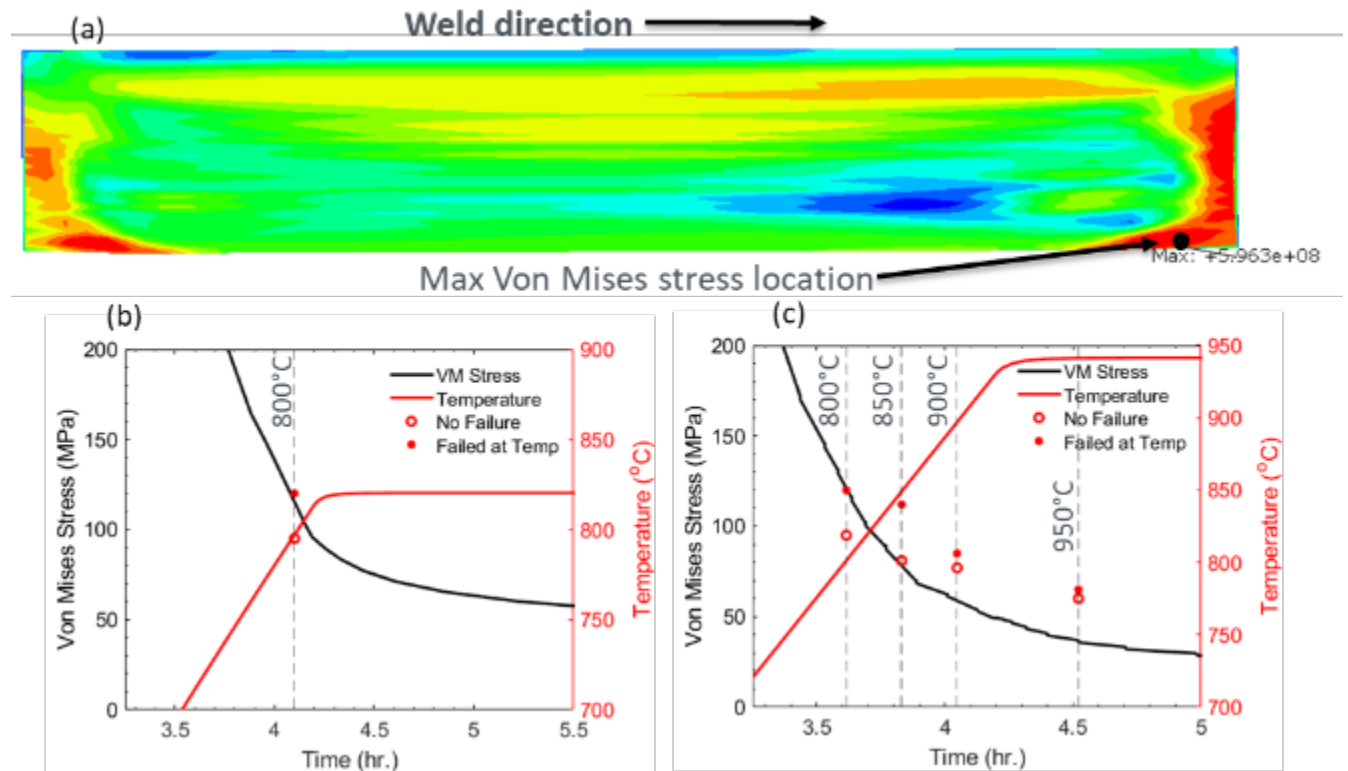


Figure 41. (a) Longitudinal cross section of as-welded FEM showing maximum von Mises stress location of 596 MPa on the back edge of the weld, (b) old PWHT model: no insulation showing stress relaxation as a function of time of maximum stress location in which the peak temperature reached no higher than 812°–820°C in maximum stress location, while (c) new model shows the stress relaxation below the threshold at 850°C and above and with peak temperatures of 928°–942°C

The von Mises stress contours upon heating to 950°C at both the quasi-steady state region and near the weld start/stop transient locations is seen in Figure 42. The old model without insulation in general shows higher stresses near the roots of the weld than the new model with insulation. The old model could be predicted to fail in both the steady state regions and the maximum stress locations. In comparison, the quasi-steady state weld within the new model with insulation shows sufficient stress relaxation below threshold and therefore no cracking is expected during PWHT at a heating rate of 222°C/h to 950°C for two hours soaking. It should be noted that the new model with insulation may experience stresses at 70 MPa and above within very limited regions near middle thickness at the start/stop locations during welding, where cracking could potentially occur. Therefore, frequent weld start/stop should be avoided during fabrication to prevent a relatively high susceptibility to cracking during PWHT and service.

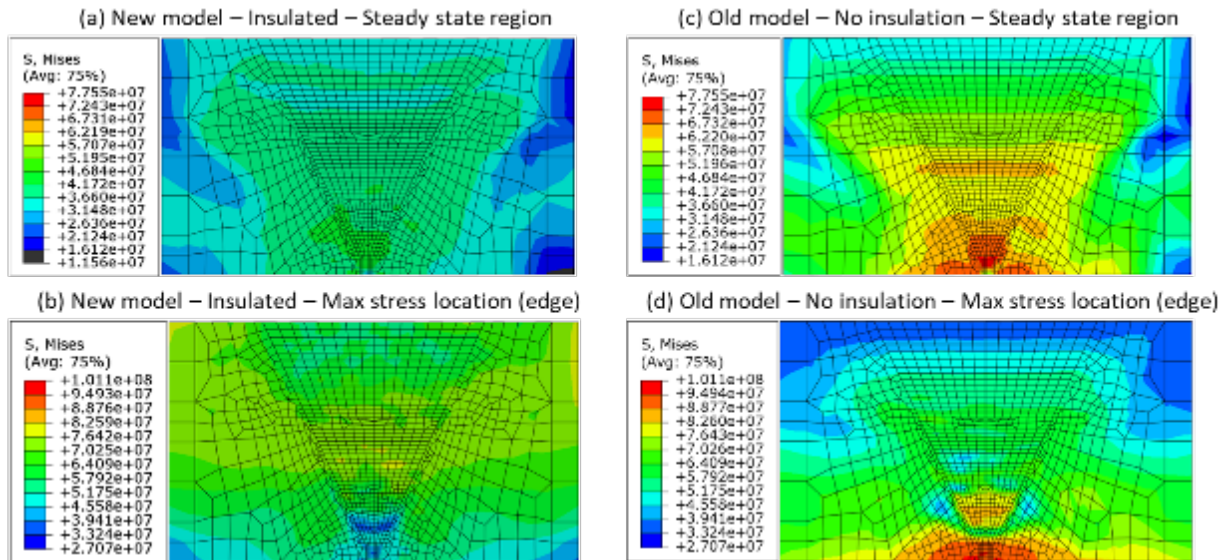


Figure 42. von Mises stress contour comparison at end of heating (upon reaching 950°C) for (a) new model in steady state region, (b) old model in steady state region, (c) new model in the maximum stress location, and (d) old model in maximum stress location. The same legend limits are restricted for (a-b) and (c-d) separately for comparative purposes.

Lessons Learned and Conclusions of Milestone 1.1.1

Based on the results and lessons learned from milestone 1.1.1, here are some conclusions:

- The allowable temperature gradients by code are generally 55°C within the soak band and through thickness region. Maximum heating and cooling rates, using codes (e.g., AWS D10.10), recommend 444 C/h/t (t-thickness in inches) and 278°C/h/t.
- FEM analysis suggests a heating rate between 222°C/h and 111°C/h be used with a peak temperature of 950°C for 2h soak. A first initial step of 600°C may be used for thermal stabilization before heating to peak soak temperature. PWHT FEM thermal profiles were validated with experimental temperature measurements using double sided insulation with a PWHT schedule of 222°C /hr heating rate with 950°C-2 hr soak on 2” thick 40-pass weld.
- Both-sided insulation is preferred for meeting ASME and AWS PWHT codes for minimizing temperature gradients for the 2” thick weld plates and prevent SRC during PWHT. Experimental problems with heater burnout, due to the lack of insulation on the backside, led to the confirmation of needing as much surrounding RCF insulation as possible to mitigate convection to the air and power burnout. This complicates PWHT, especially for floor welds, where backside insulation is not feasible for existing tanks.

4.2 Milestone 1.1.2 Heat Transfer Limitations in PWHT with Induction Heating

Two sets of experiments were carried out using two different coils, with the second coil having an appropriate coil width and insulation conditions applied.

First Set of Experiments Summary Using Ellipse-Shaped Coil

A few static induction heating experiments took place on 2" thick plates using setup and induction coil (ellipse-shaped) as illustrated in Figure 43. Pyrometers and thermocouples were both used to measure surface temperatures. All the pyrometer measurements used an emissivity value of 0.5. This value was estimated based on calibration experiments between a low temperature pyrometer and the TC1 location. Note that in the later new setups, another calibration test was performed, which is described in detail in the next section. The thermocouples were placed in the transverse direction to the center of the heat source, as shown in photos of Figure 43. The geometry of the coil and the top view of the pyrometer and thermocouple placements on the top surface relative to the primary heated (ellipse-shaped) location are shown in Figure 43 (c-d). A ½" thick ceramic fiber insulation layer was placed beneath the substrate to help retain heat.

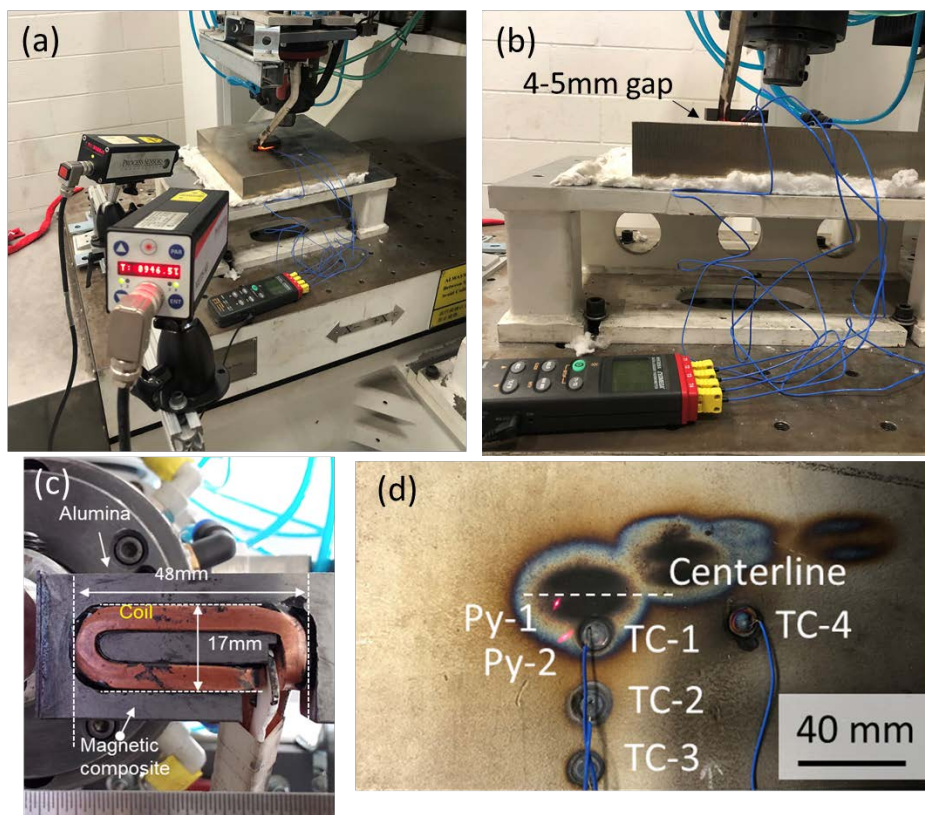


Figure 43. Experimental setup of static induction heating experiments (a) pyrometer setup (b) sideview showing 4-5 mm gap between 2" thick 347H SS substrate and induction coil, (c) geometry of coil, and (d) top view of location with pyrometer placement and thermocouple placements on top surface

Figure 44 compares the temperature recorded during two induction heating experiments (Experiment 1 and 2) with different powers of 5 and 7 kW. Temperature profiles were recorded using a pyrometer and thermocouples. As shown in Figure 44, there are two sets of data from Experiment 1, which include the peak temperatures during the 5-kW heating case reached at about 30 minutes into the simulation and 7 kW case reached at an hour. The data points are grouped according to their location transverse to the induction coil, including Pyr-1, Pyr-2 and Tc-1, Tc-2, and Tc-3. Experiment 2 for 7 kW has slightly higher temperatures than Experiment 1 for 7 kW, which can be explained by a longer test time in Experiment 2. The 7-kW case in both

experiments generates steeper temperature gradients between pyrometer 1 and 2 (i.e., 23°C/mm), while the 5-kW condition temperature gradient is shallower (i.e., 13°C/mm).

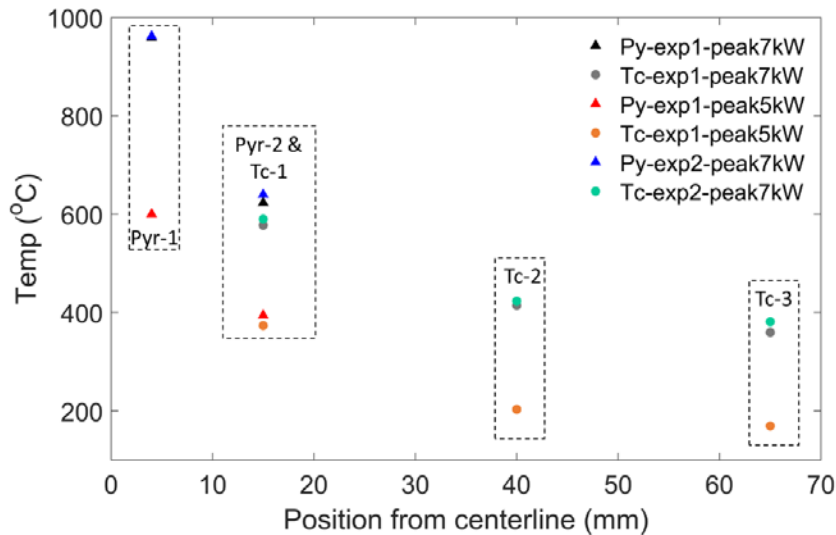


Figure 44. Temperature gradients for 7-kW and 5-kW conditions

FE Induction Heating Simulation Using Ellipse-Shaped Coil

Like ceramic heating, induction heating is also simulated with FEM using the ellipse-shaped coil geometry from the initial experiments. As shown in Figure 45, the model consists of a current-carrying coil, a plate, and surrounding air (removed from displaying for clarity). The plate size is 500mm×100mm×12mm. The coil size is shown in Figure 45. The coil is placed on the top of the plate with a 5 mm distance. The magnetic permeability of stainless-steel plate and surrounding air are 1.26000 H/m and 1.25664 H/m [47], respectively. The electrical conductivity is 1.45×10^6 S/m and 3×10^{-15} S/m for plate and air [48]. To compute the temperature distribution and time evolution, a coupled electromagnetic-heat transfer analysis is performed using the co-simulation feature of ABAQUS. A time harmonic electromagnetic analysis is employed to compute the Joule heat generated from eddy currents induced in the plate. A transient heat transfer analysis (comprised of only the plate) is employed to compute the temperature in the plate. The ABAQUS Co-simulation automatically maps the Joule heat and temperature in the plate between the two analysis procedures. The current density in the coil is set to 8.62×10^6 A/m², which is calculated from the experimental parameter 213 A / 25 mm² with a power of 7 kW.

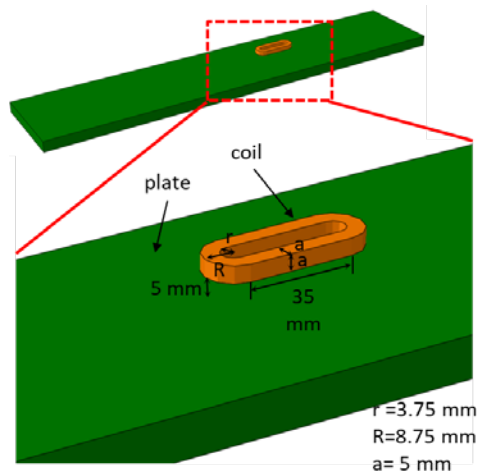


Figure 45. Schematic setup of induction heating model

The contour plots of the input electric current in coil, electromagnetic induced eddy current, and temperature in the plate are shown in Figure 46 (a), (b) and (c), respectively. The time elapsed for each image is 0 s, 6.2 s, 19.3 s, and 50 s. The peak temperature at 50 s is around 1,000°C. This preliminary data show the capability of simulating induction heating with co-simulation of electromagnetic-heat transfer analyses. Further adjustment of input parameters is needed to compare with experiments. Furthermore, it should be noticed that the coil or plate is not moving in this model, while the relative motion between them will be necessary in real PWHT because of the big size of the object. This will be considered in the future simulation work.

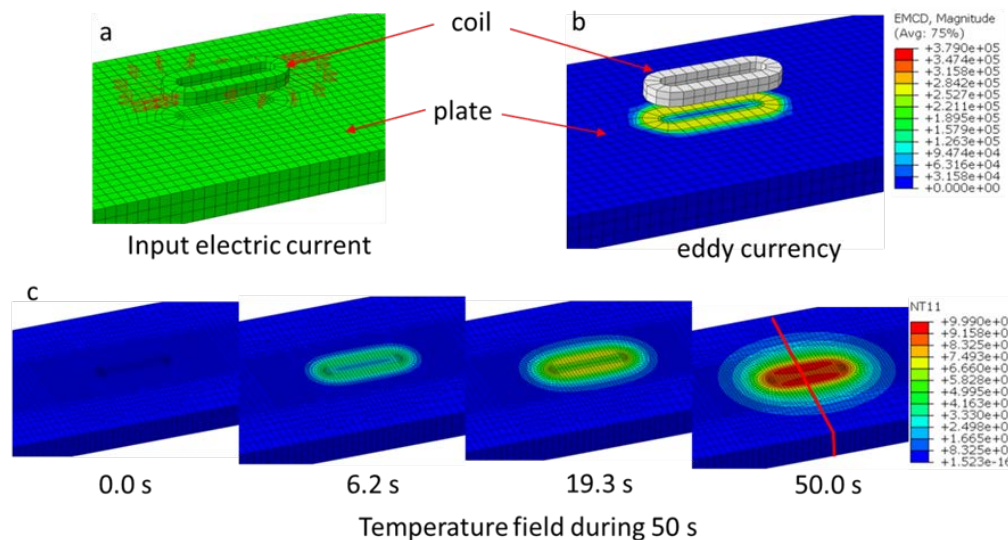


Figure 46. Preliminary results of induction heating simulation: (a) input electric current; (b) eddy current induced by electromagnetic; and (c) temperature contour maps at different time within 50-second period

To investigate the temperature distribution along thickness, cross section of the plate at peak temperature position is exposed (by cutting the plate at red line shown in Figure 46 (c)). As

shown in Figure 47, the contour map of the temperature at the cross section indicates that area near top surface is heated much more than bottom part of the plate. Figure 47(b) shows the temperature versus time for the node that experienced the highest peak temperature. Figure 47(c) shows that the temperature difference between top surface and bottom surface is around 400°C for three times of 6, 19, and 50 s. Figure 47(d) illustrates the temperature gradient along the top surface for the 100 mm width, which shows approximately a steep 40°C/mm temperature gradient on each side of the peak temperature. A modification of the coil geometry and parameters would be needed to ensure fewer steep gradients.

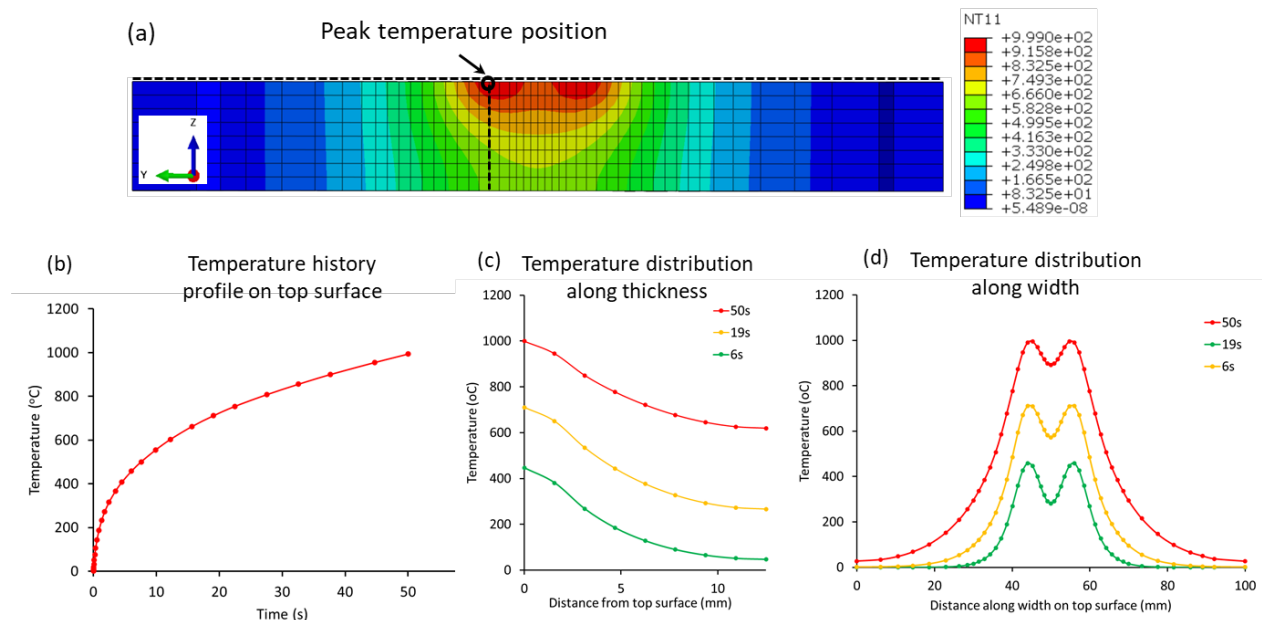


Figure 47. Temperature result at cross section (cut at the red line in Figure 46(c)) of the plate (a) contour map of temperature at 50 seconds; (b) Temperature history of peak temperature position during 50 s; and (c) Temperature distribution along thickness from top surface to bottom surface

Based on the initial experiments using manual control, 7–8 kW would be suitable for reaching 950°C. A modification of power as a function of time can be optimized to get a desired temperature. The initial heating rates are extremely fast due to the physics contributed to induction heating; however, there is some effect of heat conduction as time increases in which temperature increases. Thus, a high power may be used initially, but a decrease in power over time may be needed to get an isothermal condition. A modification of the coil geometry and parameters would be needed to ensure fewer steep gradients and prevent the cold spot under the center of the coil.

Second Set of Experimental Results Using New Coil Geometry

The new experimental setup involved the use of a new coil and setup, as seen in Figure 48. The temperature measurement locations are shown in Figure 48(d), which includes the same two pyrometers used for the old experiments and two surface thermocouples on the backside of the plate. TC5 is directly under pyr-1 and pyr-2, which is centered under the coil. TC6 is 2” away on the back-side surface, directly aligned with the short side of the coil. TC1, 2, and 3 are surface thermocouples on the top surface to measure temperature gradients.

Table 16 tabulates the experiment number and associated parameters and backing condition. Ceramic fiber insulation was wrapped around the plate in experiment 9, as shown in Figure 49, to evaluate the benefits of insulation.

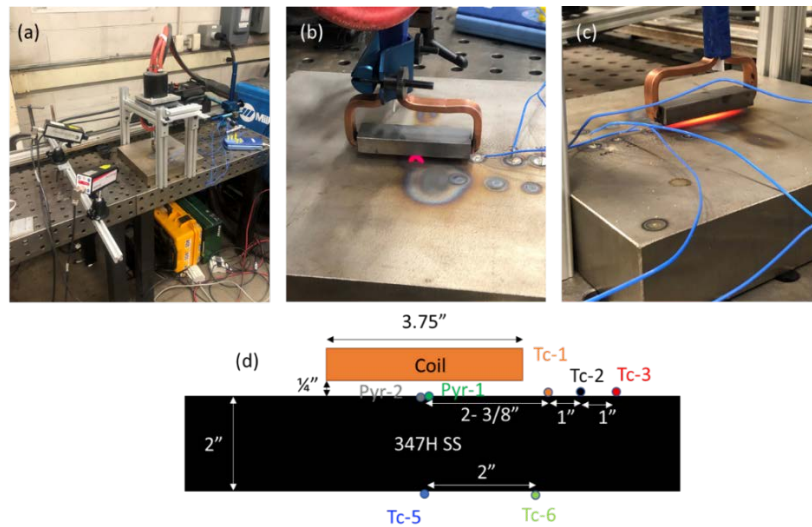


Figure 48. New induction coil (a) experimental setup, (b) location of pyrometers centered under the coil, (c) example of 10 kW test showing very hot surface under the coil, and (d) schematic showing temperature measurement locations, including pyrometers (Pyr) and thermocouple locations (TC). Conditions for Experiments 5–8.

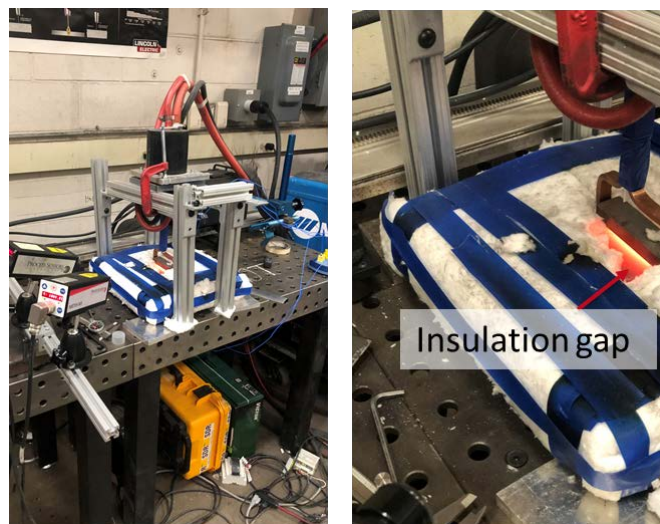


Figure 49. Induction experimental setup showing the addition of insulation and the insulation gaps needed for pyrometers measurements. Setup used for Experiment 9.

Table 16. New induction coil experimental table with power, volts, amps, and frequency parameters and backing condition specified. All experiments contained no insulating material.

Experiment #	Backside Condition	Constant Power	Volts	Amps	Frequency
4	Failed initial experimental trial with new setup				
5	Table	7 kW	325	261	21.9 KHz
6	Table	10 kW	379	305	
7	Lifted	7 kW	325	261	
8	Lifted	8.5 kW	345	280	
9	Lifted and insulated	Initial 8.5 kW then decrease for 2 hr soak			

Experiments 8–9 with a power of 8.5 kW and frequency of 21.9 KHz were selected to be compared to the ceramic heating experiments (peak at 950°–1,000°C) due to a comparable time to reach peak temperature. Experiment 8 was carried out using a power of 8.5 kW, which was a balance between 7 and 10 kW to get closer to 950°C at the Pyr-1 location. Pyr-1 measured the temperature below the coil reached about 1,000°C after 90 minutes of heating. By raising the plate and having a convective boundary condition with air instead of conduction with the support plate, the temperature gradient is better controlled compared to Experiments 5–7.

Application of insulation further minimized temperature gradients. Experiment 9 involved the use of surrounding insulation to first run a constant power for 90 minutes at 8.5 kW to reaching 1,000°C. After reaching this temperature, as seen in Pyr-1 from Figure 50, the temperature was held constant to simulate a soak time of two hours. During soak time, the temperature increased in all locations throughout the plate (~100°C). Figure 51 show the specific thermocouples temperature and pyrometer temperature readings with and without insulation after reaching 1,000°C within 90 minutes of heating. Figure 52 graphically illustrates the temperature gradient at the bottom and top surfaces that are parallel to the long edge of the coil, based on the diagram in Figure 51. There is about a 100°C improvement in the top surface thermocouples in Experiment 9 compared to Experiment 8. Further reduction of temperature gradients can be maintained by reducing the heating rates from a current 400°–500°C/hr to a maximum 222°C/hr, but ultimately for a complete comparison to the ceramic heating method, experiments using a coil with a length that covers the whole weld length would further improve temperature gradients.

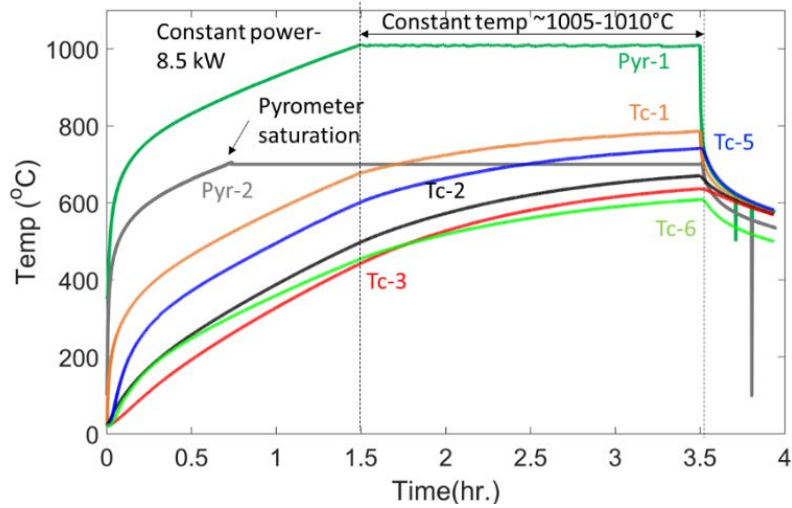
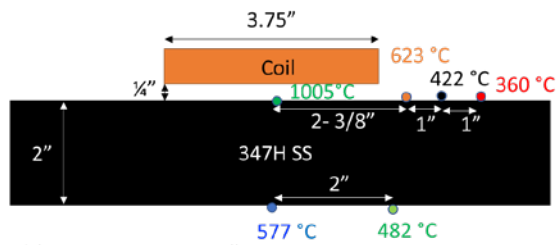


Figure 50. Experiment 9 temperature vs time for induction heating experiment with initial power of 8.5 kW for 1.5 hr, followed by decreasing power to keep a constant temperature just above 1,000°C for a 2-hr soak time

(a) Without insulation-Exp #8



(b) With insulation-Exp #9

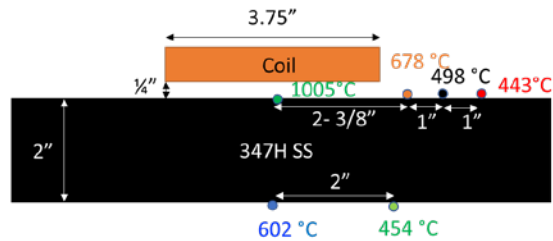


Figure 51. Comparison of temperature values of thermocouples and pyrometers: (a) without insulation during Experiment 8 and (b) with insulation during Experiment 9 after 90 minutes of heating at a constant power of 8.5 kW

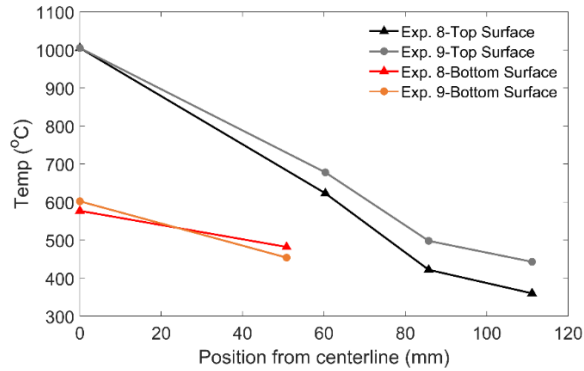


Figure 52. Temperature gradients with induction Experiments 8–9 on both the top and bottom surfaces. Adding insulation reduces temperature gradients, as seen with Experiment 9 results on the top surface.

Conclusions From Induction Heating Experiments (ST1.1.2)

1. So far, the induction heating experiments with complete insulation on both top and bottom surfaces performed slightly better in terms of temperature gradient control. Similar requirements of temperature gradient for ceramic heating would need to be applied for induction heating.
2. Induction heating as a PWHT technique has the capacity to be used as a replacement of ceramic heating techniques with the consideration of using insulation, slow heating rates and proper induction coil geometries. Coil geometry would need to be optimized according to thickness and weld geometry.

4.3 Milestone 1.2.1 PWHT Effects on Cracking Susceptibility

The objective of milestone 1.2.1 was to demonstrate the effect of PWHT on crack susceptibility control with respect to as-welded condition using quantitative metrics, such as elevated temperature ductility. Table 17 includes the milestone details.

Table 17. Milestone 1.2.1 summary

Milestone	Description	Metric	Success Value
1.2.1 Demonstration of PWHT effects on cracking susceptibility control	Coupons will be extracted from the welded thick plates before and after PWHT for reheat cracking test to demonstrate the improved ductility at service temperature. Metallurgical characterization will also be performed to characterize the microstructure before and after PWHT.	1. Hot ductility following PWHT; measured using Gleeble machine or MTS tensile equipment with furnace 2. Micro voids and microcracks measured using Metallurgical characterization using optical and electron microscopies ASME BPVC Section II and VIII (PWHT codes) and AWS D10.10	1. >80% of the base metal hot ductility 2. No noticeable micro voids and microcracks (in microns)

PWHT Effects on Microhardness

Microhardness measurements and micrographs were taken across passes 9 and 11 in E347 FZ in 1" thick lab as-welded condition in Figure 53 (a-b). A Vickers's hardness load of 300 g was used with a spacing of approximately 150 μ m apart from each other (3x the average indent size). It seems apparent that the center of the weld passes is weaker relative (205–210 HV) to the transition region between pass 9 and 11, which reached peak values of 235–240 HV. Reheated regions and weld pass boundaries may experience more local strain hardening due to cooling strains imposed by the weld thermal cycle. The reheated region of pass 9 includes locally lower δ -ferrite concentration (less dark etchant response) and exhibited higher hardness values, likely from dissolution of segregated elements that are more soluble in δ -ferrite than γ -austenite. The microhardness in these regions is generally harder than the surface microhardness, which is generally below 200 HV in the top layers. Similarities can be made with overall general hardness comparisons between samples in the lab and samples in the field, although the specific regions of the wall weld in Figure 53 below indicate higher hardness values, exceeding 250 HV. SRC has been reported to be in regions of hardness exceeding 250 HV [5], likely because ductility "exhaustion."

Figure 53 (c) represents a transverse microhardness line with respect to the welding direction, going from the HAZ into the FZ of pass 16 in matching E347 and E16.8.2 FZ, respectively. Locally, the microhardness can dip from 190–195 to 170–75 HV in the HAZ near the E347 FZ boundary. The microhardness increases back to 190–195 HV upon entering the FZ and then decreases again slightly back to ~185 HV. The E16.8.2-347H SS weld showed a similar trend but the difference in hardness in HAZ and FZ is less extreme. The HAZ microhardness dip is associated with coarsening of grains from weld-induced thermal cycle in the coarse-grained HAZ.

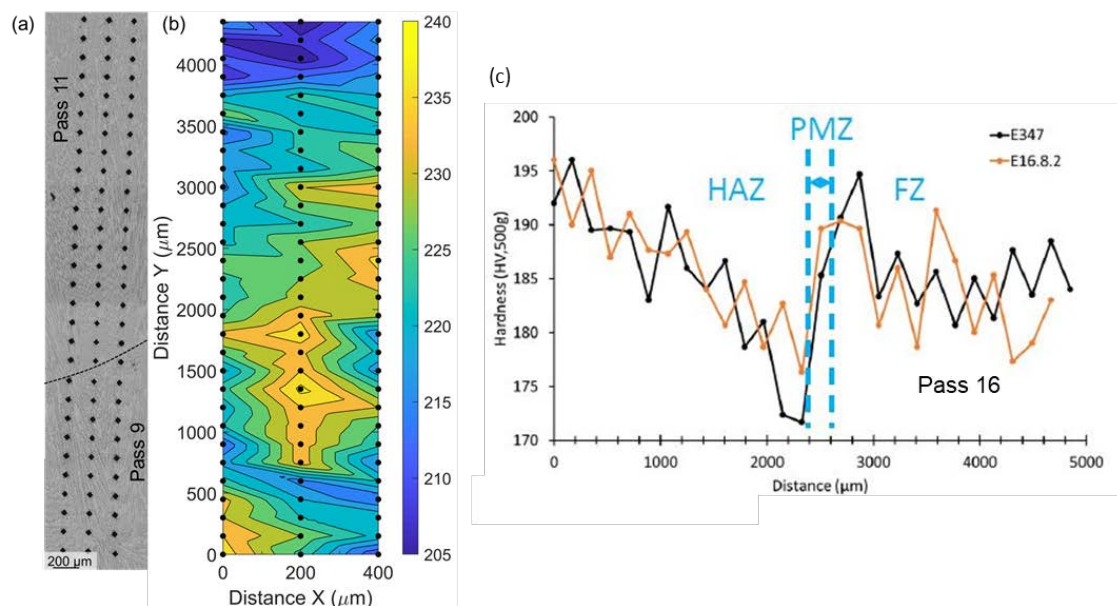


Figure 53. Microhardness in (a-b) FZ of E347 lab weld between passes 9 and 11 of 1" thick single-V weld and c) line microhardness from HAZ to FZ (pass 16) of matching filler E347-347H weld and alternative filler E16.8.2-347H weld, respectively.

Compared to previous microhardness plots on the seam field weld and after repair and to the lab as-welded sample in Figure 53, the PWHT lab weld sample that passed phased array UT (conducted at Crescent Dunes) has the lowest microhardness values in the FZ and base metal, as seen in Figure 54. FZ peaks at 225 HV and a sharp peak exists at the FZ boundary and the HAZ dips to below 200 HV. Compared to the FZ of as-welded lab sample in Figure 53 (a-b), the FZ peak hardness is lower (225 vs 240 HV) but not significantly after PWHT of lab sample at 950°C for three hours. It is likely due to a combination of some dislocation recovery and aging effects of Nb and Mo carbonitrides. Overall, it seems that the field welds (including repair weld with E16.8.2) generally contain higher microhardness values than the lab welds in the HAZ (200–220 vs 170–180 HV) and FZ (220–290 HV in as-received field weld vs 200–240 HV in lab weld).

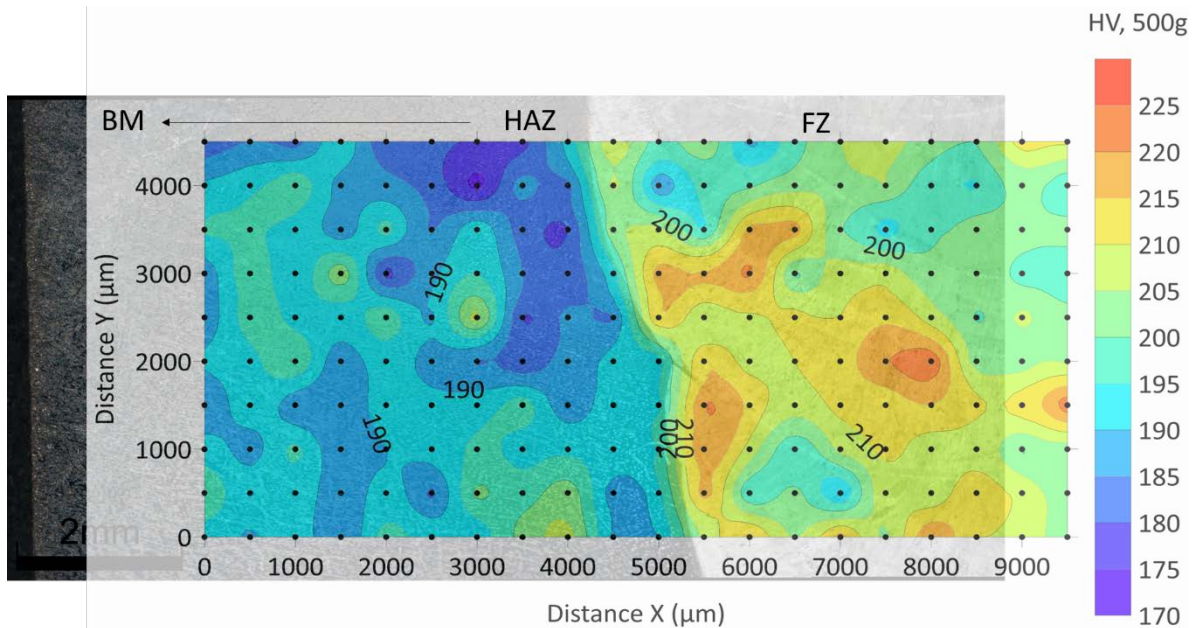


Figure 54. Microhardness map of E347-347H weld after PWHT (950°C-3hours); FZ peaks at 225 HV, base metal/HAZ below 200 HV

Tensile Tests at 600°C

Tensile tests were conducted on 347H HAZ, E347, and E16.8.2 cross welded samples before and after PWHT using the Gleeble 3500. Samples were machined using the same geometry as all SRC tests. It should be noted that the HAZ samples were pre-strained to 0.1 after the 1,335°C peak temperature thermal cycle before heating up to 600°C. All samples were held at 600°C for 4 hours prior to pulling at 0.001s⁻¹ strain rate. Table 18 represents a summary table of the mechanical properties for all samples, including the 0.2 % strain offset yield strength (Y.S.), ultimate tensile strength (UTS), peak true stress, measured true uniform strain, and calculated engineering strain up to load instability (i.e., necking). Necking and fracture occurred in the FZ of the cross-weld samples and represent the transverse orientation strength. Overall, E347 and E1682 welds meet the 80% ductility minimum after 950°C PWHT but the HAZ does not meet this minimum compared to the original ductility before PWHT. PWHT did not improve ductility in HAZ, but ductility improved with 1,050°C PWHT in the E347 cross weld sample. Samples meet the 80% ductility minimum after 1,050°C PWHT. The Y.S. is mostly impacted by PWHT

in E347 and E16.8.2 samples. The yield strength decreased by 92 MPa after 950°C in E347 and almost decreased by half (from 260 to 144 MPa) in the E16.8.2 sample.

Table 18. Tensile test at 600°C summary (4 hr at temperature prior to pulling). NOTE: HAZ samples have 0.1 pre-strain to represent strain accumulation from multi-pass welds)

Group	PWHT	Y.S. (MPa)	UTS (MPa)	Peak true stress (MPa)	True uniform strain	Uniform engineering strain
347H HAZ	none	282	411	510	0.221	0.247
	none	278	409	518	0.237	0.267
	750°C/2 hr, 1050°C/30 min	200	347	405	0.16	0.174
	950°C/2hr	223	352	416	0.167	0.181
	1050°C/30 min	193	347	415	0.179	0.196
	950°C/2hr- overheated to 1200°C	119	301	372	0.217	0.24
E347	none	302	382	447	0.159	0.172
	950°C/2hr	210	340	392	0.145	0.156
	1050°C/30 min	170	330	406	0.209	0.233
E16.8.2	none	260	372	427	0.14	0.15
	950°C/2hr	144	335	437	0.269	0.309
	1050°C/30 min	85	336	430	0.246	0.280

Gleeble Thermomechanical Test Results

All lab Gleeble samples from the PWHT lab weld (soak temperature and time of 950°C/2 hr) are transverse to the welding direction, with the intention to including samples centered on FZ (Figure 55 (a)) and samples centered on FZ boundary and HAZ (Figure 55 (b)). Half of the samples are extracted from the top ½” of the weld plate and the other half are roughly extracted from half-thickness location. However, upon receiving samples from machine shops, the offset to include HAZ in the center of the gauge length was not sufficient. Therefore, all of the samples here are primarily centered on FZ and should be compared to older FZ results shown in Figure 16 (a) (labeled as W in Figure 55 (a)).

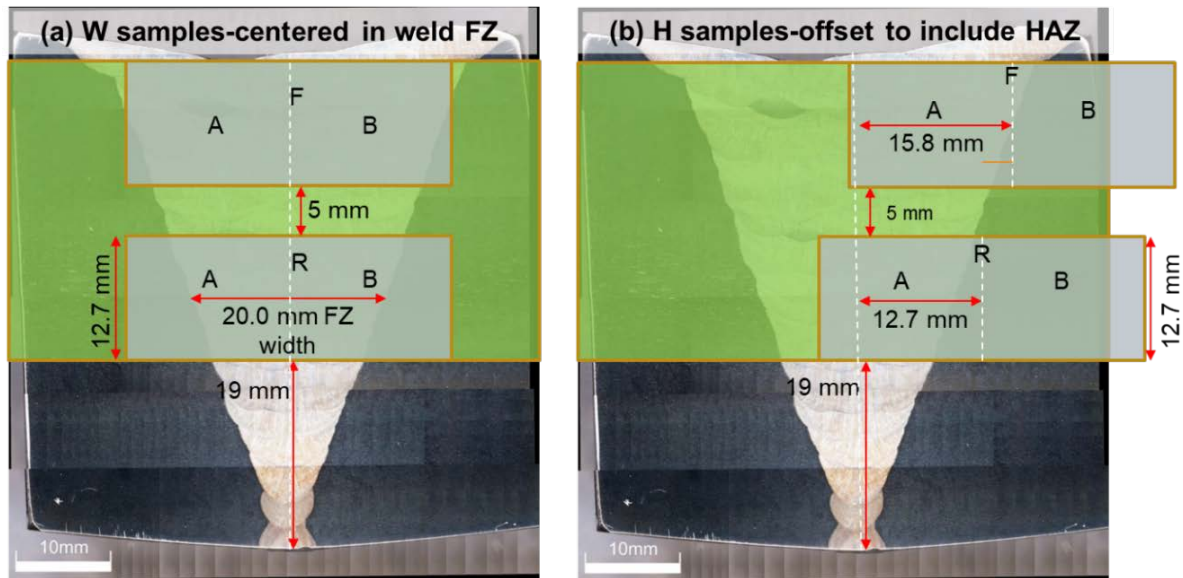


Figure 55. Sample extraction of gauge section of tensile samples with respect to weld centerline (a) FZ samples, and (b) offset samples to include HAZ

The procedure conducted is the same as previous SRC work. The four-step SRC procedure used for Gleeble experiments on lab PWHT samples in milestone 1.2.1 and field and repair welds in milestone 2.2.2 is shown below in Figure 56.

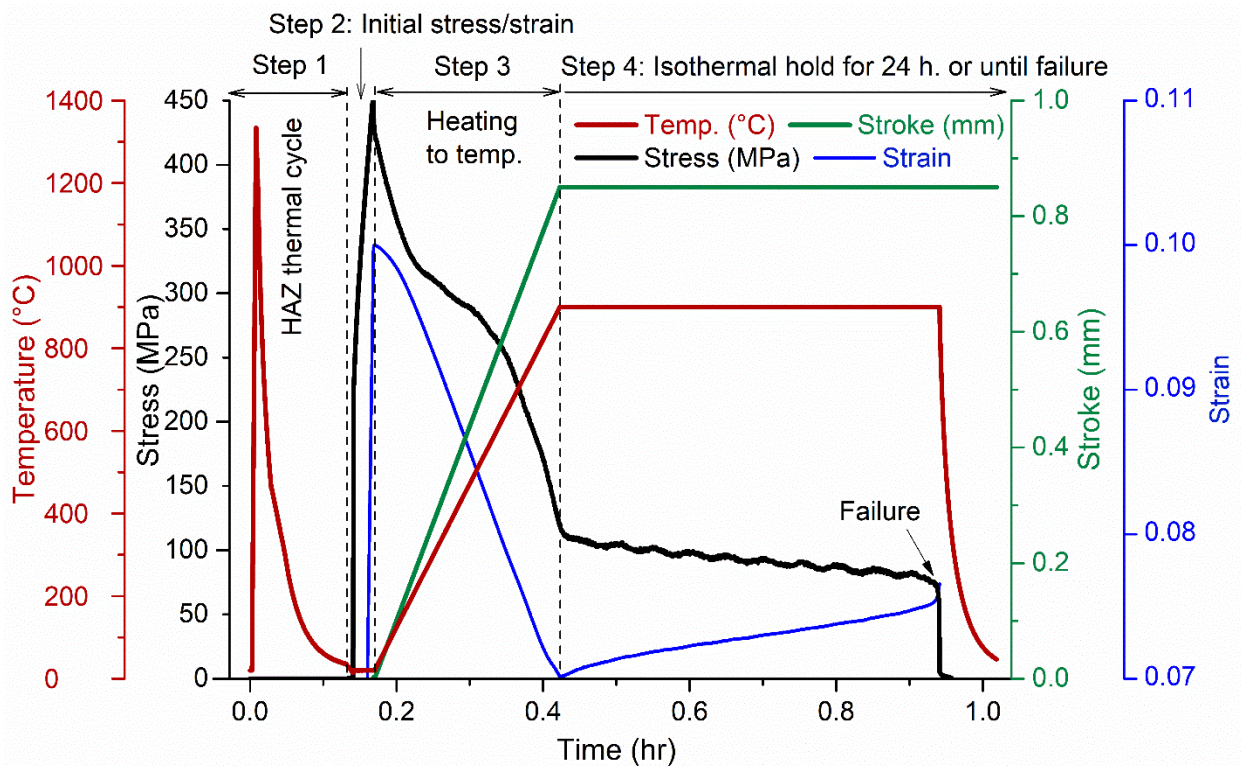


Figure 56. Gleeble four-step SRC procedure (e.g., 1335°C HAZ with 0.1 initial strain (450 MPa))

The new results from PWHT samples are detailed in Table 19. The ID corresponds to the designated machining location in Figure 55 (e.g., WF means centered on FZ and close to the top surface, while HR means centered on HAZ in mid-thickness location). The new results are tabulated using the same concept from as-welded results (shown in the 33458 project), which includes initial stress at RT, starting stress at temperature, failure conditions, time of test, and strain at temperature. The same initial stress conditions from as-welded tests were used for PWHT samples. Figure 57 illustrates a comparison of as-welded and PWHT starting stress at temperature as a function of temperature.

The first observation made pertains to the differences in starting stress at temperature with the PWHT samples, which are lower than the as-welded samples with the same starting stress at RT. PWHT samples have a lower yield strength than the as-welded samples, and therefore a higher amount of stress relaxation was observed during heating stage. In general, PWHT samples exhibited high resistance to SRC. The tests that failed at temperature (isothermally) would be the high initial stress tests up to 466–486 MPa (total of 1% strain) and reheated to 900°C. The remaining tests, all within the initial elastic stress/strain region, did not fail while at temperature for the duration of 22 hours or until the force level heat mute function was implemented, which means the force reaches close to 0 kN while at temperature with no cracking. The subsequent cooling stage incurred a rapid cooling strain while the sample was constrained, which opened cracks that didn't fully develop while at temperature. Essentially, susceptibility testing data at 800°C and 900°C in Figure 57 indicate a higher critical stress to fracture in the PWHT samples compared to the as-welded samples. For tests at 850°C and below, there were no fractures in PWHT samples while at temperature with a starting stress similar to that of the as-welded samples.

Table 19. SRC summary results of PWHT samples (FLHM stands for force level heat mute as reason for test ending)

Sample #	Temp (°C)	Initial Stress @ RT (MPa)	Starting Stress @ Temp (MPa)	Failure	Time to failure/cool	Strain @ T
WF.2	800	419	130	No	22 h	-0.5%
WF.3		421	141	Yes, cooling	22 h	1.2%
WF.4		405	130	Yes, cooling	22 h	1.05%
WF.5	850	335	109	Yes, cooling	22 h	1.4%
HF.1		332	103	Yes, cooling	19.8 h (FLHM)	0.2%
HF.2		335	108	Yes, cooling	22 h	0.95%
WF.1	900	466 (1% strain)	108	Yes, isothermal	41 min	1.5%
HF.3		486 (1% strain)	97	Yes, isothermal	1.7 h (102 min)	1.8%
HF.4		466 (1% strain)	93	Yes, isothermal	1.1 h (68 min)	1.37%
WR.1		330	89	Yes, cooling	11.1 h (FLHM)	2.28%

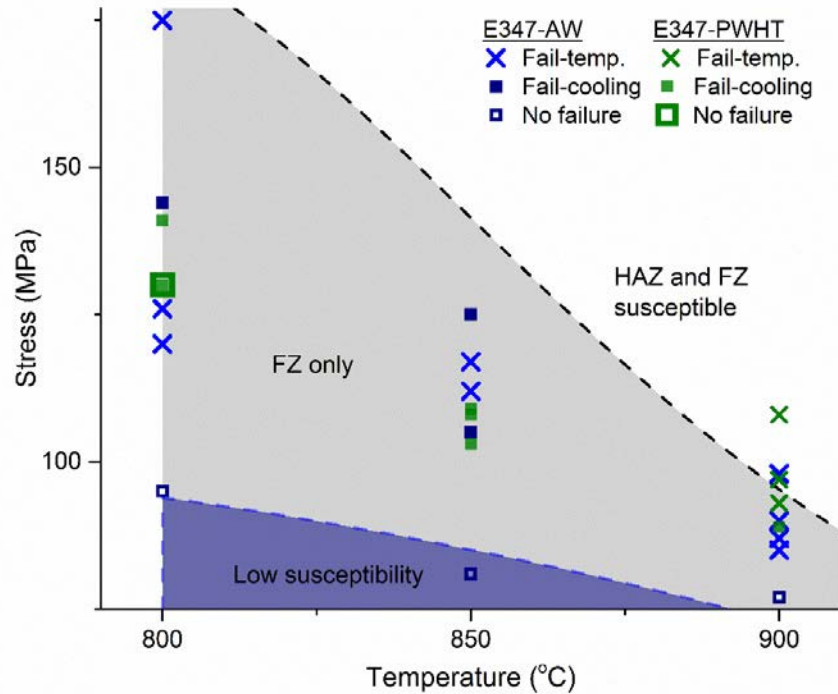


Figure 57. Starting stress at temperature as a function of temperature plot, including E347 as welded and PWHT (950°C/2h) test results. This figure is a blown-up image of Figure 16, but minus the E16.8.2 results for brevity and with included new PWHT data in green.

Additionally, the strains measured at temperature, which includes creep and possibly inelastic strain associated with phase transformations, is on average higher (>1%) in the PWHT samples vs the as-welded samples (shown in farthest right columns in Table 19). The amount of strain needed for fracture at temperature (Strain@T) in PWHT, particularly with 900°C test conditions, is higher than the strain needed for fracture in the as-welded samples, showing improvement in elevated temperature ductility.

Neutron Diffraction Results: Effect of PWHT on Residual Stress Reduction

The experiments conducted for this work were carried out at Oak Ridge National Laboratory (ORNL) using the High Flux Isotope Reactor HB-2B HIDRA Beamline (High Intensity Diffractometer for Residual Stress Analysis). The longitudinal direction (LD) of the weld, transverse direction (TD) of the weld, and normal direction (ND) of the weld are all investigated for an as-welded condition, but TD and ND were only collected in PWHT condition (870°C/3 hr). The top view of the beamline for the TD orientation is shown in Figure 58. The welding procedure was described more in the 33458 project report. For this task, two 12” x 12” welds were made using the same weld procedure and one of the welds underwent PWHT after welding. An additional weld was made to extract two 4-mm thick samples and one of the samples underwent PWHT using the same procedure for getting d_0 stress free samples. The PWHT procedure was performed using box furnace with Argon atmosphere. The d_0 stress free measurements for as-welded and PWHT conditions are shown in Figure 59.

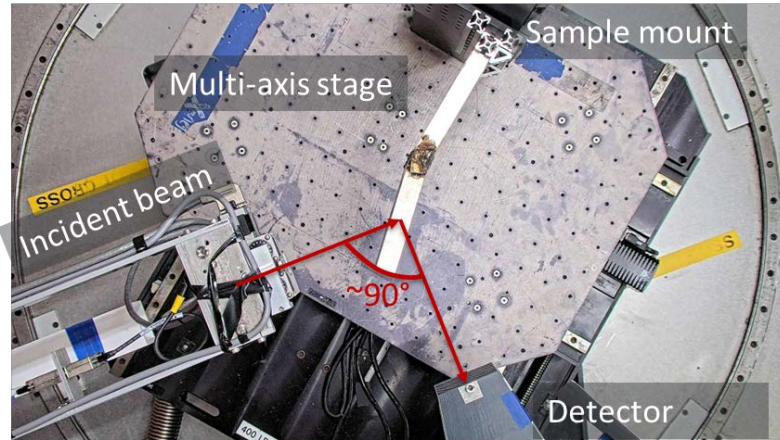


Figure 58. Top view of HB-2B (HIDRA) beamline at ORNL's High Flux Isotope Reactor showing sample in traverse direction setup

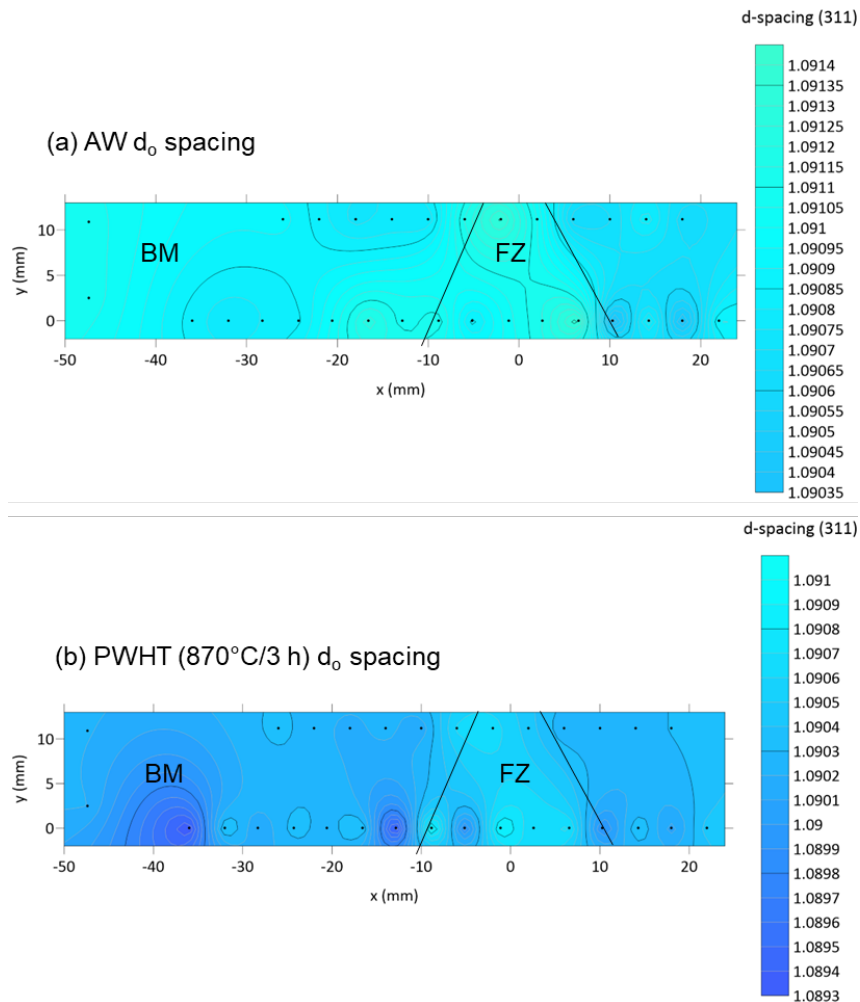


Figure 59. Neutron diffraction stress free d_0 -spacing results on single V weld (a) as-welded sample and (b) post weld heat treated sample with 870°C temperature and 3 hr soak time.

Figure 60 shows the d -spacing values for as-welded LD, as-welded TD, and PWHT TD. The as-welded LD shows the highest bulk strain in the top center E347 FZ, while the as-welded TD

shows the highest strain in the E347 FZ root passes, which is expected based on residual stress FEM prediction [36]. The comparison between as-welded TD in Figure 60 (b) can be made to PWHT TD in Figure 60 (c), where the tensile strains have normalized. d-spacing in PWHT TD in Figure 60 (c) is comparable to d_0 -spacing in Figure 59 (b). The ND showed similar trends of reducing tensile strains after PWHT.

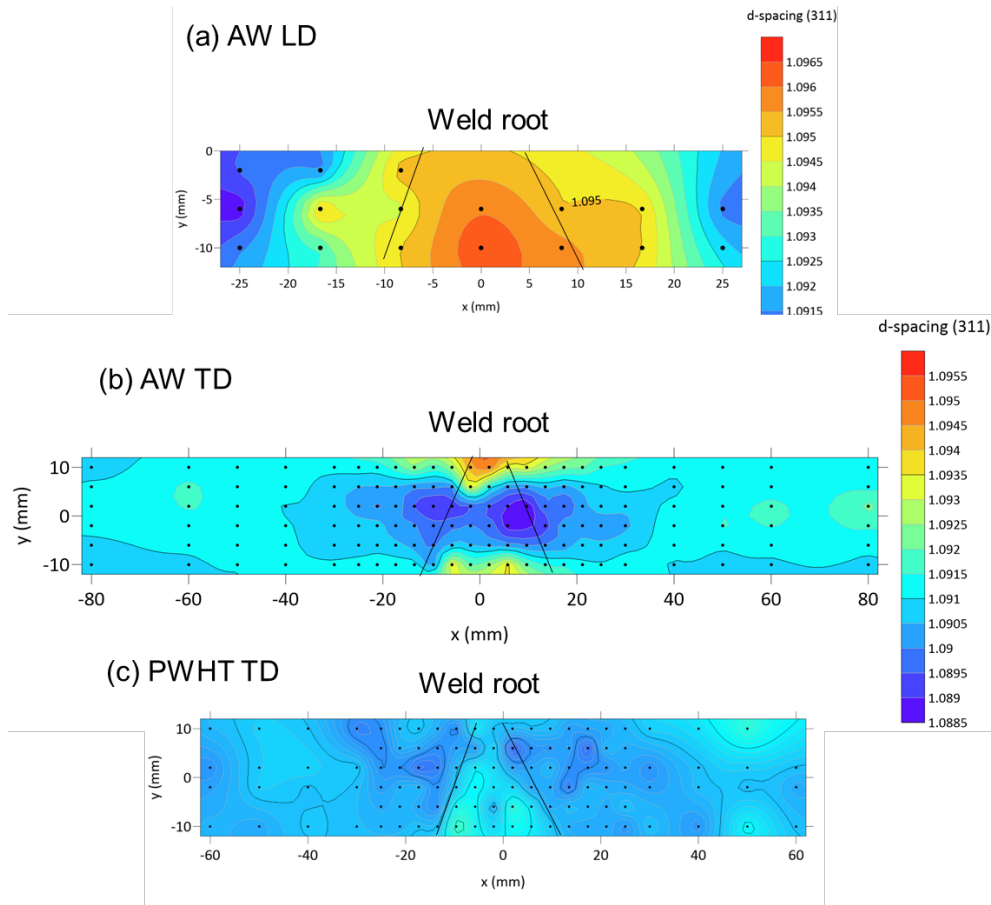


Figure 60. Neutron diffraction d-spacing results on single-V weld (a) as-welded longitudinal direction (LD), (b) as-welded transverse direction (TD), and (c) PWHT TD

Lessons Learned

Based on the results for milestone 1.2.1, some lessons learned and conclusions are:

1. Microhardness is more uniform in base metal after PWHT and has lower peak values in FZ compared to as-welded condition.
2. Residual strains in the as-welded condition are significantly reduced and homogenized through PWHT, as demonstrated by the d-spacing analysis in TD (transverse to weld direction) and ND (through thickness) directions thus far.
3. The weldments after PWHT meets the 80% of base metal strength criterion. However, the ductility of HAZ after 950°C PWHT results in <80% ductility relative to HAZ sample with no PWHT.

4. Comparison of as-welded (completed in last SRC project) to PWHT lab samples indicated improved resistance to cracking after PWHT, including no cracking at higher starting stresses at temperature that is above the as-welded critical stress threshold. The PWHT samples exhibit higher creep ductility due to a combination of stress relief and microstructure stabilization from PWHT.

4.4 Milestone 1.3.1 Detection Capability of Phased Array UT Technique for Industrial-Scale Applications

The objective of milestone 1.3.1 was to identify the detection capability of phased array ultrasonic testing (PA-UT) techniques, particularly resolution limits. Additionally, other techniques with improved resolution were investigated for potential field use; however, PA-UT continues to be the most effective non-destructive tests in the field. Table 20 includes the milestone details.

Table 20. Milestone 1.3.1 Details

Milestone	Description	Metric	Success Value
1.3.1 Identify detection capability of phased array UT technique for industrial scale application	Identify the resolution limit of phased array UT on weld discontinuities (i.e. slag inclusions, lack of fusion/penetration) and defects (e.g., micro voids, cavities and microcracks) before and after PWHT. Based on the ASTM standard, recommend commercial practice for NDE procedures for 347H SS thick-section welds.	Detection limit of discontinuity or defect based on ASTM standard maximums and area density of minor discontinuities; Detection of planar crack defects (e.g., cracks, lack of fusion, penetration). Detection using phased array UT following ASTM standard E 164, ASME BPVC section V, and AWS D1.6	Must be under the largest size, total crack length/area measured, and clearance distance maximums between indications of the detected flaw sizes for a thick weld, > 1/2", (NDE acceptance/failure criteria).

Summary of Non-Destructive Techniques for Detecting Microcracks

A survey into literature and codes, conversations with colleagues at Ohio State University (OSU), and discussions with other third party companies contributed to the knowledge learned for this subtask. Apart from surface non-destructive techniques, such as dye-penetrant testing, there are six separate techniques that were considered appropriate for thick welds. Conventional and phased array UT (PA-UT) are the most common techniques for field related inspection because of versatility and mobility and the best spatial resolution compared to other conventional non-destructive testing techniques, such as Eddy Current, which is limited based on skin effect. The non-destructive testing and non-destructive evaluation capabilities determined appropriate for the detectable range of interest is summarized in Table 21. While PA-UT can provide a minimum resolution of 500µm, the ideal detection limit to capture microcracks would be less than 100µm. A Full Matrix Capture-UT technique could possibly detect microcracks at this resolution limit by using higher operating frequencies, but the higher frequencies produce a skin effect that limits the penetrating capability. Microscopic techniques were also investigated,

including immersion UT and laser-based approaches. The main challenge with using these higher resolution techniques are surface prep (e.g., surface roughness) and thickness, which is not feasible to limit in practice. Overall, PA-UT is the most practical approach for the field, but the main con is the resolution limit of 500 μ m.

Table 21. Summary of non-destructive testing and evaluation techniques, including pros and cons

Method	Description	Pros	Cons
PA-UT	Uses ultrasonic waves with a multiple element transducer to determine flaw sizes. PA-UT improves technique by providing a scan angle range to capture more complex defects and at a faster time with more reliability	Common in the field and most known technique	Lowest spatial resolution of ~500 μ m from frequency limitations
Full Matrix Capture-UT	Uses higher operating frequencies than conventional UT or PA-UT. Covered by ASME BPVS Section V, Art. 4 App. XI and App. F	Can possibly detect 10-100 μ m microcracks based on higher frequency capabilities	Skin effect with higher operating frequencies decreases capability of penetrating thick welds to detect defects Highly dependent on material, weld filler material, and grain structure
Computed tomography (CT)	Producing 2D and 3D images from flat x-ray images	Can detect defects within 10-100 μ m range	Impractical in field applications and limited by thickness
Immersion UT	Immersion of component and transducer in water	Lower spatial resolution (~100 μ m) of thick components cm-m range	Immersion in water required which is impractical in field applications
Microscopic UT technique #1: Pitch Catch UT Probe Approach	Uses shear waves with various positions that is beneficial for detecting pore contrast	Improved spatial resolution of 1-100 μ m	Newly developed techniques and thickness limitations on resolution
Microscopic UT technique #2: Laser-Based Micro-Resolution Approach	Uses a laser vibrometer (He-Ne or infrared) and provides a better approach for internal microcracks		Same as above (thickness limitations) plus issue with laser reflection and surface roughness is important (also impractical in the field)

Phased Array UT Results and Microscopic Examination of Defects

A collaboration between Crescent Dunes and CSM)/NREL has been conducted to perform phased array UT on 40-pass 2” thick lab weld after PWHT. The phased array UT of the lab weld

did not find any detectable flaws for the whole 12” length of the weld (assuming 500µm resolution). After passing the phased array UT inspection, samples were processed to be machined from the 40-pass 2” thick lab weld for thermomechanical testing for ST 1.2.1.

A microscopic characterization of a sample from the 2” thick 40 pass weld was completed. The identifier measured maximum length, and type of weld discontinuities and defects are listed in Table 22.

Table 22. Summary of weld discontinuities in the steady state region of weld where NDE did not detect any defects >500µm. Majority of discontinuities are <100µm, but with two major indications (2, 12) >500µm with evidence of crack propagation along the HAZ

Indication #	Maximum length (µm)	Location	Type
1	38	Bottom left in FZ	Porosity
2	519	Bottom right FZ boundary (Figure 61(e))	Slag inclusion/lack of fusion void with intergranular crack developing on HAZ
3	98	Bottom right FZ boundary	Large precipitate/oxide bonded to indication #2
4 (15-20 in total)	Multiple porosity indications of ~25-30µm	Center left in re-melted FZ region (Figure 61(d))	Porosity/spherical
5	81	Center right on FZ boundary	Slag inclusion/elongated shape
6	26	Center right on FZ boundary	Porosity/spherical
7	137	Top left within FZ	Slag inclusion/elongated shape
8	26	Top left within FZ	Porosity/spherical
9	28	Top left within FZ	Slag inclusion/elongated shape
10	33	Top left within FZ	Slag inclusion/elongated shape
11	38	Top left within FZ	Porosity/spherical
12	588	Top left along FZ boundary (Figure 61(b))	Slag inclusion/lack of fusion void with intergranular crack developing on HAZ
13	38	Top middle in FZ	Slag inclusion/porosity
14	52	Top middle in FZ	Slag inclusion/porosity
14	107	Top right in FZ	Slag inclusion/elongated shape
15	40	Top right in FZ	Slag inclusion/porosity
16	87	Top right FZ boundary	Slag inclusion/lack of fusion
16 (~10 total)	Multiple slag inclusion indications of ~25-50µm	Top right FZ in second to right top bead (Figure 61(c))	Slag inclusions

Microscopic characterization of the 2” thick 40 pass weld confirmed the presence of two critical flaws measured slightly greater than 500µm, which were not detected by phased array UT as seen in Figure 61 (b-indication #12) and (e-indication #2). There seemed to be some crack initiation that developed in both locations (~15-20µm in length) along the HAZ/FZ boundary, likely during reheating with subsequent weld passes imposing stresses or stress relaxation during PWHT. While these defects are the most critical in terms of size and crack propagation during elevated temperature service, other noticeable weld discontinuities were observed under the detectable limit, including multiple slag inclusions in top right of weld (Figure 61 (c)) and

multiple smaller porosity indications in a re-melted region of FZ in the mid-thickness near the left side ((Figure 61 (d)). While this is only one cross section of the whole 12” length weld, more potential defects of similar sizes not detected by NDE may be present in the Gleeble samples.



Figure 61. Weld defects in 2” thick 40 pass lab weld. Images taken after PWHT and NDE. (a) macro cross section, (b) slag inclusion and lack of fusion-indication #12 with length of 588µm, (c) smaller slag inclusions in upper right corner of weld, (d) appreciable porosity in re-melted region in the lower left half of the weld, and (e) slag inclusion and lack of fusion in lower right corner of weld with intergranular cracking initiation

Lessons Learned/Conclusions

Based on results and lessons learned from milestone 1.3.1, some conclusions are:

1. Microhardness is more uniform in the base metal after PWHT and has lower peak values in FZ compared to as-welded condition.
2. Residual strains in the as-welded condition are significantly reduced and homogenized through PWHT, as demonstrated by the d-spacing analysis in TD (transverse to weld direction) and ND (through thickness) directions thus far.
3. The weldments after PWHT meet the 80% of base metal strength criterion. However, the ductility of HAZ after 950°C PWHT results in <80% ductility relative to the no-PWHT HAZ sample.
4. Comparison of as-welded (completed in last SRC project) to PWHT lab samples indicated improved resistance to cracking after PWHT, including no cracking at higher starting stresses at temperature that is above the as-welded critical stress threshold and higher creep ductility due to a combination of stress relief and microstructure stabilization from PWHT.

4.5 Milestone 1.4.1 Cost-Benefit Analysis of PWHT for Existing and/or Newly Fabricated Hot-Salt Tanks

Cracks in hot storage tanks at CSP plants result in significant costs due to repair costs and the loss of electricity generation revenue during months of downtime. Thus, a cost-benefit analysis is needed to provide the justification for the PWHT methods developed in this project. The objective of this task was to provide a preliminary cost-benefit analysis for PWHT, including an opportunity cost and risk analysis of losing income with a plant shut down and repair costs due to a low life-cycle weld that cracked in service.

A macro-level procedure for the PWHT of in-service Gen2 hot tanks was developed. The macro procedure covers the major steps that would be needed to perform PWHT on an in-service tank, including draining the tank and applying insulation to the interior of the tank (based on results in Task 1.1.1). For in-service tanks, localized heating of the floor and wall to perform the PWHT is likely to induce significant stresses in the surrounding welds. Depending on the induced stresses and service lifetimes, localized PWHT could induce cracking in surrounding welds. We also considered uniform heating of the entire in-service tank for the PWHT. The capability of in-service tank designs to support themselves under PWHT temperatures ($\sim 950^{\circ}\text{C}$) for several hours was not explored but is unlikely. For in-service tanks, we recommend PWHT of welds be considered on a case-by-case base. In contrast, PWHT on new tank construction can be performed locally relatively easily during tank construction.

The cost-benefit analyses compares the present cost of PWHT versus the costs of crack repair and lost electricity generation at some point in the future. Advisian performed a discounted cash flow cost-benefit analysis assuming a 100 MWe plant with a single hot-cold storage pair of tanks. The analysis assumed that PWHT was performed on all welds >0.5 " thick using the E16.8.2 filler and procedure for ceramic heating PWHT developed by CSM in Task 1.1 and 1.2 at a net additional capital expenditure of \$920,000. The assumptions for the discounted cash flow cost-benefit analysis are shown in Table 23. Key assumptions are that the PWHT avoids a crack and need for repair in 5 years, and that the repair outage lasts 16 weeks.

Table 23. Cost-benefit analysis of using ceramic heating PWHT for Gen2 347H SS hot storage tank – assumptions and results

Parameter	Value	Units/Notes
Net additional capital expenditure for PWHT	\$920,000	Today's US dollars (present value (PV))
Net plant output	100	MWe
PPA price at plant start	\$50	\$/MWh
PPA price year escalation	2%	
Assumed year of future crack (avoided by PWHT)	5	years
Repair outage duration	16	weeks
Average capacity factor during repair outage	50%	Assumes repair in winter/shoulder months
Variable O&M costs (avoided during outage)	\$5	\$/MWh
Discount rate	7%	
Future cash flow from avoided tank repair outage	\$6,677,481	US dollars (future value at year 5)
Benefit: present value of cash flow	\$4,760,951	Today's US dollars (PV)
Net present value (NPV)	\$3,840,951	Today's US dollars (PV)
Benefit/cost ratio	5.2	

The results show that in present dollars, the PWHT have a benefit/cost ratio of 5.2, or in other words, the cost of a PWHT is 1/5th the cost of experiencing a leak 5 years in the future and having a forced outage for tank repairs in present day dollars. The analysis makes conservative assumptions that the outage happens during the winter/shoulder months when generation is lower and that the discount rate is only 7%. It also does not include the cost of the future tank repair itself, so the actual benefit-cost ratio is actually higher. The analysis shows that the PWHT methods developed in this project are beneficial and should be implemented prior to hot tank service to minimize risk of future tank cracks.

4.6 Milestone 1.5.1 Protocols for Updating ASME Code on PWHT of 347 SS Welds

ASME, amongst many other functions, produces codes and standards utilized around the globe. Many ASME standards are cited by government regulatory agencies. Specific detailed codes for the design and construction of molten salt storage tanks do not exist, with the exception of ASME TES-1 “*Safety Standard for Thermal Energy Storage Systems: Molten Salt*”, which establishes high-level requirements for the design and construction of molten salt tanks, and generally references established detailed API and ASME codes used for other applications. In general, current codes do not require, nor prohibit, 347H SS welds undergo PWHT prior to service. Contribution to code changes may help prevent issues with cracking seen CSP TES hot tanks. The purpose of this task was to engage in discussions with ASME committees about recommending practice for PWHT in 347H SS thick-section welds for high temperature operation and offer recommended path forward for code case/changes.

Advisian led the effort to address ASME protocols. Advisian is highly involved in ASME Boiler and Pressure Vessel Code committees and are aware of what is needed to process code qualification of new processes. Advisian engaged subject matter experts on the ASME Codes

and Standards Non-Destructive Evaluation and Materials Committees and briefed them on the PWHT results from this project. The subject matter experts reviewed ASME Code Section II and VIII to determine if and where code language could be improved.

Based on these conversations, Advisian believes that the appropriate path is to submit a Code Revision to ASME Code. Advisian believes a few ASME Code Revisions could be made:

1. ASME Section II, Part D, Nonmandatory Appendix A, para. A-206 “Relaxation Cracking (Strain-Induced Precipitation Hardening)”. Add Welding Journal article “Residual Stress in 347H Stainless Steel Welds” to references. Possibly add an additional/substitute peer-reviewed article, if published soon.
2. ASME Section VIII, Div 1, Appendix UHA-A-4 “Relaxation Cracking”. Consider adding 2-step PWHT temperature regime, and associated temperature ramp rates, for 347H material per Welding Journal article, upcoming PWHT simulation and SRC experimental publications.
3. ASME Section VIII, Div 1, & Table UHA-44 “Post Fabrication Strain Limits and Required Heat Treatment”. Consider expanding Note 2 to include 2-step PWHT temperature regime, and associated temperature ramp rates, for when fabrication of 347H is by welding. Currently, the code recommends PWHT minimum temperatures to be at a minimum of 1,095°C based on cold forming limits (10% minimum) for service temperatures above 540°C. However, susceptibility to cracking during heating to solutionizing temperature increases with increasing temperature, and a minimum PWHT soak temperature recommendation of 1,095°C may be too high for a highly restrained 347H SS weld, particularly localized heat treatment in the field.
4. ASME Section VIII, Div 1, Appendix UHA-A-4 “Relaxation Cracking” Point (b): The need of PWHT is not solely dependent on thickness. Residual stress and therefore SRC susceptibility may depend on weld techniques, weld geometry design and # of weld passes.
5. In addition to above (or in place of if code revision not adopted), amend ASME TES-1 to reference this report and Welding Journal article, and consider adding a 2-step PWHT temperature regime, and associated temperature ramp rates.

The BPVC revisions need to be completed by mid-2024 to be included in the 2025 codes. An ASME BPVC meeting was held November 2023 to discuss code changes. Advisian managed the code revision case within ASME and facilitated CSM to virtually present on the results of this report. Advisian recommended that we present our results to the committee at that time as the first step in having this work be considered as part of an ASME Code Revision. Various committee members provided initial feedback. The next step is continued discussions with Section II, Part D committee, and attendance at the BPVC meeting in the spring of 2024, to the extent funded.

ASME TES-1 committee was not engaged as Craig Turchi of NREL is a Contributing Member and will socialize above with the standards committee for consideration.

4.7 Milestone 1.6.1 Cost Estimate and Technical Feasibility of a Grade 92/347H Clad Gen2 Hot Tank

A potential alternative to using PWHT on a 347H SS tank is to use a clad metal as the material of construction. Stainless steel cladders have been extensively used for over 50 years in combination with many steel-based backers to produce explosion welded plates. These plates are bent and welded together to produce many of the high-pressure reactors used in industrial chemical processing and oil & gas. This task performed a conceptual design and screening/feasibility level cost estimate ($\leq +50/(-)30\%$) to determine if a clad tank design would reduce cost when compared to baseline 347H SS tank.

Gr92 (ASME SA-1017 Gr 92) was chosen as the structural backer and 347H SS (ASME SA-240 Gr 347H) as the cladding for the clad tank. A Gr92/347H SS clad tank has the potential to both reduce cost and eliminate 347H SRC risk, vs. conventional 347H tank. Gr92 alloy is generally cheaper to construct with than 347H, even though it requires PWHT on all welds per code. The 347H SS provides corrosion protection. Although 347H SS might be susceptible to SRC when thick plates are welded together, this risk would be eliminated with the use of thin 347H plates as the cladder with Gr92 as the backer.

Advisian performed the conceptual design and cost estimate of the Gr2/347H SS clad Gen2 hot storage tank. The tank was designed to API-650 and ASME Section VIII codes, as is typically used for CSP thermal energy storage tanks. Advisian performed an ACEI Class 5 cost estimate using 2Q2022 prices as the cost basis and chose Tonopah, Nevada as the plant location. The cost estimate including the following:

1. Clad plate material and shop fabrication
2. Quality assurance testing
3. Transportation to site
4. Field fabrication, including PWHT of Gr92

The clad material budget quote came from NobelClad in May 2022, when metal prices were close to a peak high in recent years. The cost estimate does not include nitrate salt, insulation, tank internals, instrumentation, foundation, and any other items that would be identical to those in a 347H SS tank. Thus, the cost estimate focuses on the difference in costs between the 347H SS and clad metal options.

Using the assumptions described above, Advisian estimates the total installed cost of a Gen2 hot tank constructed from Grade 92/347H clad at \$24 million, excluding insulation and foundation, compared to a bare erected cost of \$15 million for a 347H SS design. Although the clad metal tank uses less metal—630 tons of metal vs. 730 tons for the 347H SS hot tank design—the clad metal design cost is still 60% higher than the cost of the 347H SS design. The majority of Gr92/347H SS clad metal tank design costs come from shop costs (material and shop fabrication) for the clad metal, which account for 73% of the bare erected cost. The remaining 27% of costs are related to field costs. Although the clad tank design arguably offers a more robust design with reduced SRC risk, it is significantly more expensive than the 347H SS tank design. From a purely capital cost perspective, and when the cost-benefit analysis of PWHT in

Task 1.4 is considered, the results indicate that industry would be better served by exploring PWHT for 347H SS tanks than trying to develop a Gr92/347H SS clad design.

4.8 Milestone 2.2.1 Metallurgical Characterization of Hot Storage Tank Field Samples

The details for milestone 2.2.1 are included in Table 24 below.

Table 24. Milestone 2.2.1 details

Milestone	Description	Metric	Success Value
2.2.1 Metallurgical characterization of hot storage tank field samples	Characterize both floor and wall weldments using optical microscopy (OM) and energy dispersive spectroscopy (EDS) with scanning electron microscopy (SEM) to identify susceptible microstructures to SRC, such as martensite, distribution and morphology of chromium and niobium carbides, eutectics of austenite and Nb (C, N).	Number of samples characterized.	4 total—new wall cracked sample (1) and old wall welds (3)

Failure Analysis of Wall Weld

Failure analysis of the wall weld crack sample received was conducted to understand the fracture surfaces and distribution of metallurgical phases surrounding the primary crack. In 2019, a new floor wall layer was welded to the original wall of the molten salt storage tank at Crescent Dunes due to replacement of tank floor. Earlier this year, a through-thickness crack, 12 inches (305 mm) in length, developed and caused a leak in the tank. This crack ran along the toe of the weld, as can be seen highlighted on the inner diameter (ID) wall by red dye in Figure 62 (a). The boat-shaped sample (referred as boat sample) was excavated from the outer diameter (OD) wall as shown in Figure 62 (b). The crack propagated along the HAZ just outside the weld metal region while entering the weld metal, i.e., FZ, twice as can be seen in Figure 62 (c).

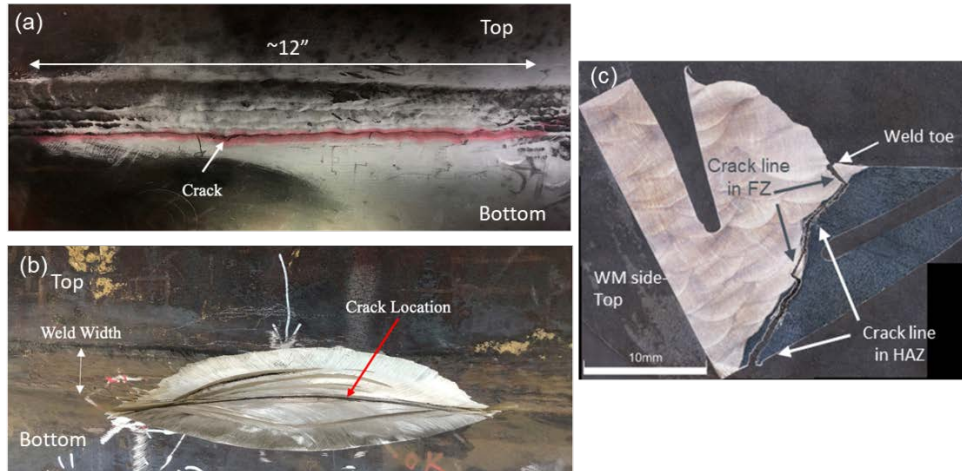


Figure 62. Wall crack and sample extraction for failure analysis. (a) 12-inch long through-thickness crack in the HAZ/PMZ of the weld as seen from the ID of the hot salt tank; highlighted in red using dye-penetrant testing, (b) excavated boat sample site on the OD of the tank wall containing the crack that was examined, and (c) cross section of weld showing crack path along HAZ on bottom side of tank (first wall section ~1.5" thick) on OD.

Discussions with Crescent Dunes confirmed that the root cause of failure was significant lack of fusion in the root of the double-sided joint, which was not observable from the samples extracted from the wall OD (shallow with respect to weld root). The lack of fusion defect was observed during repair welding procedures. Stress corrosion cracking seems unlikely for this case, as the cracks started from the root of the double-sided weld near mid-thickness (where no contact of salt occurred until cracked opened to ID) and propagated to the ID and OD surfaces of the wall. On the contrary, crack propagation via SRC mechanism is highly possible from the lack of fusion defect during elevated temperature service, as residual stresses in double sided joints are highest in the mid-thickness [36], making stress concentrations from the lack of fusion defect even more detrimental for intergranular cracking at service temperatures.

Fractography

The fracture surfaces of the wall crack largely indicate intergranular fracture, where the bright shiny surface is representative of HAZ, and the darker regions represent fracture in the weld metal or FZ as seen in Figure 63. The lack of chevron marks on the surface suggests that the failure was not a traditional brittle fracture governed by cleavage. The absence of beach-marks on the surface indicates that the crack likely did not progress by fatigue and cyclic loading but quickly fractured once the internal stress was sufficient for overload.

Regarding the other markings on the surface, the first of these is brown staining on the surface (labelled in Figure 63). The stains do not appear to be corrosive and are similar in appearance to oil or coolant residue that may have contacted the surface during or after the sample was removed from the wall. As such, the stains are considered extraneous to this investigation. The second indication is a line of three bright marks on the righthand side of Figure 63 that are circled in yellow. Under closer examination, these three marks appear to be areas where the surface collided or rubbed against another surface and are ruled out as indications pertinent to this investigation.

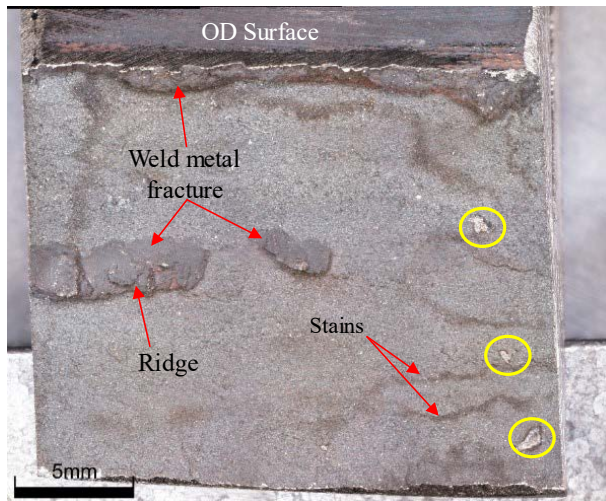


Figure 63. Macroscopic image of the fracture surface from the boat sample on the base metal side

SEM examination was performed on the main fracture surface in the HAZ as well as in the FZ regions. Figure 64 (A) is a backscatter electron image at low magnification that shows the fracture surface at the toe of a top-layer weld bead (as referenced in the above sections). The large dark region is caused by significant depth differences in the sample and is not an indicator of a difference in composition. At the top of Figure 64 (A), there are many indications that dot the surface of the weld. These indications were found across the entire surface and are a mixture of residue spots, aluminum slivers and polymer particles. The residue spots are likely from handling the samples in a dirty environment while the aluminum and polymer particles are a result of the packaging in which these samples were delivered. Figure 64 (B) is a higher magnification image of the red-highlighted region seen in Figure 64 (A) that was captured in mixed backscatter electron/secondary electron mode to highlight both topographical and compositional differences. Figure 64 (B) shows dendrites on the fracture surface and confirms that the crack likely propagated along the boundaries of the dendrite grains. Additionally, in the bottom left corner of Figure 64 (B), the outlines of grains can be seen, which indicates the intergranular fracture in the HAZ.

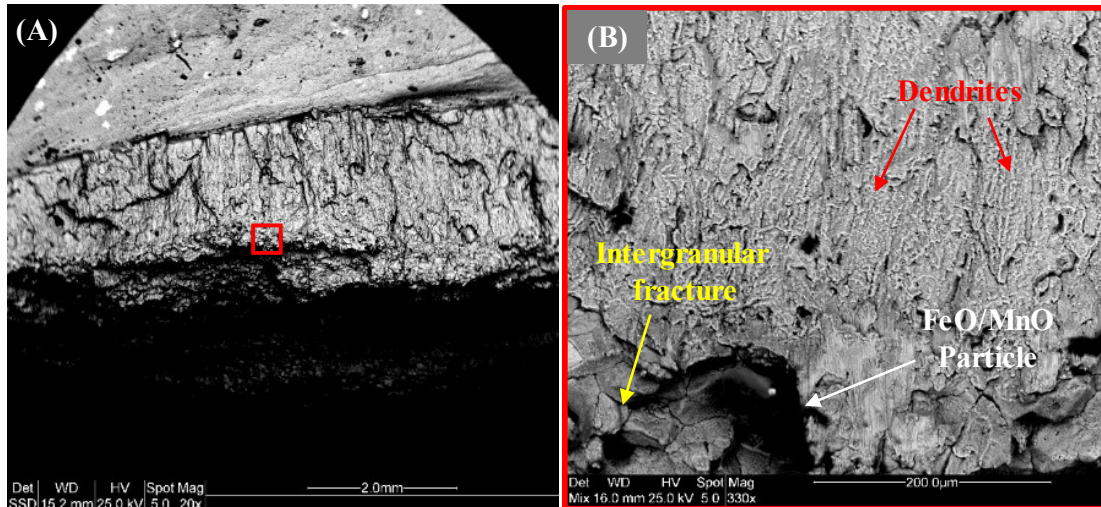


Figure 64. Images taken from the weld metal region of the fracture near the toe of a top-layer weld; A) low magnification backscatter electron image of top edge; B) blow-up image of the red highlighted region in A

The HAZ fracture surface in Figure 65 demonstrates intergranular feature with the presence of micro-voids on grain facets, which is also seen in Figure 65. Ductile dimples can be seen clearly on the fracture grain surface through a high magnification SEM image in Figure 65B. Micro-void coalescence may point to the presence of a secondary phase along the grain boundaries or simply creep void coalescence on grain boundaries, which supplements a reheat cracking issue. Similar fracture features that appear in Figure 65B have been reported in 347H SS HAZs in literature that are attributed to stress relaxation/relief cracking, where a sufficient tensile stress present at a high enough temperature leads to intergranular fracture with the presence of intergranular creep voids [6].

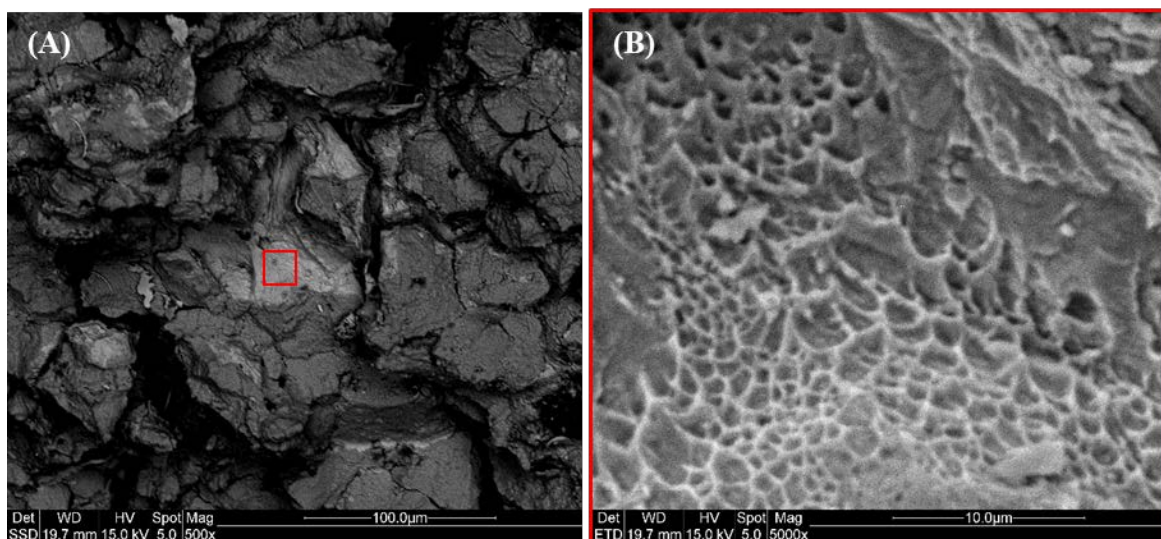


Figure 65. SEM images showing (A) micro-voids on the fracture surface of grains in the HAZ on the base metal side, and (B) ductile dimples on the grain facets in an enlarged view

3.2.2.3 Light Optical Microscopy (LOM) Examination

Note that in the following discussions, the exact crack initiation site and propagation direction comes from the weld root, and this section focuses on cracking susceptibility of different microstructure zones. As shown in Figure 66(A), the crack propagates back and forth between FZ and HAZ: the first transition is near the toe of the weld on the OD surface, which is a typical stress concentration region, and the second transition is approximately 10 mm down from the OD surface. In both locations, there is a near right-angle turn in the crack propagation direction. Near the OD surface, the crack turns shortly from the fusion line of one of the cap beads at the weld toe, as shown in Figure 66 (A) and (B), into the FZ of a previous weld pass. Figure 66 (B) and its enlarged view in Figure 67 reveal that the crack turns below the upper bead's FZ and propagates parallel to the columnar dendrite growth direction of the underlying pass. There is a clear transition line between the dendrites of the top pass FZ and the reheated region of the lower pass FZ, as observed in Figure 67. Figure 66(C) shows the second turn of the crack occurring in the coarse-grained HAZ as the crack exits the weld metal.

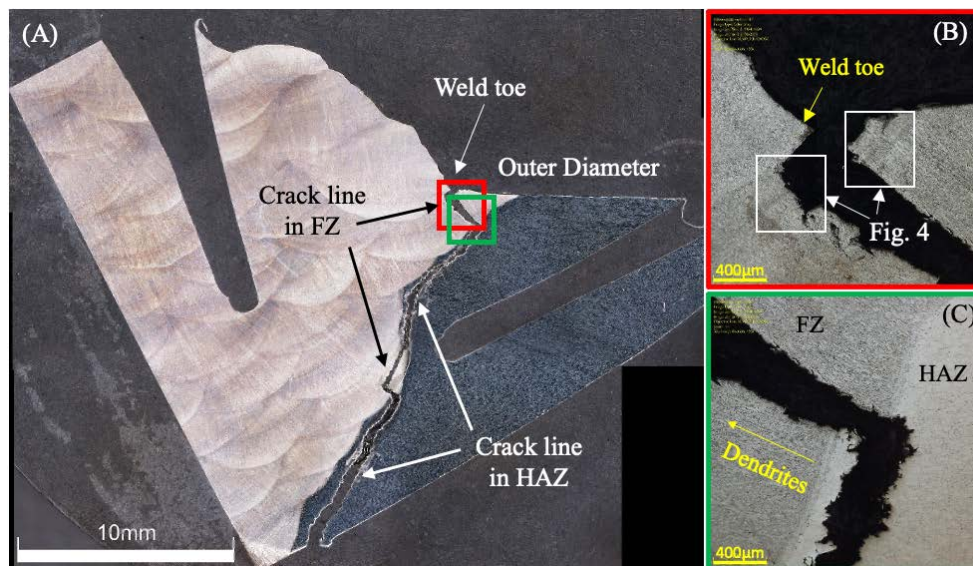


Figure 66. A) Etched cross-section of boat sample showing the location of the crack; B) Crack propagation at OD surface; C) Crack propagation from FZ into HAZ or the opposite

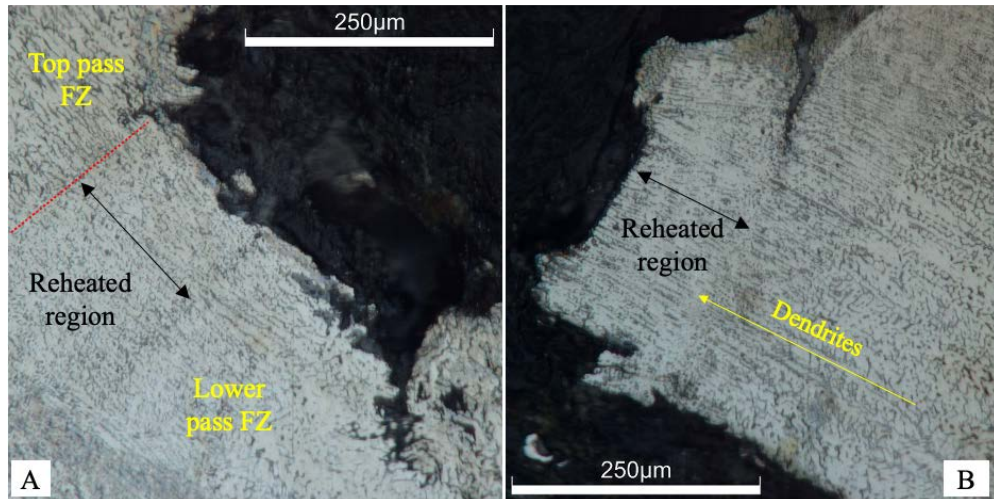


Figure 67. Crack right-angle turn near OD surface; Higher magnification view of Figure 66B; A) Weld metal side of the crack and B) Base metal side of the joint

The second turn and entrance into the weld metal underneath OD surface initially still follow the cracking orientation in the HAZ above, as observed in Figure 66 (A) and (C). Figure 68 is the enlarged view of the second turn, which shows the crack intersects the weld metal at a $\sim 104^\circ$ angle from the direction of dendrite growth, according to measurements taken in ImageJ. This is nearly perpendicular to the dendrite growth direction. On the other end of the segment, the crack intersects the weld metal nearly in-line with the direction of dendrite growth and enters the coarse-grained HAZ again. In summary, the LOM examination indicates that the weld toe region with typical high stress concentration, the long straight columnar grain boundaries within the FZ, and the coarse-grained HAZ are the least resistant paths for crack propagation.



Figure 68. Second region of crack propagation into weld metal underneath OD surface with dendrite growth direction indicated

3.2.2.4 SEM/EDS Examination

SEM and EDS examination of the same cross section used for LOM, including both the FZ and HAZ, were conducted to determine primarily if sensitization is a concern (localized Cr-depletion) and if an argument for SRC can be made based on the precipitate morphology within or near the secondary microcracks. Figure 69 first shows the EDS map in the FZ of the first secondary microcrack observed near the toe of the weld on the OD. The main observation is that cracking develops along the δ -ferrite interdendritic regions or potentially σ phase, where the Fe and Cr is enriched while Ni is depleted. Nb and Mo rich carbonitrides are spread discretely near the δ -ferrite/ γ -austenite interfaces. Cr carbonitrides may have nucleated along these boundaries as well during service, but since Cr is a δ -ferrite former, there is a high likelihood the remnant solidification structure still exists as no PWHT occurred. Note that the pitting potentials between δ -ferrite and austenite may be different, but the stress corrosion cracking susceptibility is much lower than a sensitized microstructure with extensive Cr carbides (Cr_{23}C_6) formation evidenced by their difference in stoichiometry. Figure 70 shows similar interdendritic and precipitate morphology in another microcrack location, with discretely spread Nb and Mo carbonitrides and the microcrack lying along the Cr rich/Ni depleted phases. The crack path likely occurs in the interdendritic regions surrounding the grain boundary precipitates. A precipitate free zone likely exists where the crack travels around the grain boundary precipitates and within the interdendritic δ/σ phase region.

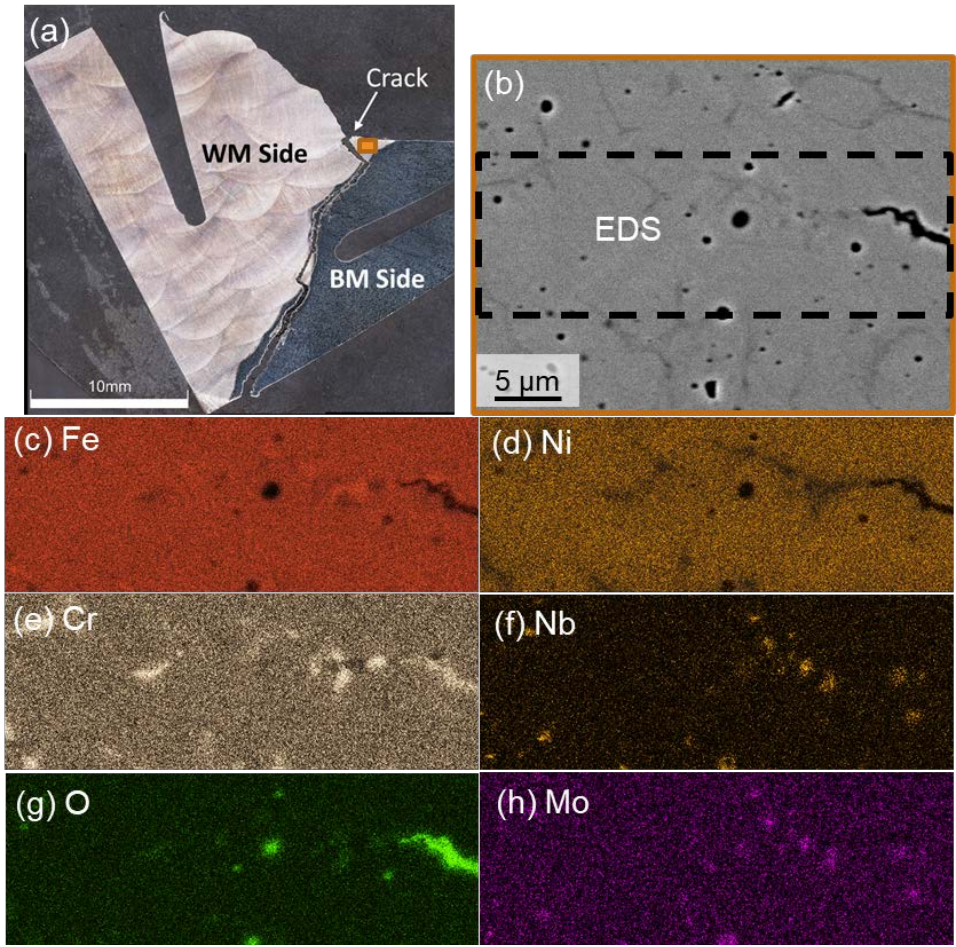


Figure 69. EDS maps of secondary crack in FZ ahead of the primary crack. (a) cross section of boat sample, (b) SEM-secondary electron image (SEI) image of EDS location indicating dendrite structure with secondary crack occurring along interdendritic δ -ferrite (Fe rich and Cr rich, Ni depleted), (c) Fe, (d) Ni, (e) Cr, (f) Nb, (g) O, and (h) Mo.

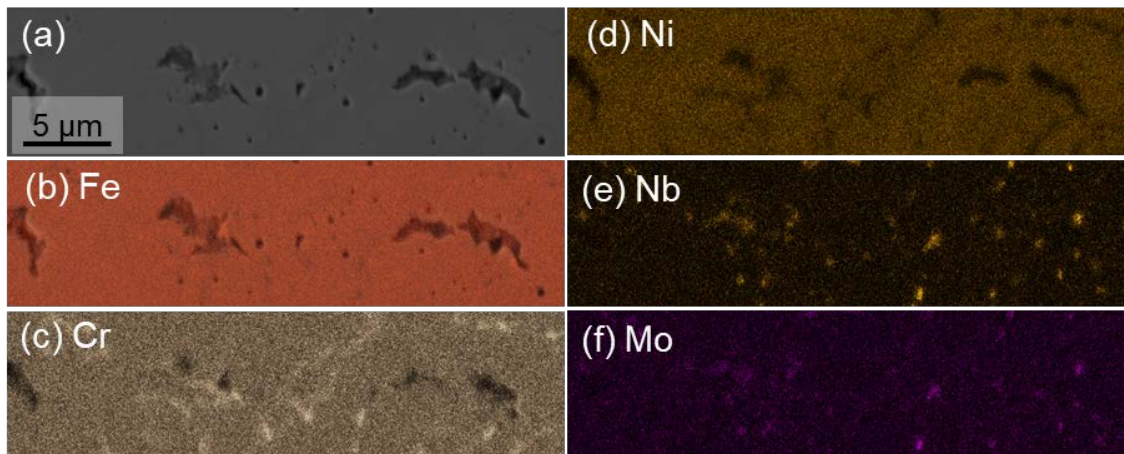


Figure 70. EDS maps of a secondary crack in FZ ahead of the primary crack. (a) SEM-SEI image of EDS location indicating dendrite structure with secondary crack occurring along interdendritic δ -ferrite (Fe rich and Cr rich, Ni depleted), (b) Fe, (c) Cr, (d) Ni, (e) Nb, and (f) Mo.

The microcrack in Figure 71 lies within the HAZ near the corner of where the primary crack protrudes from the FZ into the HAZ. The main observation here, in contrast to the FZ microcracks, is that there are fewer grain boundary precipitates, with a much finer distribution of them intragranularly. Some elongated, narrow Cr segregation stingers are observed near the tertiary crack tips, which likely indicates the presence of secondary Cr-rich phases (e.g., δ -ferrite) within the HAZ or PMZ. There does not seem to be any form of grain boundary Cr carbides within the HAZ microcracks, which implicates no presence of sensitized microstructure. Instead, there were dispersed intragranular Nb and Mo carbonitrides present near the intergranular microcracks.

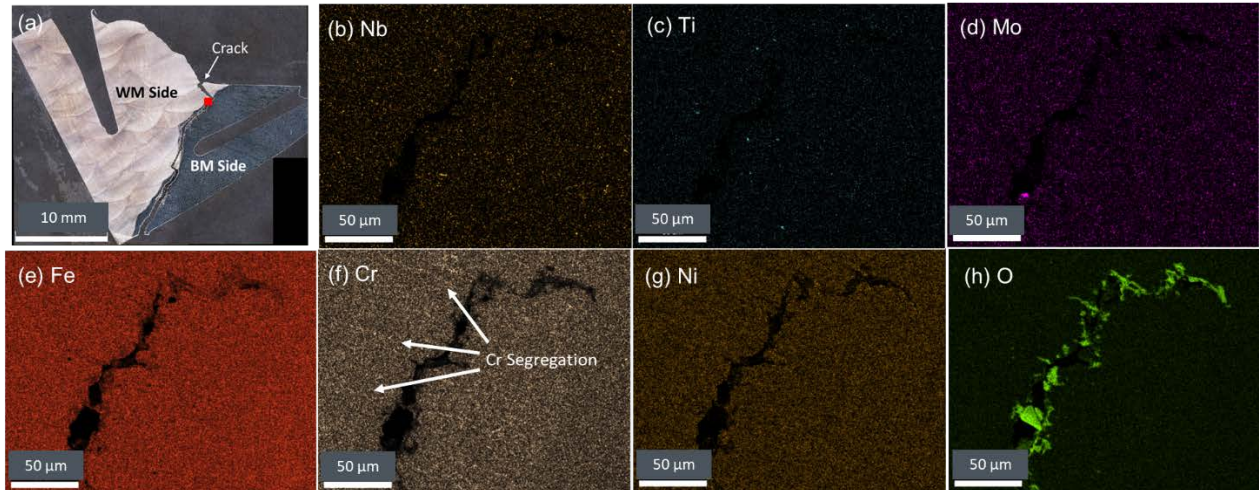


Figure 71. Microcrack propagating through HAZ at corner of primary crack with indications of Fe and Cr oxides within the crack and indications of Cr segregation within the HAZ substructure (not an indication of sensitization as this is a grain boundary phenomena)

Figure 72, Figure 73, and Figure 74 show more examples of HAZ microcracks near the primary fracture surface, all with similar observations of precipitate formation. A range of fine (0.25-1 μm) and coarser precipitates (3-10 μm) in size were surrounding the microcracks. Like the microcracks seen in Figure 71, there are no indications of grain boundary Cr carbides or δ -ferrite or sigma within or near the HAZ microcracks. Oxygen content is also shown along most maps to ensure that the enrichment of Cr or Fe was not associated with oxides and to differentiate oxides from any secondary precipitates or phases.

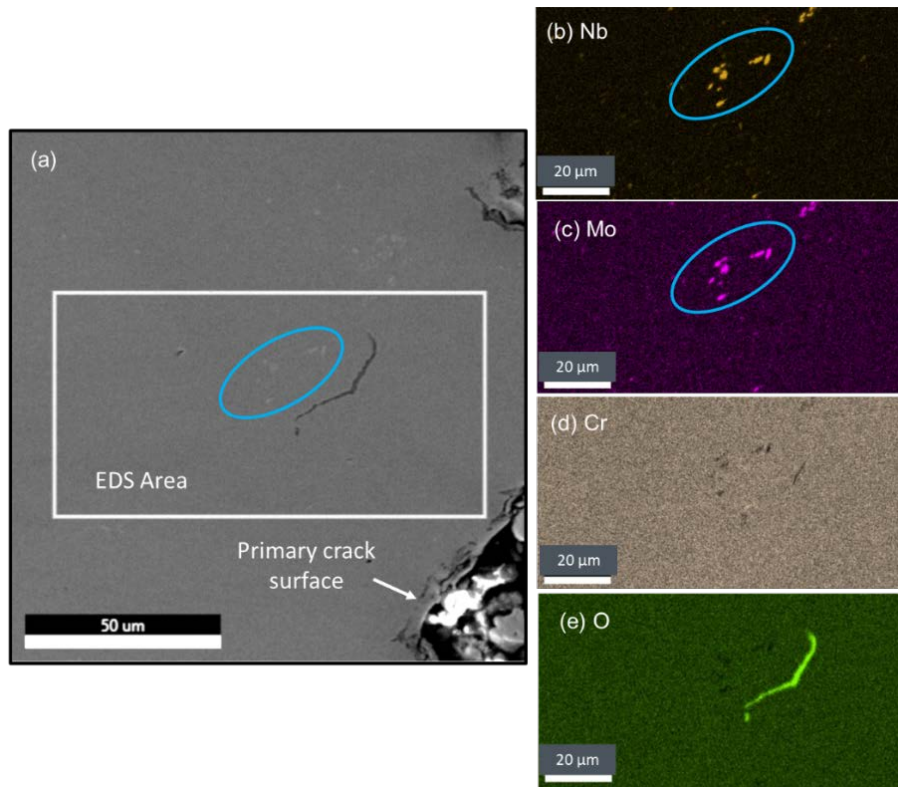


Figure 72. Microcrack in HAZ with surrounding Nb and Mo carbonitrides 3-7 μ m in size

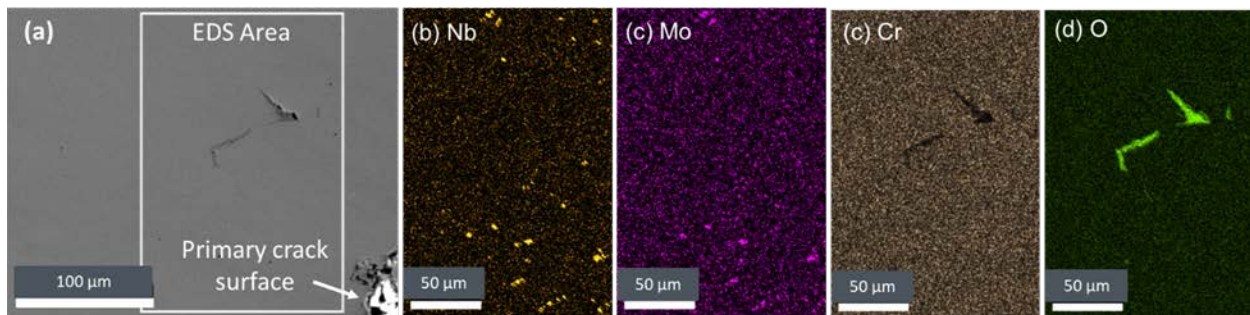


Figure 73. Microcrack in HAZ with surrounding Nb and Mo carbonitrides 3-10 μ m in size

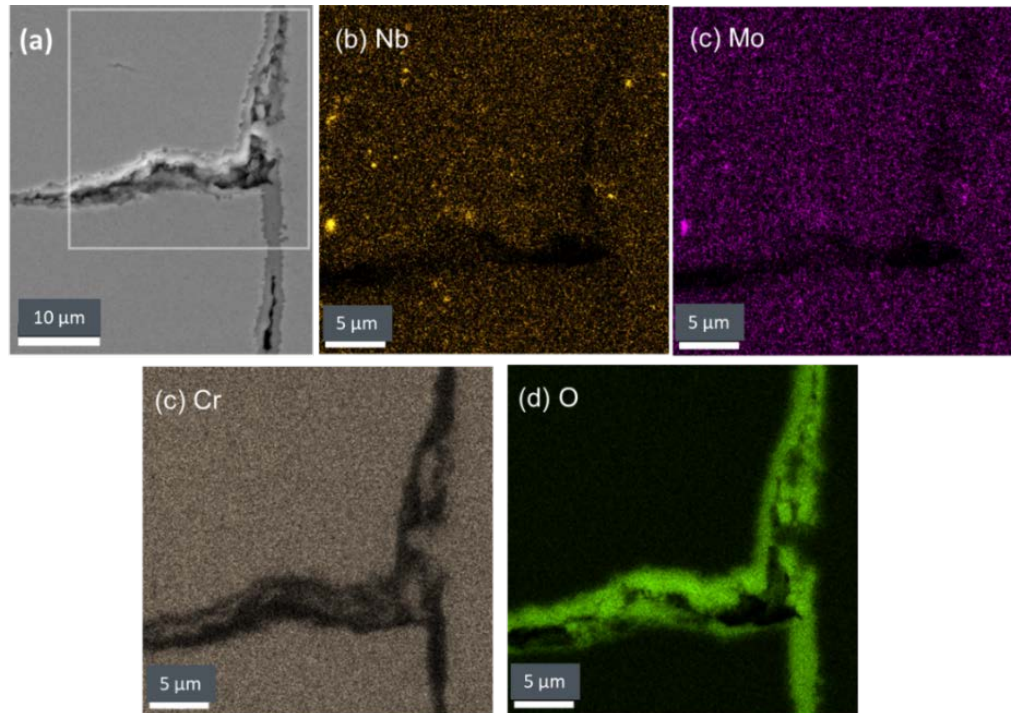


Figure 74. T-shape intergranular microcrack in HAZ with surrounding Nb and Mo carbonitrides 0.25-1 μ m in size

Metallurgical Characterization of E347-347H Field Weld Wall Seam Weld After 3 Years of Service Without Failure of Similar Wall Welds

The original wall E347-347H SS seam weld on the first wall section, as-welded and three years of service, is shown below in Figure 75 (a) where the top surface of the image represents the ID of the tanks and bottom surface represents the OD of the tank. Figure 75 (b) & (d) illustrate the HAZ and PMZ regions, where a wider PMZ is observed in the root based on the observation of eutectic microstructure. PMZ represents a location with a small width, about 1-3 grains wide, where partial melting takes place from melting depressants, such as δ -ferrite stringers. The amount and width of the PMZ depends on the intensity of δ -ferrite stringers, which are most present near the mid-thickness of the substrate or root of the weld. δ -ferrite may have higher sources for Nb since Nb is a ferrite former at very high temperatures. Liquation may be present from excessive Nb along grain boundaries as it is a melting point depressor. The eutectic NbC/ γ prime present in the PMZ is more locally associated with the stringers, and therefore is a more likely location for liquation cracks to develop. While liquation cracking is a mechanism typically occurs in the PMZ, this crack type occurs during cooling stage of welding procedure. Liquation cracks, as wide as the PMZ width, could likely contribute to further crack propagation during service. Similar observations of concentrated δ -ferrite stringers in the mid-thickness location have been observed in as-welded conditions, but not after PWHT. The FZ transition between two passes in the center of the weld, seen in Figure 75 (c), is columnar with combination of vermicular and lathy ferrite (about 3.5 vol pct).

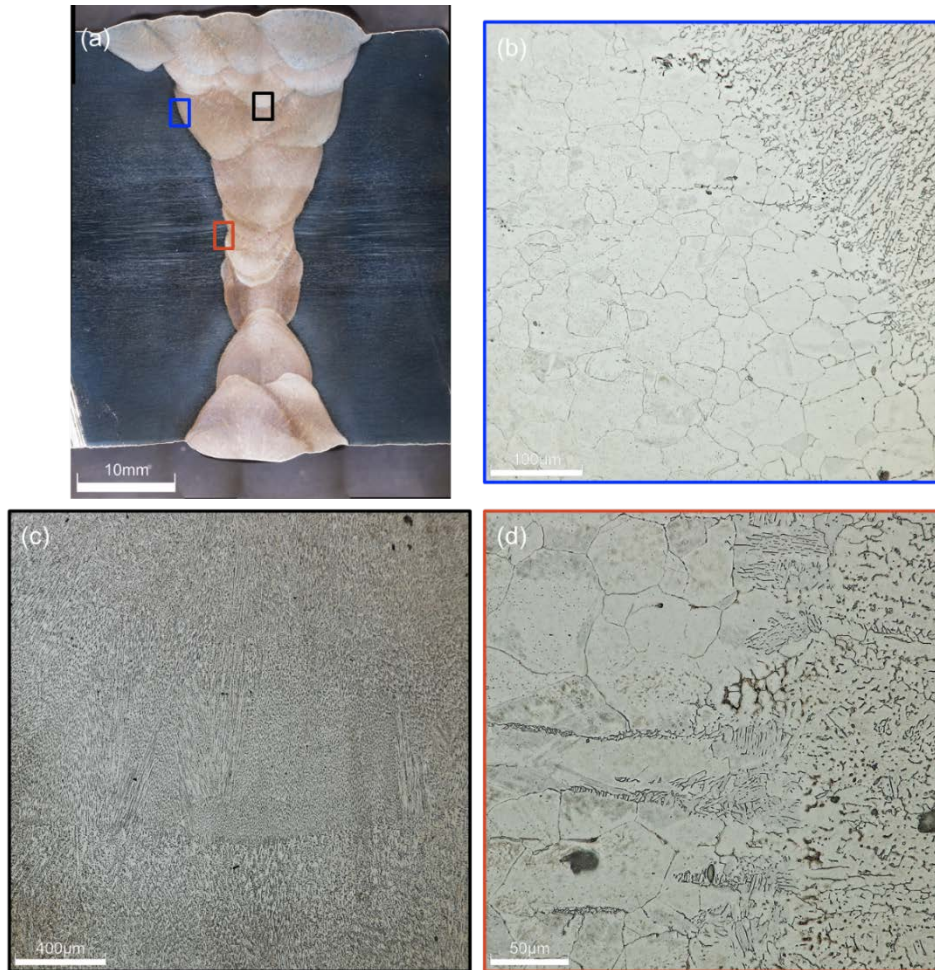


Figure 75. Microscopic examination of (a) seam wall weld (original wall weld), (b) HAZ/PMZ near top of weld, (c) FZ near top of welding showing a weld pass transition, and (d) HAZ/PMZ near weld root.

A microhardness map, as seen in Figure 76, was developed for a sample cut from a small section near the top surface of the seam weld near the ID. The main observation was the appreciable higher hardness in the FZ (250-280 HV) closer to the mid-thickness of the sample, where the lower hardness was discovered to be present closer to the surface of the weld and in the HAZ (200 HV). For reference, the typical hardness in a substrate material is 150-170 HV in solution annealed condition. With respect to SRC, the concern for cracking occurs with microhardness values greater than 250 HV [5].

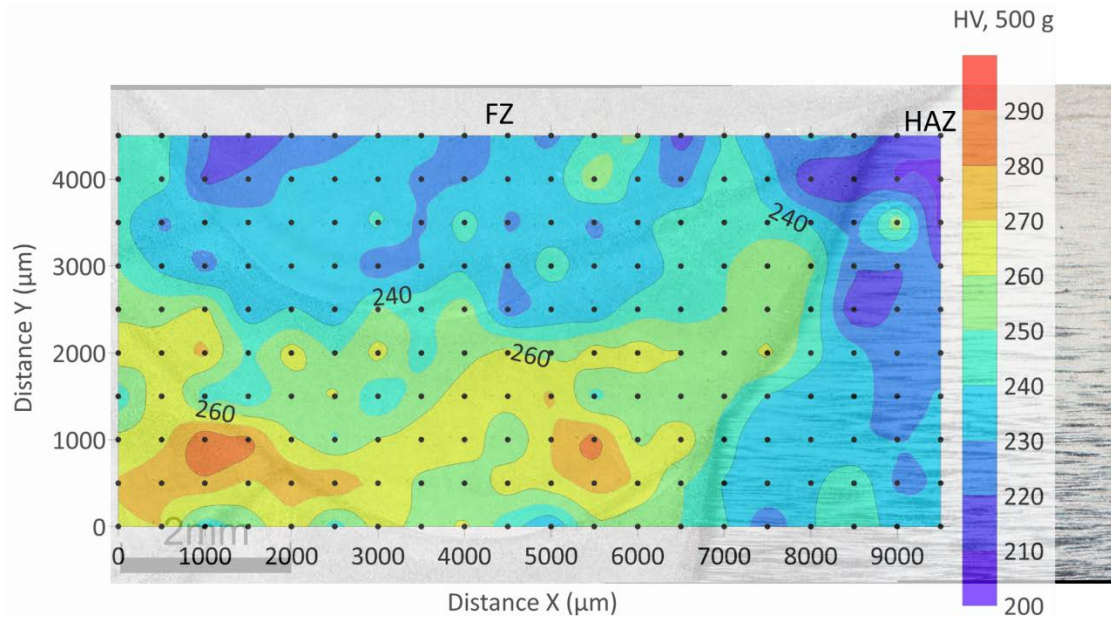


Figure 76. Microhardness map of E347-347H seam field weld in top quarter half of sample (after 3 years of service). FZ peaks at 290 HV.

SEM images were taken of various FZ and cap HAZ microstructures, as seen in Figure 77. Microstructure was electrolytically etched to help reveal more subsurface features for EDS. The morphology is dendritic with vermicular ferrite present within an austenitic matrix. The highest microhardness region in the FZ was investigated, which is the microstructures seen in Figure 77 (d-e). This region of highest local hardness lie within the reheated/remelting region between two weld passes as illustrated in the macro of the weld in Figure 77 (a). EDS chemical analysis of the HAZ and FZ microstructures (from top to bottom) are shown in Figure 78 and Figure 79, Figure 80, and Figure 81, respectively. Nb and Mo carbonitrides are distributed discretely intragranularly and intergranularly in the HAZ where there is no apparent Cr or Ni segregation. The FZ scans show Cr, Fe enriched and Ni depleted interdendritic δ -ferrite, with Nb and Mo precipitates laced along the interdendritic/dendritic sub-grain boundaries. While the distribution of precipitates is hard to discern differently for different regions in the FZ, the likelihood for increased hardness in sub-surface passes may be associated with the buildup of residual stress (i.e., higher dislocation density) due to deposition of more filler material. These locally harder regions might correlate with local ductility dips within the FZ. Thermomechanical testing across this microstructure will likely show preferred fracture in the FZ over the HAZ, which has been shown in previous studies on SRC cracking [49].

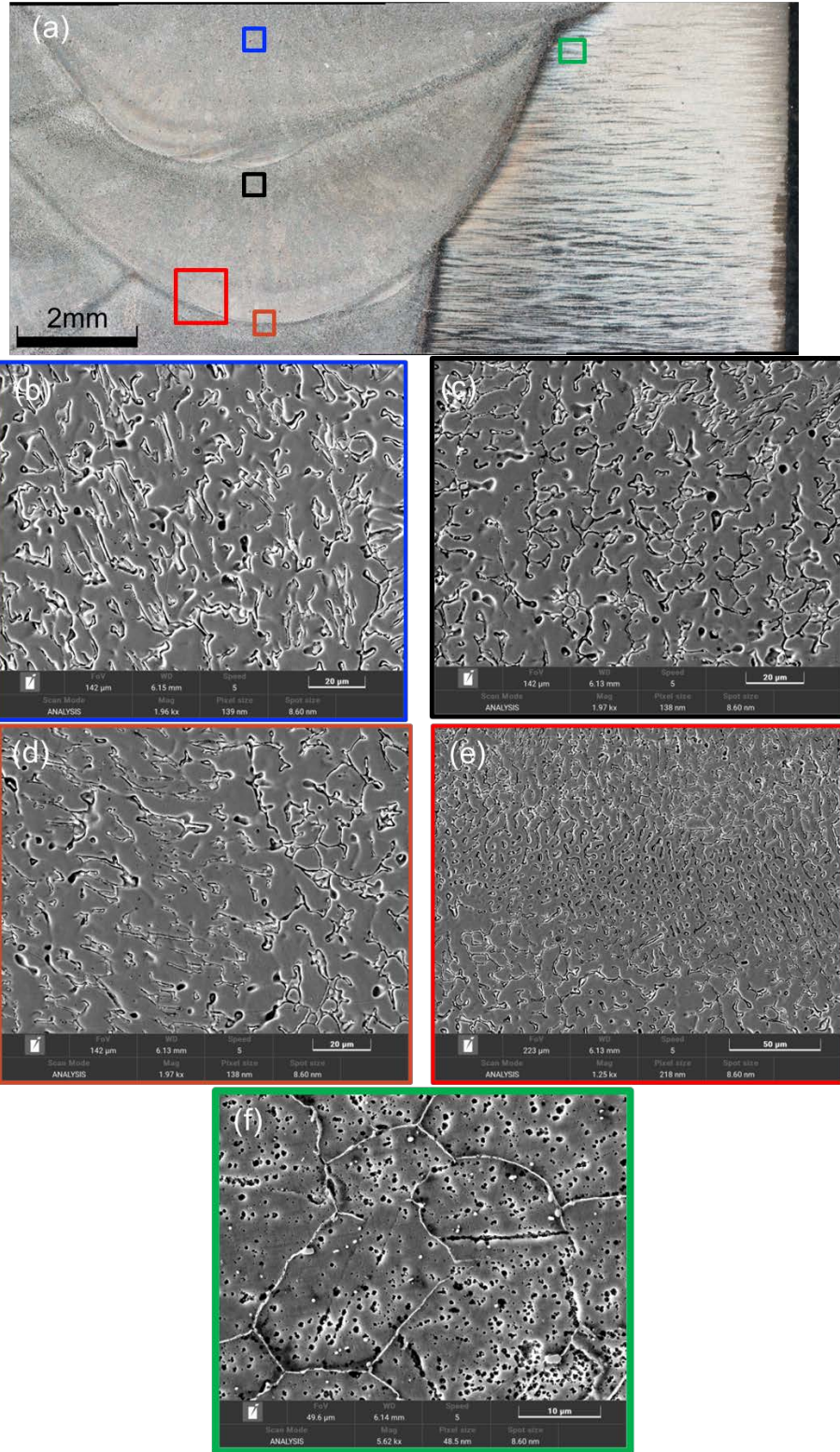


Figure 77. Electrolytic etched SEM images of (a) seam E347-347H SS wall weld, (b) cap pass FZ, (c) subsurface pass FZ, (d) pass intersection of two subsurface passes, (e) lower magnification of boundary between two FZ passes, and (f) HAZ of cap pass

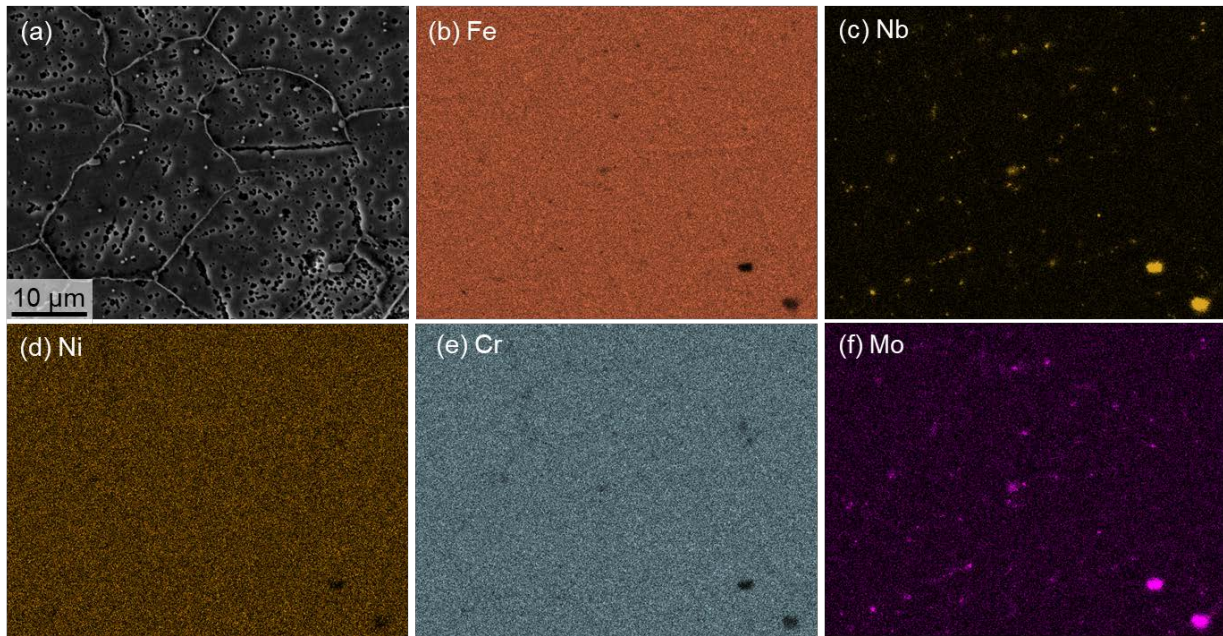


Figure 78. HAZ SEM-EDS map of E347-347H SS sample etched in electrolytical nitric acid solution (3V, 10 s) (a) field of view SEI, (b) FE, (c) Nb, (d) Ni, (e) Cr, (f) Mo

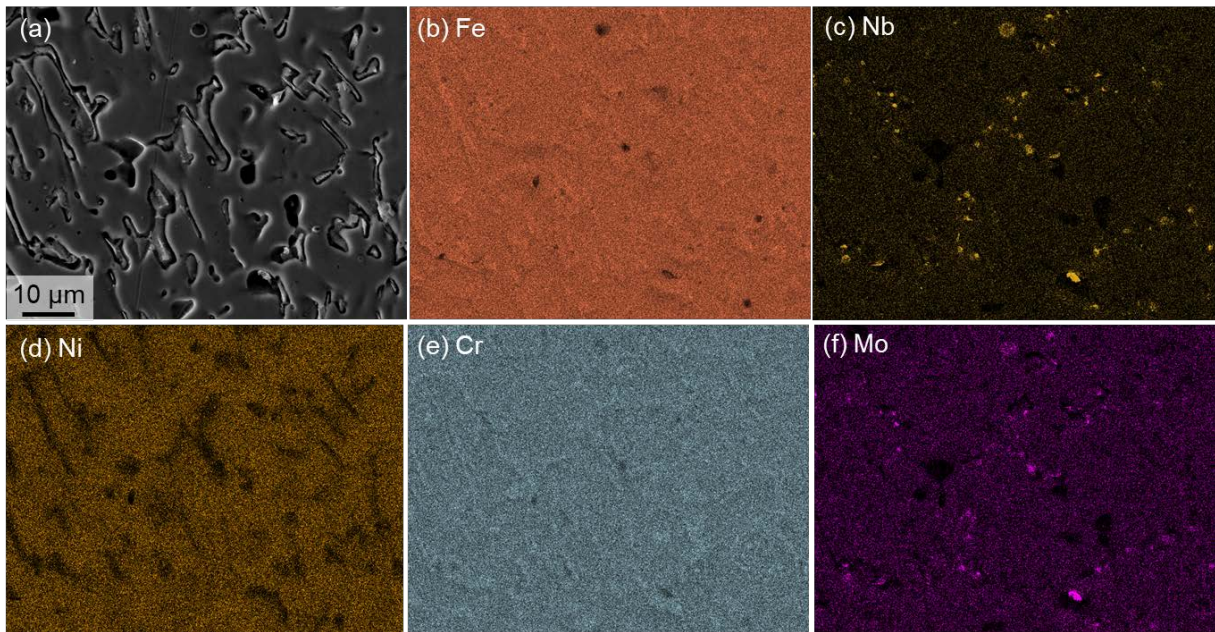


Figure 79. FZ location near top location of micrograph where microhardness is lowest (closer to surface and with a HV of SEM-EDS map of E347-347H SS sample etched in electrolytical nitric acid solution (3V, 10 s) (a) field of view SEI, (b) FE, (c) Nb, (d) Ni, (e) Cr, (f) Mo

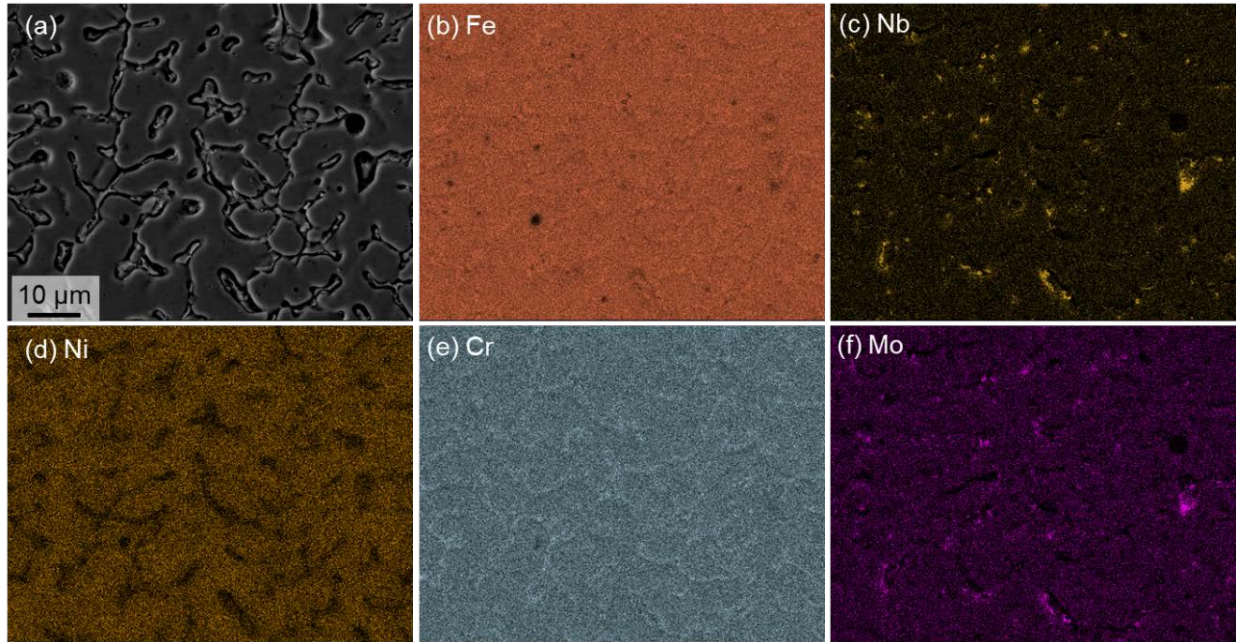


Figure 80. FZ location near middle location of microhardness indents where microhardness is greater than 250 HV SEM-EDS map of E347-347H SS sample etched in electrolytical nitric acid solution (3V, 10 s) (a) field of view SEI, (b) Fe, (c) Nb, (d) Ni, (e) Cr, (f) Mo

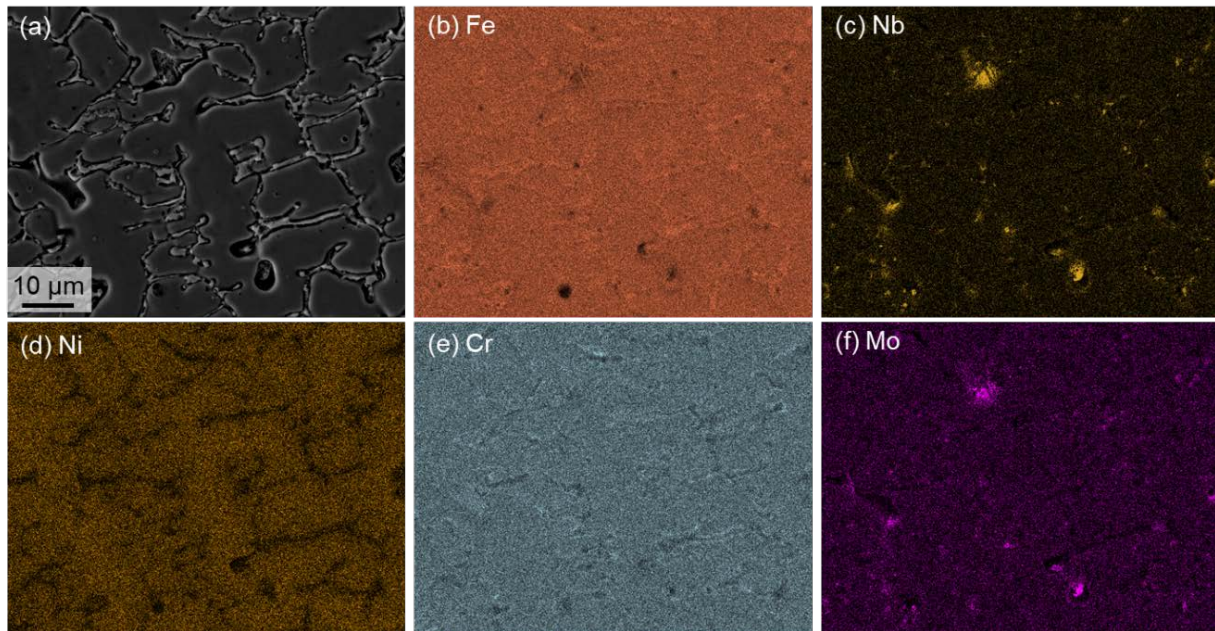


Figure 81. FZ location near bottom location of microhardness indents where microhardness is greater than 250 HV SEM-EDS map of E347-347H SS sample etched in electrolytical nitric acid solution (3V, 10 s) (a) field of view SEI, (b) Fe, (c) Nb, (d) Ni, (e) Cr, (f) Mo

Metallurgical Characterization of E347-347H SS Field Wall Girth Weld in Original Condition and After PWHT (950°C-1 or 2 hr Soak)

A macro characterization of the whole girth weld can be seen in Figure 82 (a). The girth weld is the transition weld from the first wall section to the second wall section, with the thickness transition seen on the top right side of Figure 82 (a). Considering the crack from the new hot storage tank wall, as seen in Figure 66 (a), the HAZ/FZ boundary region just below the cap pass on the OD side was briefly investigated (Figure 82 (b)). In addition, a furnace PWHT was applied (950°C) on some girth weld cross sections for 1 hr (Figure 82 (c)) and 2 hr (Figure 82 (d)) to determine if there was any effect with 1 or 2 hour soak time on the microstructure. The only noticeable feature from LOM is the equiaxed grain morphology in the HAZ and a columnar microstructure with dendrites in the un-heat treated FZ. After PWHT, both PWHT samples showed signs of metallurgical recovery and recrystallization in the FZ as the solidification grain boundaries are more noticeably etched in (c-d) with potential for further grain coarsening with the longer soak time. Further analysis using higher resolution imaging with SEM may assist in gathering more information regarding the grain boundary phases in both HAZ and FZ, and perhaps texture in the FZ, and to determine at a higher mag if the grain boundary phases have more volume fraction with longer soak time. Also, the HAZ grains possibly coarsened during longer soak time; however, the coarsening does not seem to be significant.

Another key observational difference between the old wall girth weld and the new wall girth weld with the crack is the weld process used. The shielded metal arc welding (SMAW) process seemed to be used in the boat sample in Figure 66, but based on the penetration depth of the FZ passes in Figure 82 (a) and Figure 75(a), it seems that gas metal arc welding (GMAW)/flux core arc welding (FCAW) was used for the old girth and seam weld. The composition using a different filler must be accounted for when completing the repair welds with SMAW E16.8.2 filler, as dilution may influence the susceptibility of the weld joint to SRC. Gas metal arc welding/flux core arc welds have more penetration than SMAW and maybe higher dilution, leading to reduced δ -ferrite, as the filler is typically slightly over-alloyed with Cr (δ -ferrite former) to ensure the minimum Cr requirement after dilution.

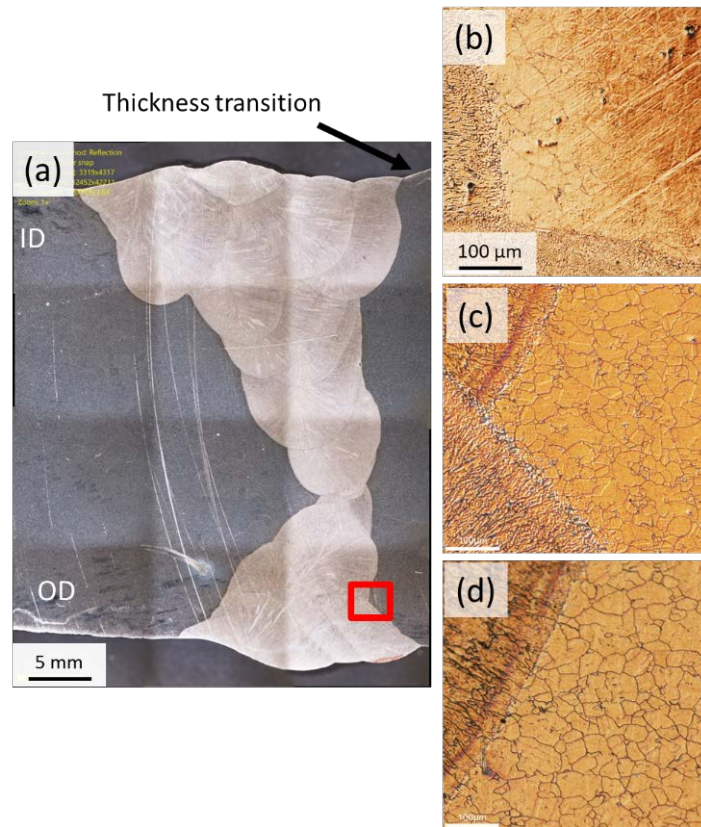


Figure 82. (a) Macro of girth wall-to-wall weld section showing thickness transition near the ID of the wall. Micrographs in the HAZ/FZ boundary beneath a cap of one of the passes near the OD for (b) no HT, (c) 950°C-1 hr soak, and (d) 950°C-2 hr soak time. Similar location to the boat-sample crack, the cracks went through this location as seen in the boat sample.

4.9 Milestone 2.2.2 Thermomechanical Testing of Field Sample Tanks Weldments

The milestone information for subtask 2.2.2 is detailed below in Table 25.

Table 25. Milestone 2.2.2 details

Milestone	Description	Metric	Success Value
2.2.1 Complete thermomechanical testing of field sample tank weldments operating and elevated temperatures (e. g. 800°C for expedited failure) to determine threshold stress/plastic strain for SRC	We will perform thermomechanical testing of tank weldments via Gleeble experiments at operating temperature (565°C) and elevated temperatures (e.g., 800°C for expedited failure).	Number of weldment types tested	Test at least three weldment types – an original condition field sample, a mock repair sample (made by grinding out filler and replacing with E16-8-2 filler) and a post weld heat treated field sample. Three duplicates for each temperature (room, 565, 800C) and type of weldment (x3)

Overall, the goal of Milestone 2.2.2 is to determine SRC susceptibility in field samples, including repair welds with both matching and alternative E16.8.2 filler. SRC testing was completed on four unique samples:

1. Original condition samples: E347 weld metal in seam weld after 3 years of service.
2. PWHT sample: Perform heat treatment (950°C/3 hr) on field E347 weld metal samples to compare to lab samples in milestone 1.2.1
3. Mock repair samples using SMAW E16.8.2 alternative filler in seam weld
4. Mock repair samples using SMAW E347 matching filler in seam weld

As extra work, residual stresses were experimentally measured and calculated for original condition and after repair welding using both fillers.

Repair Weld Procedure

As a starting point, AWS D1.6 Structural Welding Code – Stainless Steel, section 7.21 [50] has provisions for repair welding that can be followed using similar weld procedures as in the case of the original girth weld. This section details that it is necessary to use either a qualified welding procedure specification or prequalified welding procedure specification for the repair, and that the repair weld should undergo the same level of non-destructive testing scrutiny as the original weld. The section of seam weld provided is approximately 9 inches (229 mm) in length, with planned 5.75 inches of welding (ideally 4.5 inches of steady state material). For the experimental weld repair, it is assumed that there was a crack 2 inches in length 0.5 inches below the top surface for the 1-5/16 inch thick plate running parallel to the welding direction (see Figure 83). The cross section of the weld profile in the start and stop locations is also illustrated, with about a 1 inch start and no stop slope (to maximize material for testing). Ideally, both a start and stop region that is about 1.5 inches in length each is needed in addition to the crack length, with a minimum of a 1/2 inch width. This length parameter would also depend on the depth of the crack. To prepare the joint for repair welding, the existing weld metal in the location above the assumed crack was removed by angle grinder to a depth 1/8 inch below the location of the crack (~ 5/8 inch depth) to ensure full removal of the defect. The geometry of the excavated region should have a minimum of 60 degree angle but was closer to 65 degree–70 degree and included a root gap of about 5/32 inch due to the electrode diameter size of 5/32 inch.

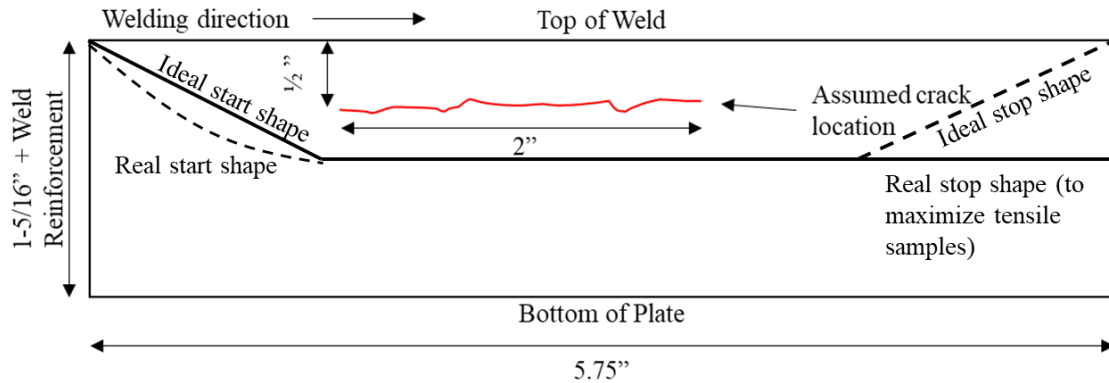


Figure 83. Side-view schematic of simulated crack location with 1/2" depth and 2" long

The repair welding experiments were completed using the SMAW process with 5/32-inch (4.0 mm) diameter E347-16 and E16-8-2-15 filler electrodes in the flat position. A total of 12 passes were required for this repair weld joint, consisting of one single pass root layer, four 2-pass layers, and a 3-pass cap layer. The maximum current was set to 155 Amps, with an average output voltage of 25 V for each weld ass. The travel speed was calculated with an average 7.5 ± 1.5 IPM for E16.8.2 weld and 6.7 ± 0.8 IPM for E347 weld with an average arc energy per unit length of 32 ± 5 kJ/in and 34.4 ± 3.4 kJ/in, respectively. The field weld sample after grinding but before welding is shown in Figure 84 (a), and the repair welded samples from a top-view are shown in Figure 84 (b-c). A rough cross section of the repair weld, including pass sequence, is compared to the original weld in Figure 85 (a-b). The machining locations with respect to the repair welds and original welds is illustrated in Figure 85 (c).



Figure 84. (a) Ground out single-V geometry form seam weld (b) after repair welding on seam weld using E16.8.2, and (c) after repair welding on seam weld using E347

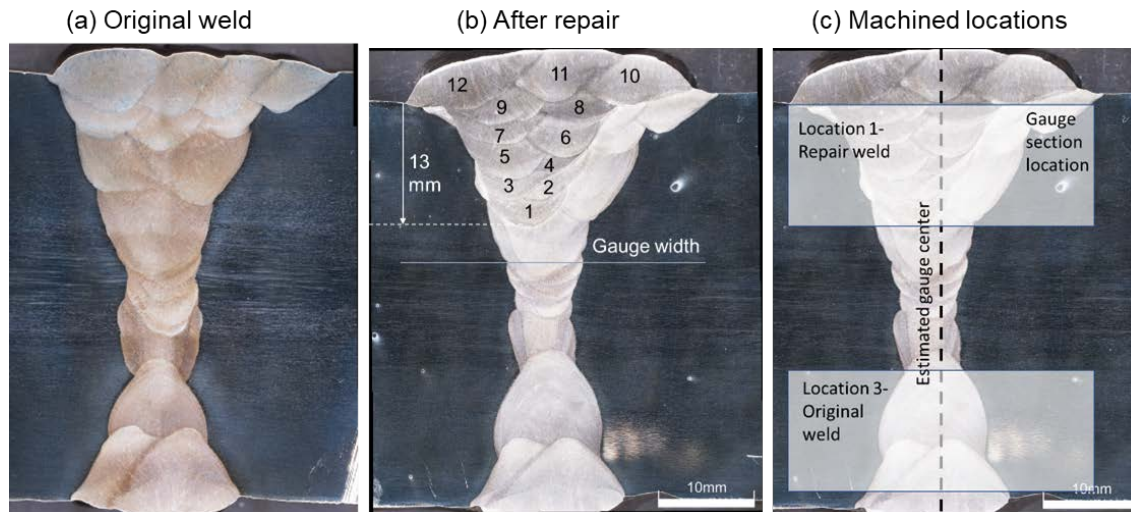


Figure 85. Macro images of seam E347-347H wall weld in (a) as-welded condition and (b) after repair using E16.8.2 to a depth of 13 mm. (c) Machined gauge sections with respect to repair weld and original weld filler

Weld Defects Observed During Machining of Tensile 2.2.2 Samples

Similar to previous sample extraction for SRC testing, the samples have an orientation perpendicular to the welding direction and are parallel to the transverse direction. The repair weld samples were machined from the 13 mm thickness location as seen in Figure 85 (b), which was appropriate for a 10 mm unreduced diameter in cylindrical samples. The gauge length includes a combination of repair passes 2-7, old E347 filler and the HAZ. The extraction location for the OG and PWHT-OG samples are located on the opposite edge of the same cross section, which encompasses three relatively larger E347 passes. It should be noted that the sample extraction of the OG samples was taken after the completion of the repair welding experiments.

During machining of the field tensile samples to get square lengths prior to turning down to cylindrical samples, huge slag inclusion/lack of fusion defect (8x5 mm) was discovered as seen in Figure 86. This defect can be seen to be sub-surface closer to the double-V groove root, which supposedly was the root cause of fracture in the girth wall fracture at Crescent Dunes. These samples were not included for further machining and SRC testing. However, this image is included here to further prove weld quality issues with Crescent Dunes welds, particularly during initial construction. General non-destructive testing procedures should have caught this weld defect and should have warranted weld repair before issuing a pass.



Figure 86. 8x5 mm slag inclusion/lack of fusion defect observed on side used for the intended OG samples. The defect extended to three 0.5” wide samples, indicating a 1-1.5” long defect along the weld direction. This was observed near the intersection and thickness transition between the seam and girth weld.

Gleeble Thermomechanical Test Results of Original Service Weld, Repair Welds, and After PWHT of Original Service Weld

The results for all four samples are tabulated below in Table 26. Based on the Gleeble SRC testing, a few observations can be made for each material set:

- The original (OG) samples (i.e., 3 years of service at 565°C peak service temperature) have comparable stress relaxation properties during heating to temperature with the as-welded lab samples, which in this instance means less stress relaxation during heating so that the starting stress at temperature is higher. At 800°C, with similar stress conditions, the samples failed around a ~3.3–4.3 hr period, while the lab samples in the as-welded condition showed a more rapid time to fracture (~17 minutes). However, under 850°C test condition, the field sample showed a more rapid fracture due to less stress relaxation during heating and a higher starting stress at temperature. Generally, the crack susceptibility is similar between lab and service weld samples.
 - The ferrite content in the OG samples is roughly 3% by volume (measured by Feritescope), while the lab samples can have a ferrite content closer to 10% by volume. The amount of ferrite content initially does not seem to correlate to differences in fracture susceptibility in the FZ.
- The repair weld samples using matching E347 filler have similar or slightly worse cracking resistance, since time to fracture seems to be similar or slightly more rapid with less starting stress at temperature compared to OG test results. When compared to lab samples, it appears that the as-welded results show general similar cracking behavior, however, the time to fracture is inversely proportional to the starting stress at temperature. Literature has suggested that repair welding samples have SRC failure sooner than the original weld [4], which can be expected in field applications.

- Repair weld samples using alternative E16.8.2 filler have shown the best resistance to cracking (no cracking observed in E16.8.2 filler), primarily due to better elevated temperature ductility compared to matching E347 filler. It should be noted that the strain at temperature of the repair E16.8.2 (1.82%) is noticeably higher than strain with matching E347 samples (0.17 to 0.57%). Also, the yield point of E16.8.2 is similar or less than E347 filler up to a certain temperature (i.e., same starting stress at temperature at 800°C as the OG E347 samples), but at higher temperature (i.e., 850°C) it appears the E16.8.2 filler may have a more appreciable lower starting stress compared to OG and repair welds with E347. While the E16.8.2 FZ did not indicate cracking, there were certain cracks that developed in the adjacent old E347 filler during the cooling step after 22 hours at temperature, as seen in Figure 94.
- Finally, the last samples, PWHT of the E347 original field samples (950°C/2h), seem to indicate improvement in crack resistance at 800°C condition (no failure) but not the 850°C condition since it failed at 17 hr at temperature. Since the yield strength is lower in these PWHT samples, the starting stress at temperature is essentially lower than the other field sample conditions. Duplicate tests need to be made to verify the first experiments, but overall, there seems to be some general improvement with PWHT in terms of delaying fracture. However, PWHT of a service component might have different, slightly worse SRC results than compared to lab samples that have no service history. This observation from Gleeble results might contribute an opinion to the benefit of PWHT on a brown field (already constructed) vs. a green field (during construction) tank, where PWHT of a green field tank will be less susceptible to SRC than after PWHT of a brown field tank.
 - Interestingly, the strain at temperature with the PWHT Gleeble field samples was essentially zero. Since the center of the gauge section is in the FZ and the gauge length includes a combination of FZ and HAZ, it's possible there is more strain accumulation in the HAZ that allows for stress relaxation to develop in HAZ over the FZ. The lack of strain development was also seen with the lab samples in milestone 1.2.1.

Table 26. SRC results of field samples, including original condition (OG), repair welds (Rep) and PWHT of original welds

<u>Sample #</u>	<u>Temp (°C)</u>	<u>Starting Stress @ RT (MPa)</u>	<u>Starting Stress @ Temp (MPa)</u>	<u>Failure</u>	<u>Time to Failure/Cool</u>	<u>Strain @ T</u>
<u>OG.1</u>	800	<u>404</u>	<u>181</u>	<u>Yes, isothermal</u>	<u>4.3 h</u>	<u>0.18%</u>
<u>OG.3</u>		<u>405</u>	<u>182</u>	<u>Yes, isothermal</u>	<u>3.35 h</u>	<u>0.4%</u>
<u>RepE347.1</u>		<u>408</u>	<u>161</u>	<u>Yes, isothermal</u>	<u>3.6 h</u>	<u>0.75%</u>
<u>RepE347.4</u>		<u>412</u>	<u>180</u>	<u>Yes, isothermal</u>	<u>3.6 h</u>	<u>1.4%</u>
<u>RepE1682.1</u>		<u>409</u>	<u>188</u>	<u>No, crack in OG E347 filler</u>	<u>22 h</u>	<u>0.82%</u>
<u>RepE1682.3</u>		<u>412</u>	<u>185</u>	<u>No</u>	<u>22 h</u>	<u>0.79%</u>
<u>RepE1682.5</u>		<u>500/470 (0.5% strain)</u>	<u>181</u>	<u>No</u>	<u>22 h</u>	<u>0.43 %</u>
<u>PWHT347.1 (OG)</u>		<u>385</u>	<u>135</u>	<u>No</u>	<u>22 h</u>	<u>-0.1%</u>
<u>PWHT347.4 (OG)</u>		<u>458/430 (1.4% strain)</u>	<u>148</u>	<u>No</u>	<u>22 h</u>	<u>-0.1%</u>
<u>OG.2</u>		850	<u>328</u>	<u>152</u>	<u>Yes, isothermal</u>	<u>1.4 h</u>
<u>OG.4</u>	<u>331</u>		<u>158</u>	<u>Yes, isothermal</u>	<u>2 h</u>	<u>N/A</u>
<u>RepE347.2</u>	<u>330</u>		<u>143</u>	<u>Yes, isothermal</u>	<u>50 min</u>	<u>0.57%</u>
<u>RepE347.3</u>	<u>330</u>		<u>140</u>	<u>Yes, isothermal</u>	<u>1.26 h</u>	<u>N/A</u>
<u>RepE1682.2</u>	<u>354</u>		<u>128</u>	<u>No, crack in OG E347 filler</u>	<u>22 h</u>	<u>1.82%</u>
<u>RepE1682.4</u>	<u>360</u>		<u>135</u>	<u>No</u>	<u>22 h</u>	<u>N/A</u>
<u>PWHT347.2 (OG)</u>	<u>317</u>		<u>122</u>	<u>Yes, isothermal in FZ</u>	<u>17.2 h</u>	<u>0%</u>
<u>PWHT347.3 (OG)</u>	<u>322</u>		<u>120</u>	<u>Yes, cooling in FZ</u>	<u>22 h</u>	<u>N/A</u>
<u>PWHT347.5 (OG)</u>	<u>284/271</u>		<u>118</u>	<u>No (crack in HAZ)</u>	<u>22 h</u>	<u>0.02%</u>

Metallurgical Characterization of Original and E347 Repair Gleeble SRC Samples

The original field weld sample fracture surfaces were observed using a stereoscope with a method for capturing depth of field, as seen in Figure 87. Overall, the fracture behavior, i.e., woody fracture associated with weld solidification (columnar morphology), is similar to the lab as-welded samples that fractured at elevated temperatures. No fracture associated with slag inclusion defects. However, some final fracture spots that fail by overload are circled, where some shiny reflections indicate some potential arcing of the sample due to thermal resistance heating in the Gleeble. These local regions seem to be more ductile. However, the whole fracture surface contains radial lines associated with columnar microstructure, where an area with almost all radial fracture propagation represents a microstructure with low ductility.

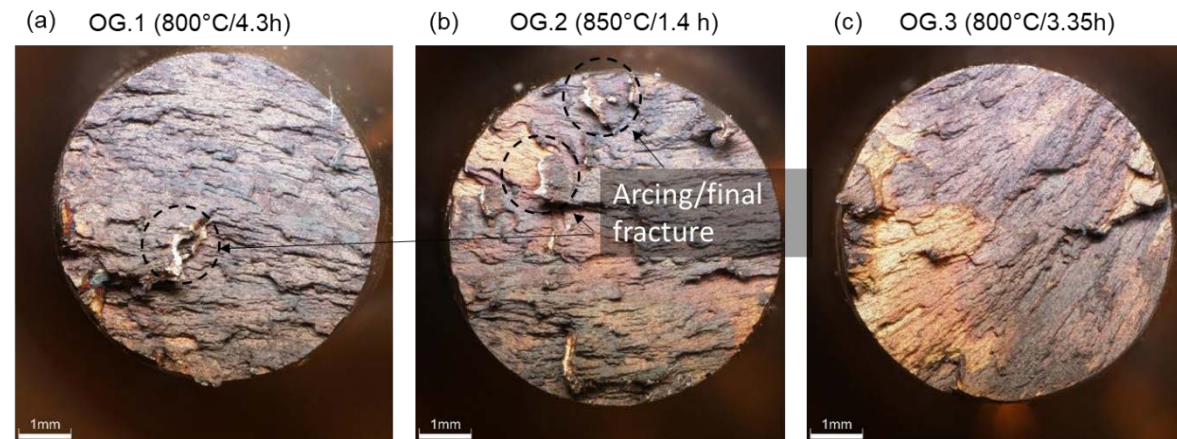


Figure 87. Fracture surfaces of original field samples (a) OG.1, (b) OG.2, and (c) OG.3

A closeup investigation of OG.3 fracture surfaces were investigated using high mag SEM-EDS for characterization of any coarse precipitates or phases. An EDS map scan of a high magnification SEM reveals mostly Nb and Mo rich precipitates. Some faint Cr enrichment seems to be present, indicating the possibility of δ -ferrite, but the Cr could also be correlated to oxygen map which could likely be chromium oxides. Overall, the fracture surface is likely along solidification grain boundary where interdendritic fracture occurs.

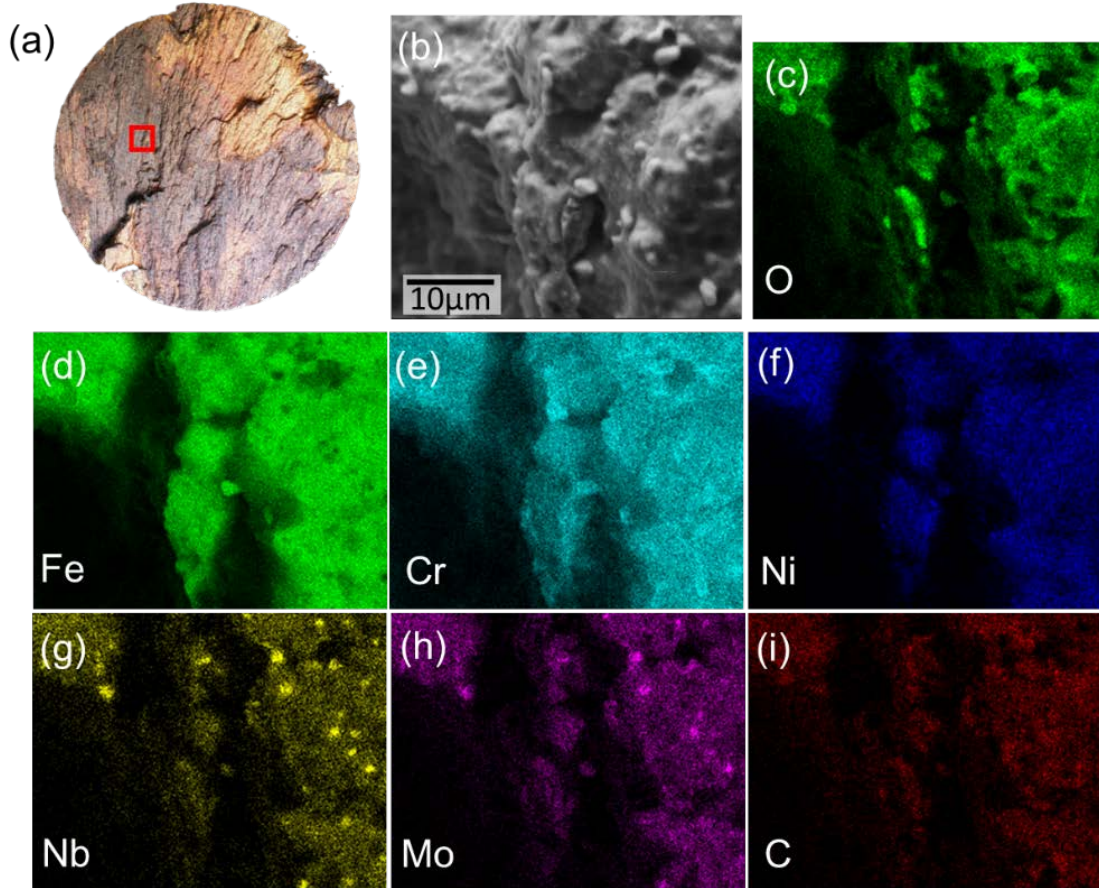


Figure 88. OG.3 (800°C/3.5 h.) Fracture surfaces integrated with SEM-EDS characterization showing Nb and Mo rich precipitates laced along the fracture surface

Figure 89 represents the secondary cracking region ahead of primary fracture in the OG.3 sample using the electron back-scatter diffraction (EBSD) technique on a high-resolution SEM. The inverse pole figure (IPF) map, which is a representation of grain structure that is color coded to represent top-view plane orientation of each grain. Figure 89 (a) indicates that the secondary cracks propagate along solidification grain boundaries with different orientations, which may be indicative of high angle misorientation between two separate solidification grains. The phase map in Figure 89 (b) represents an image that overlays the detected phases with respect to location. The OG.3 sample took 3.35 h at 800°C to fracture using 405 initial MPa stress (beneath yield strength of typical E347-347H SS weld joints). A temperature of 800°C would not be high enough to dissolve intragranular δ -ferrite (2.6 vol%) and possibly sigma phase (0.6 vol%). The presence of sigma is still questionable as the secondary cracks line the solidification boundary, which have a low confidence index (CI).

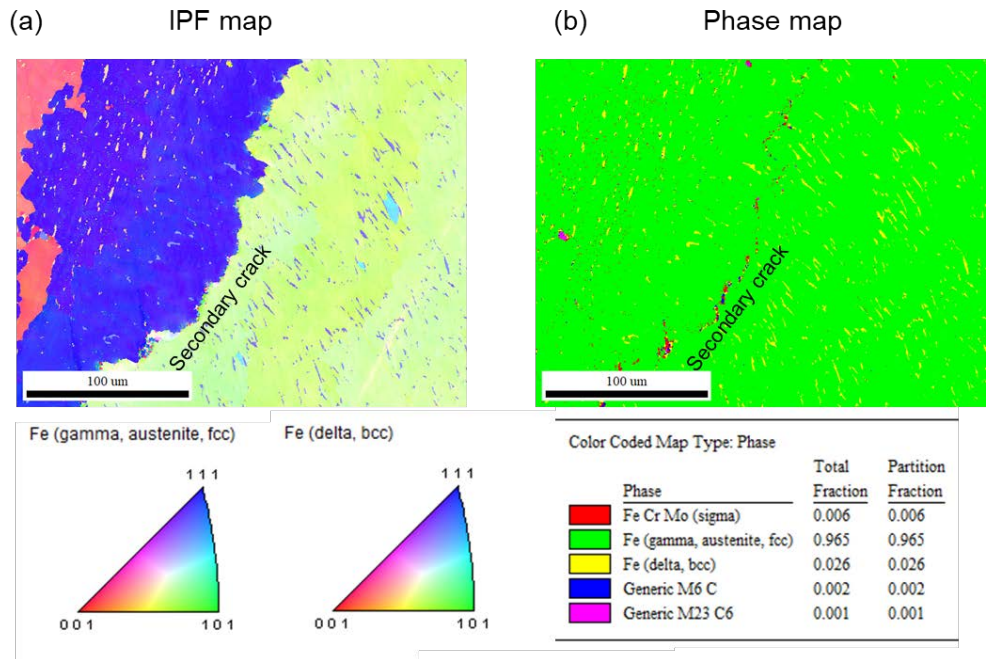


Figure 89. EBSD characterization (0.2 μ m resolution) of OG.3 samples ahead of secondary crack tips with presence of ferrite, sigma (low CI), and carbides (low CI)

33458 Lab E347 Weld Sample

As a comparison to lab samples, some of the EBSD from Gleeble lab samples with only microcracks and no complete failure during testing are shown in Figure 90. Figure 90 demonstrates cracks along the main solidification grain boundaries for the 1,050 $^{\circ}$ C condition. A very coarse scan (with a 2 μ m resolution) mainly shows FCC austenite as the primary phase, with remnants of BCC ferrite within the bulk solidification grains. A neighbor grain correlation filtering using a minimum confidence index of 0.1 was used to help clean up the EBSD IPF figure. δ -ferrite would be noticeable with finer resolutions and lower magnification images but appear as dots at the used magnification. The inverse pole figure (IPF) reveals the orientation relationships between the main solidification and sub solidification grains. A histogram was developed (see Figure 90(e)) by measuring the misorientation angle between the grain boundaries of the cracks and other grain boundaries with no cracks in the EBSD IPF maps (see Figure 90(b)). The distribution of misorientation angles between the crack solidification grain boundaries are mostly between 30–40 $^{\circ}$, which would be indicative of high angle grain boundaries. The no crack boundaries seem to have a much wider distribution ranging from \sim 6 $^{\circ}$ –60 $^{\circ}$, with most rotation angles between grains being 30–40 $^{\circ}$. Overall, the field sample in Figure 89 showed similar intergranular fracture as lab sample in Figure 90.

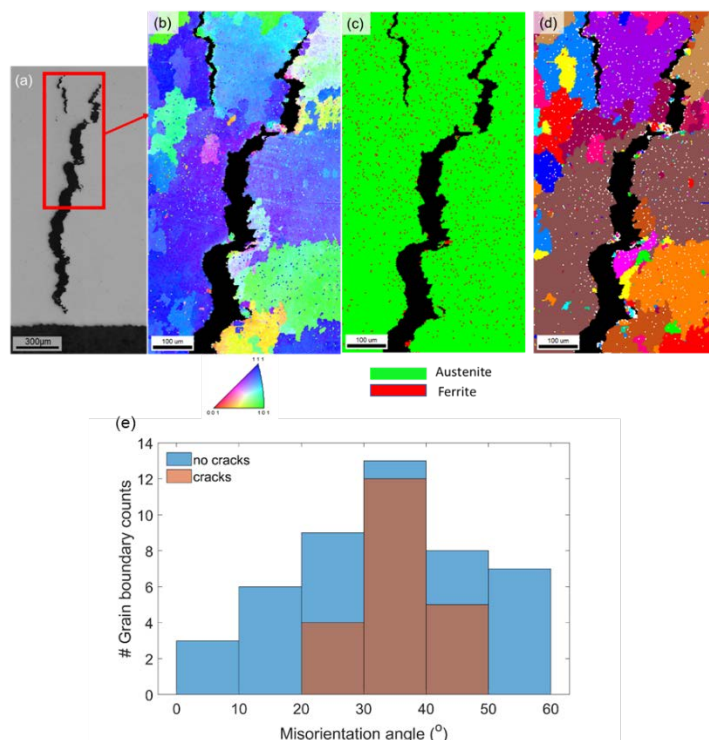


Figure 90. EBSD characterization (2 μm resolution) of 33458-GW.24 1,050°C sample with secondary cracks (a) SEM-SEI image, (b) IPF map, (c) phase map, (d) unique grain map, (e) grain misorientation angle histogram between cracks and no cracks

Microstructure and Microhardness of E16.8.2 Repair Welds

Optical microscopy examination on the mock repair weld with E16.8.2 filler (seen in Figure 91) was completed to help in understanding differences in microstructure between the original weld and repair weld. First, the E347 FZ contains higher δ -ferrite content that can be observed in Figure 91 (b) where remnant E347 filler FZ was still present in the darker etched region. Also, it is apparent that there may be very little δ -ferrite present in reheated intersection regions, such as the location in Figure 91 (c). Very little δ -ferrite is present, which may be beneficial for improved resistance to long term embrittlement, such as σ -phase formation. Also, the HAZ intersection region, including some remnant E347 original FZ, is observed in Figure 91 (d). More evidence of δ -ferrite stringers are present in this region as seen in the other sample (Figure 75(d)), but it seems that the liquation along stringers in the PMZ is suppressed compared to the original weld, which may be due to no Nb present in the E16.8.2 FZ that may backfill into the PMZ. Also, the stringers were observed more in mid-thickness, so it's likely at the $\frac{1}{4}$ thickness position there would be no stringers. Additionally, the PMZ for the E16.8.2 weld can be seen in Figure 91 (e), where the δ -ferrite content appears to be higher than the E347 FZ. Since the substrate has more Cr content than the E16.8.2 filler, this would be possible. As seen in a microhardness line example for a similar weld in Figure 53 (c), the PMZ can be a local hardened zone with respect to the coarse-grained HAZ and FZ.

Like the original weld and lab weld plots shown previously, the microhardness plot for the E16.8.2 repair weld was set up similarly. Similar trends can be observed in Figure 92 compared to the original weld in Figure 76, as the FZ generally has higher hardness sub-surface (repair weld pass 5) compared to the passes near the surface (pass 9). The HAZ and base metal, on left

side of the image, show essentially the pre-existing HAZ/base metal region prior to repair (230–250 HV), while the fresh HAZ generated from the weld repair experiment contributed to the lower hardness region where the contours appear more blue than green (210–230 HV). Essentially, the peak hardness values are slightly less extreme (~20HV) than peak values observed in the original weld with E347 filler, but overall, the microhardness profile in repair welds seems to have comparable contours and regions of similar hardness to the original weld, albeit with a fresh HAZ.

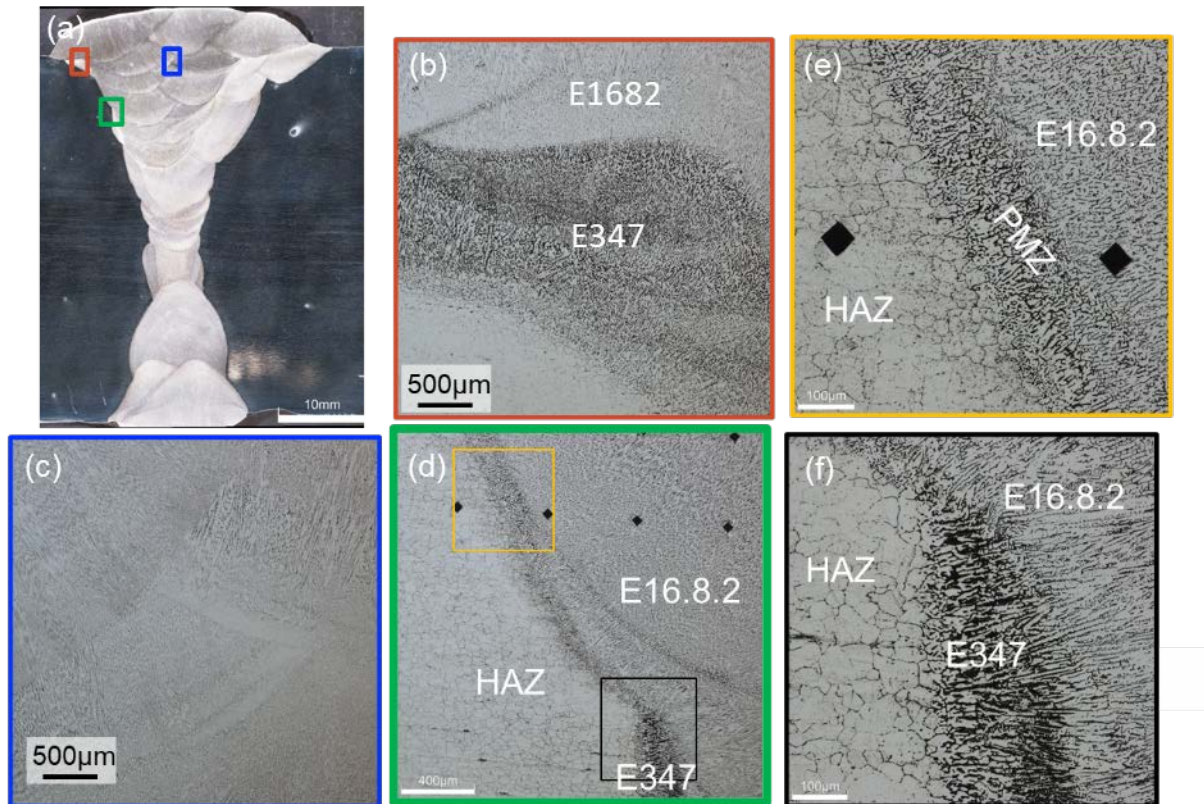


Figure 91. Repair weld on seam weld using E16,8,2 filler (a) macro graph after repair, (b) location where remnant E347 filler is observed with darker etch contrast, (c) reheat region intersection showing very little δ -ferrite content, and (d) HAZ/PMZ/FZ boundary with δ -ferrite stringers

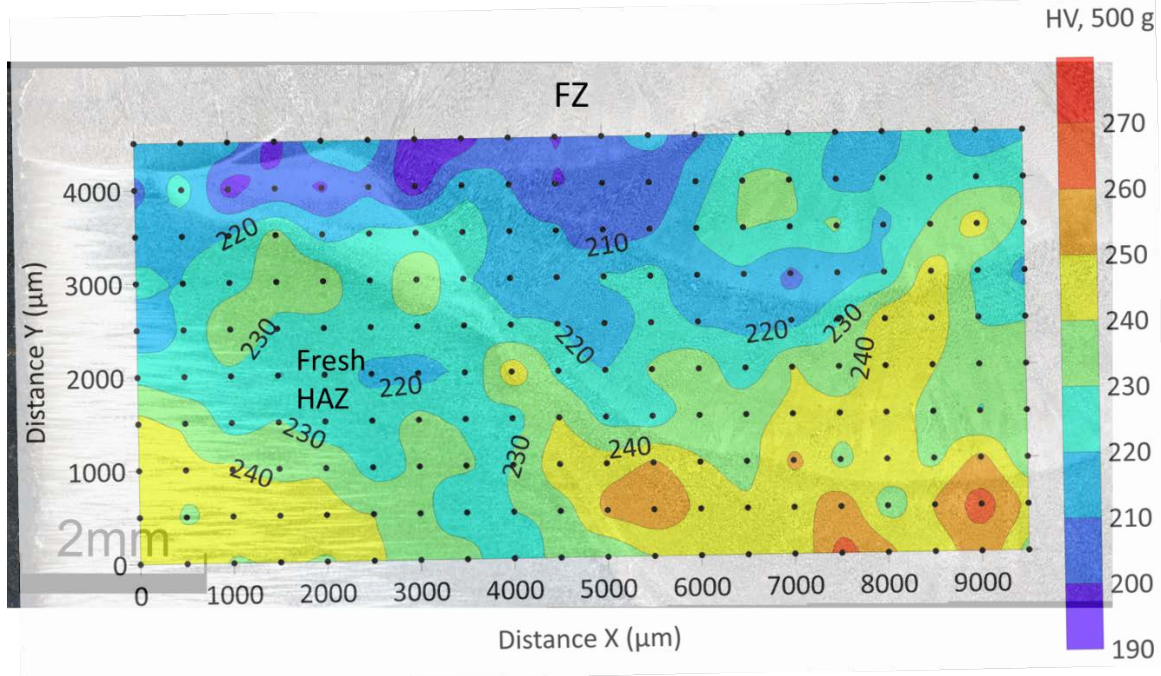


Figure 92. Microhardness map of repair seam weld (after 3 years of service) with E16.8.2 filler. FZ peaks at 270 HV, with fresh HAZ being softer than the base metal and FZ. Notice that hardness decreases closer to the top surface of the weld, as hardness is higher in passes closer to mid-thickness

The microstructure of the as-welded E16.8.2 repair FZ can also be observed via EBSD IPF and phase maps in Figure 93, which is in the general location as Figure 91 (c). Generally, the microstructure consists of columnar solidification grains with $\langle 100 \rangle$ grain orientations. The vol. fraction of δ -ferrite is sensitive to location and resolution. For instance, this location, similar to location where the SRC samples are extracted from, shows a vol. fraction of 0.003 (0.3%) at lower magnification in Figure 93 (a-b), while a higher magnification shows a 0.009 (0.9%) volume fraction as seen in Figure 93 (c). Overall, the ferrite content may be between 1-3 vol fraction %, depending on the local regions in the multi-pass weld microstructure. The Feritescope measured FN that ranged in this content, but the peak ferrite typically occurs in the center of the weld pass.

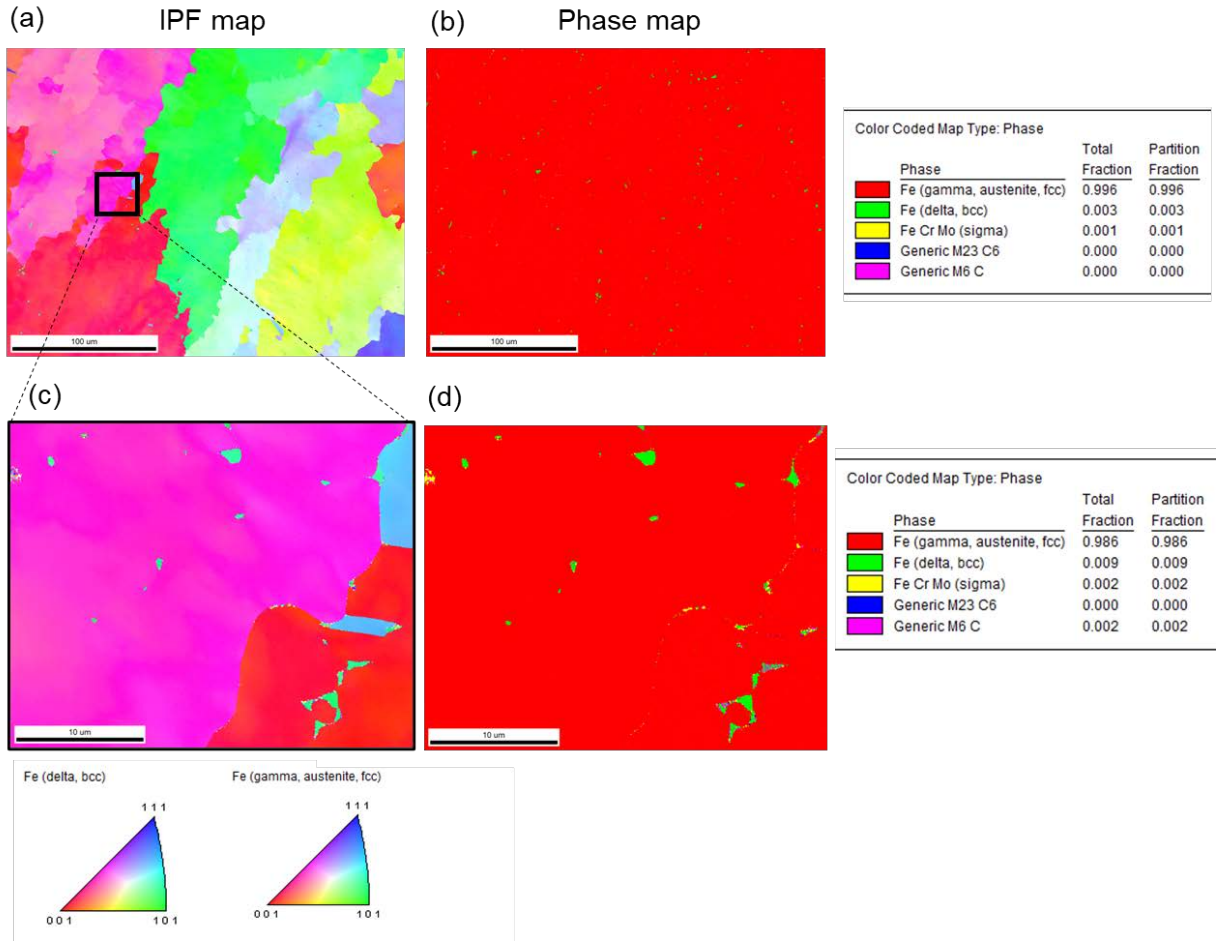


Figure 93. EBSD of E16.8.2 FZ of lower magnification (0.2μm resolution) (a) IPF and (b) phase map, and higher magnification (0.03μm resolution) of (c) IPF and (d) phase map

Microstructure of E16.8.2 Repair Weld Gleeble Samples

A couple of the repair E16.8.2 weld samples had cracking develop in the original E347 side of the weld, as seen in Figure 94. This region represents the HAZ from the repair welding process, which can be seen in Figure 94 (d). Also, no noticeable cracking in the E16.8.2 FZ was observed. SEM-EDS analysis was conducted on three separate locations, which are shown in Figure 95. The corresponding EDS maps for the three separate locations ahead or adjacent to microcracks are shown in Figure 96, Figure 97, and Figure 98. Figure 96 and Figure 98 represent regions in the E347 filler (HAZ from repair) where there is a significant distribution of Nb-rich precipitates, which appear to correlate to interfaces in the microstructure, such as solidification grain boundaries and sub-solidification grain boundaries (interfaces between δ -ferrite (Cr-rich) and γ -austenite). Location 2 in Figure 97 represents the diluted region between the old E347 filler and E16.8.2 FZ, where the distribution of Nb precipitates is less dense and fewer. Location 3 EDS map in Figure 98, which is located further out in the old E347 filler, shows a more dense population of Nb and Mo precipitates with δ -ferrite observed with Cr, Fe-enrichment and Ni depletion.

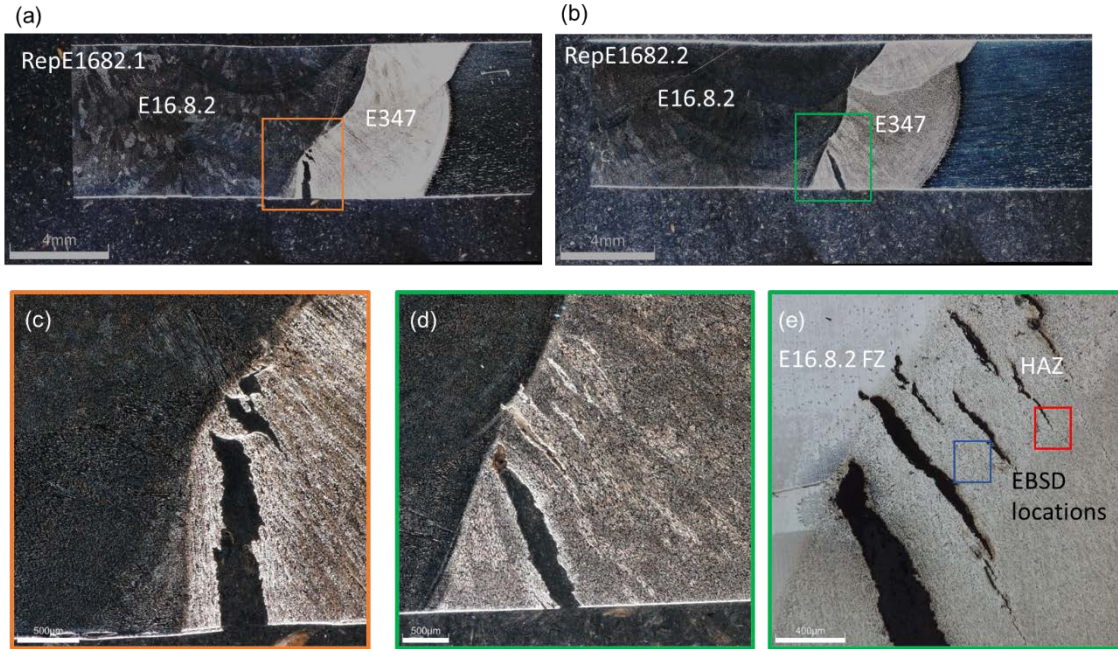


Figure 94. Cracks developed during cooling step in old E347 filler in repair welds using E16.8.2. (a) Rep E1682.1 (800°C), (b) Rep 1682.2 (850°C), (c) closer mag of cracks in Rep E1682.1 (800°C), (d) closer mag of cracks in Rep E1682.2 (850°C), and (e) LOM of same location with indication of EBSD locations within the original E347 filler (repair HAZ)

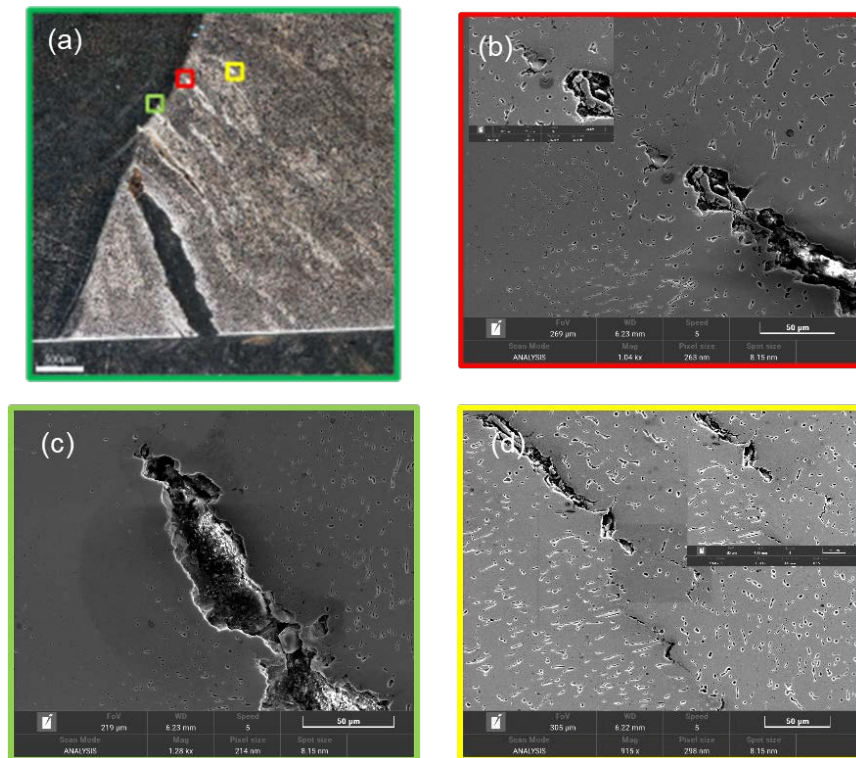


Figure 95. Rep E1682.2 SEM-EDS locations in the repair weld FZ boundary and HAZ (old E347 filler region) (a) general location of interest, (b) location 1 in E347 HAZ, (c) location 2 in FZ boundary, (d) location 3 farther in E347 HAZ

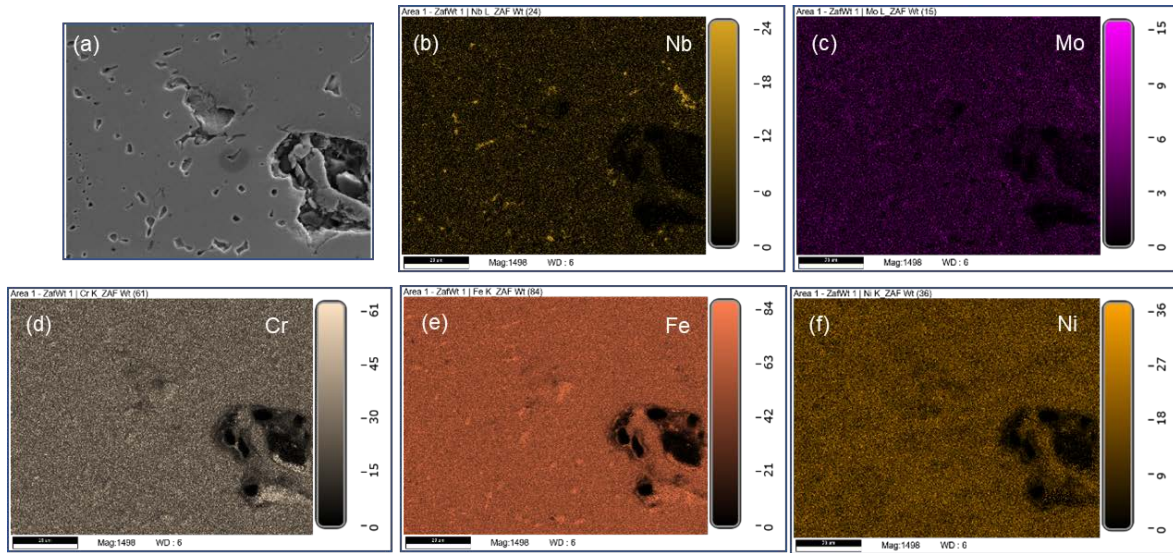


Figure 96. Rep E1682.2 SEM-EDS map (wt%) location 1 in the repair weld FZ boundary and HAZ (old E347 filler region) (a) general location of interest, (b) Nb, (c) Mo, (d) Cr, (e) Fe, and (f) Ni

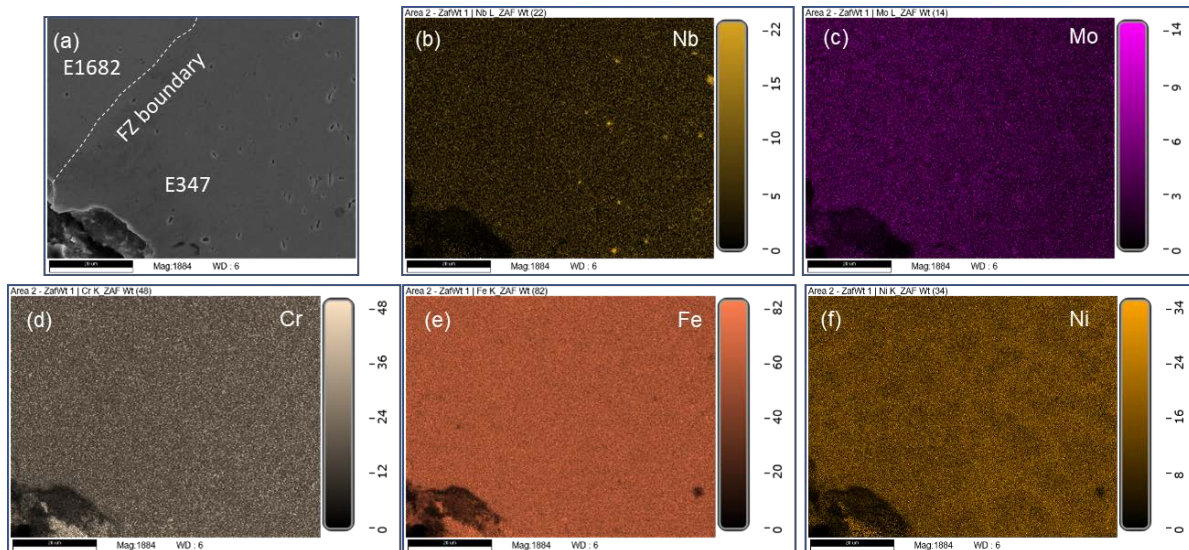


Figure 97. Rep E1682.2 SEM-EDS map (wt%) location 2 in the repair weld FZ boundary and HAZ (old E347 filler region) (a) general location of interest, (b) Nb, (c) Mo, (d) Cr, (e) Fe, and (f) Ni

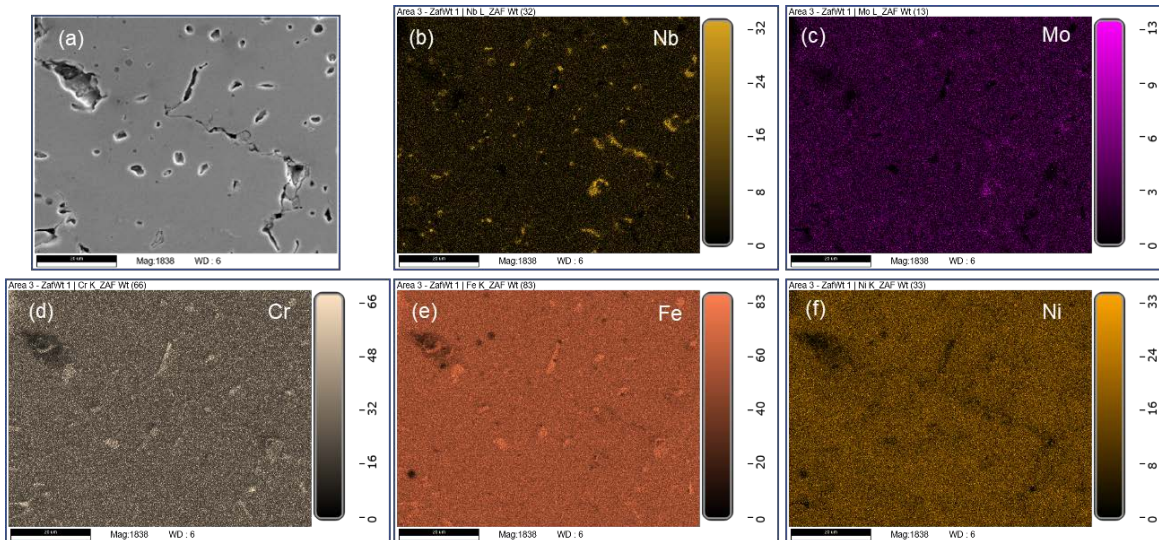


Figure 98. Rep E1682.2 SEM-EDS map (wt%) location 3 in the repair weld HAZ (old E347 filler region) (a) general location of interest, (b) Nb, (c) Mo, (d) Cr, (e) Fe, and (f) Ni

Repair HAZ (E347 Filler)

The EBSD patterns using a $0.2\mu\text{m}$ resolution in one of the microcracks in the original E347 filler (repair weld HAZ) are observed in Figure 99 for RepE16.8.2.2 (red block in Figure 94 (d)). The microcrack develops along solidification grain boundaries in a primarily austenitic localized region of the microstructure. The microcrack appears to terminate upon reaching a region with remnant solidification BCC δ -ferrite ($\sim 3\%$ vol. fraction). A higher magnification EBSD scan ($0.03\mu\text{m}$ resolution) of crack tip shows creep voids in Figure 100. δ -ferrite appears to prevent crack propagation by preventing grain boundary migration and facilitating more tortuous solidification grain boundaries. The location where cracking occurs is within the HAZ of the E16.8.2 repair weld, but this location happens to be in a higher temperature regime during the SRC Gleeble test ($800\text{--}850^\circ\text{C}$) where deformation would be highest in the original E347 filler.

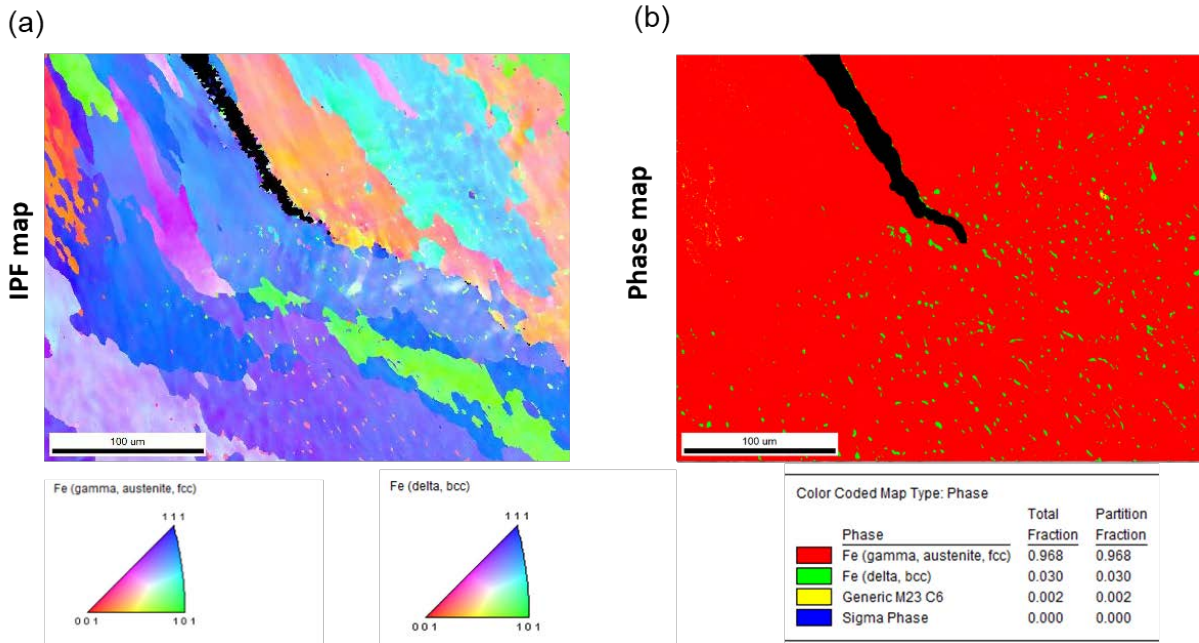


Figure 99. EBSD of E347 microcrack in HAZ of RepE1682.2 Gleeble sample (0.2µm): (a) inverse pole figure (IPF), and (b) phase map

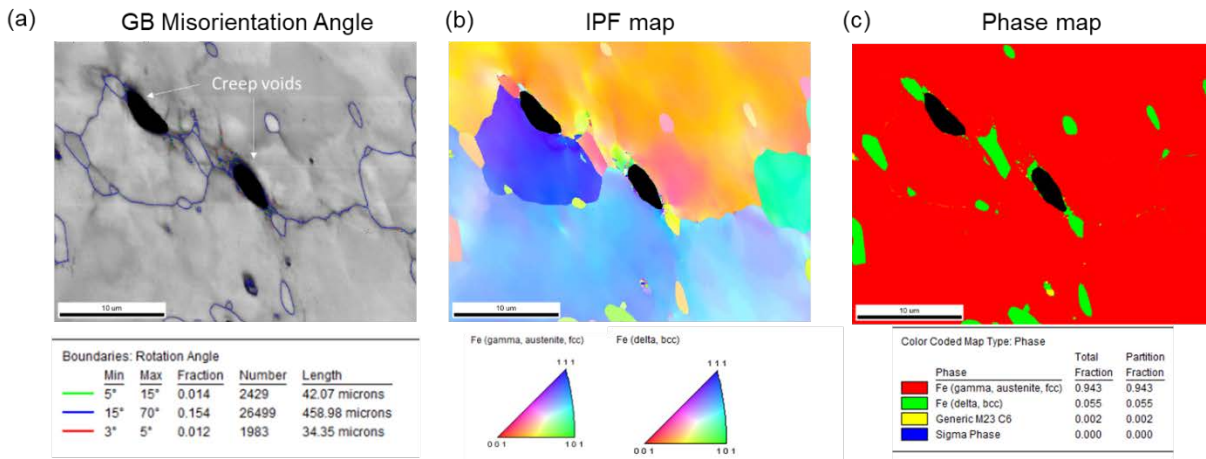


Figure 100. EBSD of microcrack tip in HAZ of RepE1682.2 Gleeble sample (0.03µm resolution): (a) GB misorientation overlaid on image quality (IQ) image, (b) IPF map, (c) phase map

Figure 101 represents the microstructure in between two microcracks within the E347 filler or repair weld HAZ. There is mostly a low misorientation angle between solidification grains in this region (2–5°) and some high misorientation boundaries (15%+) between δ-ferrite and γ-austenite. The total vol% of δ-ferrite present in this region is 3.6 vol% with no other detectable phase. More ferrite content may improve tortuosity and reduce cracking susceptibility. The more susceptible boundaries are straight, high misorientation solidification grain boundaries with no δ-ferrite and a presence of precipitates that facilitate precipitate free zones along solidification grain boundaries or migrated grain boundaries. Another example of where cracks started to develop during a Gleeble SRC test at 1,000°C, as seen in Figure 102, where the cracks develop in regions of little to no ferrite. Cracks initiating in reheated weld regions in multi-pass welds

may also be a representation of ductility dip cracking [51], but the mechanisms are not too different from SRC altogether.

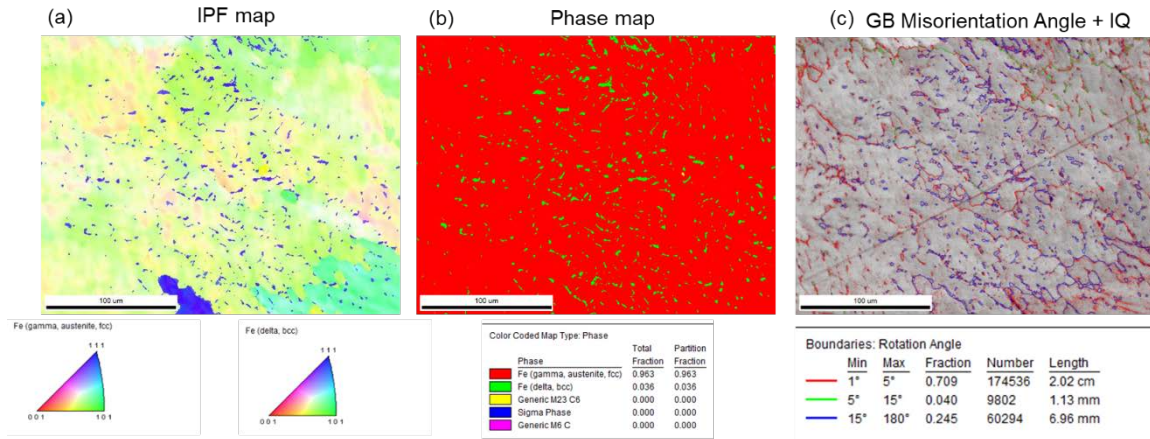


Figure 101. EBSD of microcrack tip in HAZ of RepE1682.2 Gleeble sample in between microcracks (0.2µm resolution): (a) GB misorientation overlaid on image quality (IQ) image, (b) IPF map, (c) phase map

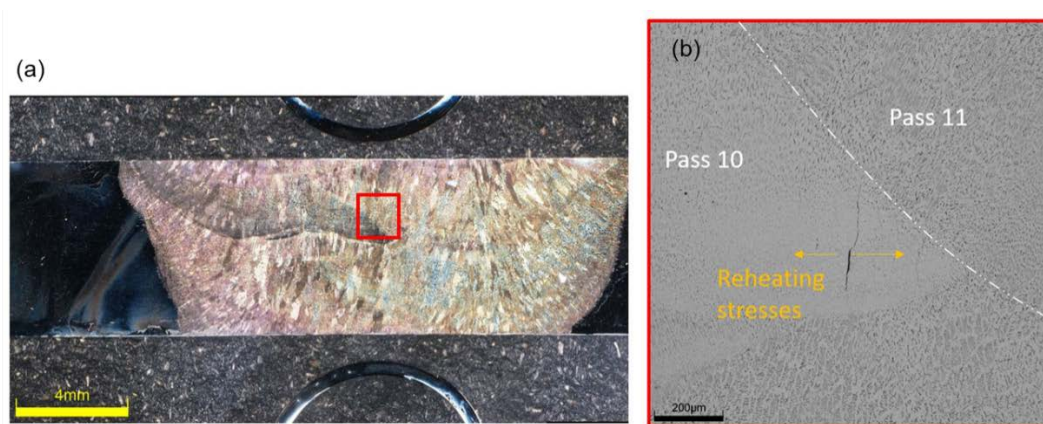


Figure 102. Microcracks observed in multi-pass weld reheated region between passes 8 and 11 where there was no observable δ -ferrite

E16.8.2 FZ

Additional EBSD analysis in the E16.8.2 FZ region (center of gauge section) after SRC testing, as seen in Figure 103, shows an increase in BCC phases that approached 9 vol. fraction %. While the test at 850°C would not appear to be a temperature for development of this amount of ferrite, it is possible the formation of apparent BCC ferrite might be athermal martensite. Theories indicate that elevated temperature influences the development of carbides that would raise the martensite start temperature. Upon further cooling to room temperature, displacive transformation from austenite to martensite could be possible [28]. Another theory could be transformation induced plasticity martensite that can develop with metastable austenite at typical room (ambient) temperatures. Room temperature tensile testing on E16.8.2-347H SS welds from early work shows that above 0.1 true strain there is an increase in strain hardening rate in E16.8.2 only as seen in Figure 104. With that said, the cooling strains do not seem to be extreme to facilitate transformation induced plasticity and the temperature of cooling strain increase is

mostly above 600°C where martensite less likely to develop from transformation induced plasticity (TRIP).

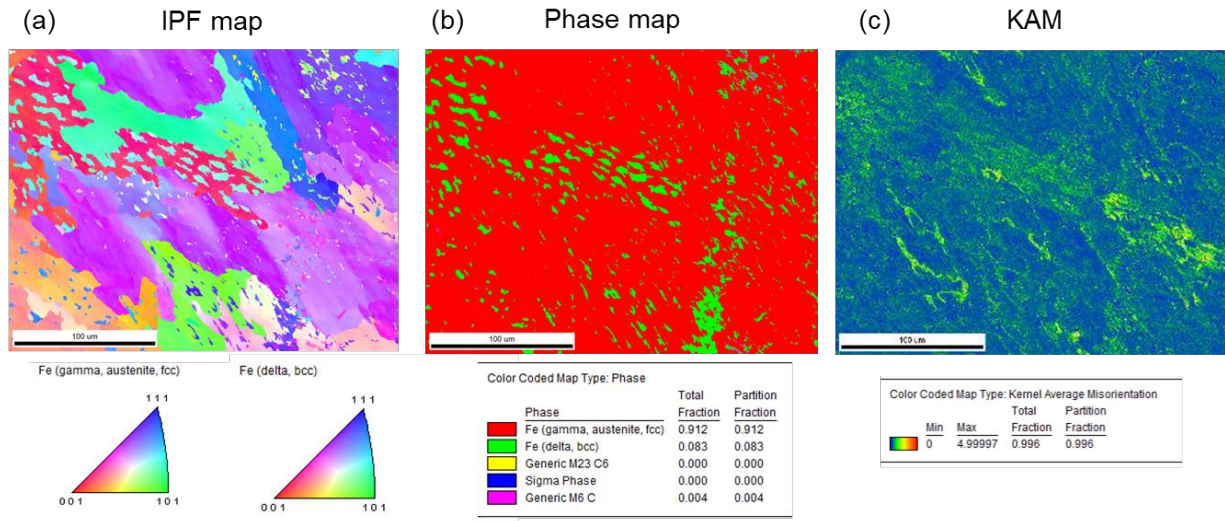


Figure 103. EBSD of microcrack tip in E16.8.2 repair weld after SRC testing (a) IPF map, (b) phase map, (c) Kernel Average Misorientation map

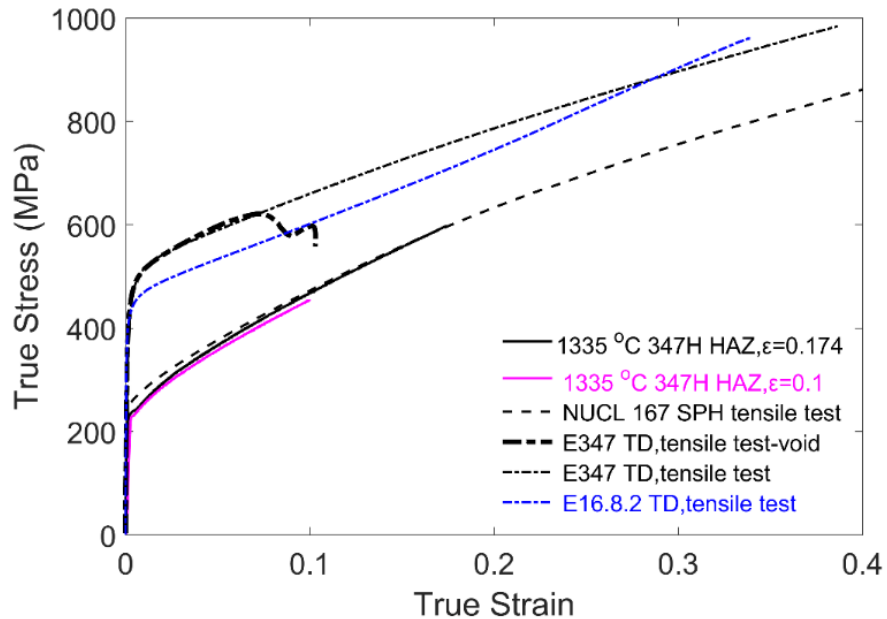


Figure 104. Room temperature tensile data from 347H HAZ, E347 FZ, and E16.8.2 FZ

Neutron Diffraction Residual Stress Results of Original Service Weld and Repair Welds

The experiments conducted for this work were carried out at Oak Ridge National Laboratory (ORNL) using the High Flux Isotope Reactor HB-2B HIDRA Beamline (High Intensity Diffractometer for Residual Stress Analysis). The same setup to gather LD, TD, and ND strains was used. The TD orientation was illustrated in Figure 58. The plates used for the bulk welding

experiments can be shown in Figure 105 with the example of the repair weld using E347 filler. Another weld was made with the same welding procedure using E16.8.2 filler. The region labeled original location on the E16.8.2 repair weld plate was investigated, and the steady state location in the repair weld locations for both welds were investigated.

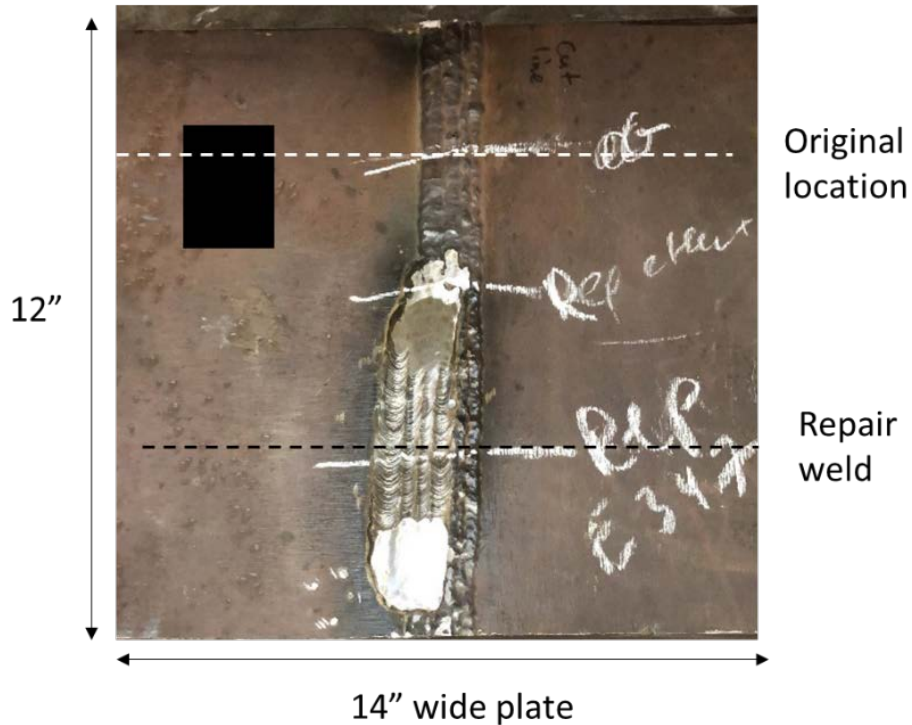


Figure 105. One of two plates used to generate residual stress data (1.7" thick plate w/ double v weld)

FCC $d_{0,311}$ -Spacing Map

The stress free d_{0311} spacing was collected from 4 mm thick samples across the weld region in a 80 x 43 mm area. The sample was sliced in various lines and cubes to provide stress relief. Figure 106 represents the spatial dimension and d-spacing contour of the reference sample overlaid on the double V weld with E16.8.2 repair, where the black dots represent the specific locations of measurement. The contour is developed using linear interpolation. Another sample was used to collect the E347 FZ d_0 -spacing. By combining and separately averaging the values for the base metal, HAZ, original E347 filler, new repair filler (E16.8.2 or E347), and a mixed diluted region between new filler and old E347 filler. The average d_0 spacing map for these separate regions can be seen in Figure 107, which is separate by region and geometrically corrected according to the welding experiments used for bulk measurement (i.e., shifting the repair location further into the HAZ relative to the d_0 sample).

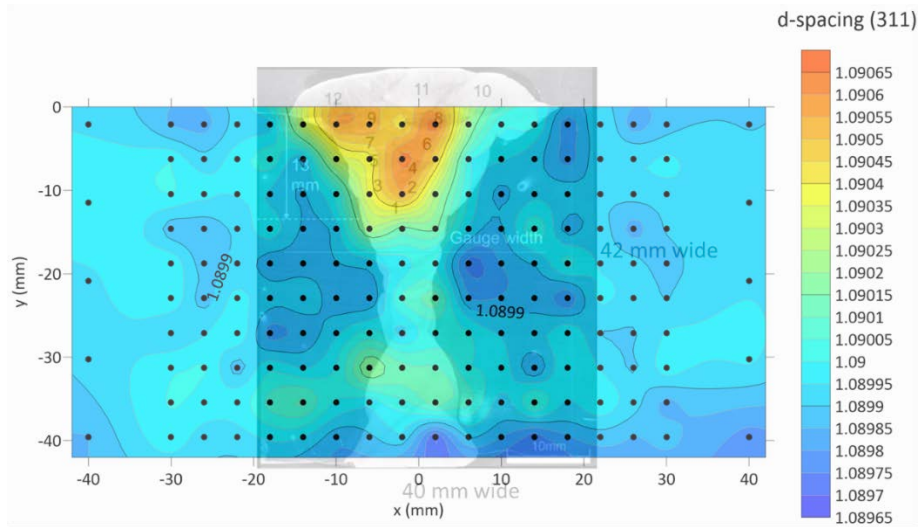


Figure 106. Stress free d_0 -spacing of Repair E 16.8.2 repair weld overlaid on cross section

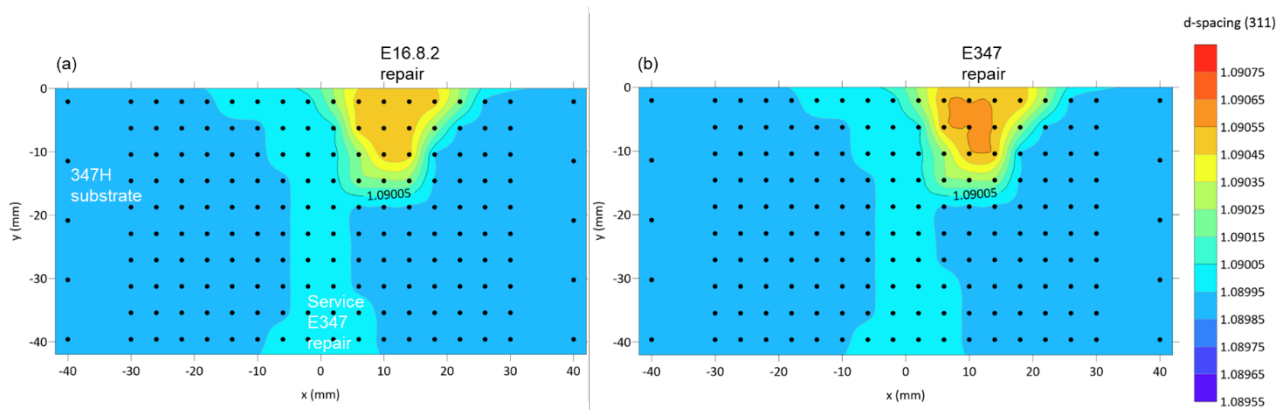


Figure 107. Stress free average d_0 -spacing of (a) E 16.8.2 repair weld and (b) E347 repair weld

FCC d_{311} -Spacing Map

The d-spacing was measured for three directions, LD, TD, and ND, which are displayed as 2D contour plots in Figure 108, Figure 109, and Figure 110, respectively. The black dots represent the locations of each measured location, representing the center of a finite gauge volume, which is represented as a 5x5 mm diamond in Figure 108. The gauge volumes of each point for LD are 5x5x5 mm, while TD and ND are 5x5x25mm.

The bulk d-spacing values for E347 are highest in the repair FZ compared to the alternative E16.8.2 repair FZ and original condition in both LD and TD. In contrast, the ND d-spacing in original condition has peak values higher than the repair welds. However, the d-spacing is higher in the repair E347 FZ than E16.8.2 FZ. Additionally, the original HAZ TD d-spacing increases after repair welding using both fillers.

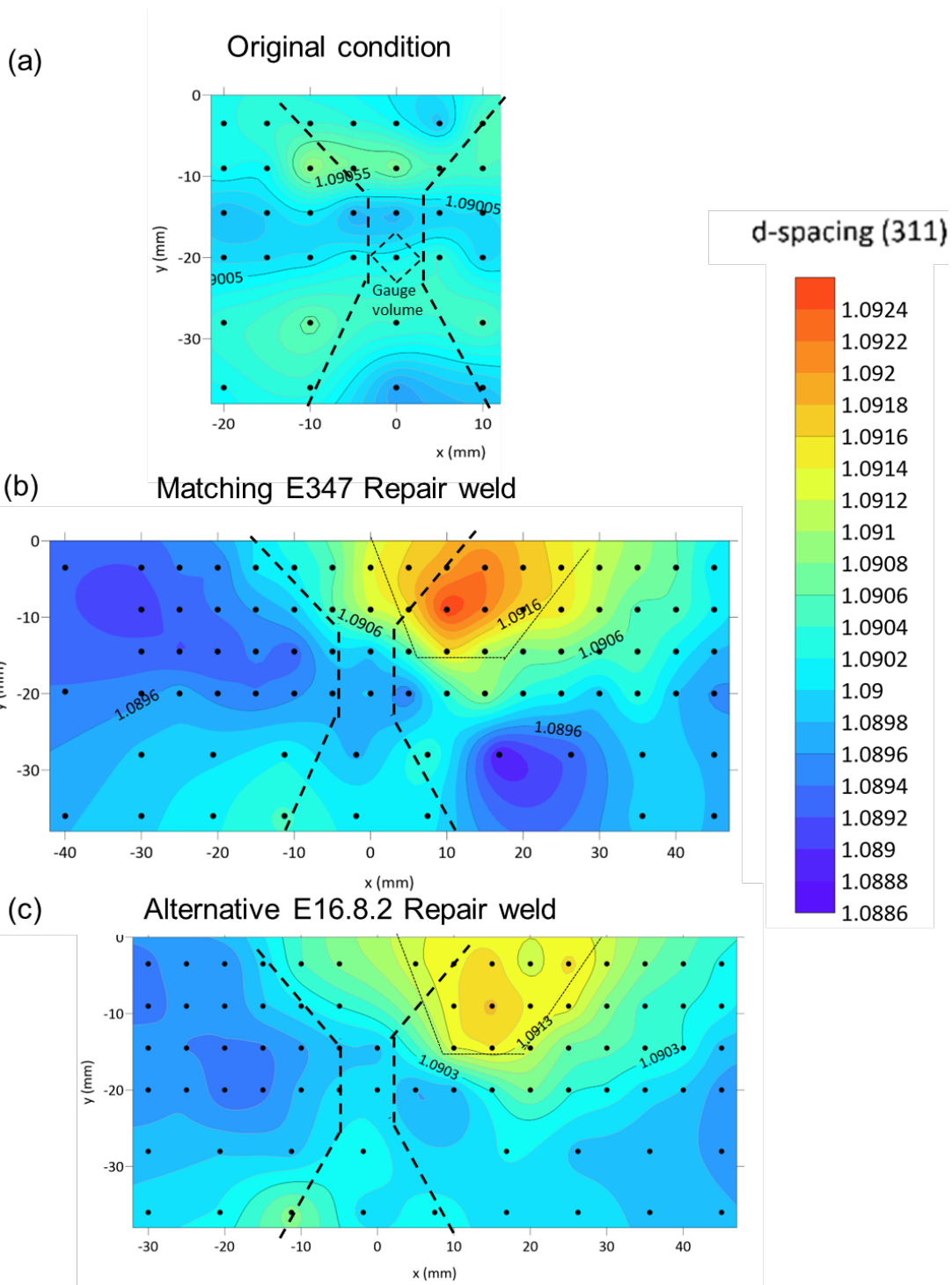


Figure 108. LD d-spacing results for (a) original weld, (b) matching E347 repair weld, and (c) alternative E16.8.2 repair weld

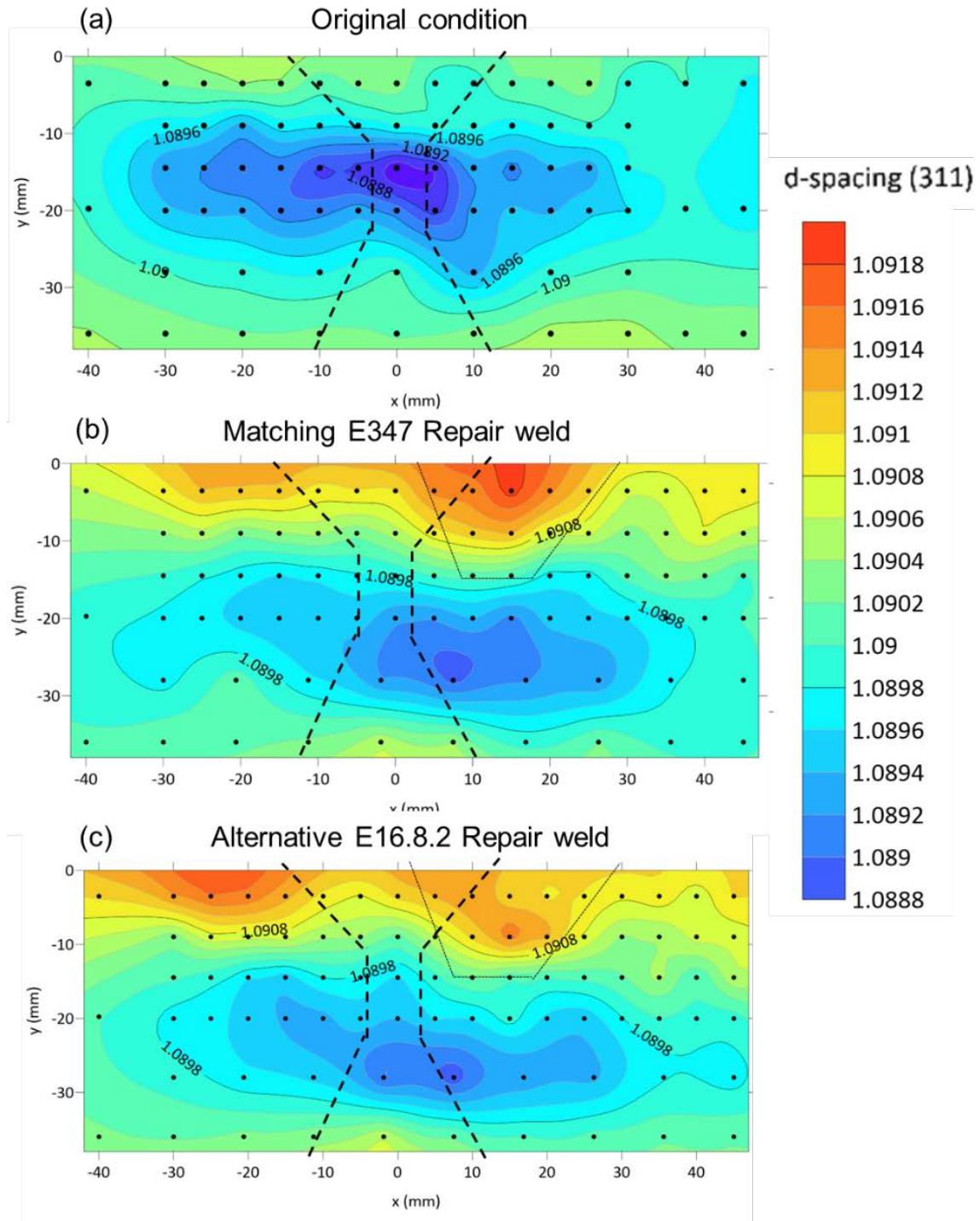


Figure 109. TD d-spacing results for (a) original weld, (b) matching E347 repair weld, and (c) alternative E16.8.2 repair weld

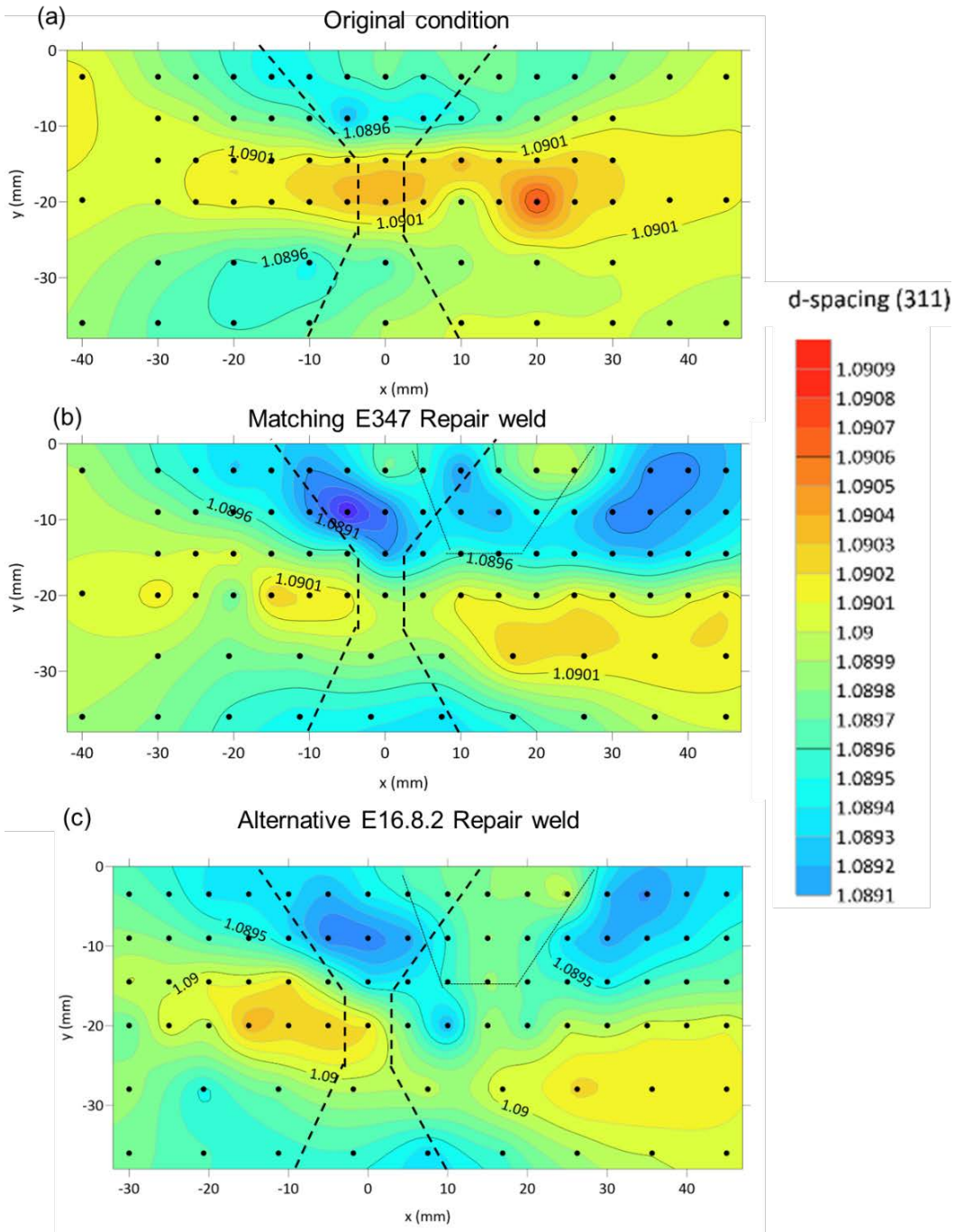


Figure 110. ND d-spacing results for (a) original weld, (b) matching E347 repair weld, and (c) alternative E16.8.2 repair weld

Residual Stress Calculations

The 3D residual stress profiles have been calculated to determine stress along the LD, TD, and ND. The strain for each direction is collected using (311) planes in FCC- γ austenite. The strain for each direction can be calculated using Eq. 4, and the stress for each direction can be calculated using Eq. 5 knowing the three directions of strain.

$$\varepsilon_{311} = \frac{d_{311} - d_{0,311}}{d_{0,311}} \quad (4)$$

$$\sigma_{x,311} = \frac{E}{1+\nu} \left(\varepsilon_{x,311} + \left(\frac{\nu}{1-2\nu} (\varepsilon_{x,311} + \varepsilon_{y,311} + \varepsilon_{z,311}) \right) \right) \quad (5)$$

where ν is Poisson's ratio (assumed 0.27) and E is Young's Modulus (assumed 197 GPa).

The original field condition residual stresses, as shown in Figure 111 (a-b), indicate LD and TD tensile stresses (maximum 180 MPa) on the surfaces and compressive stress (minimum -300 MPa) in mid-thickness of the double-V groove. The ND stresses are primarily mild tensile stresses (0-60 MPa) with similar mild compressive stresses on the top of double v joint as seen in Figure 111(c).

The same LD, TD, and ND stress profiles for the repair weld can be seen for matching E347 and alternative E16.8.2 in Figure 112 (a-c) and Figure 112 (d-f), respectively. The peak stresses, particularly LD and TD, increase in both the E347 and E16.8.2 repair weld, where the E347 repair contains higher peak tensile stresses in the repair FZ compared to E16.8.2. For both welds, the stress redistribution appears complex. For example, the TD stress increases in the original weld HAZ after repair welding in both fillers, which happens to be slightly higher in the E16.8.2 repair weld HAZ than the E347 repair weld HAZ. Overall, the E347 repair FZ has the highest LD and TD peak stresses compared to E16.8.2 repair FZ.

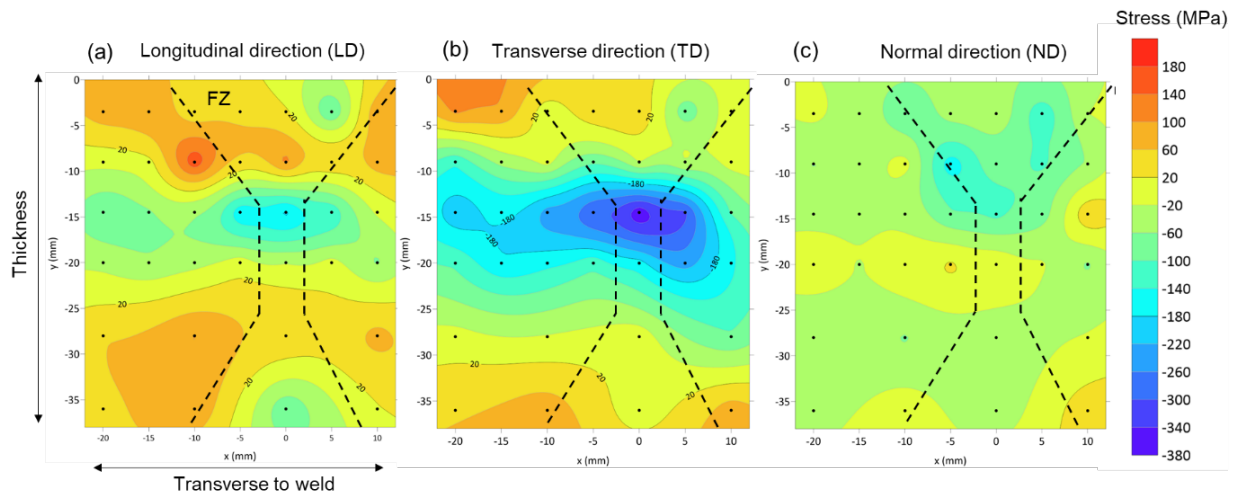


Figure 111. LD, TD, and ND stress measurements for original service weld

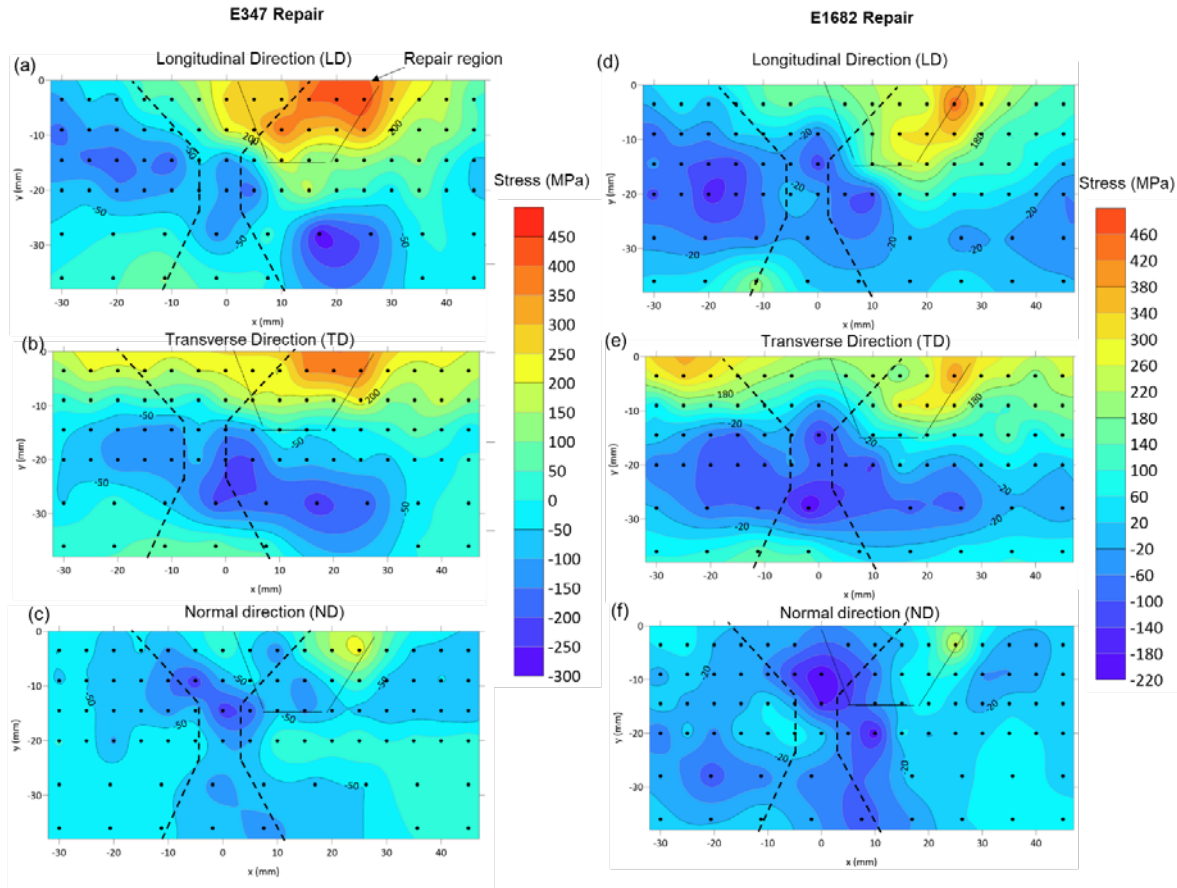


Figure 112. LD, TD, and ND stress measurements for E347 (a-c) and E1682 repair (d-f)

The calculated von Mises stress profiles are displayed in Figure 113. The original condition shows the highest stresses of ~ 220 MPa within the mid-thickness region, as seen in Figure 113 (a). The stress profile observed here can be similarly seen in earlier work completed on double-V groove FEM where the peak von Mises stresses are present in the mid-thickness of the weld joint [36]. The similar stress distribution provides some validation to the double-V groove model; however, the peak stresses are not comparable between the two scenarios (220 MPa vs. > 400 MPa in the as-welded FEM). The weld in Figure 113 (a) experienced approximately 3 years of service conditions at 565°C peak temperature before being examined, which might have contributed to peak stress reduction over a three-year period. Overall peak stresses in the E347 repair FZ exceed 400 MPa, which might be representative of peak stresses in the as-welded original condition (prior to service). The E16.8.2 has reduced peak stresses in the FZ compared to the E347 repair FZ. However, the stress in the original weld HAZ (top left of Figure 113 (c)) appears to be slightly higher using E16.8.2 repair than E347 repair, which indicates that SRC in HAZ after repair welding may not be mitigated by switching to E16.8.2 filler. The significant overall increase in residual stress from repair welding using a matching E347 filler may be a contributing factor for SRC occurring faster in service in repair welds (< 1 year) [4].

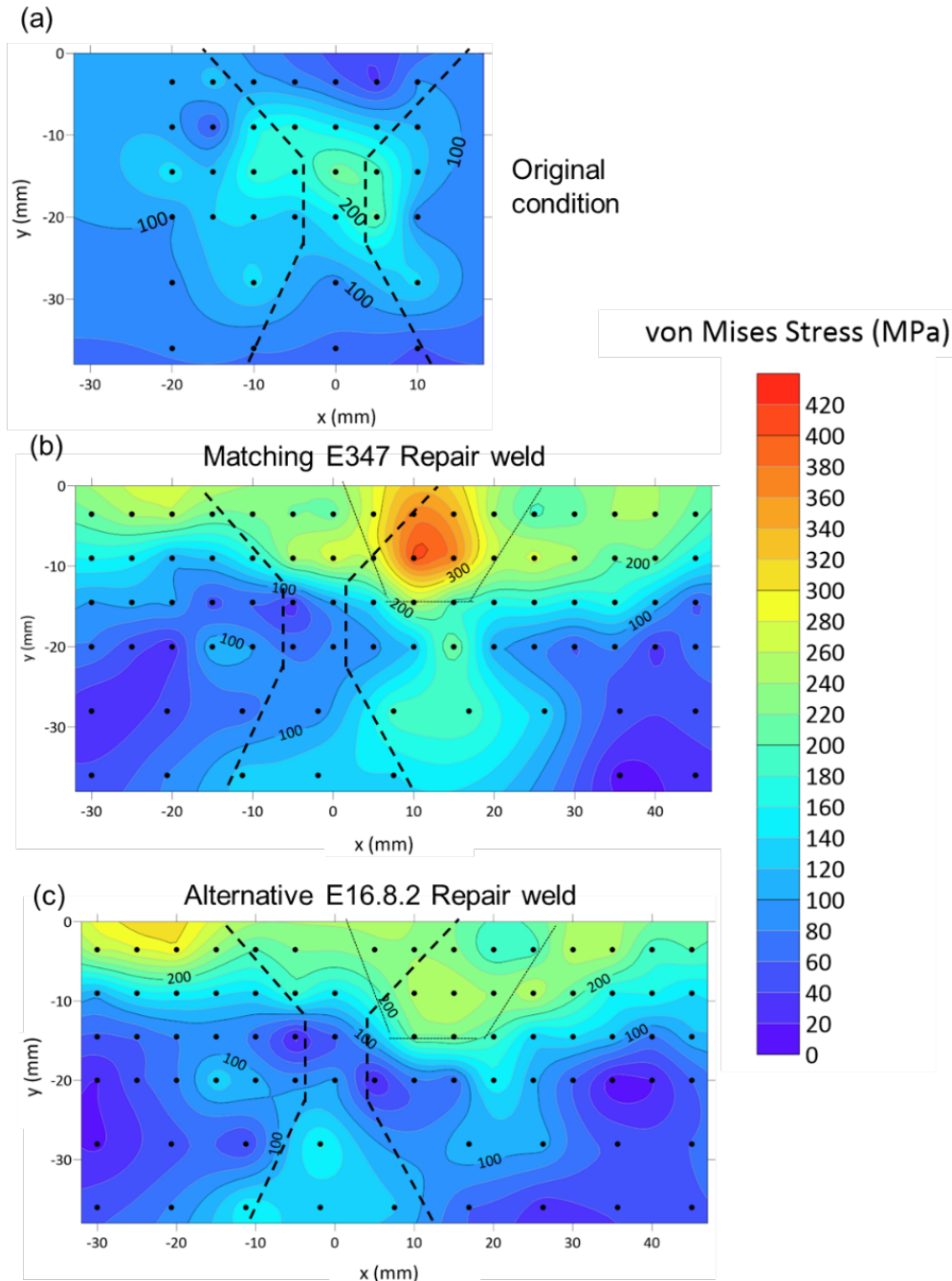


Figure 113. von Mises residual stress calculation from neutron diffraction, normalized to d_0 stress free samples for (a) original condition (serviced weld after 3 years), (b) matching E347 repair weld, and (c) alternative E16.8.2 repair weld

Lessons Learned From 2.2.1-2.2.2 (Field Welds)

The results from survey of the field welds in milestones 2.2.1-2.2.2 provided some key validation of SRC work in BP1 and 33458 with respect to lab-generated welds. Some key observations and interpretations are:

1. The original welds after service (at 565°C peak temperature in a 3 year period) have similar SRC susceptibility to the lab as-welded samples based on Gleeble SRC tests at 800 and 850°C.
2. Repair welds using matching filler E347 have similar susceptibility to cracking as original field samples but may fail at a faster time based on Gleeble SRC testing and even worse with increased weld residual stress after welding.
3. Repair welds using alternative filler E16.8.2 have more resistance to cracking, but HAZ or reheated FZ in E347 filler may still experience cracking based on a couple samples and lessons learned from 33458. Residual stresses are lower overall in the repair FZ along LD direction (parallel to weld direction) with E16.8.2 in comparison to E347. Residual TD strains/stresses in 347H SS HAZ are higher after repair welding using either fillers. The mechanism of increased SRC cracking susceptibility after repair welding (more rapid fracture) may be attributed to increase in HAZ residual stress after repair welding.

5 Significant Accomplishments and Conclusions

5.1 Conclusions

Milestone 1.1.1

1. One-sided insulation generated a 100°C temperature gradient through the 2” plate thickness, exceeding current code recommendations in AWS D10.10 (~ 55°C gradient). Issues of heater overload prior to reaching soak temperature was identified with one-sided insulation.
2. Two-sided insulation shows reasonable temp gradients in the 2” plate and meets the code recommendation without heater overload issue. FE simulations with two-sided insulation indicate full heat saturation within a 3-hour soak period at 950°C within the 2” thick plate.
3. The two evaluated heating rates, 111°C/hour and 222°C/hour, produced similar temperature gradients when reaching the peak soak temperature of 950°C. A heating rate of 111°C/hour doubles the heating time, even though soak times may be the same. For time efficiency purpose, 222°C/hour has been chosen for remaining efforts in this project.
4. FEA, using a validated temperature input, shows that reheat cracking can be controlled using a heating rate of 222°C/hr, a 950°C soak temperature, a 2-hr soak period, a maximum cooling rate of 139°C/hr, and back insulation by comparing stress evolution profile to threshold reheat cracking stress as a function of temperature.
5. Induction coils may be used but need to follow similar code requirements as ceramic heating.

Milestone 1.2.1: PWHT effect on crack susceptibility of lab weld samples

1. PWHT improves resistance to cracking, as evidenced with higher threshold SRC stress at temperature than the as-welded microstructure, and PWHT increases creep ductility due to a combination of stress relief and microstructure stabilization from PWHT.

Milestone 1.3.1: NDE techniques

1. NDE using phased array UT on the 12” x 12” x 2” thick 40 pass weld after PWHT from ST 1.1.1 was completed. Based on NDE, no defects along the whole 12” weld length within the detectable range were detected, indicating a pass for weld quality.
2. However, two major indications of 520 and 580µm defects were detected using optical microscope and these types of weld defects may allow for microcrack development in the HAZ, as seen with the 15-200µm crack lengths seen extending from the defects. These indications may facilitate SRC, which was not detected by the current state of the art technologies used in the field.
3. Some technology can detect finer defects but are limited to laboratory environments and not in-field testing

Milestone 2.2.1: Metallurgical characterization of fractured sample and old wall welds

1. Failure analysis of the hot storage tank wall sample:
 - a. The hot storage tank wall crack was likely induced from lack of fusion/penetration in the root of the repaired double-sided bevel butt joint upon further observation during repair procedure. Crack propagated from the mid-thickness to the surfaces.
 - b. Intergranular fracture was observed both within the HAZ and regions where the crack cut through the FZ, which limits the crack mechanisms to stress corrosion cracking and SRC. Secondary cracks, observed in the FZ ahead of primary fracture surface, occurred along δ -ferrite within the interdendritic regions of primary solidification grain boundaries, with Nb and Mo carbonitrides distributed discretely along surrounding grain boundaries and intragranularly.
 - c. On the other hand, secondary microcrack regions in the HAZ show only intragranular precipitates near the microcracks. No intergranular precipitation was observed.
 - d. While stress corrosion cracking (SCC) is a hypothesis among many, there needs to be evidence (not shown prevalently yet) supporting the Cr segregation with respect to the cracks. SRC may be more likely as the crack initiated from the mid-thickness to the surface, indicating that the internal crack was closed off from a corrosive environment until it reached the surface.

Milestone 2.2.1-2.2.2: Thermomechanical testing of E347-347H SS field wall welds and repair welds using alternative E16.8.2 and matching E347

1. SMAW repair welding procedures have been developed for mock repair assuming a sub-surface crack depth. The assumed depth of the crack is $\frac{1}{2}$ " and the total ground region needs to be a minimum of a 60° gouge with a gouge depth of $\frac{1}{8}$ " below the farthest depth of the crack. Mock repair welding experiments with matching E347 and alternative E16.8.2 filler have been completed using a 12 pass sequence, 70° single-V angle, and $\frac{5}{32}$ " root gap.
2. Repair weld samples using alternative E16.8.2 showed improved resistance to cracking, which is similar to previous lab sample experiments that showed little to no cracking with E16.8.2 filler. Within the field samples, cracking developed in the reheated E347 filler metal instead of the newly repaired sample with E16.8.2 filler. Repair weld samples using matching E347 showed similar or slightly worse crack susceptibility as the original service samples. Time to fracture was slightly faster in repair E347 samples than original service samples with matching E347 filler.
3. E16.8.2 repair introduced much lower residual stress in the FZ than E347 as evidenced by the neutron diffraction measurement, which further suppresses SRC, although the cracking susceptibility in HAZ may not be mitigated.
4. Original service field samples after PWHT show improvement in resisting cracking with no failure or extended time-to-failure at temperature. As observed within lab samples, the amount of stress relaxation during heating lowers the stress to below critical stress values, which reduces crack susceptibility. It should be noted that old service welds (3 years at 565°C) after PWHT show higher susceptibility than lab-control samples with no service history after PWHT.

Milestone 1.4.1: Cost-benefit analysis of PWHT for existing and/or newly fabricated hot-salt tanks

1. For existing tanks, the cost of a planned PWHT is $<1/5^{\text{th}}$ of the cost of experiencing a leak and having a forced outage for tank repairs in present day dollars.
2. There are concerns about failures occurring during PWHT of repair welds for existing tanks, but the benefits from this analysis can be applied to PWHT in new tanks as well.

Milestone 1.5.1: Protocols for updating ASME code on PWHT of 347H SS welds

1. Advisian believes a few ASME Code Revisions could be made.
2. Suggest DOE/NREL/CSM submit paperwork to ASME for spring 2024 meeting (Advisian can support, as a paid service, by being project manager and internal advocate within ASME).

Milestone 1.6.1: Cost estimate and technical feasibility of a Grade 92/347H clad Gen2 hot tank

1. For new tank construction, SS347H is significantly cheaper than using Gr92/347H clad tank. However, this tank is still susceptible to SRC unless PWHT is performed.
2. Alternative E16.8.2 filler needs further investigation in terms of (1) residual stress introduction to HAZ of SS347 to determine the need for PWHT, and (2) phase stability in service condition before recommended for new tank fabrication.

5.2 Key Takeaways

For Existing Tanks of 347H SS

1. PWHT may be feasible using 950°C as a peak temperature with a 222 °C/h heating rate based on FEM simulations and Gleeble susceptibility maps.
 - a. Gleeble results indicate improvement to crack resistance after PWHT of lab and original service weld (not repair).
 - b. PWHT is most effective for welds without repairs. However, localized PWHT model is needed on a whole tank floor to fully understand the stress redistribution.
 - c. PWHT on repaired welds may be challenging depending on the complexity of the weld joint (~75% effective with no cracking during PWHT). Repair welding prior to PWHT further enhances SRC susceptibility during PWHT.
2. Weld inspection NDE using phased array UT should be performed after welding, PWHT and repair. If feasible, periodic examination (e.g., on an annual base) is recommended.
3. E16.8.2 is less susceptible to SRC than E347 and may be best at resisting cracking since it introduces significantly lower peak residual stresses and less susceptible microstructure in FZ. FZ of E347 repairs are expected to be the most susceptible location for cracking during PWHT or service due to the high tensile stresses (e.g., > 100 MPa higher than HAZ). E16.8.2 would be recommended to use for fresh and repair welds. However, the HAZ of repair welds using either of these two fillers may still be susceptible to cracking.

For Future Tanks Being Manufactured With 347H SS

1. Weld design should be optimized, including floor plate layout, weld procedure, and joint geometry to minimize residual stress.
2. Evaluate alternative E16.8.2 filler with higher resistance to SRC (Note: Need to further evaluate phase stability under service condition).
3. PWHT, during manufacturing and prior to service, may still be needed (HAZ is still susceptible).
 - a. PWHT is challenging in fully constructed tank due to mechanical constraint. PWHT would be most effective when applied during construction to minimize distortion and residual stress. For example, the floor should undergo PWHT during assembly and prior to welding to the walls. The PWHT design would then not be limited to access issues in a fully constructed tank, i.e., challenge of backside insulation in floor due to concrete foundation.
 - b. Crack susceptibility during PWHT would be lower in original, new welds vs. repair welds. Therefore, PWHT should be considered in the construction costs to ultimately provide low residual stress weld components prior to service. The life of these components would be improved significantly compared to repair welds that re-introduce higher residual stresses.

For Future Tanks

1. Consider alternative tank materials (e.g., NUCL 167 SPH (316L w/B)) with lower SRC susceptibility (design needs to be considered)
2. PWHT may not be necessary in SRC resistant alloys, except if microstructural stability is needed to ensure the minimum mechanical properties and weldability challenges are met.

General

1. Reduce use of flux-based processes (SMAW) to reduce slag inclusions. Instead, utilize gas tungsten arc welding for all root pass welds and a low heat input arc pulsation/oscillation gas metal arc welding method for filler passes.
2. Overall, lower weld heat input (e.g., <150 Amps) reduces HAZ width and grain size (coarser grains help facilitate cracking in HAZ).
3. Maintaining minimum PWHT temperature gradient recommendations based on AWS D10.10 are critical to reduce crack susceptibility. Excessive gradients may facilitate cracking during PWHT.

6 Budget and Schedule

TWP Item Number (Tasks, Subtasks, and Milestones)	Item Description	Item Performer	Planned (Quarters by Fiscal Year. FY21 Starts 10/1/2020)												End Date or Accomplishment Date	
			Start Date	FY2021				FY2022				FY2023				
				Q3	Q4	Q1	Q2	Q3	Q4	Q1	Q2	Q3	Q4			
T-1.1	Determine heat transfer limitations of each PWHT method	CSM lead, Worley/NREL support	04/01/21	X	X	X									12/31/21	
ST-1.1.1	Identification of heating and cooling rate and temperature gradient limitations with ceramic pad for industrial scale application.		04/01/21	X											6/31/2021	
ST-1.1.2	Identification of heating and cooling rate and temperature gradient limitations with induction heating for industrial scale application.		04/01/21	X	X	X									12/31/21	
M (T-1.1.1)	Recommend the most feasible and economic heating method for commercial applications with acceptable temperature gradient within thick welded curvilinear plates.		N/A			X								12/31/21		
T-1.2	Identify PWHT effects on cracking susceptibility	CSM lead, Worley/NREL support	07/01/21		X	X	X	X						09/30/22		
ST-1.2.1	Coupons will be extracted from the welded thick plates before and after PWHT for reheat cracking test to demonstrate the improved ductility at service temperature. Metallurgical characterization will also be performed to characterize the microstructure before and after PWHT.		07/01/21		X	X	X	X	X					09/30/22		
M (T-1.2.1)	Demonstrate the effectiveness of PWHT on restoration of hot ductility of heat-affected zone and weld metal.		N/A						X					09/30/22		
T-1.3	Identify detection capability of phased array UT technique	CSM lead, Worley/NREL support	07/01/21		X	X	X	X						09/30/22		
ST-1.3.1	Identify the resolution limit of phased array UT on weld discontinuities and defects before and after PWHT.		07/01/21		X	X	X	X	X					09/30/22		
M (T-1.3.1)	Based on the ASTM standard, recommend commercial practice for NDE procedures for 347H SS thick-section welds.		N/A						X					09/30/22		
T-1.4	Cost-benefit analysis of PWHT	Worley lead	07/01/21		X	X	X	X	X	X	X			12/31/22		
ST-1.4.1	Provide preliminary cost-benefit analysis for different weld rods, heat inputs, and different PWHT methods. Include an opportunity cost and risk analysis of losing income with a plant shut down and repair costs due to a low life-cycle weld that cracked in service.		07/01/21		X	X	X	X	X	X	X			12/31/22		
M (T-1.4.1)	Provide a cost-benefit analysis for the justification of important mitigation solutions.		N/A								X			12/31/22		
T-1.5	Protocols for updating ASME code on PWHT of 347H SS welds.	Worley lead ASME, NREL/CSM lead paper prep	07/01/21		X	X	X	X	X	X	X			12/31/22		
ST-1.5.1	The technological information generated from the SRC project and this current project will generate a journal publication on application of mitigation solutions for high temperature molten salt tanks. Engage in discussions with ASME committees about recommending practice for PWHT in 347H SS thick-section welds for high temperature operation, and offer recommended path forward for code case/changes.		07/01/21		X	X	X	X	X	X	X			12/31/22		
M (T-1.5.1)	Recommend commercial practice for localized PWHT protocols for 347H SS thick-section welds in Gen2 CSP systems.		N/A								X			12/31/22		
T-1.6	Evaluate cost and feasibility of P92/347H clad Gen2 hot tank	Worley/CSM/ NREL	10/01/21			X	X	X	X	X	X			12/31/22		
ST-1.6	Perform cost estimate and feasibility of a Grade P92/347H clad Gen2 hot tank, and compare vs. baseline 347H tank.		10/01/21			X	X	X	X	X	X			12/31/22		
M (T-1.6.1)	Provide recommendation for technoeconomic solution while reducing cracking susceptibility.		N/A								X			12/31/22		
T-2.2	Evaluate cost and feasibility of P92/347H clad Gen2 hot tank	CSM/NREL	07/01/22						X	X	X	X	X	06/30/23		
ST-2.2	Characterize samples of both floor and wall weldments from formerly in-service CSP hot tank		07/01/22						X	X	X	X	X	06/30/23		
M (T-2.2.1)	Metallurgical characterization of hot storage tank field samples		07/01/22						X	X	X	X	X	12/31/22		
M (T-2.2.2)	Thermomechanical testing of field sample tank weldments		07/01/22						X	X	X	X	X	06/30/23		

Spending Summary by Budget Category							
Budget Categories	Approved Budget per SF-424A				Actual Expenses		
	BP 1	BP 2	BP 3	Total	This Quarter	Cumulative	%
a. Personnel	\$40,941	\$70,292	\$11,900	\$ 123,133	\$ 2,181	\$121,180	98%
b. Fringe Benefits	\$0	\$0	\$0	\$ -	\$ -	\$0	
c. Travel	\$0	\$0	\$0	\$ -	\$ -	\$0	
d. Equipment	\$0	\$0	\$0	\$ -	\$ -	\$0	
e. Supplies	\$0	\$0	\$0	\$ -	\$ -	\$0	
f. Contractual	\$137,836	\$167,944	\$79,758	\$ 385,538	\$ 27,654	\$375,512	97%
g. Construction	\$0	\$0	\$0	\$ -	\$ -	\$0	
h. Other	\$0	\$12,900	\$3,429	\$ 16,329	\$ 866	\$12,401	76%
i. Total Direct Charges	\$ 178,777	\$ 251,136	\$ 95,087	\$ 525,000	\$ 30,701	\$ 509,092	
j. Indirect Charges	\$ -	\$ -	\$ -				
k. Total Charges	\$ 178,777	\$ 251,136	\$ 95,087	\$ 525,000	\$ 30,701	\$ 509,092	
DOE Share	\$ 178,777	\$ 251,136	\$ 95,087	\$525,000	\$ 30,701	\$ 509,092	97%
Cost Share				\$0			
Cost Share Percentage	0%	0%	0%		0%	0%	

Project Spend Plan			Federal Share		
Quarter	From	To	Initial Plan	Actuals & Updated Plan	Cumulative
1	10/01/20	12/31/20	\$44,694.25	\$22,626.66	\$22,626.66
2	01/01/21	03/31/21	\$44,694.25	\$30,123.39	\$52,750.05
3	04/01/21	06/30/21	\$44,694.25	\$71,583.82	\$124,333.87
4	07/01/21	09/30/21	\$44,694.25	\$54,442.62	\$178,776.49
5	10/01/21	12/31/21	\$62,784.00	\$98,633.54	\$277,410.03
6	01/01/22	03/31/22	\$62,784.00	\$93,557.67	\$370,967.70
7	04/01/22	06/30/22	\$62,784.00	\$ 23,882.97	\$394,850.67
8	07/01/22	09/30/22	\$62,784.00	\$ (41,800.00)	\$353,050.67
9	10/01/22	12/31/22	\$ 31,695.67	\$ 57,316.44	\$410,367.11
10	01/01/23	03/31/23	\$ 31,695.67	\$ 57,316.44	\$467,683.56
11	04/01/23	06/30/23	\$ 31,695.67	\$ 57,316.44	\$525,000.00
Totals			\$525,000.00	\$525,000.00	\$525,000.00
			Updated Federal Spend Plan		

7 Path Forward

With respect to PWHT effectiveness on SRC reduction and the concern for weldability concerns still in the HAZ with both fillers, some future work that would help verify PWHT effectiveness could be to:

1. Model, using FE, the PWHT procedure, same as 2” thick single-V welds, on constrained floor welds (1/2” thick maximum with no backside insulation) to determine if cracking would be predicted based on stress threshold maps.
 - a. Model residual stress and deformation in floor welds as a function of thickness and number of weld passes. Weld parameters (volts, amperage, travel speed), weld pass sequence, weld direction, and weld process would be some important components to study with respect to residual stress and deformation. Performing PWHT on the various models would provide guidance for weld parameter optimization, including determining the need for insulation on backside of weld, particularly maintaining required thermal gradients and determining if stress relaxation is sufficient to prevent cracking.
2. Perform creep testing on as-welded vs. PWHT weld samples at service-related temperatures (e.g., 565°–800°C) to verify PWHT as having better creep life than as-welded condition.

With lessons learned of the austenite stability of E16.8.2 from elevated temperature, a couple key future works could be focused on:

1. Effect of service temperatures and extended periods of time (e.g., 565°C, 1,000 hr) on weld microstructure and possible long-term thermal embrittlement and corrosion resistance, such as development of α -ferrite and sigma phase.
 - a. Microstructure and corrosion test study
2. Low stress creep testing of E16.8.2-347H SS welds at 565°C for minimum 1,000 hr to determine the effect of both stress and aging on microstructure.
3. Creep testing of E16.8.2 and E347 weld microstructures at temperature range from 565°C to 800°C to capture service representative data and to verify the creep life expectancy, with the hypothesis that E16.8.2 has better creep life (i.e., creep ductility) using the same load conditions for all temperatures. This proposed work would benefit and add on to the story of higher temperature SRC testing completed in this current work such that the wide temperature range of 565°C–1,050°C is investigated, both for service and PWHT purposes. The limitation of SRC testing at lower temperatures is the lower strain rates in contrast to creep testing. Additionally, isothermal creep testing would provide additional creep parameters, which are useful for modeling efforts on life prediction.
4. Since the HAZ of 347H SS welds may still be susceptible to cracking, either during PWHT or in service, other 3XX substrates with acceptable operating maximum allowable stress for 565°C could provide materials with improved resistance to elevated temperature SRC, such as 316L w/N and B additions.

8 Inventions, Patents, Publications, and Other Results

Paper Publications

Below is a list of publications that are currently under writing regarding the contents of this project report (37373) and previous project (33458):

37373

1. PWHT modeling Paper (Milestone 1 tasks)-Chen Ni as primary author
2. Neutron paper (residual stress and precipitate analysis)-Tim Pickle as primary author
3. Gleeble field sample paper (Milestone 2 tasks)-Tim Pickle as primary author

33458

1. T. Pickle, Y. Hong, J. Vidal, C. Augustine, Z. Yu., “Stress Relaxation Cracking Susceptibility Evaluation in 347H Stainless Steel Welds”, *Welding in the World*. Submitted August 2023.
2. Y. Hong, T. Pickle, J. Vidal, C. Augustine, Z Yu., “Impact of Plate Thickness and Joint Geometry on Residual Stresses in 347H Stainless Steel Welds”, *Welding Journal*, November 2023.
3. T. Pickle, Y. Hong, J. Vidal, C. Augustine, Z. Yu., “Stress Relaxation Cracking in 347H Weldments: Susceptibility Evaluation of Heat-Affected Zone”, submitting to *Nature: Material Degradation* October 24, 2023.
4. T. Pickle, Y. Hong, J. Vidal, C. Augustine, Z. Yu. “Stress Relaxation Cracking in 347H Weldments: Susceptibility Evaluation of E347 and E16.8.2 Fusion-Zone”, (2023 submittal)

Conference Proceedings

The following oral and poster presentations have been completed over the duration of this project and are tabulated in Table 27 .

Table 27. Conference proceedings throughout duration of project

Full Author List	Paper Title	Session/Conference	Conference Location	Date
T. Pickle, Y. Hong, J. Bunn, E. A. Payzant, C. Augustine, J. Vidal, Z. Yu.	Stress Relaxation Cracking Susceptibility in 347H SS Welds and Their Repairs	FABTECH/AWS Professional Program	Chicago, Il.	Sept. 13, 2023
Z. Yu, T. Pickle, Y. Hong, J. Vidal. C. Augustine.	Stress Relaxation Cracking Susceptibility Evaluation in 347H Stainless Steel Welds	International Institute of Welding (IIW) Annual Conference	Singapore	July 2023
Z. Yu, T. Pickle, Y. Hong, J. Vidal. C. Augustine.	Residual Stress and Stress Relaxation Cracking Susceptibility in Stainless Steel Welds	SHUG Conference	Oak Ridge National Laboratory	June 2023
Z. Yu, T. Pickle, Y. Hong, J. Vidal. C. Augustine.	Stress Relaxation Cracking and Post Weld Heat Treatment in Gen2 347H Tanks	Virtual Workshop CSM Gen2 Hot Tank Reliability	Hosted by National Renewable Energy Laboratory (NREL), Golden, CO.	March 28, 2023
Z. Yu, T. Pickle, Y. Hong, J. Vidal, C. Augustine.	Stress Relaxation Cracking Susceptibility Evaluation in 347H Stainless Steel Welds	International Institute of Welding Sub-commission II-C Testing and Measurement of Weld Metal, 2023 Intermediate Meeting	Technical University of Munich, Munich, Germany	March 7, 2023
Z. Yu, T. Pickle, Y. Hong, C. Augustine, J. Vidal.	Stress Relaxation Cracking & Mitigation Solutions for Hot Tank Welding	Seminar in the Department of Mechanical and Aerospace Engineering	University of Central Florida.	Dec. 2, 2022
Z. Yu	Risk Analysis and Mitigation Solutions for Failures in Stainless Steel Welds	Seminar in the Department of Materials Science and Engineering	The Ohio State University	Oct. 3, 2022
Z. Yu	Crack Susceptibility in 347H SS Welds and Potential	International Materials, Applications & Technologies (IMAT) 2022	New Orleans, Louisiana	Sept. 12-15, 2022

Full Author List	Paper Title	Session/Conference	Conference Location	Date
	Mitigation Solutions			
Z. Yu, T. Pickle, Y. Hong, C. Augustine, Judith Vidal	Mechanical Failure Risk Analysis in Stainless Steel Welds	Monthly seminar series hosted by the high temperature steering committee, presented to the Neutron Scattering Division	Oak Ridge National Laboratory	Sep. 1, 2022
Z. Yu	Stress Relaxation Cracking (SRC) and Tank Welding	Kicking-off Webinar on Concentrating Solar - Thermal Power Process Enhancement and Refinement for Operations, Reliability, and Maintenance (CSP PERFORM)	DOE Solar Energy Technology Office	May 12, 2022
Z. Yu	Effects of Microstructures and Residual Stress on Weld-Related Failures	Seminar at Mechanical Engineering Department at Virginia Tech	Blacksburg, Virginia	November 5, 2021
T. Pickle, Y. Hong, J. Vidal, C. Augustine, Z. Yu	Crack Susceptibility in 34H Welds and Potential Mitigation Solutions	AWS Fabtech	Virtual	September 2021
T. Pickle, Y. Hong, J. Vidal, C. Augustine, Z. Yu	Mitigation of Stress Relaxation Cracking in Hot Thermal Energy Storage Tanks Welds	Solar Paces 2021	Virtual	September 29, 2021
T. Pickle, Y. Hong, J. Vidal, C. Augustine, Z. Yu	Preventing Stress Relaxation cracking in Stainless Steel Thermal Energy Storage Tank Welds for Elevated Temperature Service	Turbine Joining Forum	Golden, CO	October 5-7, 2021

Appendix: PWHT Memorandum to Crescent Dunes

MEMORANDUM

TO: Ilias Nikolaidis (Crescent Dunes Plant Manager) and Tomás Fanjul Benito (ACS)

FROM: Prof. Zhenzhen Yu and Tim Pickle (Colorado School of Mines)

SUBJECT: Repair Welding and PWHT Procedures for Cracked Floor Welds

DATE: 2023-04-21

Introduction:

This memo discusses the details associated with repair welding and PWHT recommendations for 347H SS floor welds, which referenced AWS 10.10 “*Recommendations Practices for Localized Heating in Piping and Tubing*” [43], WRC 452 “*Recommended Practices for Local Heating of Welds in Pressure Vessels*” [45], and ASME section VIII (subsection B) [42]. Based on research completed and knowledge learned with using matching E347 filler, PWHT seems to be the main solution in 1) reducing weld residual stress and thus reducing total effective stresses during service (internal + external), and 2) metallurgical recovery and stabilization. The ASME code contain the basic rules and thermal gradients during PWHT and definition of the soak band (SB), while AWS D10.10 and WRC 452 provide more detailed information of transverse gradients and definitions of the surrounding regions of the soak band, which include the heated band width (HB-the width of the ceramic resistant heat pads) and gradient control band (GCB), which is the region of surrounding welds and base metal that includes insulation to provide temperature gradient control of approximately 50°C/in Repair welding recommendations are briefly included as well.

Repair welding recommendations in addition to normal weld procedures:

1. Based on CSM Gleeble-SRC results, using alternative filler, E16.8.2, reduced cracking susceptibility in 347H SS welds, as E16.8.2 filler is more ductile. If E347 is used, PWHT is recommended.
2. Grinding procedures should include a dedicated transient region on each end of the crack. For instance, if the crack is 10” long for a ½” thick weld, you would want to repair weld an inch at the beginning and end of the crack to get an approximate 12” long repair weld. Therefore, grinding out the crack and 1” of non-crack regions on each end helps provide a smooth transition, instead of initiating your weld start/stop where the crack starts/ends. Higher thickness would require slightly longer transient lengths.
3. Add dwell time (~2s) at weld start to prevent lack of fusion in transient regions.
4. Maximum interpass temperature should be roughly ~150°C, measured within the FZ and HAZ regions. Thermocouples or temperature-indicating crayons should be used to measure temperature if possible.

PWHT Parameter Recommendations:

There are a few options as to how PWHT could be performed. In all cases, heating and cooling rates are extremely important in reducing steep temperature gradients in surrounding colder material:

1. Data from literature [2, 25] indicate an 80% residual stress reduction when PWHT is conducted at a soak temperature of 900°C. However, moderating stress via temperature control during heating is critical to prevent cracking during this procedure based on CSM results. Soak temperature of 950°C is therefore recommended and has been demonstrated effective in both stress relief and avoiding stress relaxation cracking during and after PWHT in our study.
2. Based on CSM’s study, a two-step method with a 950°C soak temperature is recommended.
 1. First step (initial holding for temperature stabilization): 600°C for a short amount of time (~30 min – 1 hr) to help stabilize temperature gradients. Heating rates to 600°C is less critical than the second step, but still important as time helps with temperature stabilization.
 2. Second step (stress relief and microstructural stabilization): ramp up to 950°C with a 111 (safer but slower)-222°C/hr heating rate and soak for approximately 1-2 hr. The temperature provides sufficient stress relief and stabilization of precipitates. Heating rate cannot exceed 222°C/hr A faster heating rate may lead to stress relaxation cracking during PWHT.
 3. Cooling rate from 950°C should be a maximum of 222°C/hr/thickness (in). If the thickness of the welded plates and the backing plates are approximately at 1” total, a 222°C/hr would be approximately the maximum. The cooling rate can be controlled with the ceramic resistant pads and should be controlled when cooling from 950°C to 427°C. Below this temperature, the cooling rate is not limited based on code. However, it is recommended to make sure the cooling conditions are conservative to avoid excessive temperature gradients (maximum of 50°C/in).

Reference PWHT guidelines for heating and cooling rates in the soak band as a function of thickness are listed in Table 28.

Table 28. Heating and Cooling Rate Recommendations for PWHT

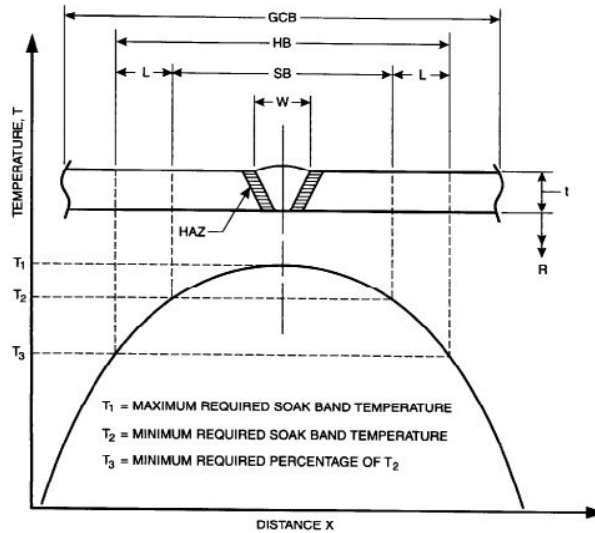
Fabrication Code	Maximum Heating Rates	Maximum Cooling Rates	Ranking of Rates
B31.1	333°C/hr/0.5t (inches) above 316°C (333°C/hr/ max)	333°C/hr/0.5t (inches) 2 in thickness above 316°C → 333°C/hr	Maximum allowable rates
ASME Section VIII Subsection B	222°C/hr/t (in) above 427°C (222°C/hr/ max)	222°C/hr/t (in) above 427°C (222°C/hr/ max); 55°C/hr minimum	Lowest allowable rates
AWS D10.10	444°C/hr/t (in) using heat band width recommendations	278°C/hr/t (in) using heat band width recommendations	Intermediate rates

Localized PWHT Details:

Figure 114 displays the regions for localized PWHT adapted in AWS D10.10 code “*Recommended Practices for Localized Heating of Welds in Piping and Tubing*”. This code discusses more in detail the specifics for localized PWHT which ASME codes are limited on. The method of heating that is commonly used are ceramic heating pads with refractory ceramic fiber (RCF) as insulating material due to the maximum allowable temperature usage of 1093°C. Other insulating materials, such as mineral wool, break down above 650°C. Induction heating may be used, but the same guidelines in both AWS D10.10 and ASME Section III should be applied for both ceramic heating pads and/or induction coils. CSM performed PWHT using ceramic heating pads with insulations on both top and bottom surfaces. For tank floor, at least insulation on top surface is recommended.

Three regions of importance, in mitigating temperature gradient issues, are:

1. **Soak band: Region that** includes the region of interest (most affected residual stress region) and the designed peak soak temperature, which is at a minimum four times the thickness and the weld width ($4t+w$). Based on the code recommendation, if the thickness of the plates is 13/32” thick with an inch wide FZ, the width of the soak band would be at least 3” centered on the repair weld. *Based on CSM’s simulation study, the area with residual stress above 100MPa can be as wide as 5.5 inches (~140 mm) with weld in the center for tank floor welds. Therefore, the soak band width is recommended to be no less than 5.5 inches. As peak soak temperature is 950°C, the minimum temperature on the edge of the soak band should not be below 895°C. Essentially, the width of this soak band should encompass the fusion zone, the heat affected zone (HAZ) and some base metal.*
2. **Heated band:** Region that includes the width and length of the heat resistant ceramic pads used to ensure temperature gradients are maintained well within the soak region. Since the maximum heating is present in the center of the heat pad (which is the soak band width), a certain width of the heated pad needs to be designed to reduce the temperature gradients present away from the center of heat. This width is usually needed to make sure that a $\sim 50^\circ\text{C}/\text{in}$ maximum temperature gradient is maintained, and that the edge temperature of the heated pad be greater than half (450°C) of the edge temperature of the soak band (895°C). A heated band with a width about 22 inches or more is therefore recommended, i.e., approximately 8 inches wide on each side of the soak band edge. Same consideration needs to be given for heated band length calculation along the weld direction.
3. **Gradient control band:** The gradient control band would be the width of the insulation that lies on top of the ceramic heating pads and surrounding exposed metal, which is about double the length and width of the heat pad surface area. It assists to regulate the temperature gradient away from the heat pad. AWS D10.10 and WRC 452 recommends a maximum 55°C temperature gradient through thickness. These standards provide more details on this region with respect to the different pressure vessel geometries.



Nomenclature:
W = Widest width of butt or attachment weld.
HAZ = Heat-affected zone.
SB = Soak band (width of the volume of the material where the holding temperature equals or exceeds the minimum and equals or is below the maximum required. The minimum width is typically specified as W plus a multiple of t on each side of the weld).
L = Minimum distance over which the temperature may drop to a percentage of that at the edge of the soak band.
HB = Heated band (width of heat source).
GCB = Gradient control band (minimum width of insulation and/or gradient heat source).
t = Nominal thickness of piping, branch connection, nozzle neck, or attachment.
R = Inside radius of piping, branch connection, or nozzle neck.

Figure 114. Schematic for PWHT conditions, including soak band, heated band and gradient control band

In field operation, multiple heat pads may be necessary to generate the required band widths and lengths as illustrated in Figure 115. Thermocouples should be used around the heated band and soak band to ensure proper temperature gradient control.

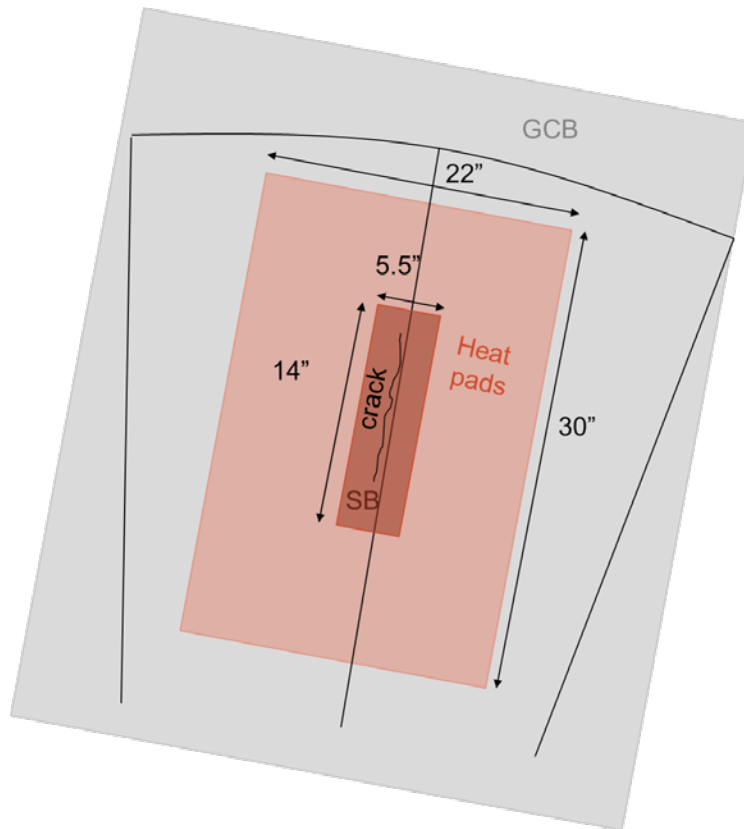


Figure 115. Rough schematic of soak band (SB), heat band (HB) or heat pads, and gradient control band (GCB)

Extra Information:

1. NDE inspection is recommended to check on defects such as lack-of-fusion repair and cracks potentially induced by PWHT.
2. If wrinkles (bulging) are observed on the floor, PWHT is recommended for both the wrinkled area and the nearby weld region to avoid further development of SRC.

Concerns with PWHT on Foundation: Discussions have come up during the recent workshops on Gen2 CSP pertaining to the concerns of PWHT on the integrity of the foundation floor, particularly if a 950°C peak temperature is used. Three concerns arise from this: 1) steam bubble formation in the concrete foundation that may cause cracking in the foundation; 2) if the salt is saturated in foundation material, a 950°C temperature would decompose the salt to a mix of nitrides and oxides, in which the oxides may be chemically aggressive and lead to high metal loss rates in the 347H SS floor; and 3) if the foundation material is expanded clay and salt is saturated within from the leak, the high temperature generated from the PWHT may chemically break down the clay from one oxide to another, which can lead to the production of nitric oxide (NO_x) that is dangerous to the staff involved and the surrounding environment.

Literature PWHT Parameters: For your reference, in literature a three-step heat treatment has been used in industry and has been claimed to be more beneficial than a single-step soak temperature and less susceptible to reheat cracking, primarily due to the addition of a lower temperature first step.

- a. First step (initial stress relief): 600°C for 2hr for each inch of thickness to help stabilize temperature gradients. Heating rates for this first step is less critical, but still important as time helps with temperature stabilization. Typically, heating and cooling rates below 427°C can be as fast as possible per ASME Section III-subsection NB.
- b. Second step (solutionizing): ramp up to 1,050°C with a 111-222°C/hr and soak for approximately 1 hr Heating rates are extremely critical here, both from a temperature gradient and cracking susceptibility perspective. Shorter heating rates help with temperature gradients, but too much time at temperature within the reheat cracking regime could lead to cracking. The heating rate should be limited to 222°C/hr for all thickness. NOTE: based on CSM's study, 1,050°C may introduce very fast SRC cracking during PWHT.
- c. Third step (precipitate stabilization): Controlled cooling to 950°C at about 90-180°C/hr and hold for one hour per inch to facilitate precipitation of Nb (C, N) and tying up C to prevent Cr depletion (Cr carbides). Stress should be relieved from step two, and thus reheat cracking is negligible in this step. After the temperature is sufficient, cooling rates should be limited to 222°C/hr per inch of thickness, but should not go above this rate for any thickness below one inch.

References

- [1] M. Mehos, C. Turchi, J. Vidal, M. Wagner, Z. Ma, C. Ho, *et al.*, "Concentrating Solar Power Gen3 Demonstration Roadmap," NREL/TP-5500-67464 2017.
- [2] J. R.D. Thomas and R. W. Messler, "Welding Type 347 Stainless Steel-An Interpretive Report," *Welding Research Council Bulletin*, vol. Bulletin 421, 1997.
- [3] R. D. Thomas, Jr., "HAZ Cracking in Thick Section of Austenitic Stainless Steels-Part 2," *Welding Journal*, 1984.
- [4] H. van Wortel, "Control of Relaxation Cracking in Austenitic High Temperature Components," presented at the NACE Corrosion, Nashville, TN, 2007.
- [5] E. C. B. Dillingh, A; Aulbers, A.P., "Stress Relaxation Cracking-Augmented Recommended Practice," TNO2016.
- [6] R. Kant and J. N. DuPont, "Stress Relief Cracking Susceptibility in High-Temperature Alloys," *Welding Journal*, vol. 98, pp. 29-49, 2019.
- [7] J. Lippold and D. Kotecki, "Ch. 6 Austenitic Stainless Steel," in *Welding Metallurgy and Weldability of Stainless Steels*, ed: John Wiley and Sons, Inc., 2005.
- [8] R. D. Thomas, Jr. and R. W. Messler, "Welding Type 347 Stainless Steel- An Interpretive Report," WRC Bulletin1997.
- [9] ASTM, "A240/A240M-20a: Standard Specification for Chromium and Chromium-Nickel Stainless Steel Plate, Sheet, and Strip for Pressure Vessels and for General Applications," ed, 2021.
- [10] B. S. Amirkhiz, S. Xu, J. Liang, and C. Bibby, "Creep properties and TEM characterization of 347H stainless steel," presented at the 36th Annual Conference of the Canadian Nuclear Society and 40th Annual CNS/CNA Student Conference, Toronto, ON, Canada, 2016.
- [11] ASME, "Boiler and Pressure Vessel Code," in *II-Part D: Materials*, ed, 2019.
- [12] AWS, "A5.9/A5.9M," in *Welding Consumables-Wire Electrodes, Stripe Electrodes, and Rods for Arc welding of Stainless and Heat Resisting Steels*, ed, 2017.
- [13] A. W. Marshall and J. C. M. Farrar, "Lean austenitic Type 16.8.2 stainless steel weld metal," *Stainless Steel World*, 2001.
- [14] J. M. Leitnaker, "Prevention of Chi and Sigma Phases Formation in Aged 16-8-2 Weld Metal," *Welding Journal*, 1982.
- [15] R. W. Messler and L. Li, "Weld heat affected zone liquation cracking in type 347 stainless steel," *Science and Technology of Welding and Joining*, vol. 2, p. 10, 1997.
- [16] C. D. Lundin, C. H. Lee, R. Menon, and V. Osorio, "Weldability evaluations of modified 316 and 347 austenitic stainless steels part 1 " *Welding Journal*, 1988.
- [17] T. M. Cullen and J. W. Freeman, "Metallurgical Factors Influencing Hot Ductility of Austenitic Piping at Weld Heat Affected Zone Temperatures," *ASME Jnl. of Engineering for Power*, pp. 151-164, 1963.
- [18] C. D. Lundin and e. al, "Ferrite-fissuring relationship in austenitic stainless steel weld metals," *Welding Journal*, 1975.
- [19] K. J. Irvine, J. D. Murray, and F. B. Pickering, "The Effect of Heat Treatment and Microstructure on the High-Temperature Ductility of 18%Cr-12%Ni-1%Nb Steels," *Journal of Iron and Steel Institute*, pp. 166-179, 1960.
- [20] K. X. Guan, X.; Xu, H.; Wang, Z. , "Effect of Aging at 700 Deg C on Precipitation and Toughness of AISI for 321 and AISI 347 Austenitic Stainless Steel Welds," *Nuclear Engineering and Design*, vol. 235, pp. 2485-2494, 2005.

- [21] J. C. van Wortel, "Prevention of Relaxation Cracking By Material Selection and or Heat Treatment," 2000.
- [22] C. E. v. d. Westhuizen, "Stress Relaxation Cracking of Welded Joints in Thick Sections of a TP347 Stabilized Grade of Stainless Steel," *Corrosion & NACE International*, 2008.
- [23] A. Dhooge, "Survey on reheat cracking in austenitic stainless steels and Ni base alloys," *Welding in the World*, vol. 41, pp. 206-219, 1998.
- [24] L. Li and R. W. Messler, "Stress Relaxation Study of HAZ Reheat Cracking in Type 347 Stainless Steel," *Welding Journal*, pp. 137-144, 2000.
- [25] N. Morishige, M. Kuribashi, H. Okabayashi, and T. Naiki, "On the Prevention of Service Failure in Type 347 Stainless Steel," presented at the Third International Symposium of the Japan Welding Society, 1978.
- [26] H.-s. Lee, J.-s. Jung, D.-s. Kim, and K.-b. Yoo, "Failure analysis on welded joints of 347H austenitic boiler tubes," *Engineering Failure Analysis*, vol. 57, pp. 413-422, 2015.
- [27] J. A. Siefert, J. P. Shingledecker, J. N. DuPont, and S. A. David, "Weldability and weld performance of candidate nickel based superalloys for advanced ultrasupercritical fossil power plants Part II: weldability and cross-weld creep performance," *Science and Technology of Welding and Joining*, vol. 21, pp. 397-428, 2016.
- [28] C. Fink, H. Wang, B. T. Alexandrov, and J. Penso, "Filler Metal 16-8-2 for Structural Welds on 304H and 347H Stainless Steels for High Temperature Service," *Welding Journal*, vol. 99, 2020.
- [29] J. W. Elmer, D. L. Olson, and D. K. Matlock, "The Thermal Expansion Characteristics of Stainless Steel Weld Metal," *Welding Journal*, 1982.
- [30] M. A. Ghalambaz, M.; Eslami, A.; Bahrami, A., "A case study on failure of AISI 347H stabilized stainless steel pipe in petrochemical plant," *Case Studies in Engineering Failure Analysis*, vol. 9, pp. 52-62, 2017.
- [31] C. Sarich, B. Alexandrov, A. Benatar, and J. Penso, "Test for stress relief cracking susceptibility in creep resistant chromium-molybdenum steels," *Science and Technology of Welding and Joining*, vol. 27, pp. 265-281, 2022.
- [32] K. Strader, B. T. Alexandrov, and J. C. Lippold, "Stress-Relief Cracking in Simulated-Coarse-Grained Heat Affected Zone of a Creep-Resistant Steel," in *Cracking Phenomena in Welds IV*, ed: Springer, 2016, pp. 475-493.
- [33] J. G. Nawrocki, J. N. Dupont, C. V. Robino, J. D. Puskar, and A. R. Marder, "The Mechanism of Stress-Relief Cracking in a Ferritic Alloy Steel," *Welding Research*, p. 11, 2003.
- [34] V. O. B. Messer, T. Phillips, "Optimized Heat Treatment of 347 Type Stainless Steel Alloys for Elevated Temperature Service to Minimize Cracking," *Corrosion*, 2004.
- [35] J. Goldak, A. Chakravarti, and M. Bibby, "A new finite element model for welding heat sources," *Metallurgical Transactions B*, vol. 15, p. 7, 1984.
- [36] Y. Hong, T. Pickle, J. Vidal, C. Augustine, and Z. Yu, "Impact of Plate Thickness and Joint Geometry on Residual Stresses in 347H Stainless Steel Welds," *Welding Journal*, 2023.
- [37] F. R. Larson and J. Miller, "A Time-Temperature Relationship for Rupture and Creep Stresses," in *Trans. ASME*, 1952.
- [38] Y. Cui and C. D. Lundin, "Ferrite number as a function of the Larson-Miller Parameter for Austenitic Stainless Steel Metals after Creep Testing," *Metallurgical and Materials Transactions A*, vol. 35A, 2004.

- [39] H. J. Frost and M. F. Ashby, *Deformation-Mechanism Maps: The Plasticity and Creep of Metals and Ceramics*: Pergamon Press, 1982.
- [40] G. E. Dieter, *Mechanical Metallurgy*, 3rd ed.: McGraw-Hill Education, 1986.
- [41] M. B. Prime, R. J. Sebring, J. M. Edwards, D. J. Hughes, and P. J. Webster, "Laser surface-contouring and spline data-smoothing for residual stress measurement," *Experimental Mechanics*, vol. 44, pp. 176-184, 2004.
- [42] ASME, "Boiler and Pressure Vessel Code," in *VIII: Rules for Construction of Pressure Vessels*, ed, 2019.
- [43] A. W. Society, "AWS D10.10 Standard: Recommended Practices for Local Heating of Welds in Piping and Tubing," ed, 1999, p. 107.
- [44] J. Siefert, J. Shingledecker, and T. Lolla, "Stress Relaxation Cracking (SRxC) and Strain Induced Precipitation Hardening (SIPH) Failures," in *DOE Workshop: Evaluation of Welding Issues in High Nickel and Stainless Steel Alloys for Advanced Energy Systems*, 2021.
- [45] W. R. Council, "452: Recommended Practices for Local Heating of Welds in Pressure Vessels," ed, 2000.
- [46] P. J. Bouchard, D. George, J. R. Santisteban, G. Bruno, M. Dutta, L. Edwards, *et al.*, "Measurement of the residual stresses in a stainless steel pipe girth weld containing long and short repairs," *International Journal of Pressure Vessels and Piping*, vol. 82, pp. 299-310, 2005.
- [47] https://www.engineeringtoolbox.com/permeability-d_1923.html.
- [48] <https://www.thoughtco.com/table-of-electrical-resistivity-conductivity-608499>.
- [49] T. J. Pickle, Z. Yu, J. Vidal, K. O. Findley, and S. Liu, "Effect of PWHT and Filler Metal on Stress Relaxation Cracking Susceptibility in 347H Stainless Steel Welds for Elevated Temperature Service-M.S. Thesis," Colorado School of Mines, Arthur Lakes Library, 2021.
- [50] A. W. Society, "D1.6 Structural Welding Code-Stainless Steel," ed, 2007.
- [51] G. A. Young, T. E. Capobianco, M. A. Penik, B. W. Morris, and J. J. McGee, "The Mechanism of Ductility Dip Cracking in Nickel-Chromium Alloys," *Welding Journal*, vol. 87, 2008.